DYNAMICS OF GREENLAND'S GLACIAL FJORDS

by

Rebecca H. Jackson

B.S., Yale University (2010)

Submitted in partial fulfillment of the requirements for the degree of

Doctor of Philosophy

at the

MASSACHUSETTS INSTITUTE OF TECHNOLOGY

and the

WOODS HOLE OCEANOGRAPHIC INSTITUTION

June 2016

©2016 Rebecca H. Jackson.
All rights reserved.
The author hereby grants to MIT and WHOI permission to reproduce and to distribute publicly paper and electronic copies of this thesis document in whole or in part in any medium now known or hereafter created.

Author ....
Joint Program in Oceanography/Applied Ocean Science & Engineering
Massachusetts Institute of Technology & Woods Hole Oceanographic Institution
April 12, 2016

Certified by..
Dr. Fiamma Straneo
Senior Scientist in Physical Oceanography
Woods Hole Oceanographic Institution
Thesis Supervisor

Accepted by ....
Dr. Lawrence J. Pratt
Senior Scientist in Physical Oceanography
Woods Hole Oceanographic Institution
Chair, Joint Committee for Physical Oceanography

DYNAMICS OF GREENLAND'S GLACIAL FJORDS

by

Rebecca H. Jackson

Submitted to MIT-WHOI Joint Program in Oceanography and Applied Ocean Science and Engineering,
in partial fulfillment of the requirements for the degree of Doctor of Philosophy in Physical Oceanography

ABSTRACT

Glacial fjords form conduits between glaciers of the Greenland Ice Sheet and the North Atlantic. They are the gateways for importing oceanic heat to melt ice and for exporting meltwater into the ocean. Submarine melting in fjords has been implicated as a driver of recent glacier acceleration; however, there are no direct measurements of this melting, and little is known about the fjord processes that modulate melt rates. Combining observations, theory, and modeling, this thesis investigates the circulation, heat transport, and meltwater export in glacial fjords.

While most recent studies focus on glacial buoyancy forcing, there are other drivers – e.g. tides, local wind, shelf variability – that can be important for fjord circulation. Using moored records from two major Greenlandic fjords, shelf forcing (from shelf density fluctuations) is found to dominate the fjord circulation, driving rapid exchange with the shelf and large heat content variability near the glacier. Contrary to the conventional paradigm, these flows mask any glacier-driven circulation in the non-summer months. During the summer, when shelf forcing is reduced and freshwater forcing peaks, a mean exchange flow transports warm Atlantic-origin water towards the glacier and exports glacial meltwater.

Many recent studies have inferred submarine melt rates from oceanic heat transport, but the fjord budgets that underlie this method have been overlooked. Building on estuarine studies of salt fluxes, this thesis presents a new framework for assessing glacial fjord budgets and revised equations for inferring meltwater fluxes. Two different seasonal regimes are found in the heat/salt budgets for Sermilik Fjord, and the results provide the first time-series of submarine meltwater and subglacial discharge fluxes into a glacial fjord.

Finally, building on the observations, ROMS numerical simulations and two analytical models are used to investigate the dynamics of shelf-driven flows and their importance relative to local wind forcing across the parameter space of Greenland's fjords. The fjord response is found to vary primarily with the width relative to the deformation radius and the fjord adjustment timescale relative to the forcing timescale. Understanding these modes of circulation is a step towards accurate modeling of ocean-glacier interactions.

Thesis Supervisor: Dr. Fiamma Straneo
Title: Senior Scientist in Physical Oceanography
Woods Hole Oceanographic Institution

Acknowledgments

I have many people to thank for contributing to this work and for making my time in the Joint Program so enriching and enjoyable. First, I would like to thank Fiamma for being a wonderful advisor and mentor to me. Her support and her holistic approach to mentoring – promoting scientific growth, career development, and work-life balance – have made my graduate experience a very positive one. I appreciate how she has given me ample freedom to explore ideas while also helping me to stay focused and see the big picture. I would like to thank her for six exhilarating field trips to Greenland and for countless other opportunities. Working and traveling with Fiamma has been a ton of fun, and I look forward to ongoing collaborations in the years to come.

I owe many thanks to my committee for their input and support along the path to this thesis. I would like to thank Steve Lentz for providing constructive feedback at all stages of this work and for being incredibly generous with his time. Steve's insightful questions have often propelled my work forward and have constantly stoked my curiosity. I have learned so much from our conversations. I would like to thank Rocky Geyer for his feedback and enthusiasm, and for bringing an estuarine perspective to my work. I always leave our meetings with a long list of exciting ideas. I would like to thank Glenn Flierl for his insightful comments and for his attention to detail – this thesis has greatly benefited from his sharp eye. I would like to thank Patrick Heimbach for his support and for helping me to see my work in the context of larger modeling efforts. In addition to my committee, I would like to thank Claudia Cenedese for chairing my thesis defense and for many stimulating conversations over the years.

Many scientists in the Physical Oceanography department at WHOI have contributed valuable input and have helped make this a wonderful place for me to work. In particular, I would like to thank Ken Brink for sparking my interest in coastal PO and for productive discussions about my research. I would also like to thank Jake Gebbie for providing the computing resources that made it possible to run the ROMS simulations at a quick pace.

I would like to thank the members of Fiamma's group, past and present, for all their help and for creating a lively and tight-knit community of collaborators: Clark Richards, Ben Harden, Marilena Oltmanns, Andree Ramsey, Roberta Sciascia, Ken Mankoff, Mattias Cape, Nick Beaird, Nat Wilson and Laura Stevens. There are also many people to thank for their role in collecting the data used in this thesis, including Dave Sutherland, Magdalena Andres, Will Ostrom, Jim Ryder, John Kemp and the WHOI Mooring Group, Dan Torres, Andree Ramsey, and the crew of the M/V Viking. In particular, I would like to thank Will Ostrom: his expertise in moorings made this work possible and his sensor of humor and boundless energy made the fieldwork a total blast.

I would like to thank my officemates, Isabela Le Bras and Deepak Cherian, not only for being superb company but also for their contributions to my research through many conversations and brainstorming sessions in our office. Deepak was instrumental in my work with ROMS, patiently helping me work towards a good model setup. I would also like to thank all of my PO classmates for constant support and camaraderie. In particular, Melissa Moulton and Dan Amrhein have helped me out at so many stages, always there with the right piece of Matlab code, food, or advice.

The Academic Programs Office takes wonderful care of the JP students, for which I am very grateful. Thank you to Jim, Meg, Lea, Julia, Christine, Valerie and all members of APO for their support and for making everything run so smoothly in the JP. I would also like to thank all of the administrative staff in the Physical Oceanography department, especially Annie, Jean and Hazel, for their patient help on a regular basis.

I would like to thank my friends in Woods Hole and Cambridge for making my graduate years so much fun and filled with many adventures. And a huge thank you to Nick for all his support

and encouragement. Lastly, I owe endless thanks to my family for their unwavering support and for being a constant source of inspiration.

Funding for this thesis was provided by the National Science Foundation (OCE-1130008, OCE-1434041 and OPP-909373), WHOI Coastal Ocean Institute, WHOI Ocean Climate Change Institute, and the Kerr Foundation.

Contents

Chapter 1

Introduction

1.1 Ocean-glacier interactions in Greenland

Many outstanding questions regarding the earth's climate lie at the nexus of ocean and cryosphere. The Greenland Ice Sheet is losing 260 Gt/yr of ice and contributing 0.6 mm/yr to global sea level rise (Shepherd et al., 2012). The mass loss is concentrated around the margins of the ice sheet, where glaciers that drain the ice sheet come into contact with the ocean (Fig. 1-1). The largest uncertainties in sea level projections arise from the unknown drivers of ice sheet mass loss in Greenland and Antarctica (IPCC 2013).

For an ice sheet in steady state, snow accumulation over the interior balances ice loss at the margins, through surface melting at the ice-atmosphere boundary and ice discharge at the ice-ocean boundary. The ice discharge can be further subdivided into submarine melting and iceberg calving. For most glaciers around Greenland, the majority of ice is discharged via icebergs (Enderlin and Howat, 2013), in contrast to Antarctica where submarine melting is the dominant mode of ice discharge. Despite its relatively small role in the overall balance mass of the Greenland Ice Sheet, submarine melting has been implicated as a trigger for the recent mass loss.

Approximately one half of the recent mass loss from Greenland is attributed to increased surface melting (van den Broeke et al., 2009), a well understood process: warmer air temperatures have led to more surface melting. The other half of the mass loss comes from changes in ice discharge – glaciers that drain the ice sheet have accelerated and retreated – but this dynamic component of mass loss is more complicated and poorly understood. The synchronous acceleration of many outlet glaciers originated at their marine termini (Nick et al., 2009; Vieli and Nick, 2011; Howat et al., 2007) and coincided with warming ocean temperatures around Greenland (Holland et al., 2008a;

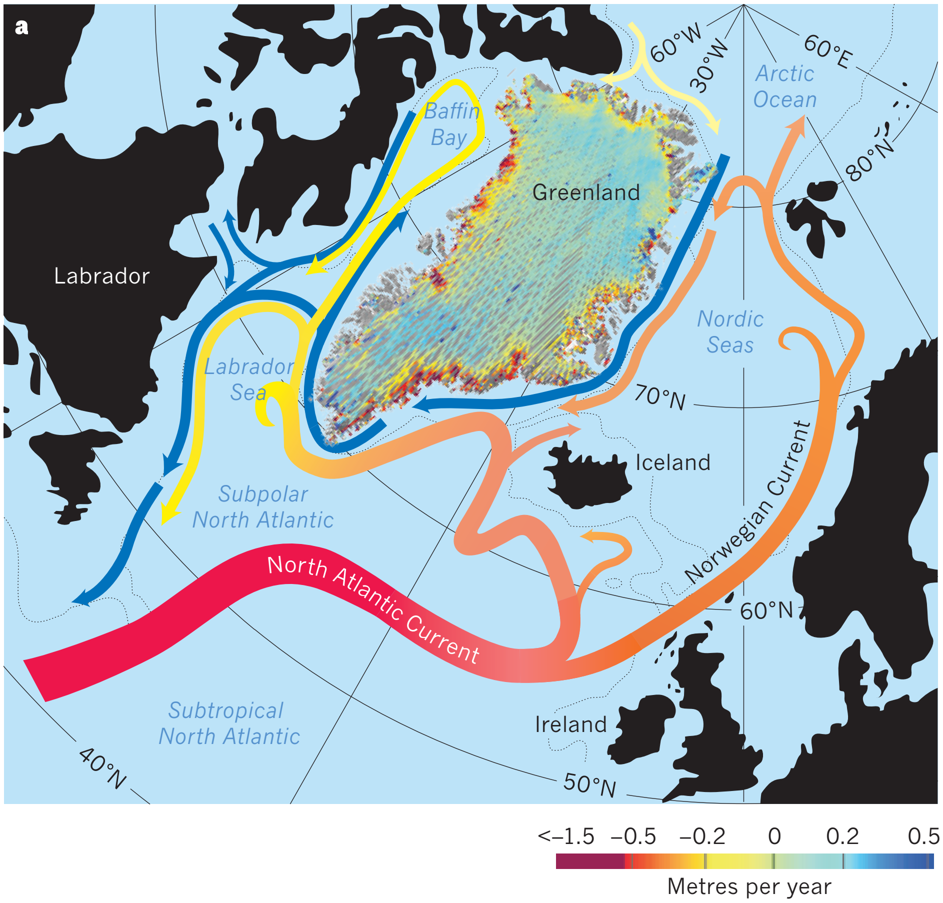

Figure 1-1: Schematic of ocean currents around Greenland from Straneo and Heimbach (2013), with ice sheet surface elevation change from Pritchard et al. (2009), showing mass loss concentrated around the ice sheet's margins. Ice change measurements cover the period of 2003-2007. Currents carrying warm Atlantic-origin water are shown in red/orange/yellow, with the color fading to represent the cooling of Atlantic water as it transits around the Arctic. Blue currents carry Polar-origin water.

Våge et al., 2011). While there are several possible mechanisms at play, a leading hypothesis is that increased submarine melting at the glaciers' termini triggered a dynamic ice acceleration (Murray et al., 2010; Joughin et al., 2012; Straneo and Heimbach, 2013). Thus, changes in the subpolar North Atlantic and in the Atlantic-origin water that circulates around Greenland (Fig. 1-1) might play a role in driving ice sheet mass loss.

In the other direction, changes in the ice sheet also impact the ocean. The Greenland Ice Sheet is a growing source of freshwater to the polar ocean (Bamber et al., 2012) that could potentially alter coastal currents and eventually the meridional overturning circulation (Weijer et al., 2012; Lenaerts et al., 2015). In addition to providing buoyancy forcing and a net freshening, the input of meltwater at depth drives upwelling of heat and nutrients around the margins of the ice sheet

(Jenkins, 1999; Cottier et al., 2010; Beaird et al., 2015). The fjords of Greenland are estuaries where glacial freshwater is mixed and exported; they form a conduit between the ice sheet and the large-scale ocean. Any change in the ice sheet or ocean that is felt by the other must be communicated through fjord processes.

1.2 Unknown dynamics in glacial fjords

Understanding the coupled evolution of the ocean and ice sheet involves many oceanic scales, from the gyre-scale circulation at $\mathcal{O}(1000\text{ km})$ down to turbulent fluxes at ice-ocean boundary layer, $\mathcal{O}(1\text{ m})$. While the large-scale ocean circulation around Greenland has been studied for many years, the glacial fjords – where ocean and glaciers directly interact – have been largely overlooked until the past decade.

To set the scene, most of Greenland's marine glaciers terminate in fjords with a vertical calving front, often 100 to 1000 m deep (Fig. 1-2). The major outlet glaciers flow into the ocean at ∼10 km/yr (Moon et al., 2012), discharging a volume flux of iceberg and submarine meltwater on the order of 1000 m^3/s. An ice melange of floating icebergs and sea ice often extends in front of the glacier, rendering the near-glacier waters inaccessible by boat.

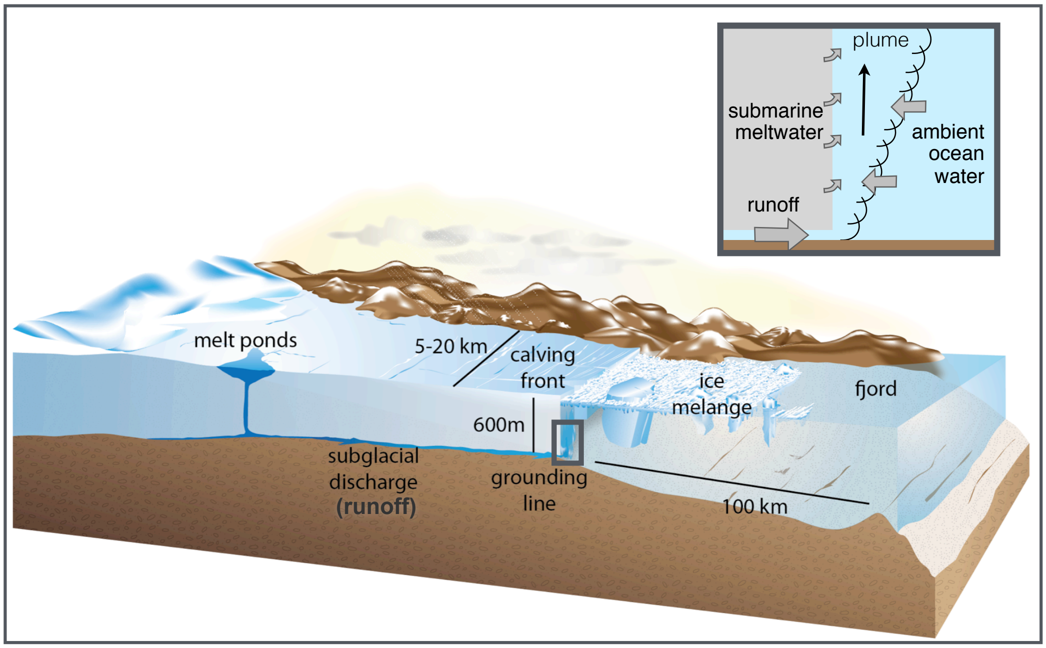

Figure 1-2: Schematic of a typical tidewater glacier/fjord system in Greenland. Inset magnifies the region near the grounding line, where a buoyant plume fed by runoff and submarine meltwater entrains ambient ocean water. Schematic adapted from Straneo et al. (2013).

Submarine meltwater is only one source of liquid freshwater to glacial fjords; surface melt also drains through a systems of moulins and channels to the base of the glacier and enters the fjord as subglacial discharge/runoff (Fig. 1-2; Chu, 2014). Thus, the glacier provides two sources of liquid freshwater that form turbulent buoyant plumes at the ocean/ice interface (Jenkins, 2011). The plumes upwell and then, depending on their entrainment rate, either reach the surface or outflow subsurface (e.g. Salcedo-Castro et al., 2011; Sciascia et al., 2013; Stevens et al., 2015). These glacial plumes enter fjords that are typically deep, strongly stratified and composed of the two water masses from the shelf: warm, salty Atlantic-origin water at depth and cooler, fresher Polar-water at the surface (Straneo et al., 2012).

It is warming in this Atlantic-origin water that is believed to have triggered an acceleration of outlet glaciers in the past decade (Holland et al., 2008a; Murray et al., 2010; Straneo and Heimbach, 2013). However, this hypothesis is difficult to test because there are no direct measurements of submarine melting and only a limited understanding of the fjord circulation or variability. The drivers of heat transport and meltwater export are largely unknown.

The majority of recent work on Greenland's glacial fjords is based on brief summer surveys or modeling. On the modeling side, studies have focused on the upwelling plumes and near-glacier circulation ($\mathcal{O}$(100 m) of the terminus) where there are almost no observations. Modeling studies that explore the controls on submarine melting all show that the melt rate increases with subglacial discharge and with ambient ocean temperature (e.g. Jenkins, 2011; Xu et al., 2012; Sciascia et al., 2013). These modeling results, however, are sensitive to their parameterizations of turbulent fluxes, which are tuned to match plume theory. Furthermore, even if these model-derived relationships between ocean temperature, subglacial discharge, and submarine melting are correct, all three of these pieces are poorly constrained by observations.

In the first of these three pieces, the ocean temperature and its variability near glaciers is not well measured. Most studies are based on synoptic shipboards surveys – icebergs pose major obstacles to moorings – and are primarily focused on summer conditions (e.g. Holland et al., 2008a; Rignot et al., 2010; Straneo et al., 2011; Mortensen et al., 2011; Chauché et al., 2014). These studies have provided novel insights into the water masses, stratification, and the spread of glacially modified water (often subsurface) (e.g. Johnson et al., 2011; Straneo et al., 2011; Inall et al., 2014). However, given the limited temporal resolution of these fjord surveys and few velocity measurements, little is known about the temperature variability or modes of fjord circulation.

The other two pieces, the subglacial discharge and the submarine melt rate – the direct link between ocean and ice – are also poorly constrained. Neither has been directly measured at the terminus of a tidewater glacier. Subglacial discharge is typically estimated with regional climate models (e.g. Mernild and Liston, 2012; Andersen et al., 2010; Van As et al., 2014). A growing number of studies attempt to infer submarine melting from measurements of ocean heat transport. However, these have been based on brief synoptic measurements, and the prevalent equations of this method are oversimplified, with many implicit and untested assumptions. The complete glacial fjord budgets – of heat, salt and mass – that underlie such methods have never been explored.

Furthermore, modeling studies have focused on the glacier's buoyancy driven circulation, both in the near-glacier region and at the fjord-scale (Xu et al., 2013; Sciascia et al., 2013; Kimura et al., 2014; Carroll et al., 2015). According to the conventional paradigm for Greenland's fjords as a buoyancy-driven regime, the freshwater inputs from glaciers control renewal of water and heat into the fjord, allowing for positive feedbacks between melting and heat transport. There are, however, many other potential drivers of fjord circulation, including tides, local wind forcing, and shelf forcing, that could play an important role in transporting heat and exporting meltwater. Answering questions about the ocean's impact on the glaciers or the glacier's impact on the ocean requires resolving the dynamics of Greenland's glacial fjords.

1.3 Glacial fjords: outliers in the estuarine world

Glacial fjords are fundamentally estuaries. The extensive estuarine and fjord literature, however, does not adequately account for these rogue estuaries. While typical estuaries and fjords have freshwater input at the surface, freshwater from a glacier often enters hundreds of meters below the surface. While typical fjords have a shallow sill and only one oceanic water mass inside the fjord, Greenland's glacial fjord are usually deep and strongly stratified with multiple water masses from the shelf. While friction plays a dominant role in most estuaries, often balancing an along-estuary pressure gradient, friction should be relatively weak in the deep fjords of Greenland. Lastly, instead of being spread throughout the estuary or concentrated at topographic features, the vast majority of mixing in glacial fjords occurs where convective plumes emanate from the glacier. For these and other reasons, the existing estuarine paradigms are largely inapplicable to Greenland's glacial fjords.

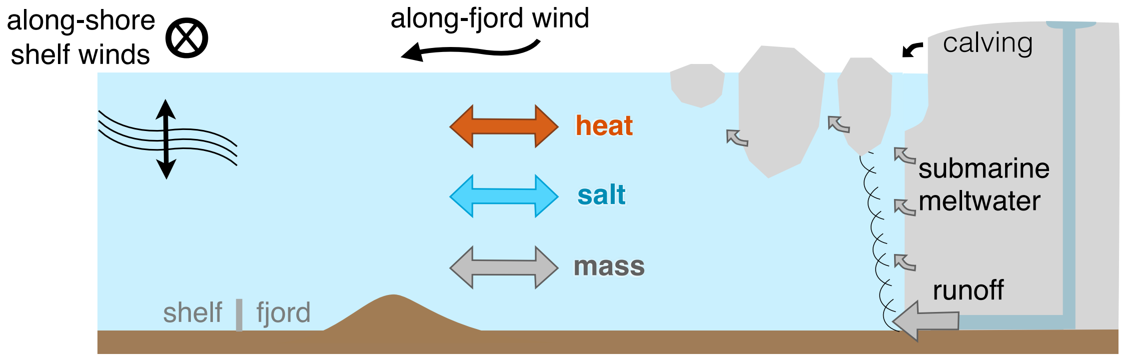

Figure 1-3: Schematic of glacier, fjord and shelf, including some potential drivers of circulations: shelf winds and shelf density variability; local along-fjord winds; and freshwater from the glacier (submarine melting and runoff).

1.4 Driving questions of this thesis

This thesis aims to answer fundamental questions about the dynamics of Greenland's glacial fjords. Observations, theory, and numerical modeling are used to investigate the drivers of fjord circulation, heat transport and freshwater export near outlet glaciers. The driving questions of this thesis, which are also illustrated in Fig. 1-3, are as follows:

Chapter 2:

- What are the dominant drivers of circulation in east Greenland's glacial fjords?
- What drives temperature variability near glaciers?

Chapter 3:

- What are the dominant balances in the heat, salt and mass budgets for a glacial fjord?
- How are heat, salt and meltwater transported through the fjord?
- What are the magnitudes and seasonality of the freshwater fluxes (submarine melting and runoff) into glacial fjords?

Chapter 4:

- How does shelf density variability drive fjord flows in fjords around Greenland?
- What is the relative importance of shelf forcing versus local wind forcing?

Thesis outline

In Chapter 2, the drivers of fjord circulation and variability are explored in two major fjords of east Greenland. Moored records of velocity and water properties show rapid exchange between the shelf and fjords that is driven by shelf density fluctuations (which are primarily associated with along-shore winds). These synoptic shelf-driven flows allow the fjords to track shelf variability on short timescales and result in large temperature fluctuations in the upper fjord, near the glacier. Contrary to the conventional paradigm for glacial fjords, these flows mask any glacier-driven circulation during the non-summer months. The submarine melt-rate is dependent on the near-glacier temperature and velocity, so these shelf-forced dynamics are important for accurate modeling and prediction of submarine melting.

In Chapter 3, the heat, salt and volume budgets for glacial fjords are explored in order to understand the dominant balances and modes of transport, and also to quantify the heretofore unknown freshwater fluxes and their seasonality. Building on estuarine studies of salt budgets, we present an alternative framework for decomposing fjord budgets and new equations for inferring meltwater fluxes. These methods are then applied to moored records from Sermilik Fjord, near the terminus of Helheim Glacier, to evaluate the dominant balances in the fjord budgets and to estimate freshwater fluxes. Seasonally, we find two different regimes of heat, salt and meltwater transport. Our results highlight many important components of fjord budgets, particularly the storage and barotropic terms, that have been neglected in previous estimates of submarine melting. Additionally, these provide the first timeseries of subglacial discharge and submarine meltwater fluxes into a a glacial fjord.

In Chapter 4, the dynamics of shelf-forced flows in fjords are investigated with numerical simulations and theory to explore the nature of shelf-driven circulation and how it varies across different fjords. Building on the observations Sermilik Fjord, we use ROMS numerical simulations and two analytical models to study the dynamics of shelf-driven flows and their competition with local forcing within a fjord. We investigate the relative importance of the shelf forcing in driving fjord/shelf exchange across a wide parameter space of fjord geometries and stratifications.

Overall, this thesis investigates the drivers of fjord circulation, heat transport, and meltwater export in Greenland's glacial fjords, aiming to make a step towards understanding ocean-glacier interactions and towards accurate modeling of coupled ice sheet/ocean evolution in a changing climate.

Chapter 2

Externally-forced fluctuations in ocean temperature at Greenland glaciers in non-summer months

This chapter was originally published as: Jackson, R. H., Straneo, F. & Sutherland, D. A.: Externally forced fluctuations in ocean temperature at Greenland glaciers in non-summer months. *Nature Geoscience*, 7, 503-508 (2014). Used with permission as granted in the original copyright agreement.

2.1 Abstract

Enhanced submarine melting of outlet glaciers has been identified as a plausible trigger for part of the Greenland Ice Sheet's accelerated mass loss (Thomas, 2004; Holland et al., 2008a; Vieli and Nick, 2011), which currently accounts for a quarter of global sea level rise (Shepherd et al., 2012). However, our understanding of what controls the submarine melt rate is limited and largely informed by brief summer surveys in the fjords where glaciers terminate. Here, using continuous water property and velocity records from September through May in two large fjords – into which Helheim and Kangerdlugssuaq Glaciers drain – we show that water properties, including heat content, vary significantly over synoptic timescales 3 to 10 days. This variability results from frequent, shelf-forced pulses that drive rapid exchange with the shelf and mask any signal of a glacial freshwater-driven circulation. Our results suggest that, during non-summer months, the melt rate varies substantially and is dependent on externally-forced ocean flows that rapidly translate changes on the shelf towards

the glaciers' margins.

2.2 Introduction

The submarine melt rate depends on near-glacier ocean temperature and circulation (e.g. Jenkins et al., 2010). Recent studies assume that both these things are governed by the glacier's freshwater inputs (Motyka et al., 2003; Rignot et al., 2010; Jenkins, 2011; Xu et al., 2012; Sciascia et al., 2013), and that other drivers, such as tides, air-sea fluxes and shelf-driven exchange, can be neglected. In this prevailing framework, submarine meltwater and subglacial discharge (surface meltwater draining at the glacier's base) form buoyant plumes, entrain ambient water and drive an overturning circulation that transports shelf waters towards the glacier. Under this assumption, enhanced subglacial discharge increases ocean heat transport, submarine melting, and the renewal of near-glacier waters (Jenkins, 2011; Xu et al., 2012; Sciascia et al., 2013).

However, the extent to which the glacier-driven circulation influences the renewal of warm water in the fjords is unclear. Limited velocity data indicates that shelf variability may play an important role in driving fjord flows (Rignot et al., 2010; Straneo et al., 2010), though conclusive evidence is absent. Furthermore, most observational studies rely on brief, summer surveys (Holland et al., 2008a; Rignot et al., 2010; Christoffersen et al., 2011; Straneo et al., 2011; Johnson et al., 2011; Xu et al., 2013; Inall et al., 2014) that offer limited insight into drivers of summer variability and no information about non-summer months.

2.3 Setting

Here, we present new insight into fjord dynamics from moored records in Sermilik and Kangerdlugssuaq Fjords (Fig. 2-1a), where Helheim and Kangerdlugssuaq Glaciers deposit freshwater as submarine meltwater, subglacial discharge, surface runoff, and icebergs. These are the fifth and third largest outlets of the Greenland Ice Sheet, respectively, in terms of total ice discharge (Enderlin et al., 2014). The vertical calving fronts of both glaciers ground ∼600 m below sea level at the head of their respective fjords (Straneo et al., 2012). The fjords, which are ∼70/100 km long and ∼7 km wide, connect the glaciers to the continental shelf. The predominant water masses of Greenland's southeast shelf form a two-layer structure within Sermilik Fjord: cold, fresh Polar water (PW) overlies warm, salty Atlantic-origin water (AW), with some modification due to glacial inputs (Fig. 2-1; Sutherland and Pickart, 2008; Straneo et al., 2010, 2011). A similar water mass structure is found in Kangerdlugssuaq, with additional dense Atlantic water originating in the Nordic Seas (Christoffersen et al., 2012). In both Sermilik and Kangerdlugssuq fjords, the shallowest sills (at 530 and 550 m, respectively) are well below the AW/PW interface (Schjøth et al., 2012; Sutherland et al., 2013; Inall et al., 2014), allowing for relatively unimpeded exchange between the fjord and shelf (bathymetry shown in Fig. 2-1a & b). The shelf region of southeast Greenland outside both fjords is characterized by frequent, strong, along-shore winds (Harden et al., 2011) and fast ocean currents (Sutherland and Pickart, 2008).

Winds and glacial freshwater discharge – two potential drivers of fjord circulation – exhibit a strong seasonality in this region. From September through May, shelf winds are strong along Greenland's southeast coast (Harden et al., 2011), and subglacial discharge is negligible as air temperatures drop below freezing (Mernild et al., 2010; Andersen et al., 2010). During summer, winds weaken, and subglacial discharge increases, becoming a larger freshwater source than submarine melt (Mernild et al., 2010; Andersen et al., 2010). This seasonality likely modulates the glacier-driven circulation and submarine melt rate; one modeling study estimated the summer melt rate at Helheim Glacier to be twice the non-summer rate due to variations in subglacial discharge (Sciascia et al., 2013). According to this scaling, nevertheless, 60% of the annual submarine melt would occur in non-summer months, an important but unstudied period.

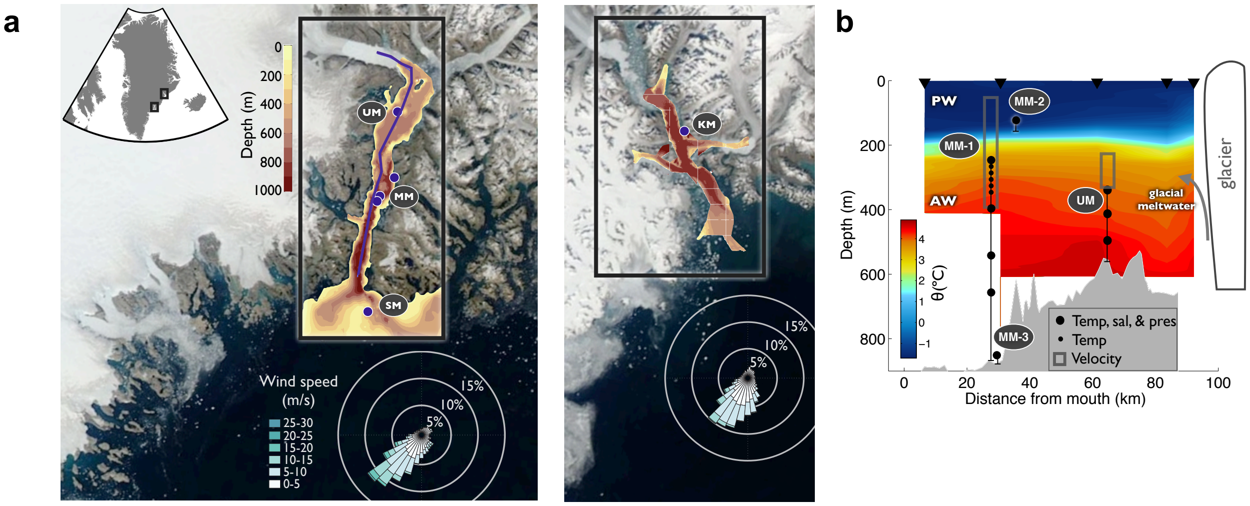

Figure 2-1: **a.** Satellite images of Sermilik and Kangerdlugssuaq Fjords with bathymetry overlaid. Circles indicate mooring locations and line shows path of along-fjord Sermilik profile in (b). Wind roses of speed and direction on the shelf are from ERA-Interim Reanalysis from 2009-2013. **b.** Along-fjord potential temperature from 2010 winter survey of Sermilik (Straneo et al., 2011) with schematic of Sermilik moorings (shelf mooring, SM, not shown), instruments and water masses. AW = Atlantic-origin water; PW = Polar-origin water.

2.4 Data: moorings and wind

Extensive oceanic water property and velocity records were collected during the non-summer months in 2011-2012 from Sermilik Fjord and the adjacent shelf (Fig. 2-2a-d) and in 2009-2010 from Kangerdlugssuaq Fjord (excluding velocity, Fig. 2-2e).

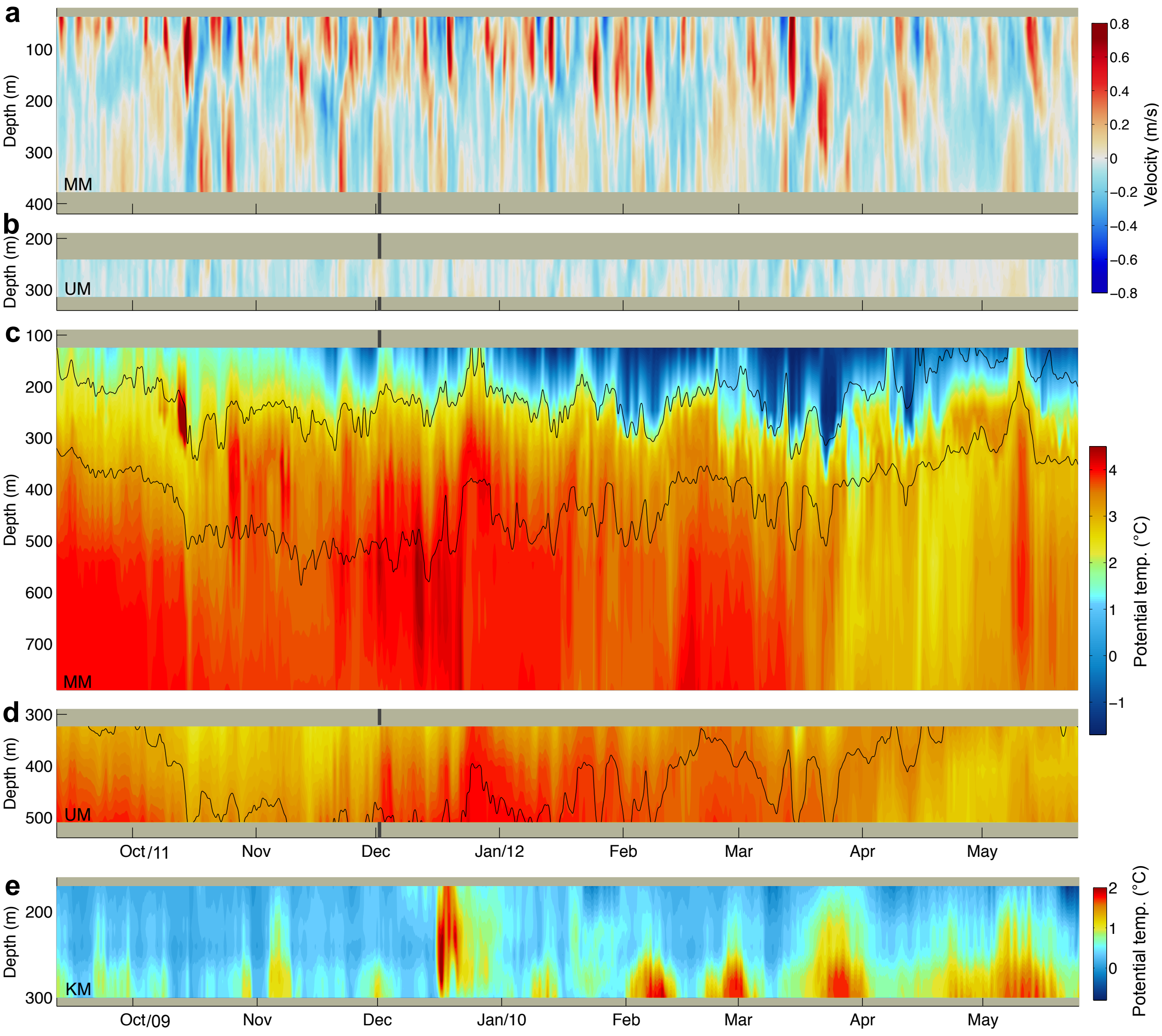

Figure 2-2: **a.** Along-fjord velocity in Sermilik at mid-fjord mooring (MM1); **b.** Along-fjord veloicty at upper-fjord mooring, UM. In both positive indicates up-fjord flow, towards the glacier. **c.** Potential temperature in Sermilik at mid-fjord, MM1-3. **d.** Potential temperature at upper-fjord, UM. Contours of $\sigma_\theta = [27.0, 27.5]$ kg/m^3 overlaid. **e.** Potential temperature in Kangerdlugssuaq at mid-fjord (KM1-3) for same nine months but different years (2009-2010). All records are low-pass filtered with a 4th order 26-hr Butterworth filter. Black line in a-d marks an up-fjord flow in the lower layer that is highlighted in Fig. 2-8.

In the Sermilik region, we deployed five moorings (SM, MM 1-3 and UM; locations in Fig. 2-1) to capture velocity in the fjord and water properties in the fjord and on the shelf. An upward-facing 75 kHz Acoustic Doppler Current Profiler (ADCP) on MM-1 measured velocity in 10 m bins between 388 m and the surface from August, 2011 through June, 2012. The upper three bins (centered at 28, 18 and 8 m) were discarded due to side-lobe contamination. An upward-facing 300 kHz ADCP on UM measured velocity in 8 m bins between 313 and 233 m from August, 2011 to September, 2012. Both instruments measured 10-minute averaged velocity every hour. Gaps in the records – often from instrument contamination (e.g. icebergs) or low-backscatter – were filled by removing a tidal fit, interpolating linearly, and adding back the tidal component. The along-fjord velocity was determined by rotating the velocity field into its principal axes and extracting the component along the major axis, which falls parallel to local bathymetry at both locations (32° and 35° from north at MM-1 and UM, respectively). The across-fjord velocities along the minor axis were smaller (with variance ∼90% smaller than along-fjord variance) and are not discussed here.

Concurrently, nine conductivity-temperature-pressure sensors (Seabird SBE 37SMs and RBR XR-420s at 291 m on SM, 125, 246, 396, 542, 657 and 851 m on MM 1-3 and 323, 406 and 510 m on UM) and five temperature sensors (Onset Tidbit v2 at 266, 286, 306, 326, and 346 m on MM 1-3) recorded water properties. All temperature records from the mid-fjord moorings, MM 1-3, were combined to make the depth versus time contour plots in Fig 2-2d, thereby neglecting horizontal variability between the nearby moorings. This approximation is supported by the synoptic surveys of the fjord and moored records, which show that the horizontal spatial variability within several kilometers is small compared to the variability in depth and time. Hydrographic surveys of the fjord were conducted upon mooring deployment and recovery and used to calibrate the moored instruments.

In Kangerdlugssuaq Fjord, we deployed three mid-fjord moorings (KM1-3) from August, 2009 to September, 2010 (location in Fig. 2-1). Two temperature-conductivity-depth sensors (RBR XR-420s) were deployed at 166 m and 225 m on KM1 and KM2, respectively. KM3 was equipped with a depth recorder (RBR DR-1050) at 223 m and seven temperature sensors (Onset Tidbit v2) at 223 243, 253, 263, 273, 283 and 303 m depths.

The ERA-Interim reanalysis, deemed successful at capturing winds on the shelf of southeast Greenland (Harden et al., 2011), is used to assess the shelf wind field. Outside of Sermilik and Kangerdlugssuaq Fjords, the velocity component along the principle axis (230° and 210° from north, respectively) at a point 45 km offshore of each fjord's mouth was extracted for an along-shore wind time-series (locations and wind roses in Fig.2-1a; time-series in Fig. 2-4a). By this convention, downwelling-favorable winds from the northeast are positive.

2.5 Results

In Sermilik Fjord, the records indicate that AW and PW are always present, but their properties and thicknesses vary over timescales of hours to months (Fig. 2-2c & d). The upper water column near the AW/PW interface exhibits the largest variability, a result of both seasonal trends (Straneo et al., 2010) – e.g. PW deepening and cooling in the winter – and higher frequency fluctuations in the interface's depth, often exceeding 50 m over several days (Fig. 2-2c & d). Within the AW layer, temperature ranges from 2°C to 5.2°C and exhibits transient fluctuations (typically 0.3-0.7°C) that last several days, and more sustained shifts, such as an abrupt cooling in late March. Significant variability even exists at 851 m, well below sill depth.

The fjord's persistent stratification and occasional increases in heat content preclude internal mixing (which would reduce stratification and redistribute heat) or surface fluxes (which would reduce stratification and cool) from being the primary drivers of these changes. Instead, as will be shown here, we attribute the variability to rapid exchange with the shelf, driven by energetic, sheared flows in the along-fjord direction (Fig. 2-2a & b).

2.5.1 Description of velocity field

These pulses last several days and frequently exceed 50 cm/s in the upper layer, with mid-fjord root mean squared (RMS) velocities at all depths between 10 and 20 cm/s – much larger than the ∼2.5 cm/s root-mean square tidal component (Fig. 2-2a). The velocity typically reverses direction at the AW/PW interface (i.e. pycnocline) and is faster in the upper layer.

An EOF analysis of the mid-fjord velocity shows that the velocity structure is consistent with the first baroclinic dynamical mode calculated from the fjord stratification. An EOF analysis was performed both in a standard depth coordinate and in a rescaled depth coordinate based on the density field. In this latter transformed space, zero corresponds to the top of the velocity record, one to the bottom of the record, and 0.5 to the depth of the $\sigma = 27$ kg/m^3 isopycnal (after detrending with a 30-day 4th order Butterworth filter and adding back the mean), which is a proxy for the pycnocline or AW/PW interface. This rescaled depth variable was used to account for the variability in layer thicknesses. Similar results were found in both EOF analyses, with almost identical mode structures, although the first EOF in transformed space captured slightly more of the record variability (67% versus 62%). A section of the raw velocity record and the velocity reconstructed from the first EOF are shown in Fig. 2-3a, with the isopycnal used for scaling. This two-layer flow has peak variability at 4-10 day periods, i.e. synoptic timescales, as shown in the power spectrum of the first EOF's principle component (Fig. 2-3c).

We find that the first EOF mode structure closely resembles the first baroclinic mode based on the fjord stratification (Fig. 2-3b). Winter profiles from a survey of Sermilik Fjord in March, 2010 (Straneo et al., 2011) were used in conjunction with the moored water properties to construct a mean stratification profile and then compute the first baroclinic mode structure.

Upper-fjord velocities at UM (Fig. 2-2b) are reduced but well correlated with mid-fjord flow. RMS velocities in the upper fjord are approximately 5 cm/s, compared to a tidal component of 1 cm/s. If the AW/PW interface movements are approximately coherent throughout the fjord over the pulse timescale, we would expect the velocity to decay linearly towards the glacier in a rectangular fjord. Thus, we expect the upper-fjord speeds to be approximately 36% of those mid-fjord, based on the distance between UM and the head of the fjord (20 km) and between MM and UM (37 km), which is consistent with our observations. The velocities at UM and MM in the 320-290 m depth range are significantly correlated for every velocity bin (correlation coefficients all greater than $>$ 0.45).

2.5.2 Mid-fjord volume flux

The velocity pulses drive large volume transports and significant exchange with the shelf over short timescales. To calculate a time-series of volume fluxes in Sermilik (Fig. 2-4c), we assume that the mid-fjord velocity field is uniform across the width of the fjord at the mooring location. This is based on previous studies of lowered ADCP and CTD sections (Straneo et al., 2011; Sutherland and Straneo, 2012) that show small lateral shear across the fjord. Thus, we calculate volume flux in the upper layer as:

$$Q = \Sigma_{i=1}^{n} v_i W h \tag{2.1}$$

where: h equals 10 m, the depth range of each bin; W equals 7 km, the approximate width the fjord at the mooring location; n is the last bin above the AW/PW interface. This interface was chosen to be the 27 kg/m^3 potential density contour from the 30-day high-pass filtered density field. The

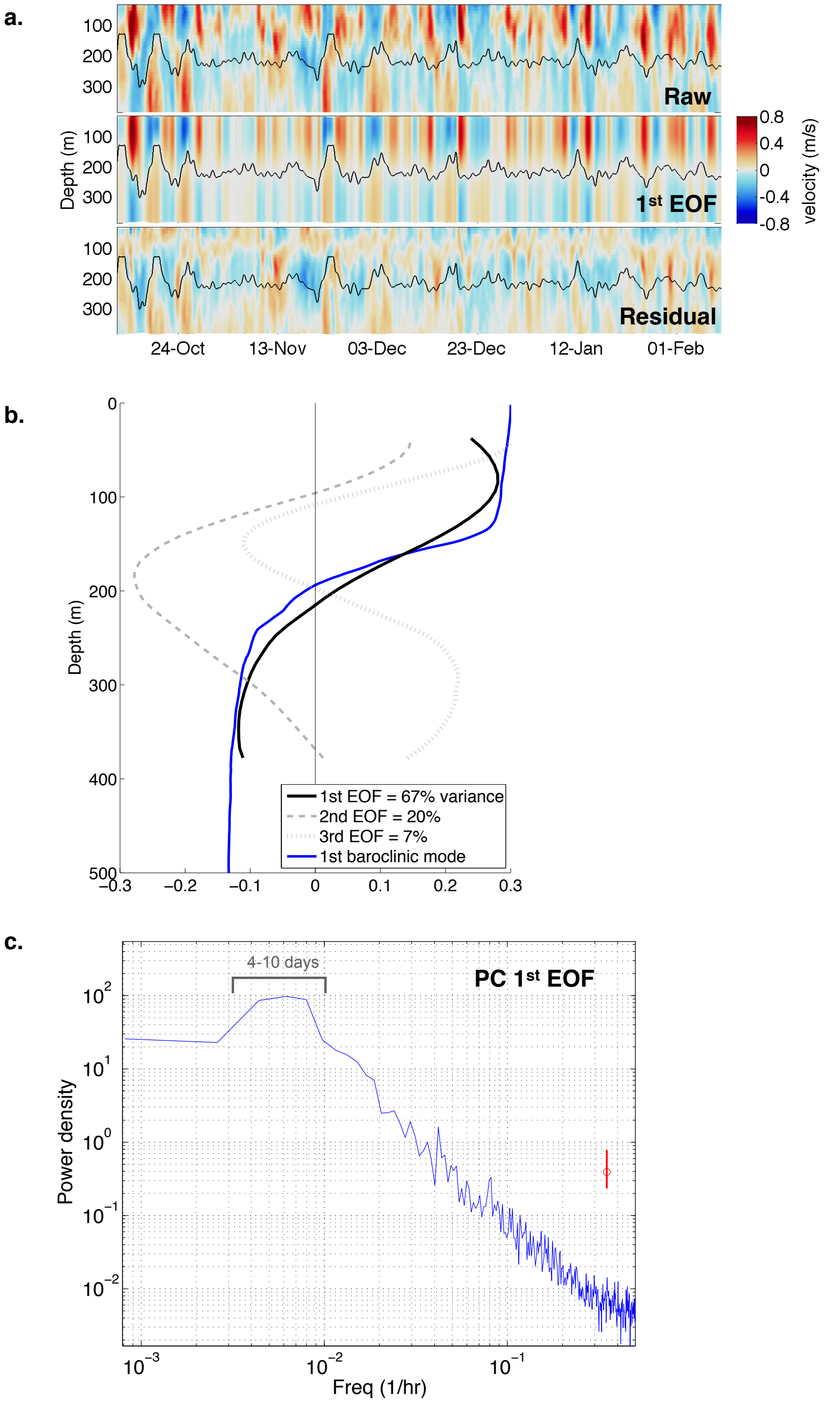

Figure 2-3: **a.** Subsection of velocity record: raw (upper), first EOF multiplied by its principal component (middle), and residual after removing first EOF (lower). Density contour used for rescaling depth overlaid. **b.** Vertical structure of the first three EOFs of the velocity record and the first baroclinic mode as calculated from the density structure. **c.** Power density spectrum of the principle component of first mode EOF as a function of period, with peak at 4-10 day periods marked.

velocity record excludes the top 33 m of the water column, so four methods are used to extend the velocity profile to the surface and put an error estimate on the volume flux (Fig. 2-4c). The surface velocities were filled in with: 1) a constant value equal to the top bin, 2) an extension of the mean shear observed in the depth range of 33 to 73 m, 3) a linear shear such that the velocity goes to zero at the surface, and 4) no velocity. The lower layer volume flux was not directly calculated because the velocity record ends at 400 m; however, we can infer it to be of approximately equal magnitude and opposite direction as the upper layer flux based on our knowledge of the density profile and presumed conservation of fjord volume.

The average volume exchanged in each layer over the 16 strongest pulses is $8.5 \pm 0.8 \times 10^{10}$ m^3 – equivalent to ~50% of the average upper layer volume in the entire fjord or ~25% of the lower layer. This was determined by time-integrating the upper layer volume flux over a pulse to determine the total volume exchanged and then comparing it to each layer's total volume in the fjord based on a mean interface depth of 180 m. Average volume exchanged during a pulse is compared to the total volume of each layer, though the fraction of water exchanged would be 35% higher if compared to the volume of each layer upstream of the mooring, i.e. between the mooring and the glacier.

2.5.3 Fjord flows driven by shelf variability

We attribute these large volume fluxes to forcing from the shelf, through a pumping mechanism that is sometimes called the intermediary circulation. Shelf winds, waves, or other phenomena drive density fluctuations and sea surface height anomalies at the fjord's mouth that can propagate up-fjord and drive flow within the fjord (e.g. Stigebrandt, 1981; Klinck et al., 1981). This mechanism has been found to force more fjord/shelf exchange than tidal or estuarine flows in some Scandinavian fjords (Stigebrandt, 1990; Arneborg, 2004). A previous summer study of Sermilik hypothesized that shelf forcing may be important for flushing the fjord (Straneo et al., 2010); however, until now, no direct evidence of this mechanism or its associated variability existed in Greenland's fjords.

Examination of the velocity pulses in our data reveals a structure consistent with strong shelf forcing. Composites of the mid-fjord velocity, mid-fjord density, shelf density and shelf pressure (Fig. 2-5) were created by averaging these fields over the 16 strongest velocity pulses. These events were defined by an up-fjord volume flux (26-hr low-pass filtered) in the upper layer exceeding 3.7×10^5 $m^3\ s^{-1}$and aligned by the time of peak volume flux. The pulses are identified by grey shading in Fig.2-4a. The composites illustrates the basic features of these pulses: the PW layer thickens, associated with depressed isopycnals, as a strong up-fjord flow develops above the interface and a

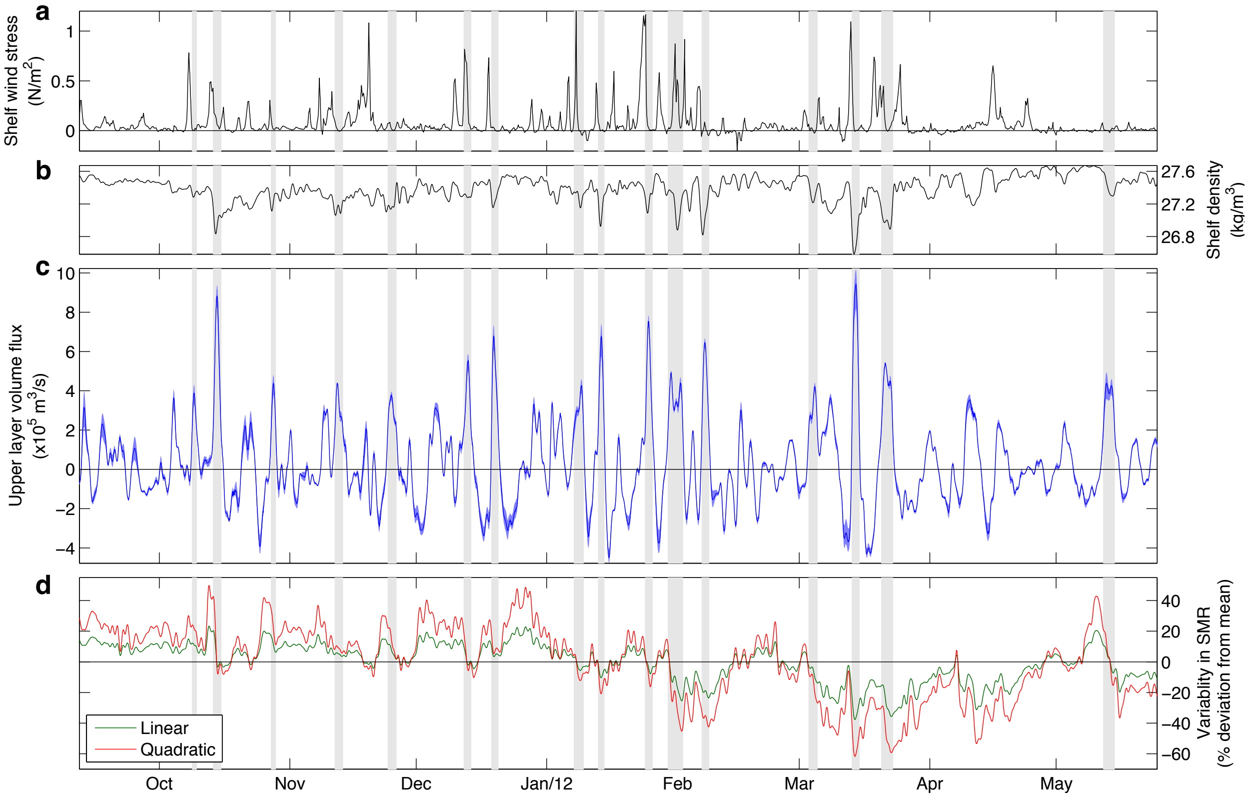

Figure 2-4: **a.** Along-shore wind stress on the shelf outside Sermilik; positive winds are to the southwest, i.e. downwelling-favorable. **b.** Potential density from shelf mooring (SM) at ∼291 m depth. **c.** Volume flux in upper layer at mid-fjord mooring (MM), assuming uniform across-fjord velocity; positive indicates flow towards the glacier. **d.** Variability (as percent deviation from the mean) in submarine melt rate based on a linear or quadratic scaling law between melt rate and average water column temperature (Appendix 2.A). Shading in all panels over the 16 strongest pulses, which were used to for the composites in Fig. 2-5.

weaker out-flow below. Velocity in each layer then reverses as the density field rebounds. These pulses originate on the shelf with a negative density anomaly and positive bottom pressure anomaly (indicating a positive sea-surface height anomaly), and the density anomaly then propagates up-fjord at speeds approximately matching the first baroclinic mode gravity wave phase speed.

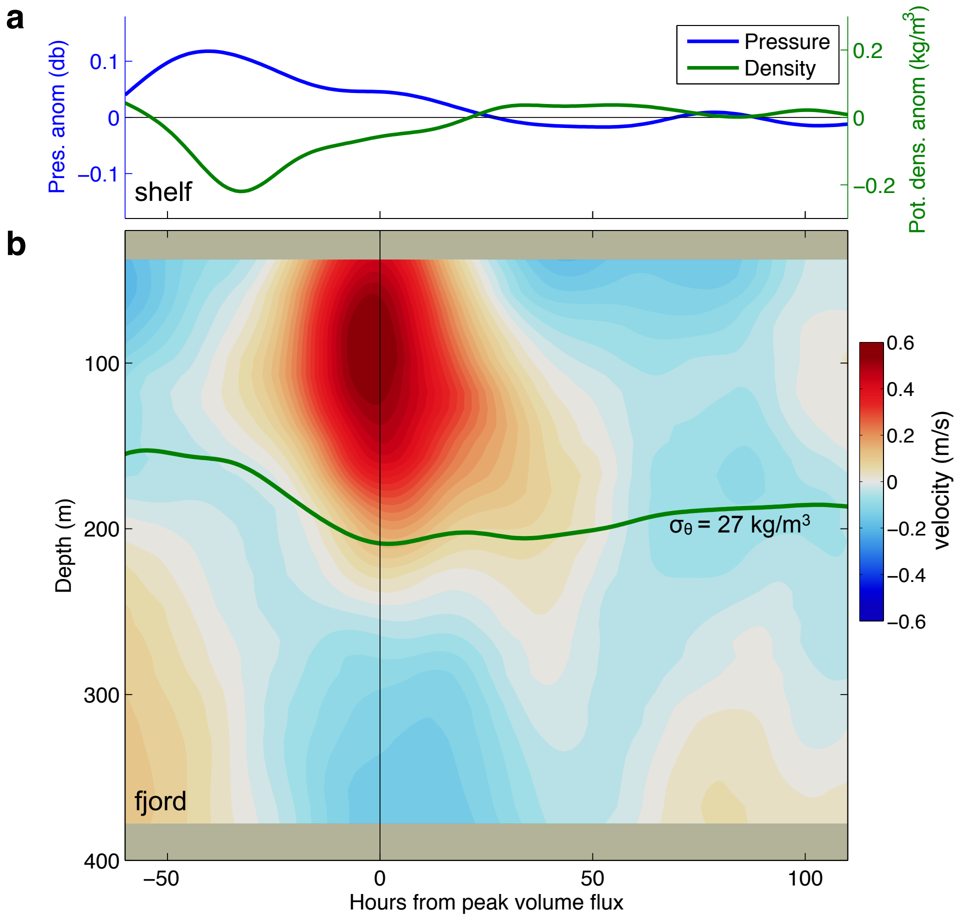

Figure 2-5: Composites of various records over 16 strongest velocity pulses (defined by up-fjord volume flux in upper layer exceeding 3.7×10^5 m^3 s^{-1}; see Fig. 2-4a). **a.** Composites of potential density anomaly (30-day low-pass signal removed) and bottom pressure anomaly from shelf mooring (SM) at ∼291 m depth. **b.** Composite of mid-fjord velocity (MM) with contour of $\sigma = 27.0$ kg/m^3 from composite of mid-fjord potential density (30-day low-pass signal removed, mean added back). Positive velocities indicate flow up-fjord, towards the glacier.

The structure of velocity pulses shown in the composite (Fig. 2-5) is confirmed by a high coherence amplitude between fjord velocity, fjord density and fjord bottom pressure on synoptic timescales of 2-10 day periods (Fig. 2-6a) with 95% confidence. The coherence phase between these records confirms that negative density anomalies coincide with, and positive pressure anomaly precede, inflow in the upper layer. The records on the shelf are also highly coherent with the fjord records in the same synoptic timeband (Fig. 2-6b), with phases confirming the origin of these signals on the shelf. The shelf mooring is dynamically up-stream of the fjord in the East Greenland Coastal Current and thus we do not expect its signal to be significantly influenced by the fjord.

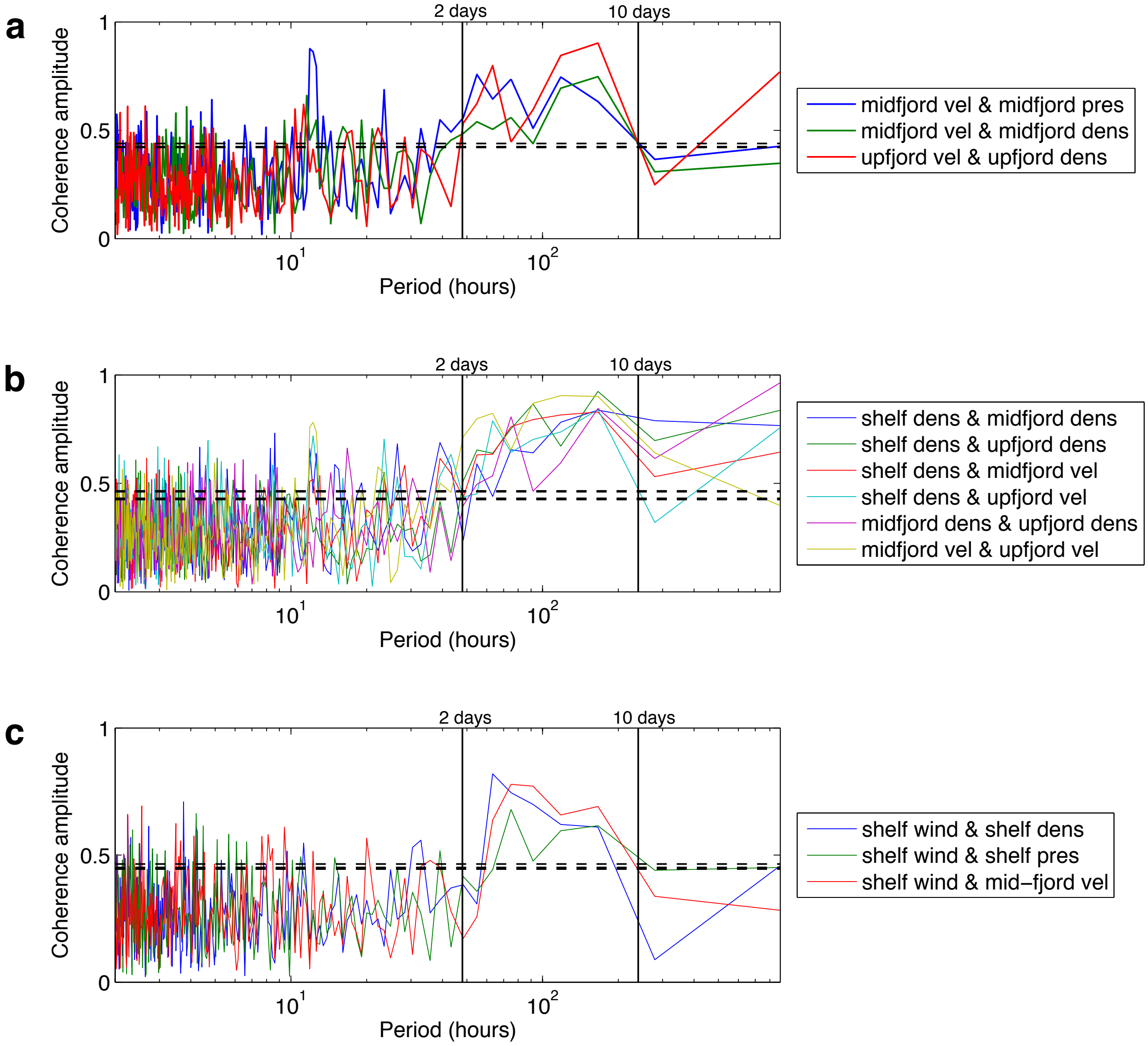

Figure 2-6: Coherence amplitude as a function of period (in hours) for many pairs of records from moorings and wind field (see legends): **a.** at the same fjord moorings, **b.** at different fjord/shelf mooring locations, and **c.** between wind and moored records. Significance at 95% confidence shown with black dashed lines. Vertical black lines bracket 2-10 day periods.

All fjord velocity pulses are associated with shelf density fluctuations, and most are also preceded by along-shore, downwelling-favorable winds on the shelf that are typical of this region (Fig. 2-4). These winds depress isopycnals and raise the sea surface towards the coastline, resulting in the shelf/fjord set-up described above. The link between shelf wind and shelf fluctuations – which create shelf/fjord gradients – can be seen in the high coherence between along-shore wind, shelf pressure and shelf density at 2-10 day periods (Fig. 2-6c). We speculate that other phenomena such as coastally trapped waves and eddies can generate fjord/shelf pressure gradients, resulting in occasional pulses without associated winds (Fig. 2-4).

Preceding most in-flowing pulses in the upper layer, the bottom-mounted pressure (after detiding, smoothing with a 26-hr Butterworth filter and removing a 30-day trend) at SM and MM both show an average positive pressure anomaly of 0.1 db (e.g. Fig. 2-5). This bottom pressure can be a function of density changes as well as changes in sea surface height:

$$P(z) = \rho_0 g\eta + \int_z^0 \rho(z)dz + P_a \tag{2.2}$$

where $P(z)$ is the pressure at depth z, η is the sea surface height, ρ is the density, and P_a is the atmospheric pressure. At MM, we can estimate the contribution to bottom pressure from density variability with the CTD records (Fig. 2-2) and find that it opposes the average pressure anomaly by $\sim$5 cm, and thus we estimate the average change in surface height to be $\sim$15 cm. This sea surface set-up on the shelf and in the fjord is consistent with on-shore transport from downwelling-favorable winds.

A cross-correlation analysis of the density records and shelf wind (Table 2.1) illustrates the shelf forcing and propagation of signals between moorings. Negative density anomalies are associated with downwelling-favorable (positive) winds, hence the negative correlation between wind and density. Density at all three locations have cross-correlation coefficient greater than 0.7 with each other. Density at mid-fjord lags density on the shelf by 14 hours, while upper-fjord density lags mid-fjord by 17 hours. For comparison, we expect these signals to propagate at the first baroclinic mode phase speed, which we estimate to be 1 m/s based on the density stratification. The shelf/mid-fjord and mid-fjord/upper-fjord distances are 32 km and 37 km, respectively. These result in expected propagation times of 10 and 11 hours, respectively. Thus, the propagation speeds that we observed are similar, though somewhat slower (which could be explained by the presence of icebergs in the fjord (MacAyeal et al., 2012)).

2.5.4 Changes in heat content

Regarding the glacier, these pulses significantly alter the fjord's heat content via changes in layer thickness and property shifts within layers. All pulses have, at least, a transient response from

	correlation coeff.	lag (hours)
shelf τ / shelf σ	-0.41	25
shelf τ / mid-fjord σ	-0.32	45
shelf τ / upper-fjord σ	-0.33	55
shelf σ / mid-fjord σ	0.71	14
shelf σ / upper-fjord σ	0.75	34
mid-fjord σ / upper-fjord σ	0.91	17

Table 2.1: Peak correlation coefficient and lag at peak correlation between various records: shelf wind, shelf density at SM, mid-fjord density at MM and upper-fjord density at UM. τ is wind; σ is density. All correlations are statistically significant at 99% confidence. Positive lags indicates first record leads second record.

the first effect, e.g. up-fjord flow in the PW layer thickens that layer, increasing the volume of PW relative to AW and decreasing the average water-column temperature. The PW/AW interface moves $\sim$50 m vertically during each velocity pulse, resulting in large heat content fluctuations. The average water column temperature above 630 m (the glacier's grounding line depth), shown in Fig. 2-7, consequently drops by 0.6°C on average with strong in-flow in the upper PW layer. The upper layer volume flux and average water column temperature are highly coherent (>95% confidence) at 2-11 day periods.

All pulses drive transient changes in layer thickness and are associated with heaving isopycnals on the shelf. Only some pulses, however, advect new properties into the fjord, which, we argue, reflect changes in water properties on the shelf. Shifts in AW temperature often coincide with lower layer in-flow during energetic pulses. For example, Fig. 2-8 highlights one such event where the temperature at both MM and UM increases in the thermocline and in AW layer, coinciding with up-fjord velocity in the AW layer (black line in Fig. 2-2).

To compare AW layer properties at mid- and upper-fjord, the potential temperature records from MM and UM were each interpolated onto a 10-m vertical grid and averaged between 350 m and 530 m. A cross-correlation of the average AW temperature between UM and MM shows that the upper-fjord lags mid-fjord by 26 hours (correlation coefficient = 0.55), corresponding to a propagation speed of 0.4 m/s. This is significantly slower than the density signal, which appears to propagate along the pycnocline as a first baroclinic mode wave. This suggests that the temperature anomalies within the AW layer, which typically do not have a strong density signal, are being advected by the flow at approximately 0.4 m/s – a speed that compares well to the mean velocity over one direction of a pulse.

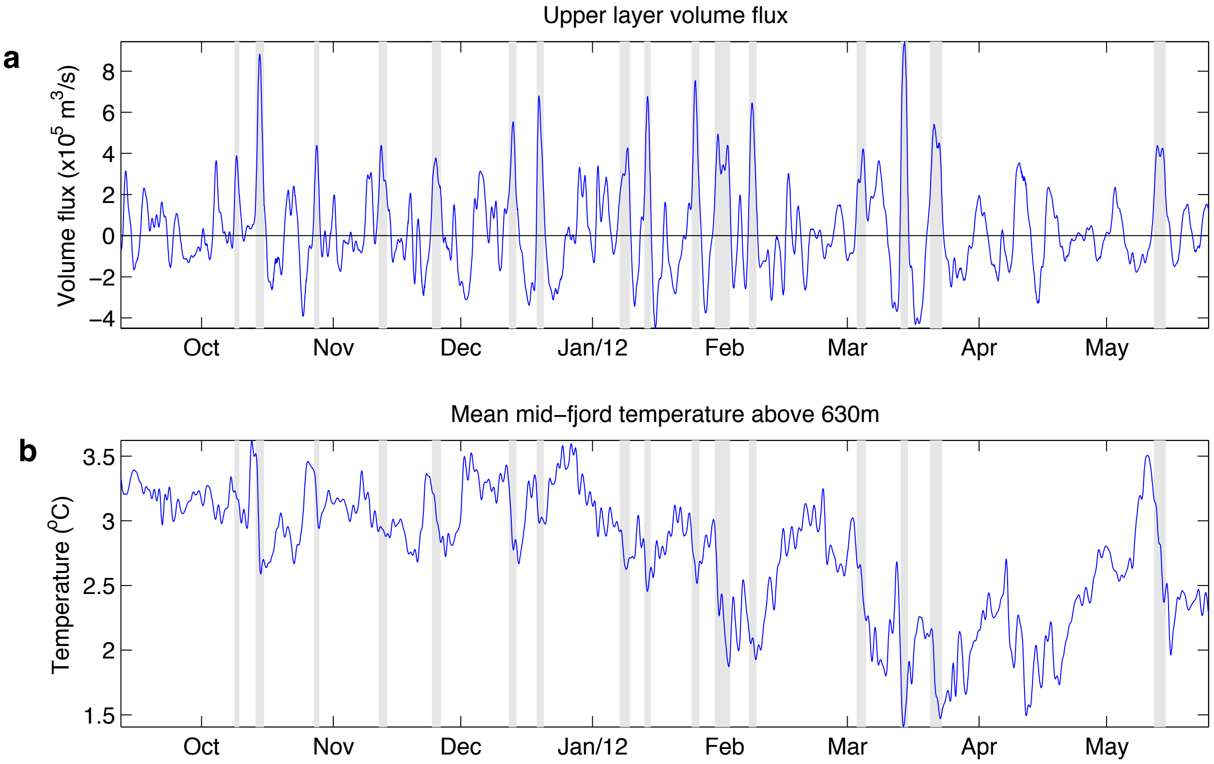

Figure 2-7: **a.** Upper layer volume flux (same as Fig. 2-4c) **b.** Average water column potential temperature above 630 m (i.e. the depth range of glacier's face) from mid-fjord records. Grey bars highlight the 16 strongest up-fjord pulses.

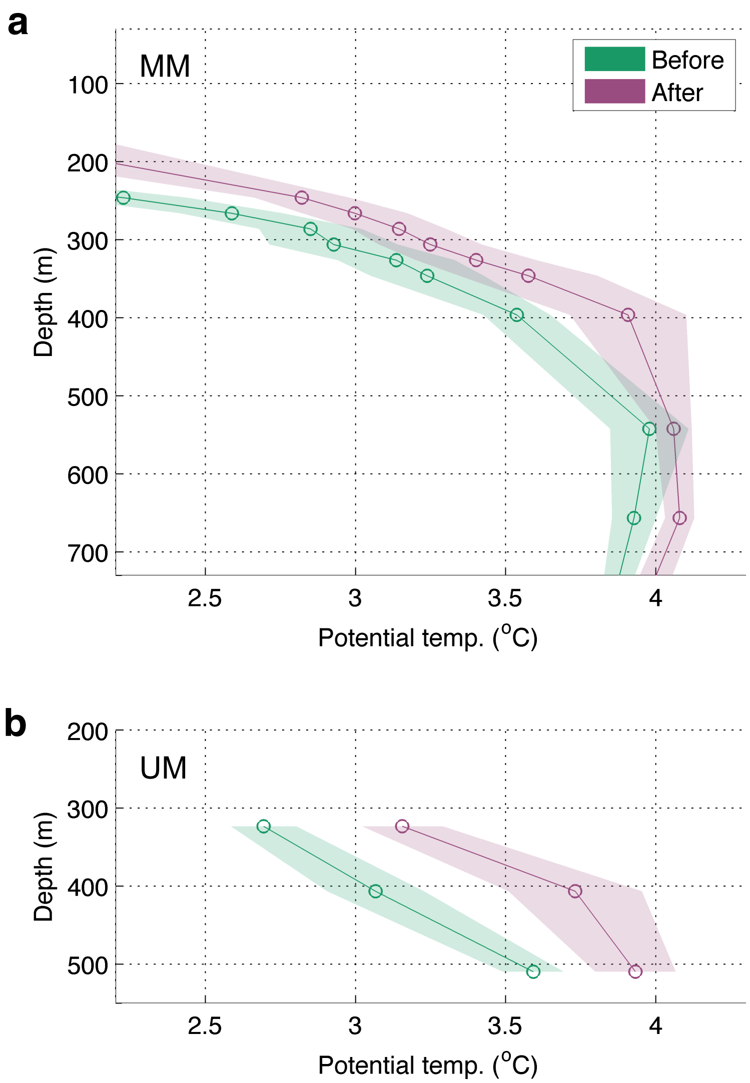

Figure 2-8: Potential temperature profile during 4-day periods proceeding and following a strong up-fjord flow (indicated with black lines in Fig. 2-2) in the AW layer at mid-fjord mooring (a) and upper-fjord mooring (d). Circles show average temperature at instrument during each period; shading indicates 95% range of all measurements over this period.

2.5.5 Shelf forcing in Kangerdlugssuaq Fjord

The mid-fjord water properties from Kangerdlugssuaq Fjord exhibit similar variability to Sermilik: large-amplitude fluctuations in the thermocline (Fig. 2-2e) and significant variability at synoptic timescales. We find a statistically significant peak in coherence between the density records in Kangerdlugssuaq at 3-12 day periods, similar to the results from Sermilik.

The relationship between shelf wind and fjord properties indicates that shelf-forcing is likely a dominant driver of variability in Kangerdlugssuaq (Fig. 2-9). Without a shelf mooring outside

Kangerdlugssuaq, we cannot directly attribute this fjord variability to intermediary circulations from shelf density fluctuations. However, significant coherence between fjord properties (density, pressure and temperature) and along-shore shelf winds suggests that the same intermediary circulations are present and forced by along-shore shelf winds. Strong shelf wind events, which are all downwelling-favorable, usually correspond to positive bottom-mounted pressure anomalies and negative potential density and temperature anomalies in the fjord (Fig. 2-9). A cross-correlation between de-tided bottom-pressure at KM-1 and KM-2 shows that they are significantly correlated with shelf winds (correlation coefficients > 0.44), with fjord pressure lagging shelf wind by 5 hours. A cross-correlation analysis of shelf winds with density and temperature anomalies at KM-2 and KM-3 shows a lag of 25-35 hours for all records. (Anomaly records are created by smoothing with a 26-hr Butterworth filter and subtracting a 15-day smoothed record.)

Not all fjord variability in Kangerdlugssuaq is associated with shelf winds. This is consistent with Sermilik, where not all intermediary flows (and the associated shelf density fluctuations) were driven by shelf winds. We speculate that shelf density fluctuations driven by other mechanisms (e.g. waves, eddies) can drive intermediary flows in the absence of local winds.

2.6 Discussion and Conclusions

In summary, water properties and heat content within Sermilik and Kangerdlugssuaq Fjords vary significantly on synoptic timescales throughout non-summer months. This variability is attributed to strongly sheared pulses driven by shelf density fluctuations, primarily due to along-shore winds. Individual events, lasting only several days, rapidly translate signals from the shelf to the upper fjord.

Our results have several important implications. The shelf-driven flow allows the fjords to track shelf variability on short timescales (days to weeks), as opposed to the longer timescales (months) associated with glacier-driven circulation, which we expect to have velocities of less than 2 cm/s in winter (Sciascia et al., 2013). While there must be a net export of freshwater from the glacier and import of heat for melting, the externally-forced flow entirely masks any signal of a glacier-driven flow in our nine-month records. Thus, the renewal and variability of AW does not appear to be controlled by glacial inputs for the majority of the year, reducing the possibility of a positive feedback between glacial meltwater and shelf exchange.

Our results also suggest that the submarine melt rate should vary significantly throughout

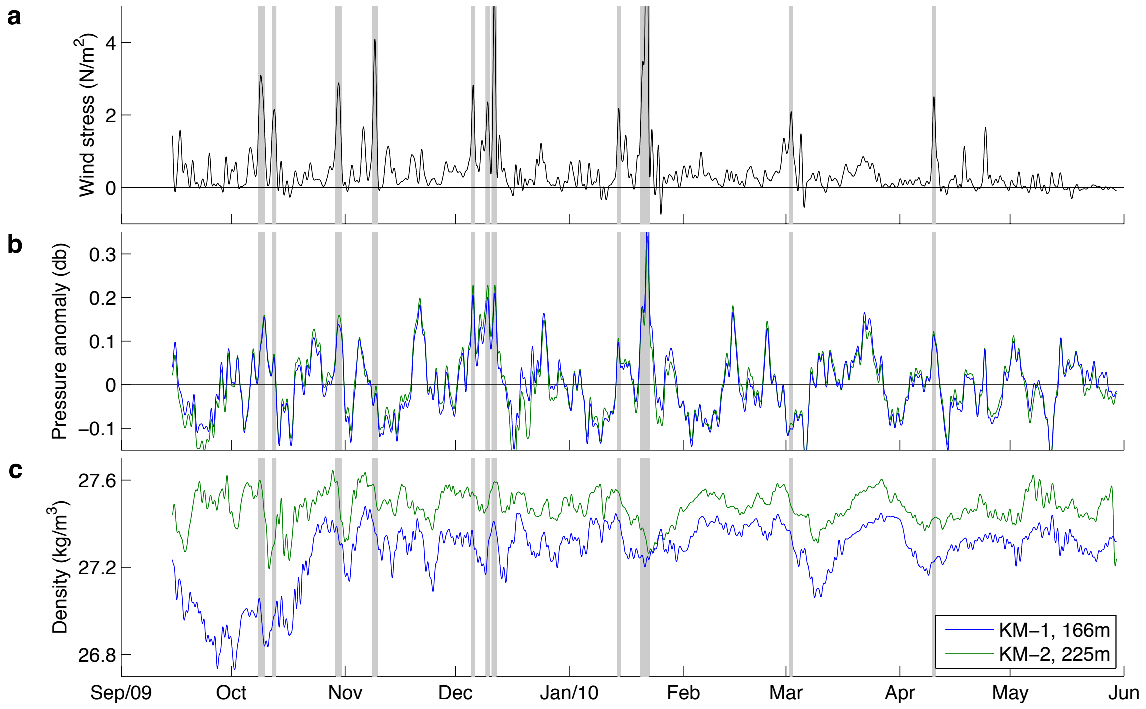

Figure 2-9: **a.** Along-shore wind stress outside Kangerdlugssuaq Fjord at location of wind rose in Fig. 2-1a; positive winds are to the southeast, i.e. downwelling-favorable. **b.** De-tided and de-trended pressure records from KM-1 and KM-2. **c.** Potential density from KM-1 and KM-2. All records are smoothed with a 26-hour Butterworth filter. Grey shading indicates times when shelf wind stress exceeds 2 N/m^2.

non-summer months due to the observed fluctuations in temperature which, we assume, are representative of property changes near the glacier. To estimate submarine melt variability, we rely on modeling studies that, in the absence of subglacial discharge, find melt to scale linearly or quadratically with ambient water temperature (Holland et al., 2008b; Jenkins, 2011; Sciascia et al., 2013). When we apply this scaling to our temperature observations in Sermilik Fjord, we find that the submarine melt rate would vary by ±20-50% of its mean value on synoptic timescales (Fig. 2-4d, Appendix 2.A). These externally-forced pulses might also change the kinetic energy at the ice boundary layer (and hence the submarine melt rate) or impact the ice melange, which could affect glacier stability (Amundson et al., 2010).

The scope of our results should be highlighted. We do not have records from the glacier/ocean boundary layer but from the 'far-field' ocean conditions that the glacier experiences. The velocity pulses and property variability at our moorings, however, suggest that the observed fluctuations penetrate far into the fjord. Rather than resolving processes at the glaciers' margins, our results provide the first non-summer oceanic boundary conditions one might use to force a glacier model. Additionally, we speculate that the fjord dynamics will be different in the summer months. When subglacial discharge increases and winds weaken, we expect a competition between shelf-driven and glacier-driven flows, though the nature of their interaction is currently unclear. Helheim and Kangerdlugssuaq are two of the Greenland Ice Sheet's largest outlets, contributing ∼20% of the current ice sheet discharge anomaly (Enderlin et al., 2014), and their dynamics alone are worth understanding. We also expect, however, our results from Sermilik and Kangerdlugssuaq Fjords to be applicable to other fjords around Greenland, though the magnitude of the shelf forcing will depend on a variety of factors including the shelf variability and sill depth.

Appendix

2.A Melt-rate variability

To estimate the variability in submarine melting, we calculated a depth-averaged water column temperature by interpolating our temperature records from MM onto a 10-m vertical grid and averaging between 125 m and 530 m. This depth range was chosen to best represent the water column in direct contact with the glacier (i.e. above the 530 m sill depth in the upper fjord) to the extent that we could resolve without extrapolation. While we neglect the upper 125 m, we also know that the PW is close to the freezing temperature in winter and likely does not contribute significantly to submarine melting. We used this depth-averaged temperature to estimate the variability in the submarine melt rate (M_s), assuming a linear or quadratic relationship between the melt rate and the temperature: $M_S \propto (T - T_f)$ or $M_S \propto (T - T_f)^2$, where T is the average water column temperature and T_f is the freezing temperature. By this scaling, the deviation in the submarine melt rate (from its time-mean value) would be:

$$PD = \frac{M_S - \overline{M_S}}{\overline{M_S}} \times 100 = \frac{(T - T_f) - (\overline{T - T_f})}{\overline{T - T_f}} \times 100 \text{ linear} \tag{2.3}$$

$$= \frac{(T - T_f)^2 - (\overline{T - T_f})^2}{\overline{T - T_f}} \times 100 \text{ quadratic} \tag{2.4}$$

where PD is the percent deviation about the mean submarine melt rate. It should be noted that this a crude scaling and melting should also be a function of the temperature profile; even different profiles with the same depth-averaged temperature could result in different melt rates.

Chapter 3

Measuring meltwater in glacial fjords: heat, salt, and freshwater budgets for Sermilik Fjord, southeast Greenland

3.1 Abstract

Fjords connect the ocean to outlet glaciers of the Greenland Ice Sheet. Since submarine melting may have triggered part of the recent ice sheet mass loss, observations of ocean heat transport in fjords are increasingly being used to infer submarine melt rates. The complete heat, salt and mass budgets that underlie such methods, however, have been largely neglected. Here, we develop a new framework for exploring glacial fjord budgets. Building on estuarine studies of salt budgets, we decompose the heat, salt and mass transports through the fjord and present new equations for calculating freshwater fluxes from submarine meltwater and runoff. This method is applied to moored records from Sermilik Fjord, near the terminus of Helheim Glacier, to evaluate the dominant balances in the fjord budgets and to estimate the freshwater fluxes. Throughout the year, we find two different regimes. In the non-summer months, advective transports are balanced by changes in heat/salt storage within our ability to measure; freshwater fluxes cannot be inferred as a residual. In the summer, a mean exchange flow emerges consisting of inflowing Atlantic water and outflowing glacially modified water. This exchange transports heat towards the glacier and is primarily balanced by changes in storage and latent heat for melting ice. The total freshwater flux increases over the summer, reaching 1200±700 $\mathrm{m}^3\ \mathrm{s}^{-1}$ of runoff and 1500±500 $\mathrm{m}^3\ \mathrm{s}^{-1}$ of submarine meltwater from

glaciers and icebergs in August. Our methods and results highlight important components of fjord budgets, particularly the storage and barotropic terms, that have been neglected or mishandled in previous estimates of submarine melting.

3.2 Introduction

The Greenland Ice Sheet is currently losing mass, raising global sea levels by 7 mm between 1992 and 2012 (Shepherd et al., 2012). This mass loss is attributed to both surface processes and glacier dynamics at the ice sheet's margins (van den Broeke et al., 2009), with the largest uncertainties in future sea level rise tied to the latter (Lemke et al., 2007). In the past decade, the simultaneous speed-up, thinning, and retreat of many outlet glaciers originated at their marine termini and coincided with ocean warming around Greenland (Howat et al., 2007; Holland et al., 2008a). Consequently, submarine melting of these outlet glaciers has been implicated as a driver of dynamic glacier changes (Nick et al., 2009). Our understanding of this submarine melting, however, is hindered by an absence of any direct measurements and a limited understanding of ocean dynamics near the ocean-ice boundary (Straneo and Heimbach, 2013).

Submarine melting, along with other freshwater inputs from Greenland, is also critical for unraveling the ice sheet forcing on the ocean. Greenland is a significant and growing source of freshwater to the ocean (Bamber et al., 2012), discharged in the form of submarine melting, runoff, and icebergs. Proglacial fjords are the estuaries where liquid freshwater from the ice sheet is mixed and exported into the ocean, yet our understanding of proglacial fjord processes is limited in two ways. First, the magnitude and variability of the liquid freshwater fluxes are poorly constrained around Greenland. Estimates of submarine melting have been made with ocean measurements, but they are often derived from simplified equations and limited data (e.g. Sutherland and Straneo, 2012; Rignot et al., 2010). Runoff into proglacial fjords is not directly measured but estimated with regional models and reanalyses that often differ significantly (e.g. Mernild et al., 2010; Andersen et al., 2010; Van As et al., 2014). Second, the glacier-driven circulation from these inputs of freshwater is not well understood. We expect a buoyancy-driven circulation from the freshwater forcing, but, due to the great depth of fjords, this component will often have weak velocities and be hard to measure. Additionally, proglacial fjord dynamics are complicated by a variety of time-dependent flows, like tides and externally-forced circulations, that can mask the signal of glacier-driven flow (Farmer and Freeland, 1983; Stigebrandt, 2012).

In order to improve our understanding of (a) how the ocean impacts glaciers through submarine melting, and (b) how glaciers impact the ocean through freshwater forcing, we need better estimates of the heat, salt and freshwater fluxes in fjords. A growing number of studies attempt to infer submarine melt rates from measurements of ocean heat transport in the fjords where outlet glaciers terminate (Motyka et al., 2003; Johnson et al., 2011; Sutherland and Straneo, 2012; Rignot et al., 2010; Christoffersen et al., 2011; Motyka et al., 2013; Xu et al., 2013; Inall et al., 2014; Mortensen et al., 2014). Water properties and velocity, usually measured over a brief period, are used to estimate ocean heat transport through a fjord cross-section. The heat transported towards the glacier is assumed to melt glacial ice, allowing a submarine melt rate to be calculated. Several studies also compute a salt budget to aid in extrapolating or constraining their velocity fields (e.g. Motyka et al., 2003; Rignot et al., 2010). Bartholomaus et al. (2013) employs a variation on this method by calculating meltwater fractions in a fjord and inferring submarine melting from meltwater transport. While several different varieties of this technique have emerged, none includes a discussion of the complete heat, salt and mass budgets that underly such estimates. These published estimates are based on many implicit or explicit assumptions, some of which we will show are hard to justify generally. Improved equations, along with more comprehensive measurements, are needed to accurately estimate submarine melting and the total freshwater export from the ice sheet.

The unique environment of glacial fjords poses many obstacles to obtaining sufficient data. Many of Greenland's major glaciers have an ice mélange, a thick pack of icebergs and sea ice (Amundson et al., 2010), that renders the near-terminus region inaccessible by boat. Transiting icebergs outside the mélange also impede shipboard and moored observations. As a result, ocean measurements in these fjords are sparse and mostly limited to synoptic surveys (Straneo and Cenedese, 2015).

Here, we explore a more thorough formulation of heat, salt and mass budgets for glacial fjords, and we present an alternative framework for inferring the freshwater inputs from Greenland's glaciers. Building upon the expansive literature on salt budgets in estuaries, we decompose the transport through a fjord cross-section and present complete equations for calculating meltwater inputs. Our method is applied to two-year moored records from Sermilik Fjord, near the terminus of Helheim Glacier, to assess the terms in the heat and salt budgets and to infer freshwater fluxes.

3.3 Constructing & decomposing fjord budgets

3.3.1 Greenlandic glacier-fjord systems

Greenland's glacial fjords share many basic features that distinguish them from the better-studied river estuaries of lower latitudes. Long, narrow and deep, these fjords connect to the coastal ocean at one end and are bounded by a glacier (or sometimes multiple glaciers) at the other end. The geometry of the glacier termini range from vertical calving fronts to expansive floating tongues (e.g. Stearns and Hamilton, 2007; Nick et al., 2012).

Freshwater enters glacial fjords in several ways. Surface melt at the atmospheric boundary of the ice sheet transits through a system of moulins and channels to the base of the glacier and into the fjord at the grounding line, well below the sea surface (Chu, 2014). This freshwater is called subglacial discharge or, more generically, runoff. In addition, the glacier discharges freshwater from its terminus in both solid and liquid form: as calving icebergs and submarine melting at the ocean-ice interface. Subsequent melting of icebergs can result in an additional liquid meltwater source to the fjord. Unlike typical estuaries, the aforementioned types of liquid freshwater (runoff and submarine melting of glaciers/icebergs) primarily enter the fjord at depth, not at the surface. Additional inputs of freshwater at the surface include terrestrial runoff, precipitation, and sea-ice melt.

3.3.2 Heat, salt and mass budgets for a glacial fjord

Here, we construct heat, salt and mass budgets for a generic glacial fjord. These budgets are the basis for inferring freshwater fluxes from measurements of heat and salt transport. The control volume for the budgets, illustrated in Fig. 3-1, is the ocean water that is bounded by a fjord cross-section at the seaward end, where ocean measurements might be made, and by a glacier at the other end. The other boundaries of the control volume are with the atmosphere at the surface, with icebergs, and with the sidewalls and bottom of the fjord. It is assumed that there is no transfer of heat, salt or mass through the sidewalls or bottom of the fjord.

For the purpose of this analysis, we group together submarine melting of the glacier and submarine melting of icebergs within the control volume into one meltwater volume flux, Q_{MW}. While iceberg and glacier melting are distinct processes that might have different effects on the ice sheet and ocean, they are indistinguishable in the context of salt, heat and mass budgets since both meltwater types enter at the seawater freezing point and require latent heat from the ocean to drive melting (e.g. Jenkins, 1999). Therefore, any submarine melting that is inferred from the budgets

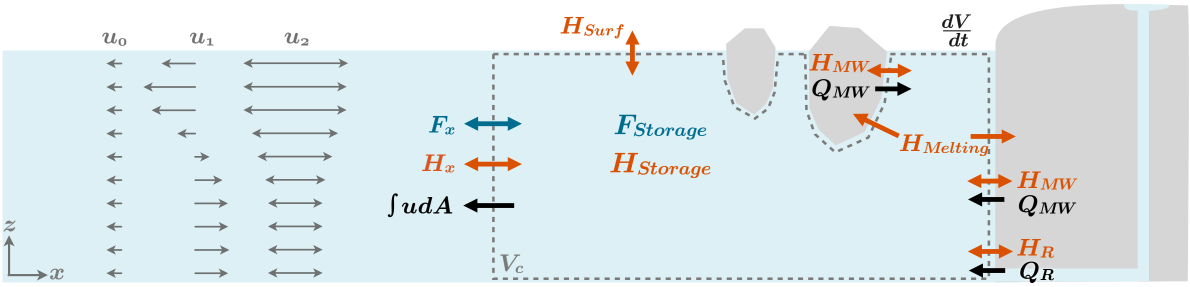

Figure 3-1: Schematic of terms in the mass, salt and heat budgets for a control volume (V_c) shown by the grey dashed rectangle. Note that the control volume does not include the icebergs; it contains only liquid water between the cross-section and the glacier. Orange terms are the heat budget, blue the salt budget, and black the mass budget. Iceberg submarine meltwater and glacier submarine meltwater have been combined as Q_{MW}. The left side shows the velocity decomposition ($u = u_0 + u_1 + u_2$) in an idealized case of a two layer exchange (inflow at depth, outflow at the surface). The mean barotropic velocity, u_0, is away from the glacier and balances the mean input of meltwater (Q_{MW}) and runoff (Q_R); u_1 is the mean exchange velocity (time-averaged with spatial-average removed); and u_2 is the fluctuating velocity (spatial- and time-average removed).

will be the sum of glacial melt and iceberg melt within the control volume. Furthermore, we lump together the terrestrial and subglacial discharge into a single runoff volume flux, Q_R, which enters the fjord at a temperature near the freshwater freezing point but does not require latent heat from the ocean to melt. Hence, there are two primary freshwater components that enter the fjord in liquid form: runoff (Q_R) that enters at θ_R, the freezing temperature of freshwater; and meltwater (Q_{MW}) that enters at θ_{MW}, the freezing temperature of seawater in contact with ice. Additionally, evaporation and precipitation over the surface of the control volume result in a volume flux of Q_{Surf}.

In a mass budget for the liquid water, the volume fluxes of liquid freshwater will be balanced by a volume flux through the cross-section (A_x) that bounds the control volume (V_c):

$$\int_{A_x} udA + Q_R + Q_{MW} + Q_{Surf} = \frac{\partial V_c}{\partial t} \tag{3.1}$$

where u is the velocity perpendicular to the cross-section and $\partial V_c/\partial t$ reflects changes in control volume size from variations in sea surface height, in the concentration of solid icebergs, or in the glacier terminus position. (Using the Boussinesq approximation, variations in density are neglected in the mass budget.) By convention, the velocity and volume fluxes are positive when directed into the control volume (see Table 3.1 for list of variables and Fig. 3-1 for a schematic).

To construct a heat budget for the control volume, it is useful to start with the general form for

Variables			**Terms in heat/salt budgets**		
Symbol	**Meaning**	**Units**	**Symbol**	**Meaning**	**Units**
ρ	density of water	kg/m^3	H^a	advective heat flux	J/s
ρ_{ice}	density of ice	kg/m^3	H_x^a/H_x	advective heat flux through A_x	J/s
c_p	heat capacity of water	J/kg/^{o}C	H_{MW}^a/H_{MW}	advective heat flux from meltwater	J/s
c_i	heat capacity of ice	J/kg/^{o}C	H_R^a/H_R	advective heat flux from runoff	J/s
Q_{MW}	meltwater volume flux	m^3/s	H_{Surf}^a	advective heat flux from Q_{Surf}	J/s
Q_R	runofff volume flux	m^3/s	H_{Surf}	turb./cond./radiative surface heat flux	J/s
Q_{Surf}	surface volume flux	m^3/s	$H_{Melting}$	heat used for melting ice	J/s
θ_{MW}	temperature of Q_{MW}	^{o}C	$H_{Storage}$	heat storage in V_c	J/s
θ_R	temperature of Q_R	^{o}C	F_x^a/F_x	advective salt flux through A_x	kg/s
θ_{Surf}	temperature of Q_{Surf}	^{o}C	$F_{Storage}$	salinity storage in V_c	kg/s
θ_r	reference temperature	^{o}C			
θ_i	ice temperature	^{o}C			
L	latent heat of fusion	J/kg			
A_x	cross-section area	m^2			
V_c	control volume	m^3			

Table 3.1: Relevant variables and budget terms with their meaning and units.

an ocean heat budget. The heat conservation equation for an incompressible fluid is:

$$\underbrace{\rho c_p \oint \theta \boldsymbol{u} \cdot \boldsymbol{dA}}_{H^a} = \underbrace{\rho c_p \frac{\partial}{\partial t} \int_{V_c} \theta dV}_{H_{Storage}} + H_f \tag{3.2}$$

where $\boldsymbol{u} \cdot \boldsymbol{dA}$ is the inward velocity perpendicular to the boundary, θ is potential temperature, c_p is heat capacity of seawater, and ρ is the density of seawater. The heat capacity and density are treated as constants since they vary by less than one percent (except when the salinity approaches zero). The first term in Eq. (3.2) is the advective heat flux through all boundaries (H^a), the second term is the change in heat content of the control volume ($H_{Storage}$), and the third term captures turbulent, conductive or radiative heat fluxes through the boundaries of the control volume (H_f).

In a glacial fjord, H_f will include surface fluxes and heat used for melting ice: $H_f = H_{Surf} + H_{Melting}$. The advective heat fluxes (H^a) through the control volume's boundaries include transport through the fjord cross-section (H_x^a) as well as heat transports from runoff, meltwater and surface mass fluxes ($H_R^a + H_{MW}^a + H_{Surf}^a$). We assume that horizontal fluxes through the cross-section are resolved by the advective component and thus do not include a horizontal turbulent flux across A_x. Vertical turbulent fluxes can be important in fjords but will not appear in this budget formulation since the control volume is bounded vertically by the free surface and fjord bottom. (See Geyer and Ralston, 2011, for a review of fjords as strongly stratified estuaries.) The heat budget can thus be written as:

$$\underbrace{\rho c_p \int_{A_x} u\theta dA}_{H_x^a} + \underbrace{\rho c_p Q_R \theta_R}_{H_R^a} + \underbrace{\rho c_p Q_{MW} \theta_{MW}}_{H_{MW}^a} + \underbrace{\rho c_p Q_{Surf} \theta_{Surf}}_{H_{Surf}^a} = \underbrace{\rho c_p \frac{\partial}{\partial t} \int_{V_c} \theta dV}_{H_{Storage}} + H_{Melting} + H_{Surf} \tag{3.3}$$

where $H_{Melting}$ and H_{Surf} are positive if the control volume loses heat. There are now four components to the advective heat fluxes on the left side, and these are balanced by changes in heat storage, heat to melt ice, and surface fluxes. The total heat extracted from the ocean to melt ice ($H_{Melting}$) can be written in terms of the submarine meltwater flux, Q_{MW}:

$$H_{Melting} = \rho Q_{MW} \left[L + c_i(\theta_{MW} - \theta_i)\right] = \rho Q_{MW} L_{adj} \tag{3.4}$$

where L is the latent heat to melt ice, c_i is heat capacity of ice, θ_i is the ice temperature, and $L_{adj} = L + c_i(\theta_{MW} - \theta_i)$ is an adjusted latent heat that takes into account both the heat required to raise ice to the melting temperature and the latent heat to melt ice.

The salt budget is less complex since the runoff, meltwater, and surface mass fluxes do not add or remove salt – they are all mass fluxes of zero salinity. Therefore, the only advective salinity transport will be through the fjord cross-section, and this will be balanced by changes in salt storage:

$$\underbrace{\int_{A_x} uSdA}_{F_x^a} = \underbrace{\frac{\partial}{\partial t} \int_{V_c} SdV}_{F_{Storage}} \tag{3.5}$$

Eq. (3.1), (3.3) & (3.5) are full mass, heat and salt budgets for a generic glacial fjord. Before proceeding, two more assumptions are made that should hold for many Greenlandic fjords, though not necessarily all. First, the volume flux through the surface of the control volume (Q_{Surf}) and its associated advective heat fluxes (H_{Surf}^a) are both assumed to be negligible. This is based on the assumption that evaporation minus precipitation (E-P) over the surface of V_c is small compared to the other mass fluxes. The non-advective surface heat flux (H_{Surf}) from radiative, latent and sensible heat fluxes, however, is retained. Second, changes in the size of the control volume ($\frac{\partial V_c}{\partial t}$) from iceberg/glacier variability or sea surface height changes are neglected (see justification in

Section 3.6 and Appendix A). With these assumptions, the budgets become:

$$\textsc{Mass:} \qquad \int_{A_x} u dA + Q_R + Q_{MW} = 0 \tag{3.6}$$

$$\textsc{Heat:} \quad \underbrace{\rho c_p \int_{A_x} u\theta dA}_{H_x^a} + \underbrace{\rho c_p Q_R \theta_R}_{H_R^a} + \underbrace{\rho c_p Q_{MW} \theta_{MW}}_{H_{MW}^a} = \underbrace{\rho c_p \int_{V_c} \frac{\partial \theta}{\partial t} dV}_{H_{Storage}} + \underbrace{\rho Q_{MW} L_{adj}}_{H_{Melting}} + H_{Surf} \tag{3.7}$$

$$\textsc{Salt:} \qquad \underbrace{\int_{A_x} uS dA}_{F_x^a} = \underbrace{\int_{V_c} \frac{\partial S}{\partial t} dV}_{F_{Storage}} \tag{3.8}$$

The terms from these budgets are illustrated in Fig. 3-1, with variables defined in Table 3.1.

3.3.3 Time-averaging budgets and decomposing transports

The budgets in Eq. (3.6)-(3.8) are not yet in a practical form to use with observations. First, time-averaging is often necessary to separate high frequency flows from an underlying residual exchange and to reduce the impact of transient changes in heat/salt storage. Second, the barotropic component of the velocity, associated with a net mass transport through the fjord cross-section, should be separated from the baroclinic flow to ensure that mass is conserved in the control volume (as will be explained). To address these two issues, the budgets are time-averaged over a timescale, τ, and the cross-section transports are decomposed in a manner similar to studies of estuarine salt fluxes. Following Lerczak et al. (2006), MacCready and Banas (2011) and others, the along-fjord velocity at the cross-section is decomposed into a time and spatially averaged field, u_0, a time averaged and spatially varying field, u_1, and the time and spatially varying residual, u_2:

0. Mean barotropic: $u_0(t) = \overline{\frac{1}{A_x} \int_{A_x} u dA}$

1. Mean exchange: $u_1(y,z,t) = \overline{u(y,z,t)} - u_0(t)$

2. Fluctuating: $u_2(y,z,t) = u(y,z,t) - u_1(y,z,t) - u_0(t)$

such that $u = u_0 + u_1 + u_2$, and the overbar indicates a temporal running mean over τ (Fig. 3-1). The same decomposition can be applied to the salinity and temperature fields: θ_0 and S_0 are time and spatially averaged properties; θ_1 and S_1 are time averaged and spatially varying; and θ_2 and S_2 are the residuals.

The decomposition above makes no assumption about the timescale, τ. In practice, τ is typically chosen to (perhaps crudely) distinguish between a mean exchange flow and higher frequency modes, e.g. tides, wind-driven flows, etc. For typical estuarine studies, the averaging timescale τ is between 30 and 50 hours such that u_2 is primarily tides and u_1 captures the subtidal exchange flow. Different timescale decompositions, however, may be appropriate for different systems, and the averaging timescale τ should be chosen based on the variability in the estuary/fjord. For example, in Sermilik Fjord, shelf-forced intermediary circulations are the dominant signal in the velocity field, with peak energy at periods of 3-10 days (Jackson et al., 2014), so a τ of several weeks will be required to separate these flows from a residual exchange flow.

Using the decomposed velocity and water properties, the time-averaged fluxes through the cross-section have three components:

$$\begin{aligned}
\overline{H}_x^a &= \rho c_p \overline{\int_{A_x} (u_0 + u_1 + u_2)(\theta_0 + \theta_1 + \theta_2) dA} = \underbrace{\rho c_p u_0 \theta_0 A_x}_{H_0} + \underbrace{\rho c_p \int_{A_x} u_1 \theta_1 dA}_{H_1} + \underbrace{\rho c_p \overline{\int_{A_x} u_2 \theta_2 dA}}_{H_2} \\
\overline{F}_x^a &= \overline{\int_{A_x} (u_0 + u_1 + u_2)(S_0 + S_1 + S_2) dA} = \underbrace{u_0 S_0 A_x}_{F_0} + \underbrace{\int_{A_x} u_1 S_1 dA}_{F_1} + \underbrace{\overline{\int_{A_x} u_2 S_2 dA}}_{F_2}
\end{aligned} \tag{3.9}$$

Six of the cross terms have been dropped due to the averaging properties of the decomposed fields: the spatial average of the mean exchange is zero ($\int_{A_x} u_1 dA = 0$, $\int_{A_x} S_1 dA = 0$, etc.) and the time-average of the fluctuating fields is approximately zero ($\overline{u_2} \approx \overline{S_2} \approx \overline{\theta_2} \approx 0$). The time-average of the fluctuating field would be exactly zero if a simple average were performed over the whole record; however, because the overbar denotes a running average (i.e. a low-pass filter), the dropped cross-terms are not exactly zero. In Appendix 3.A, it is shown that the small errors from dropping these cross-terms are negligible in the budgets.

In the estuarine literature, F_0 is typically called the river salt flux, F_1 the exchange flux, and F_2 the tidal flux (e.g., MacCready and Geyer, 2010). We generalize these terms to 'mean barotropic' (F_0, H_0), 'mean exchange' (F_1, H_1) and 'fluctuating' (F_2, H_2) fluxes, since the freshwater inputs are not from a river, and tides are not necessarily the dominant mode of variability. Note that our definition of 'mean barotropic' is slightly nonstandard because it is a spatial average of the cross-section, not just a depth average. Using these decomposed transports, the time-averaged budgets become:

$$\textsc{Mass:} \quad \underbrace{u_0 A_x}_{-\overline{Q}_{FW}} + \underbrace{\overline{Q}_R + \overline{Q}_{MW}}_{\overline{Q}_{FW}} = 0 \tag{3.10}$$

$$\begin{aligned}\textsc{Heat:} \quad & \underbrace{\rho c_p u_0 \theta_0 A_x}_{H_0} + \underbrace{\rho c_p \int_{A_x} u_1 \theta_1 dA}_{H_1} + \underbrace{\overline{\rho c_p \int_{A_x} u_2 \theta_2 dA}}_{H_2} + \underbrace{\rho c_p \overline{Q}_R \theta_R}_{\overline{H}_R} + \underbrace{\rho c_p \overline{Q}_{MW} \theta_{MW}}_{\overline{H}_{MW}} \\ & = \underbrace{\overline{\rho c_p \int_{V_c} \frac{\partial \theta}{\partial t} dV}}_{\overline{H}_{Storage}} + \underbrace{\rho L_{adj} \overline{Q}_{MW}}_{\overline{H}_{Melting}} + \overline{H}_{Surf}\end{aligned} \tag{3.11}$$

$$\textsc{Salt:} \quad \underbrace{u_0 S_0 A_x}_{F_0} + \underbrace{\int_{A_x} u_1 S_1 dA}_{F_1} + \underbrace{\overline{\int_{A_x} u_2 S_2 dA}}_{F_2} = \underbrace{\overline{\int_{V_c} \frac{\partial S}{\partial t} dV}}_{\overline{F}_{Storage}} \tag{3.12}$$

where $\overline{Q}_{FW} = \overline{Q}_R + \overline{Q}_{MW}$ is the total freshwater input and the 'a' superscripts denoting 'advective' (e.g., $\overline{H}_R^a$) have been dropped.

Subtracting a reference temperature from the heat budget does not alter the total budget, though it will change the relative magnitude of certain advective components. When a reference temperature, θ_r, is subtracted from the heat budget in Eq. (3.11), it becomes:

$$\begin{aligned}& \underbrace{\overline{\rho c_p \int_{A_x} u_2 \theta_2 dA}}_{H_2} + \underbrace{\rho c_p \int_{A_x} u_1 \theta_1 dA}_{H_1} + \underbrace{\rho c_p u_0 (\theta_0 - \theta_r) A}_{H_0} + \underbrace{\rho c_p \overline{Q}_R (\theta_R - \theta_r)}_{\overline{H}_R} + \underbrace{\rho c_p \overline{Q}_{MW} (\theta_{MW} - \theta_r)}_{\overline{H}_{MW}} \\ & \qquad = \overline{H}_{Storage} + \overline{H}_{Melting} + \overline{H}_{Surf}\end{aligned} \tag{3.13}$$

One can see that H_1 and H_2 are independent of the reference temperature, whereas H_0, $\overline{H}_R$, and $\overline{H}_{MW}$ – the terms associated with non-zero mass fluxes – will change their relative magnitudes as a function of the reference temperature. These latter terms can be considered the barotropic heat fluxes across different boundaries: across the fjord cross-section in H_0, across the ocean/ice boundaries in $\overline{H}_{MW}$ and across the openings of runoff channels in $\overline{H}_R$. It is a well-known problem that the heat transports across partial boundaries of a control volume can be dependent on the reference temperature, while the integrated transport over all boundaries is not (Montgomery, 1974). Accordingly, the three terms in Eq. (3.13) that are dependent on the reference temperature sum to

$\overline{H}_0^{tot}$, which is independent of the reference temperature:

$$\begin{aligned}\overline{H}_0^{tot} = H_0 + \overline{H}_R + \overline{H}_{MW} &= \rho c_p u_0(\theta_0 - \theta_r)A_x + \rho c_p \overline{Q}_R(\theta_R - \theta_r) + \rho c_p \overline{Q}_{MW}(\theta_{MW} - \theta_r) \\ &= \rho c_p \overline{Q}_R(\theta_R - \theta_0) + \rho c_p \overline{Q}_{MW}(\theta_{MW} - \theta_0) \qquad (3.14)\end{aligned}$$

where the second line has been rewritten using mass conservation (Eq. 3.10). $\overline{H}_0^{tot}$ can be called the barotropic heat flux divergence: mass enters the control volume at θ_R and θ_{MW} and leaves, in the barotropic component, at θ_0. Thus the total heat budget can be rewritten so that each term is now independent of the choice of the reference temperature:

$$H_2 + H_1 + \overline{H}_0^{tot} = \overline{H}_{Storage} + \overline{H}_{Surf} + \overline{H}_{Melting} \qquad (3.15)$$

This will be the best form for comparing the magnitude of heat budget components in Section 3.5 such that the results do not depend on the choice of a reference temperature.

3.3.4 Estimating freshwater fluxes from observations

Consider the typical case where ocean measurements of velocity, temperature and salinity are made at a fjord cross-section with the goal of inferring submarine melting or runoff. Assuming that neither of the glacial inputs are known *a priori*, there are three budget equations [Eq. (3.11)-(3.10)] along with (at least) three unknowns: the two freshwater inputs, $\overline{Q}_R$ and $\overline{Q}_{MW}$, and the barotropic velocity, u_0.

We consider u_0 to be an unknown because it is too small to be directly measured in almost all fjords. By mass conservation, u_0 is the total freshwater flux, $\overline{Q}_{FW}$, divided by the cross-sectional area [Eq. (3.10)]. In Sermilik, for example, we expect the total freshwater flux, $\overline{Q}_{FW}$, to be less than 2000 m^3 s^{-1} (see Section 3.5) and the cross-sectional area to be greater than 4.2 km^2, such that $u_0 < 4 \times 10^{-4}$ m s^{-1}. This is well outside our ability to measure with current technology. Even in a small fjord (e.g., $A_x = 3$ km$\times$100 m) with the same large freshwater flux, the barotropic velocity would still be unmeasurable at 0.006 m s^{-1}. This is an important point: the mean barotropic velocity through the cross-section is crucial for balancing the mass input of freshwater, but it is not directly measurable. It should, however, be possible to observe the exchange and fluctuating velocity fields, u_1 and u_2, in most fjords.

The heat, salt and mass budgets can be combined to solve for the three unknowns ($\overline{Q}_R$, $\overline{Q}_{MW}$, and u_0) in terms of quantities that can theoretically be measured (F_1, H_1, F_2, H_2, $F_{Storage}, H_{Storage}$ and H_{Surf}). To start, we use the time-averaged salt budget in Eq. (3.12) to solve for u_0 or $\overline{Q}_{FW}$ in terms of the exchange and fluctuating transports and salt storage:

$$\overline{Q}_{FW} = -u_0 A_x = \frac{1}{S_0}\left[F_1 + F_2 - \overline{F}_{Storage}\right] \tag{3.16}$$

The last two terms on the right hand side will drop out if the system is in steady state. This is effectively an inversion of the Knudsen relationship (Knudsen, 1900; MacCready and Geyer, 2010), which is typically used to infer the exchange flow from a salinity profile and known freshwater flux.

In the heat budget of Eq. (3.11), u_0 can be rewritten in terms of $\overline{Q}_{FW}$ ($-u_0 A_x = \overline{Q}_{FW}$) and $\overline{Q}_R$ in terms of $\overline{Q}_{MW}$ and $\overline{Q}_{FW}$ ($\overline{Q}_R + \overline{Q}_{MW} = \overline{Q}_{FW}$), which allows an expression for $\overline{Q}_{MW}$ in terms of $\overline{Q}_{FW}$ and other measurable components:

$$\overline{Q}_{MW} = \frac{1}{\beta}\left[\rho c_p \overline{Q}_{FW}(\theta_R - \theta_0) + H_1 + H_2 - \overline{H}_{Storage} - \overline{H}_{Surf}\right] \tag{3.17}$$

where $\beta = \rho L_{adj} - \rho c_p(\theta_{MW} - \theta_R)$ and $\overline{Q}_{FW}$ is calculated from Eq. (3.16). The runoff flux is then the difference between the total freshwater and the meltwater:

$$\overline{Q}_R = \overline{Q}_{FW} - \overline{Q}_{MW} \tag{3.18}$$

Thus, in Eqs. (3.16), (3.17), and (3.18), the three budgets have been combined to solve for $\overline{Q}_{FW}$, $\overline{Q}_{MW}$ and $\overline{Q}_R$ in terms of potentially measurable quantities.

We do not explicitly include sea ice in this derivation: sea-ice meltwater would be grouped in with Q_{MW} if the ocean supplied the latent heat to melt, whereas it would fall within Q_R if the atmosphere drove melting. Sea ice formation would contribute a negative freshwater flux.

Amongst other things, this decomposition highlights that, in fjords that have significant runoff (likely many Greenlandic fjords in the summer), there is no way to accurately measure submarine melting from a heat budget alone. There are at least two independent unknowns, $\overline{Q}_{MW}$ and $\overline{Q}_R$, in the heat budget equation [Eq. (3.11)], which means that this equation alone cannot be used to solve for $\overline{Q}_{MW}$. Another constraint, such as a salt budget, is necessary if runoff is not known a priori. Put another way, volume must be conserved in the control volume: since one cannot measure the net volume fluxes directly, an additional constraint (i.e. the salt budget) is required to ensure volume conservation in the heat budget.

3.4 Observations from Sermilik Fjord

3.4.1 Background on Sermilik Fjord region

Sermilik Fjord is long (90 km), narrow (5-10 km) and deep (>800 m), with no shallow sill to impede exchange with the shelf – the shallowest point in a thalwag between the shelf and glacier is 530 m in the upper fjord (Fig. 3-2). Helheim Glacier, the fifth largest outlet of the Greenland Ice Sheet in terms of total ice discharge (Enderlin et al., 2014), drains into the northwest corner of Sermilik Fjord. Two smaller glaciers, Fernis and Midgård, also drain into the fjord in the north and northeast corners. Based on satellite-observed ice velocities and estimated ice thickness, the total ice discharges (iceberg calving plus submarine melting) from Helheim, Midgård, and Fernis are 821±82, 174±32, and 79±16 m^3 s^{-1} water equivalent, respectively, from 1999-2008 (Mernild et al., 2010).

The water masses found in the fjord are a combination of shelf water masses – Atlantic Water (AW) and Polar Water (PW) – and glacially modified water from submarine meltwater and runoff (Straneo et al., 2011). Because there are at least four different water mass end-members, the meltwater fraction cannot be unambiguously calculated with measurements of temperature and salinity alone (Beaird et al., 2015). One can, however, qualitatively identify regions of glacial modification based on where fjord properties diverge from the shelf water masses.

At the mouth, the fjord connects to an energetic and highly variable shelf region. The southeast shelf of Greenland is subjected to intense along-shore winds, called barrier winds, which occur when low pressure systems encounter Greenland's steep topography (Harden et al., 2011). Outside of Sermilik, these strong winds are typically from the northeast, which is downwelling-favorable from an oceanographic perspective. The shelf region is characterized by strong oceanic fronts and large variability in water properties, with a series of troughs diverting the East Greenland Coastal Current in close proximity to Sermilik's mouth (Sutherland and Pickart, 2008; Harden et al., 2014). Sermilik Fjord is also subjected to intense, localized along-fjord wind events from downslope flow off the ice sheet (Oltmanns et al., 2014). The fjord is only rarely covered by land-fast sea ice (Andres et al., 2015).

Icebergs are a prominent feature in the fjord – certainly a challenge to obtaining ocean observations and likely a modifier of fjord dynamics. A thick mélange of icebergs extends 10-20 km from the glacier's terminus (Foga et al., 2014), rendering this region inaccessible by boat. The rest of the fjord is littered with transiting icebergs – often moving faster than 0.1 m s^{-1} (Sutherland et al.,

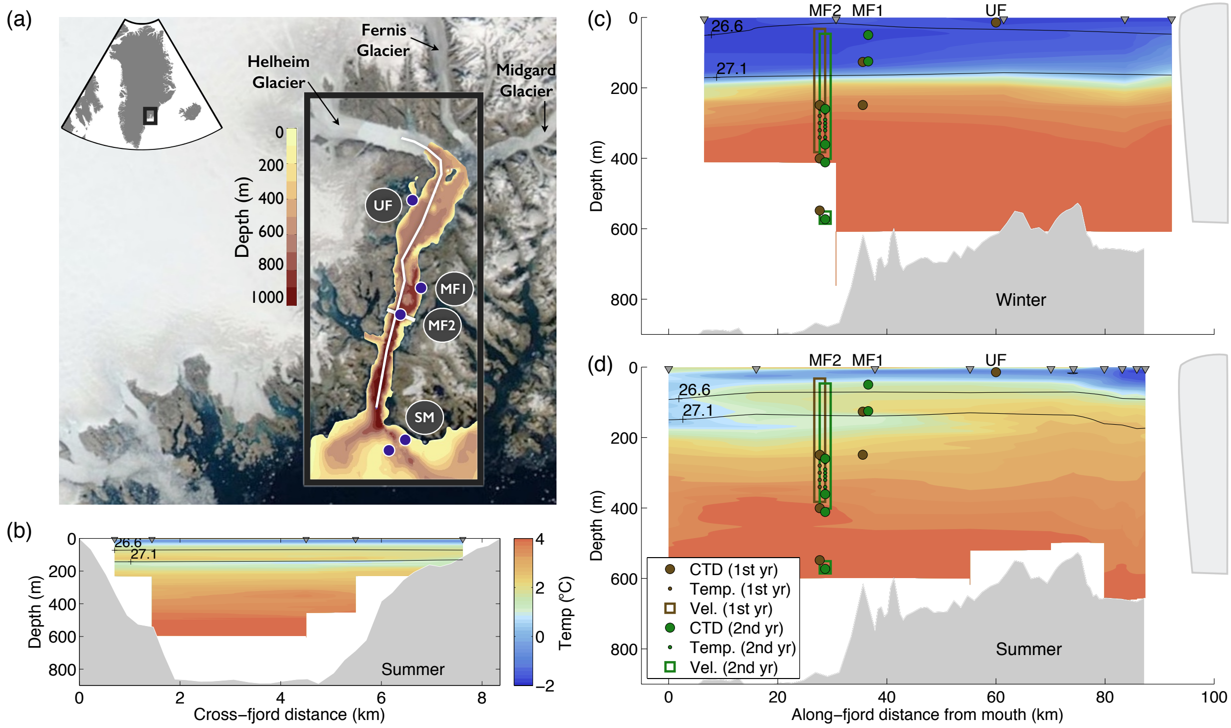

Figure 3-2: (a) Satellite image of the Sermilik Fjord region with bathymetry overlaid. Mooring locations and major glaciers are indicated. (b) Cross-fjord section of potential temperature at mooring MF2 location in summer from August 2011 hydrographic survey. (c) Along-fjord section of potential temperature in winter from March 2010 hydrographic survey (Straneo et al., 2011) with depth of instruments from mooring sites MF1, MF2 and UF overlaid. (d) Same as (c) except with along-fjord potential temperature of summer conditions from August 2011 hydrographic survey. Isopycnals of $\sigma = [26.6, 27.1]$ kg m^{-3} are overlaid in (b), (c), and (d). Carrots at top indicate the CTD station locations used to create temperature section. Locations of cross- and along-fjord sections are shown with white lines in (a). The same colorbar for temperature is used in (b), (c), and (d).

2014a) and with keels deeper than 300 m (Andres et al., 2015) – that interfere with shipboard surveys and imperil moorings in the upper water column.

3.4.2 Oceanic, wind and runoff data from Sermilik Fjord

Records of velocity and water properties, shown in Fig. 3-3, were obtained from two consecutive deployments of mid-fjord moorings in Sermilik Fjord. (See Fig. 3-2 and Table 3.2 for instrument locations and information.) The records span from August, 2011 to August, 2013, with a three month gap during the summer of 2012 when the primary current profiler failed. Temperature, salinity and pressure were measured at six depths ranging from 14 to 541 m in 2011-2012 and from 50 to 567 m in 2012-2013. Temperature was also recorded at six additional depths in each year. An upward-facing 75 kHz ADCP measured velocity in 10 m bins from 396 m to the surface in the first year and in 15 m bins from 411 m to the surface in the second year. Due to sidelobe contamination from the surface, the bins centered at 27 m and shallower were discarded in the first year and the bins centered at 39 m and shallower were discarded in the second year. Additionally, a current meter recorded velocity at 567 m for the second year. The water properties were sampled at intervals between 7.5 and 30 minutes, while the ADCP sampled with 30 ping ensembles at 1 and 2 hour intervals in the first and second year, respectively. The velocity measurements have an uncertainty of ±1 cm/s.

Two moorings on the shelf (SM in Fig. 3-2a) recorded temperature, salinity and pressure at approximately 280 and 300 m for both years (records described in Harden et al., 2014). These time-series are only used in $\theta - S$ diagrams for context in interpreting fjord water properties. Additionally, synoptic surveys of the fjord and shelf were conducted with XCTDs in March 2010 (Fig. 3-2c, Straneo et al., 2010) and with lowered CTDs in August 2011 (Fig. 3-2b/d), September 2012, and August 2013. These were used to correct drift in the moored CTDs and to provide context for the spatial variability within the fjord.

The water properties from the mid-fjord moorings are treated as though they were from the same horizontal location, thus neglecting lateral variability between mooring locations and allowing us to create the depth versus time plots in Fig. 3-3. This assumption is supported by the synoptic surveys of the fjord, which show small lateral variability on the scale of several kilometers compared to variability in depth, time or lateral variability over the fjord length-scale (Jackson et al., 2014). Furthermore, instruments at MF1 (in the middle of the fjord) and MF2 (on the side of the fjord) both recorded properties within ten meters of 260 m depth in 2011-2012, and they show nearly

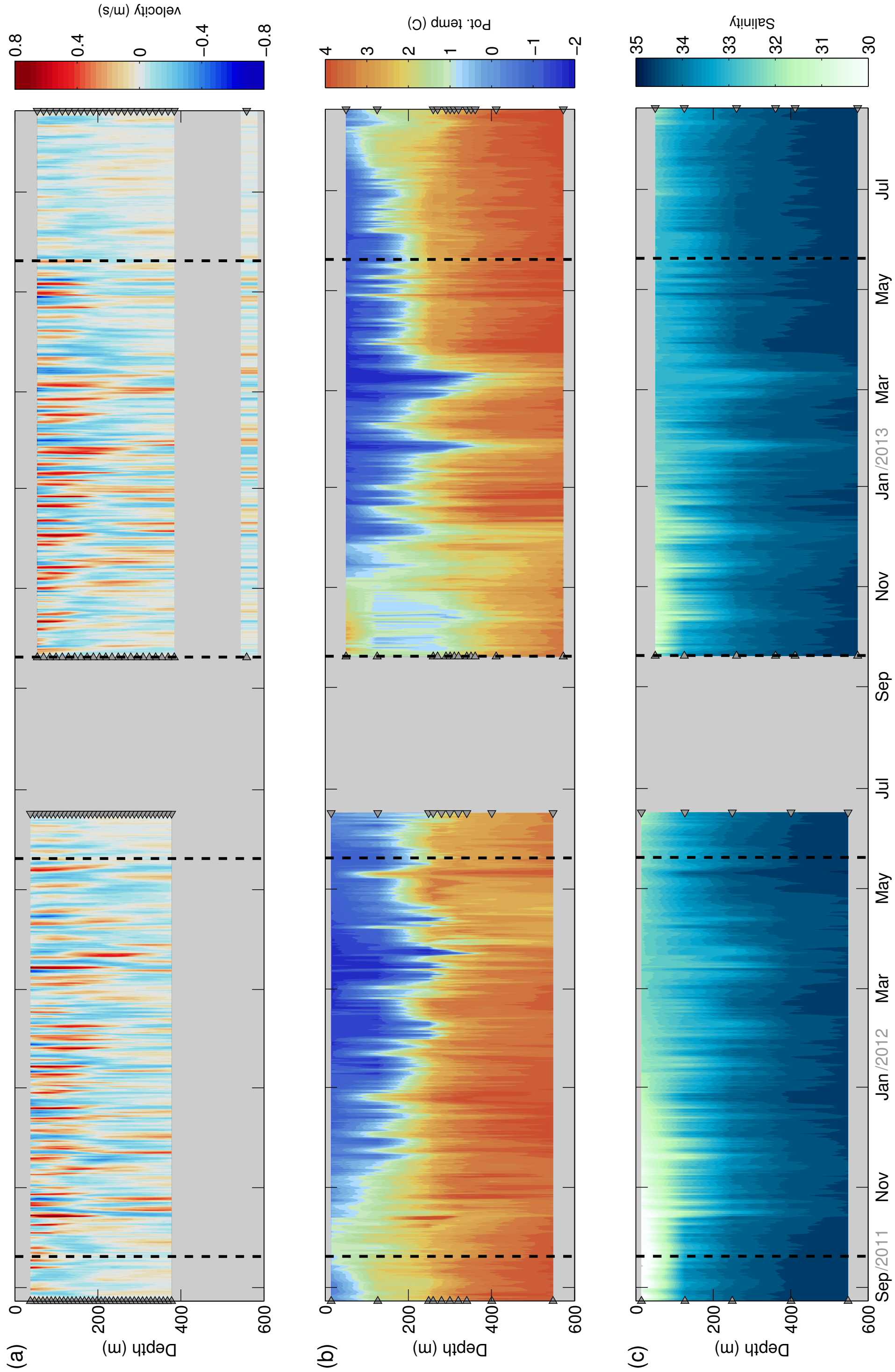

Figure 3-3: Two-year records from mid-fjord moorings, MF1 and MF2. (a) Along-fjord velocity, with positive values towards the glacier and negative towards the fjord mouth. (b) Potential temperature. (c) Salinity. Grey triangles indicate the depths of instruments. Vertical dashed black lines at September 20 and May 20 of both years demarcate the summer versus non-summer regimes.

Mooring	**Instrument**	**Measured properties**	**Sampling period (min)**	**Average depth (m)**
UF1-2011	SBE 37 MicroCAT CTD	conductivity, temperature, pressure	7.5	14
MF1-2011	SBE 37 MicroCAT CTD	conductivity, temperature, pressure	7.5	125
	SBE 37 MicroCAT CTD	conductivity, temperature, pressure	7.5	261
MF2-2011	RBR XR-420 CTD	conductivity, temperature, pressure	30, 15	246, 657
	Onset HOBO TidbiT v2 Temperature Logger	temperature	30	256, 276, 296, 316, 336, 396
	75 kHz RDI Teledyne Workhorse Long-Ranger ADCP (upward-facing)	velocity	120	396 to surface (10 m bins)
	SBE 37 MicroCAT CT(D)	conductivity, temperature, (pressure)	7.5	396, 541
MF1-2012	RBR DR-1050 Depth Recorder	pressure	7.5	50
	SBE 37 MicroCAT CT	conductivity, temperature	7.5	50
	RBR DR-1050 Depth Recorder	pressure	7.5	125
	SBE 37 MicroCAT CT	conductivity, temperature	7.5	125
MF2-2012	75 kHz RDI Teledyne Workhorse Long-Ranger ADCP (upward-facing)	velocity	60	411 to surface (15 m bins)
	Onset HOBO TidbiT v2 Temperature Logger	temperature	30	268, 288, 298, 308, 318, 338, 348
	RBR XR-420 CTD	conductivity, temperature, pressure	30	257, 567
	SBE 37 MicroCAT CT(D)	conductivity, temperature, (pressure)	7.5	357, 407
	Nortek AquaDopp Current Meter	velocity	10	567
	RBR DR-1050 Depth Recorder	pressure	10	257

Table 3.2: List of instruments from mid-fjord moorings (MF1 and MF2) and upper-fjord moorings (UF1). The 2011 instruments recorded from August 23, 2011 to June 16, 2012 (or longer for some instruments). The 2012 instruments recorded from September 19, 2012 to August 19, 2013. Shelf mooring (SM) data, used only for background of $\theta - S$ diagrams, is described in Harden et al. (2014).

identical salinity and temperature records.

The ERA-Interim reanalysis, which has been shown to accurately capture winds on the southeast shelf of Greenland (Harden et al., 2011), is used to assess the seasonality of the shelf wind forcing. Outside of Sermilik Fjord, the velocity component along the principal axis (230 degrees from north) at a point 45 km offshore of the fjord mouth was extracted for an along-shore wind record. Additionally, the Regional Atmospheric Climate Model v2.3, a high resolution climate model forced by atmospheric reanalysis (RACMO2.3; Van As et al., 2014; Noel et al., 2015), was used to estimate runoff that drains into Sermilik Fjord. Its runoff field provides an estimate of the liquid water that leaves the ice sheet (or terrestrial) surface, but it does not take into account storage or transit within the ice sheet. RACMO2.3 simulations from 1981 to 2013 were used to estimate the runoff flux into the upper half of Sermilik Fjord (i.e. the control volume, or north of our mooring locations) based on the catchment basins in Mernild et al. (2010). The RACMO runoff time-series provides context for the seasonality of freshwater fluxes and a point of comparison for our inferred runoff flux. Lastly, we use bathymetry data from Sutherland et al. (2013) and Schjøth et al. (2012)

for Sermilik Fjord and the adjacent shelf region (Fig. 3-2).

3.4.3 Seasonality: summer versus non-summer conditions

There is a strong seasonality in fjord conditions that leads us to separate a summer regime (May 20 to September 20) from the non-summer months (September 20 to May 20), as demarcated by dashed vertical lines in Fig. 3-3 and subsequent figures. The basic features of the water properties and circulation during the first non-summer period, September 2011 to May 2012, have been described in Jackson et al. (2014). In that study, it was found that fjord circulation in the non-summer months is dominated by a fast (>0.5 m/s), fluctuating two-layer flow. These pulses originate on the shelf and are driven by fluctuations in the shelf pycnocline. Shelf density fluctuations, in turn, are primarily associated with along-shore shelf winds (Jackson et al., 2014; Harden et al., 2014). The shelf-forced flows drive large volume fluxes into and out of the fjord, causing significant variability in heat content and salinity – due both to heaving of isopycnals and also to advective property changes within isopycnal layers (Jackson et al., 2014).

In our two-year records here, we find that these shelf-forced flows persist throughout both years but are much less energetic during the summer. This coincides with a reduction in wind forcing from the shelf. The along-shore shelf winds have a strong seasonality, with frequent strong events in the non-summer months and weaker forcing in the summer. A climatology of the ERA-Interim reanalysis wind field shows that along-shore wind strength outside Sermilik peaks in February and reaches a minimum in July (Fig. 3-4b). During our observational period, the wind seasonality matches that of the climatology, with frequent barrier winds in the non-summer months and few in the summer. Thus, as one would expect, the amplitude of fjord density fluctuations and resulting intermediary circulation are significantly reduced in the summer (Fig 3-3). The standard deviation of the pycnocline depth, approximated as the $\sigma = 26.6$ kg m^{-3} isopycnal, is reduced by 57% in the non-summer months, while the mean speed is reduced by 59% (Fig. 3-4c,d).

Direct forcing from along-fjord winds has a similar seasonality, with occasional down-slope events in the non-summer months and almost none in the summer (Oltmanns et al., 2014). We expect this local wind forcing to drive out-flow in the upper layer of the fjord, as suggested in Sutherland et al. (2014a) (see also Moffat, 2014), though it is difficult to separate this effect from that of the shelf winds in our records, since down-slope wind events in Sermilik almost always follow strong along-shore shelf winds.

The buoyancy forcing from glacial inputs is likely, though not proven, to have an opposite

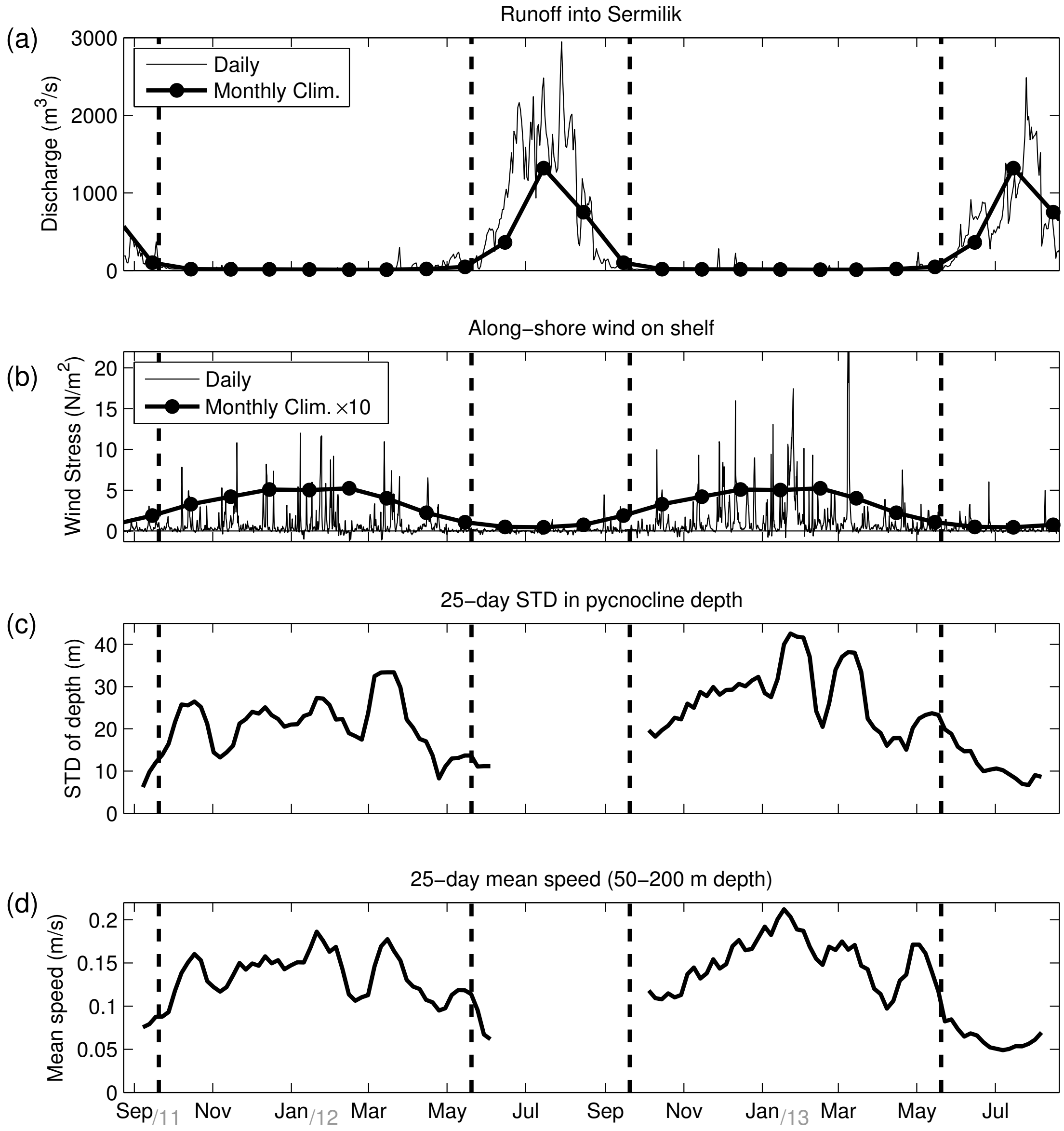

Figure 3-4: (a) Runoff from RACMO2.3 into upper Sermilik Fjord for 2011-2013 as well as monthly climatology from 1981-present. (b) Along-shore wind stress on the shelf, 45 km offshore of Sermilik's mouth, for 2011-2013 as well as monthly climatology (multiplied by a factor of 10) from 1964-present. Positive values indicate winds to the southwest, i.e. downwelling favorable. (c) Proxy for variability in fjord pycnocline: 25-day running standard deviation in the depth of the $\sigma = 26.6$ kg m^{-3} isopycnal. (d) Proxy for fjord velocity: 25-day running average speed of 50-200 m depth range. Vertical dashed lines separate the summer regime from the non-summer.

seasonality from the shelf forcing in the Sermilik Fjord region. Surface runoff from the ice sheet will only form when air temperatures are above freezing, which is primarily June through August (e.g. Mernild et al., 2010). RACMO2.3 runoff into Sermilik (Fig. 3-4a) gives an estimate of melt that leaves the surface of the ice sheet, but it can only provide a rough guess at when and in what quantity runoff actually enters the fjord. In Fig. 3-4a, one can see that runoff is close to zero during the non-summer months, ramps up during June, peaks in July and decays towards zero in September. These seasonalities in freshwater and shelf forcing lead us to demarcate the summer from the non-summer months. (The opposing seasonalities in runoff and wind forcing of Sermilik Fjord are not causal and are not necessarily a general pattern for fjords around Greenland.)

Runoff is only one source of freshwater, however, and we can only speculate about the seasonality of the submarine melting. Modeling studies indicate that submarine melting of glaciers increases with subglacial discharge (e.g., Jenkins, 2011; Xu et al., 2012; Sciascia et al., 2013; Carroll et al., 2015), which suggests that the seasonality of submarine melting might match that of runoff in the absence of other controls on submarine melting. There are, however, a variety of other factors that could cause different seasonal patterns in submarine melting – e.g., the temperature of the AW, the density of the mélange, the fjord's stratification, the presence or absence of PW, the amplitude of intermediary circulations and isopycnal heaving, etc.

The observed water properties at the fjord moorings also exhibit a strong seasonality, as previously suggested from hydrographic surveys (Straneo et al., 2011). In the winter, the fjord is largely a two-layer system, with a strong pycnocline and peak stratification between 150 and 250 m (Fig. 3-5a). During the summer, the fjord is more strongly stratified and the stratification increases towards the surface. Fig. 3-5b shows the seasonal evolution of temperature-salinity (θ-S) diagrams for fjord and shelf properties, with meltwater and runoff mixing lines (see Gade, 1979; Straneo et al., 2011) in the background. Throughout the year, Atlantic-origin water (AW) fills the fjord below $\sim$200 m, and the fjord matches the shelf in this depth range. The upper water column of the fjord, on the other hand, often differs from the shelf. In the summer and fall months, the fjord waters above $\sim$200 m appear to be modified by mixing with both submarine melting and runoff, suggesting that much of the upper layer is a mixture of deep AW that is upwelled through mixing with glacial freshwater. In the winter and spring, there appears to be no modification due to runoff, and the fjord properties collapse into a tighter θ-S relationship. During this period (February-May in Fig. 3-5b), fjord properties in the upper layer converge towards the shelf PW properties, with modification due to submarine melting near the mid-depth pycnocline and perhaps also near the

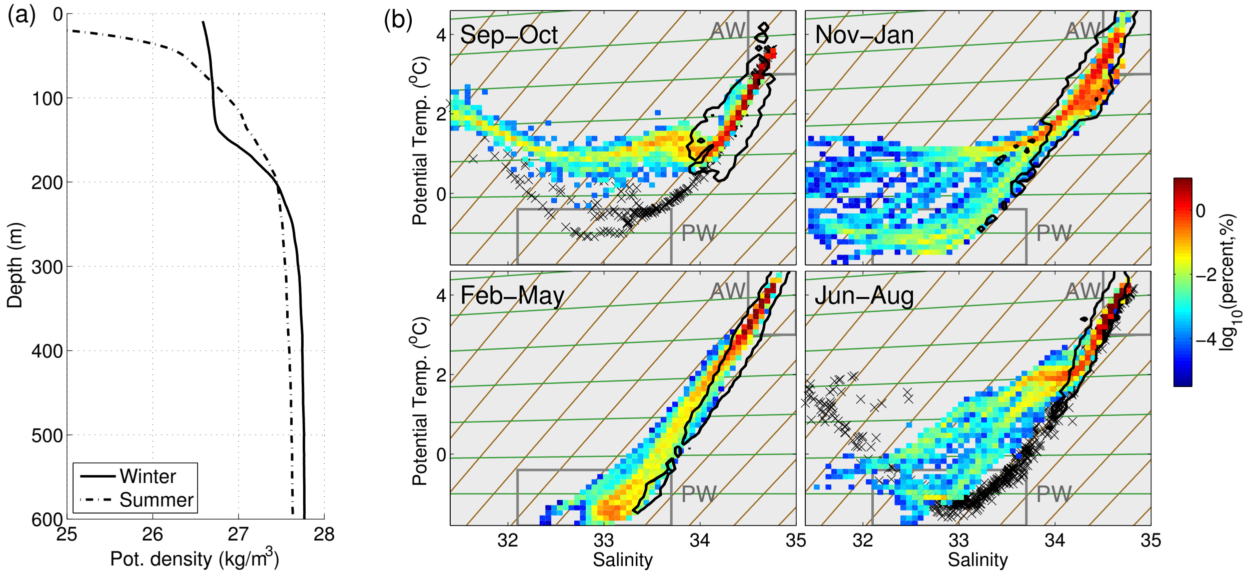

Figure 3-5: (a) Average potential density profiles from fjord surveys in summer (August 2011) and winter (March 2010). (b) Potential temperature-salinity diagram of fjord and shelf for the second year (2012 - 2013). Color: histogram of mid-fjord properties from data shown in Fig. 3-3 (using bins of $\Delta S = 0.06$, $\Delta\theta = .13°\text{C}$) with logarithmic colorbar of percent points within each bin. Black contour outlines the shelf properties from CTDs in 280-301 m depth range: the contour traces the bins (also of size $\Delta S = 0.06$, $\Delta\theta = .13°\text{C}$) that contain more than 0.1% of the shelf points. Black crosses in first and last panel are from CTD surveys of the shelf in September 2012 and August 2013, respectively. Thin brown lines are meltwater mixing lines and thin green lines are runoff mixing lines (see text). Grey boxes outline typical location of AW and PW properties in $\theta - S$ space.

surface.

3.5 Budgets for Sermilik Fjord

3.5.1 Calculating budgets from moored records

Budgets were assessed in Sermilik Fjord for the volume of water upstream of the MF2 mooring site, i.e. the northern half of the fjord that receives the discharge from Helheim Glacier and two smaller glaciers, Fernis and Midgård. The moored records at the southern end of the control volume were used to calculate the measurable terms in the heat and salt budgets: the exchange transport (H_1, F_1), the fluctuating transport (H_2, F_2) and the storage ($\overline{H}_{Storage}, \overline{F}_{Storage}$). Although our records are more comprehensive than previous studies of glacial fjords, particularly in temporal coverage, the spatial coverage of our moorings is still rather limited (Fig. 3-2 and 3-3).

Budget terms were calculated from the records of velocity, temperature and salinity from the mid-fjord moorings that are separated by several kilometers (MF1 and MF2 in Fig. 3-2, Table 3.2), where the lateral variability between these moorings has been neglected (see Section 3.4.2). We grid the velocity and water properties in depth and time to match the ADCP bins: for the first year, 10 m in depth and 1 hour in time; and for the second year, 15 m in depth and 2 hours in time.

To calculate the exchange, fluctuating and storage terms, the velocity and water properties were extrapolated at each timestep so that they spanned from the surface to 800 m depth. The velocity records were extrapolated with four different methods: [a] extrapolation to the surface assuming a constant value equal to the top ADCP bin, then extrapolation to the bottom with a constant value that gives zero mass flux; [b] extrapolation to the surface assuming a constant shear equal to the average shear over the top three ADCP bins, then extrapolation to the bottom with a constant value that gives zero mass flux; [c] extrapolation at the bottom assuming a constant value equal to the deepest ADCP bin, then extrapolation at the surface with a constant value that gives zero mass flux; and [d] extrapolation at the bottom assuming zero velocity at 800 m and linear shear between 800 m and the deepest ADCP bin, then extrapolation at the surface with a constant value that gives zero mass flux. In all of these cases, zero mass flux is defined as:

$$\int_{H}^{0} u_{ex}(z,t)W(z)dz = 0$$

where H = 800 m, u_{ex} is the extrapolated velocity field, and W(z) is the width of the fjord as a function of depth at the MF2 mooring site. Fig. 3-2b shows bathymetry at the fjord cross-section; the width varies from approximately 8 km at the surface to 3 km at 800 m depth. We extrapolate to require zero mass flux so that the extrapolated velocity is essentially a purely baroclinic field. As discussed in Section 3.3, there must be a mean outflowing barotropic velocity, u_0, to balance the inputs of freshwater, but it is too small to measure with an ADCP ($\ll 1$ cm s^{-1}). Thus, we do not assume that there is zero mass flux: u_0 is an unknown and non-zero. Instead, we assume that our measured extrapolated velocity is an estimate of the baroclinic fields ($u_1 + u_2$) such that $u(z, t) = u_0(t) + u_{ex}(z, t)$.

The temperature and salinity records were extrapolated to 800 m depth by assuming a constant value equal to the deepest CTD. This is supported by the very weak stratification observed below 500 m (see profiles in Fig. 3-5a and moored records in Jackson et al., 2014). Water properties were extrapolated to the surface by assuming: [a] a constant value equal to the top CTD, and [b] a constant gradient based on the top two CTD observations. A comparison with the shipboard surveys of the fjord suggests that this spread of extrapolations does well at capturing the surface conditions in the winter, when there is deep mixed layer, but it might overestimate the salinity of the top 10 m in the summer when stratification increases towards the surface (Fig. 3-5a).

The spread from these various extrapolation techniques was included as part of the estimated uncertainty in our calculations. Each version of the velocity field (4 versions) was combined with each version of the water properties (2 versions) to calculate the budget terms and freshwater fluxes in eight different ways. The total spread from these results is included in all subsequent error bars (e.g. Fig. 3-7, 3-8, etc.) and uncertainties.

There is a 530 m deep sill in the upper fjord between the mooring site and the glacier (Fig. 3-2), which suggests that the water below 530 m at the mooring site could be largely isolated from heat, salt and mass exchanges with the glacier. We performed the extrapolations and budget calculations for the water column above 530 m, but the results were similar and are not sensitive to the depth of extrapolation.

To decompose the velocity, temperature and salinity fields, we neglected cross-fjord variability and use the depth-variable fjord width (Fig. 3-2). Because we have extrapolated the velocity field to require zero mass flux, there is no need to remove the barotropic velocity when calculating u_1

and u_2 from the observed velocity field, u_{ex}. Accordingly, the decomposed fields are:

$$u_0 = \text{[unknown]}, \qquad u_1(z,t) = \overline{u_{ex}(z,t)}, \qquad u_2(z,t) = u_{ex}(z,t) - u_1(z,t)$$

$$\theta_0(t) = \frac{1}{H}\int_H^0 \overline{\theta_{ex}(z,t)}W(z)dz, \quad \theta_1(z,t) = \overline{\theta_{ex}(z,t)} - \theta_0(t), \quad \theta_2(z,t) = \theta_{ex}(z,t) - \theta_1(z,t) - \theta_0(t)$$

$$S_0(t) = \frac{1}{H}\int_H^0 \overline{S_{ex}(z,t)}W(z)dz, \quad S_1(z,t) = \overline{S_{ex}(z,t)} - S_0(t), \quad S_2(z,t) = S_{ex}(z,t) - S_1(z,t) - S_0(t)$$

where u_{ex}, θ_{ex} and S_{ex} are the extrapolated fields, H = 800 m, and the overbar represents a running mean over timescale τ (i.e. a boxcar filter). The mean exchange and fluctuating transports from Eq. 3.11 & 3.12 were then calculated from these quantities. For example, the exchange and fluctuating salt transports are calculated as:

$$F_1(t) = \int_H^0 u_1(z,t)S_1(z,t)W(z)dz \tag{3.19}$$

$$F_2(t) = \int_H^0 \overline{u_2(z,t)S_2(z,t)}W(z)dz. \tag{3.20}$$

For this analysis, we use an averaging timescale (τ) of 25 days, based on peak energy in the intermediary circulation at 3-10 day periods (Jackson et al., 2014). Thus, u_2 is predominantly a reversing, two-layer velocity field that is driven by shelf variability, while u_1 is the low frequency exchange flow (Fig. 3-6). The choice of τ involves a tradeoff between a longer averaging timescale to reduce the impact of shelf-forced flows and a shorter timescale to retain seasonal signals in glacial inputs and fjord conditions. Unlike the tides, the intermediary circulation is not a narrow-band signal, so separating it from other modes of circulation is difficult. Caution is required when assigning physical meaning to this timescale decomposition.

The heat and salt storage terms were calculated by assuming that the variability observed at the moorings was representative of the variability upstream of the moorings, over the whole control volume. The salinity storage of Eq. (3.12) can be rewritten as $\overline{F}_{Storage} = \frac{\partial \langle \overline{S} \rangle}{\partial t} V_c$ where $\langle \overline{S} \rangle$ is the time- and volume-averaged salinity over the control volume, V_c. Thus, by assuming that the volume-averaged salinity is approximately equal to the section averaged salinity (i.e. $\langle \overline{S} \rangle \approx S_0$), we calculated the salt storage term as: $\overline{F}_{Storage} = \frac{\partial S_0}{\partial t} V_c$. Following the same logic, the heat storage term is: $\overline{H}_{Storage} = \rho c_p \frac{\partial \theta_0}{\partial t} V_c$. The upstream control volume, V_c, was estimated to be 330 ± 50 km^3 using the bathymetry in Fig. 3-2 and MODIS satellite imagery.

In calculating the storage terms this way, we make a significant assumption that water property

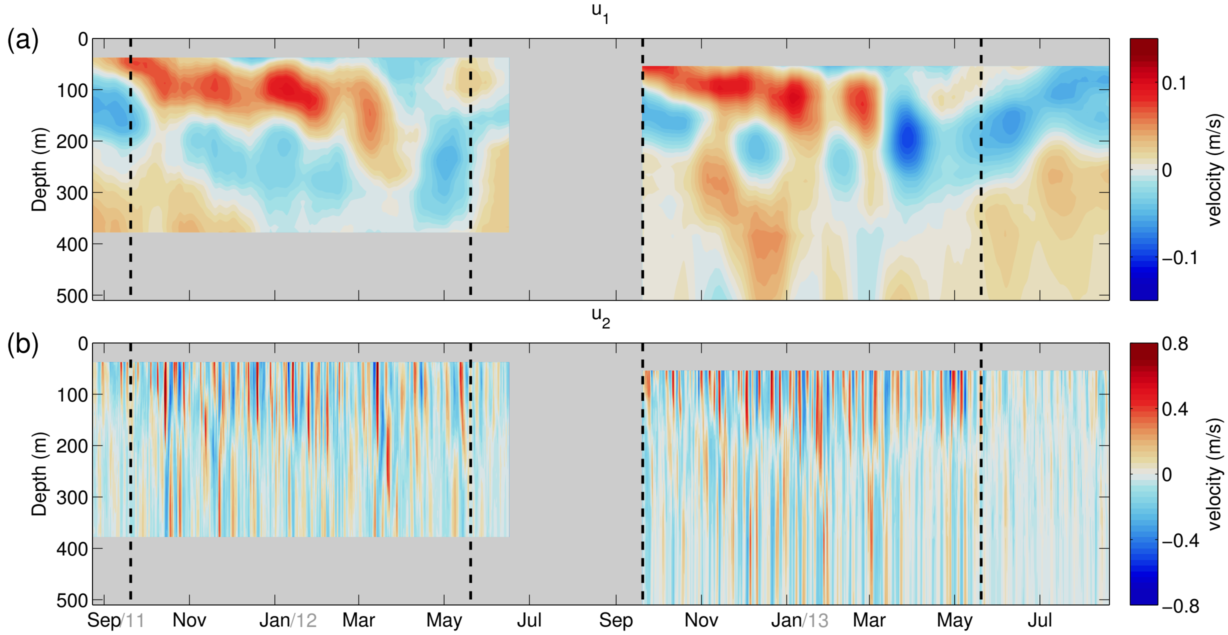

Figure 3-6: Velocity decomposition for measured part of water column. (a) Mean exchange velocity, u_1; (b) fluctuating velocity, u_2. Note different scales on colorbars. Extrapolated parts of the water column are not included.

variability at mid-fjord is, to first order, representative of the variability in the whole control volume. This assumption is supported by analysis from Jackson et al. (2014) and Sutherland et al. (2014b). The dominant temperature and salinity variability in the fjord arises from vertical displacements of the pycnocline. A comparison of mid-fjord and upper-fjord moorings in Sermilik found a high coherence and lagged correlation in water properties between the two locations (Jackson et al., 2014). These pycnocline fluctuations occur over synoptic timescales but take less than a day to propagate up fjord (see below) and thus the pycnocline heaving is approximately uniform throughout the fjord on timescales longer than a day. Additionally, the shelf-forced flows not only drive heaving (i.e. thickness changes in the PW/AW layers) but they also advect variability in AW/PW water mass properties from the shelf through the main part of the fjord on synoptic timescales (Jackson et al., 2014). The method used for calculating the storage terms here is based on observations from Sermilik and might not be justified in other systems or when measurements are made close to a glacier, in the region of convective plumes.

The measurable terms of the heat and salt budgets (F_1, H_1, F_2, H_2, $F_{Storage}$, $H_{Storage}$) for the second year are shown in color in Fig. 3-7 and Fig. 3-8. Using Eqs. (3.16) - (3.18), these quantities were used to infer freshwater fluxes of meltwater and runoff, as shown in Fig. 3-9. In calculating the

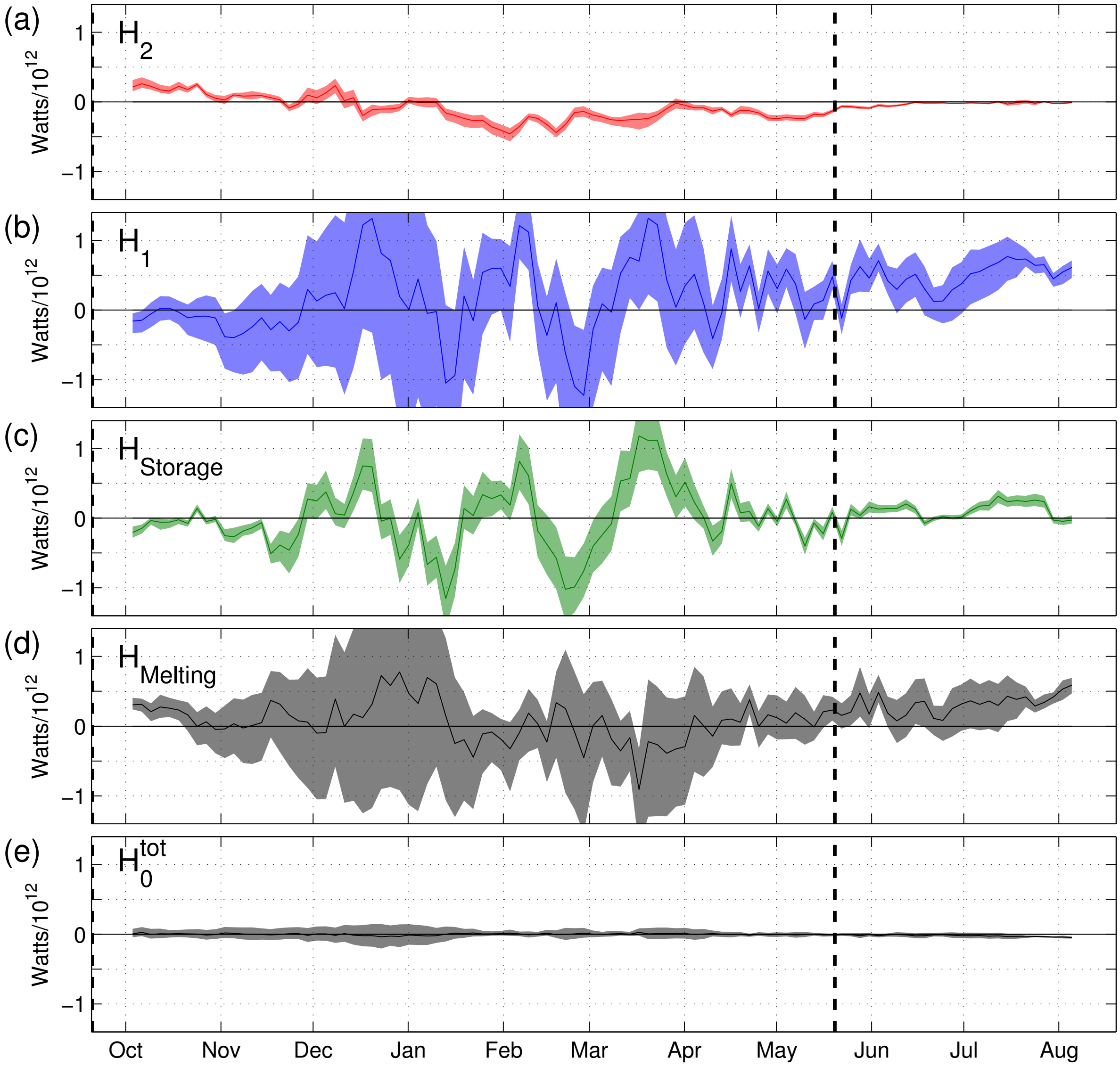

Figure 3-7: Measured and inferred components of the heat budget (in the form of Eq. 3.15) for 2012-13. (a)-(c) Directly measured fluctuating, exchange and storage terms in heat budget. (d) Inferred heat for melting ice, $H_{melting}$. (e) Inferred barotropic heat flux divergence, H_0^{tot}. Error bars here and in subsequent figures are 95% confidence intervals. Colored time-series are measured quantities; black are inferred.

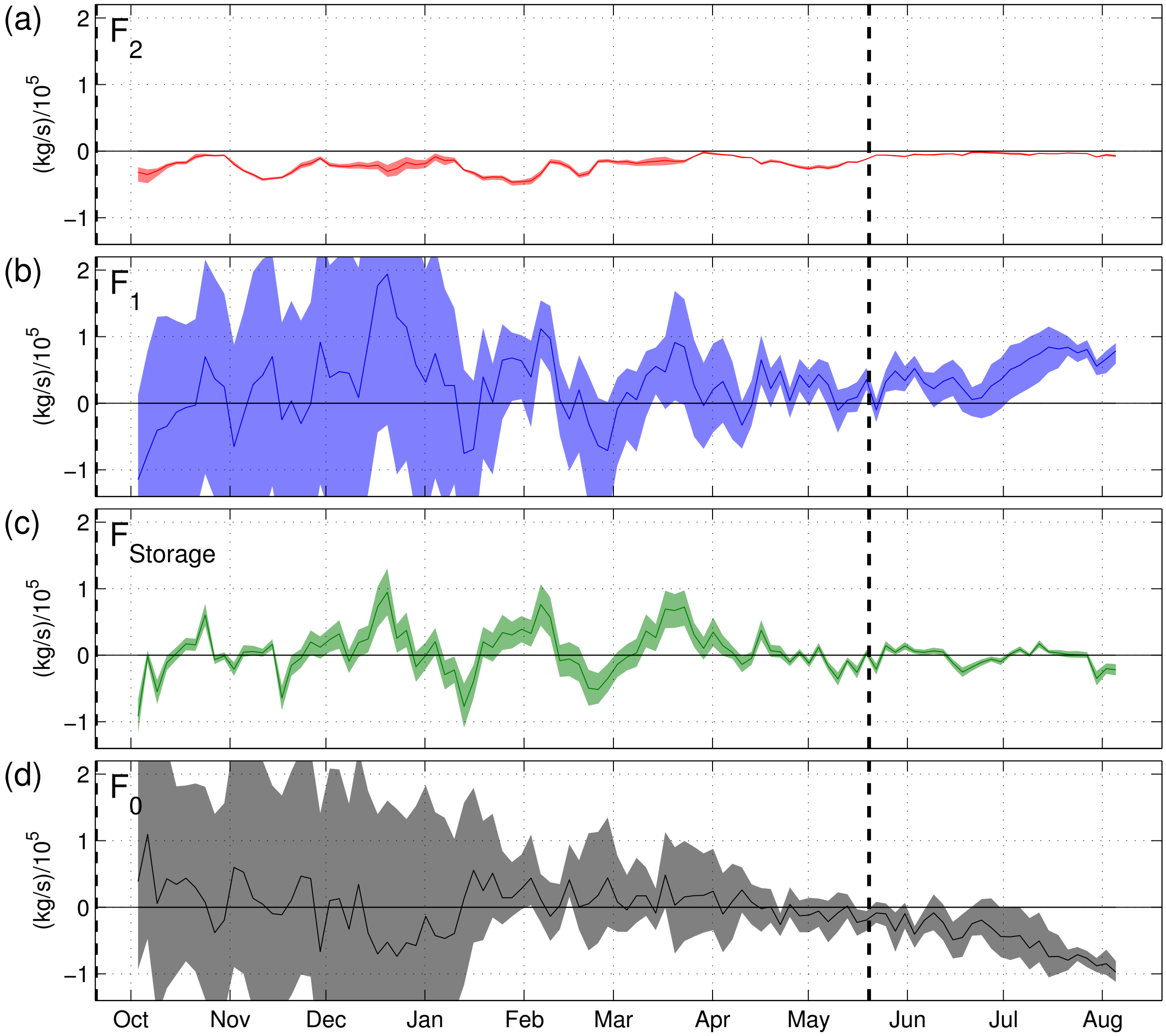

Figure 3-8: Measured and inferred components of the salt budget (in the form of Eq. 3.12) for 2012-13. (a)-(c) Directly measured fluctuating, exchange and storage terms in salt budget. (d) Inferred barotropic salt transport, F_0. As in Fig. 3-7, colored time-series are measured quantities; black is inferred.

freshwater fluxes, we assume that runoff enters the fjord at -0.25 ± 0.25°C, the in-situ freezing point of freshwater at 0 to 630 m depth (covering runoff that enters anywhere from the surface to the base of Helheim Glacier's), and that meltwater enters at -2.0 ± 0.4 °C, based on the freezing point of seawater at a depth of 0-630 m and with a salinity of 30-35 (i.e. the property range of seawater that could drive melting). Additionally, the inferred freshwater fluxes were used to calculate the residual components of the heat and salt budgets: the heat to melt ice ($\overline{H}_{Melting}$, Eq. 3.4) and the barotropic heat flux divergence ($\overline{H}_0^{tot}$, Eq. 3.14) in Fig. 3-7; and the barotropic salt flux (F_0) in Fig. 3-8. We neglect surface heat fluxes, though their potential impact is mentioned in Section 3.5.2 and explored in Appendix C.

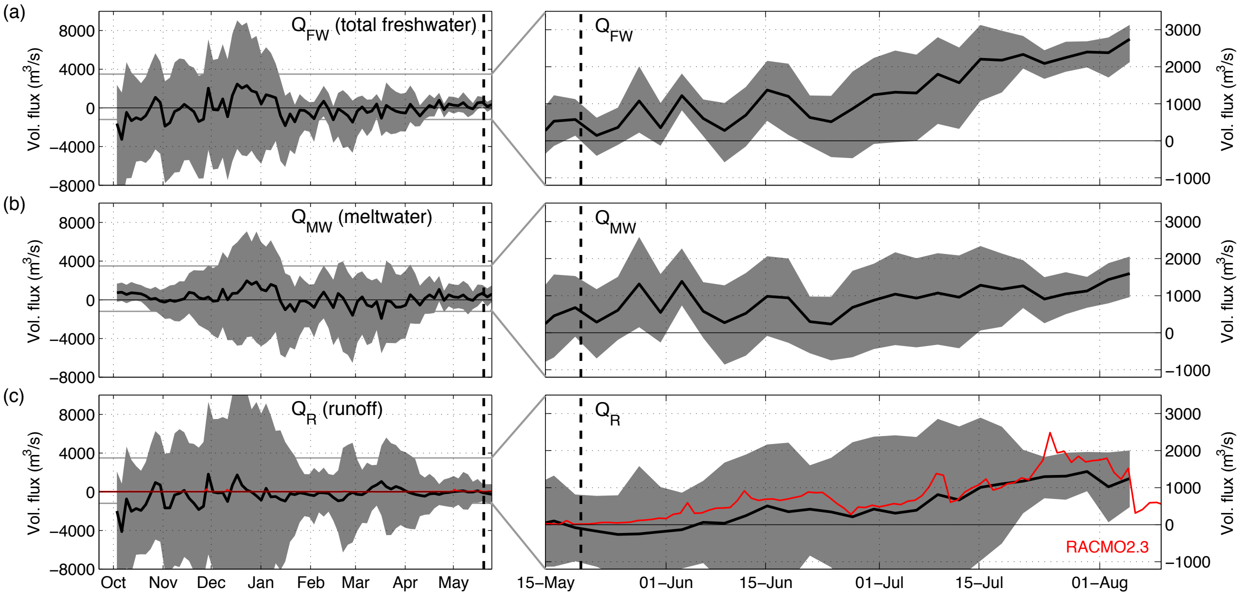

Figure 3-9: Inferred freshwater fluxes from 2012-2013: (a) total freshwater; (b) meltwater; (c) runoff, along with runoff output from RACMO2.3 for Sermilik Fjord (upstream of cross-section). Left panels show non-summer period; right panels show summer months on a different scale. Thin horizontal grey lines in left panels indicate the y-axis range from the right panels.

Seasonal averages for the heat budget components, salt budget components, and freshwater fluxes are reported in Table 3.3.

3.5.2 Seasonal evolution of the heat/salt budgets

Before discussing the inferred freshwater fluxes, the dominant balances in the heat and salt budgets are examined. We focus on the second year of records (2012-2013) that cover both non-summer and summer months, but all of the main conclusions reported here about the non-summer months were

	Non-summer	**Summer**
$H_{Storage}$	$-0.3 \pm 7.5 \times 10^{10}$ W	$9.9 \pm 3.6 \times 10^{10}$ W
H_2	$-9.1 \pm 2.0 \times 10^{10}$ W	$-3.1 \pm 0.9 \times 10^{10}$ W
H_1	$1.5 \pm 2.3 \times 10^{11}$ W	$4.8 \pm 1.5 \times 10^{11}$ W
H_0^{tot}	$0.0 \pm 2.3 \times 10^{10}$ W	$-2.2 \pm 1.6 \times 10^{10}$ W
$H_{Melting}$	$0.6 \pm 2.0 \times 10^{11}$ W	$3.1 \pm 1.4 \times 10^{11}$ W
$F_{Storage}$	$7.0 \pm 5.4 \times 10^{3}$ kg/s	$-2.9 \pm 3.2 \times 10^{4}$ kg/s
F_2	$-2.2 \pm 0.2 \times 10^{4}$ kg/s	$-4.9 \pm 0.6 \times 10^{3}$ kg/s
F_1	$2.4 \pm 3.5 \times 10^{4}$ kg/s	$4.7 \pm 1.5 \times 10^{4}$ kg/s
F_0	$0.6 \pm 3.3 \times 10^{4}$ kg/s	$-4.5 \pm 1.4 \times 10^{4}$ kg/s
Q_{FW}	-140 ± 1100 m^3 s^{-1}	1330 ± 450 m^3 s^{-1}
Q_{MW}	160 ± 900 m^3 s^{-1}	900 ± 540 m^3 s^{-1}
Q_R	-300 ± 2000 m^3 s^{-1}	430 ± 990 m^3 s^{-1}

Table 3.3: Averages from 2012-13 records over the non-summer and summer for components of heat budget, components of salt budget, and freshwater fluxes.

found in both years.

3.5.2.1 Dominant balances in the non-summer months

In the non-summer months, the measured advective transports are balanced by changes in storage: within our ability to measure, $H_1 + H_2 \approx \overline{H}_{Storage}$ and $F_1 + F_2 \approx \overline{F}_{Storage}$. Consequently, the residual terms in the heat and salt budgets (F_0, H_0^{tot}, and $\overline{H}_{Melting}$) are indistinguishable from zero within our error bars (Fig. 3-7 & 3-8), as are the freshwater fluxes (Fig 3-9). The budget results are summarized in the schematic of Fig. 3-10.

Storage balances advective transports of heat and salt Shelf forcing, which is strongest in the non-summer months, has a strong imprint on the fjord budgets. The storage terms, which are leading order components of the non-summer budgets (Fig. 3-7 & 3-8), are largely associated with the shelf-forced circulation. The shelf-forced pulses drive temperature and salinity variability through two (intertwined) mechanisms: large pycnocline fluctuations that change the relative thickness of the PW and AW layers, and rapid exchange with the shelf that advects shelf water into the fjord (Jackson et al., 2014). If the pycnocline heaves uniformly throughout the fjord, a simple expression for the volume-averaged temperature, $\langle\theta\rangle$, is:

$$\langle\theta\rangle = \frac{\theta_U h + \theta_L (H - h)}{H} \tag{3.21}$$

where h is the depth of the interface between layers, H is the total depth, and θ_U and θ_L are the average temperatures of the upper and lower layers, respectively. The assumption of uniform

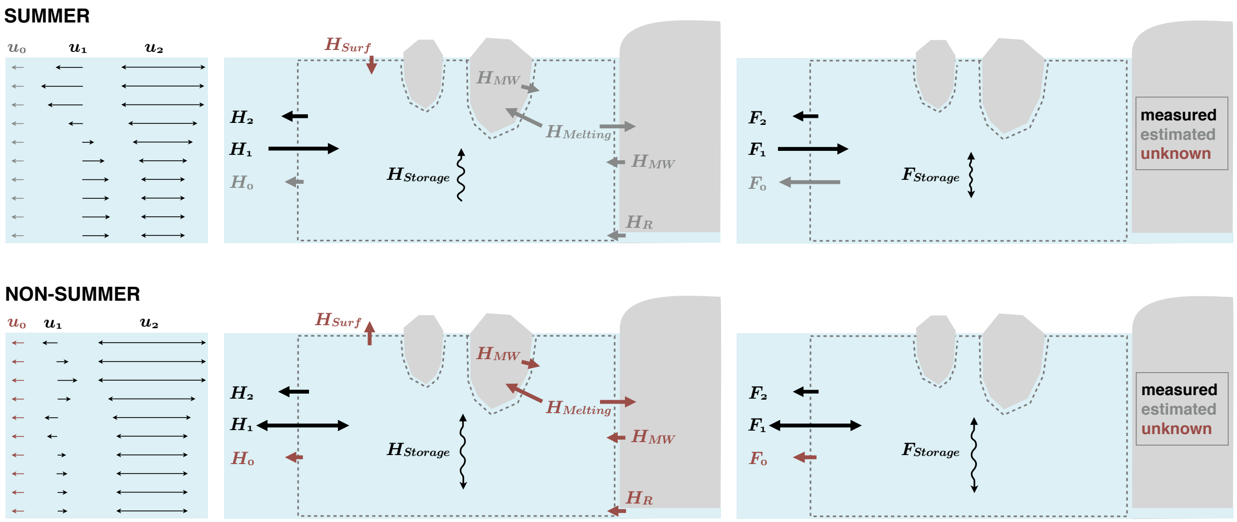

Figure 3-10: Schematic of decomposed velocity field, heat budget, and salt budget for summer (top) and non-summer months (bottom). Terms are color-coded by whether they were directly measured (black), estimated from the residual of the budgets (grey), or unknown (red). For measured or estimated terms, the size of the arrow is approximately proportional to the magnitude. Note: the sign of H_0, H_R and H_{MW} are dependent on the choice of a reference temperature; only their sum (H_0^{tot}) is independent of the reference temperature, and H_0^{tot} should always be negative. Summer is May through September; non-summer is September through May.

pycnocline heaving throughout the fjord was found by Jackson et al. (2014) to be a relatively good approximation in Sermilik: pycnocline displacements have been found to propagate up the fjord at the first baroclinic mode phase speed of $\sim$1 m s^{-1}, so a signal would take 22 hours to travel from the mouth to the head of the fjord (based on comparison of moored density records from the shelf, mid-fjord and upper fjord in Jackson et al., 2014). This propagation timescale is relatively short compared to the forcing timescale of 3-11 days. Thus, to first order, the interface heaves uniformly in the fjord on timescales longer than a day – something that has also been found in other fjords with intermediary circulations (e.g. Arneborg, 2004).

Using the isopcynal of $\sigma_\theta = 27$ kg m^{-3} as a proxy for the interface, we can reconstruct much of the average temperature variability at the Sermilik moorings with Eq. 3.21 (Fig. 3-11). This reconstructed temperature record captures the vast majority of variability in the observed water column temperature, with a correlation coefficient of 0.82 (p<.01) and a statistically significant coherence amplitude over all periods between 18 hours and 66 days. We do not, however, expect these measured and inferred records to match exactly, in part due to temperature changes within each layer.

Although a significant portion of this variability is transient, averaging over 25 days does not

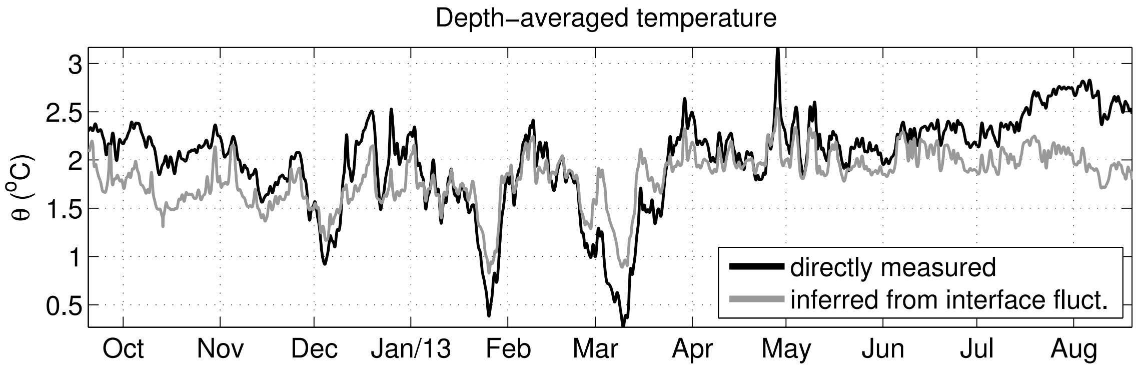

Figure 3-11: Comparison of depth-average temperature, $\langle\theta\rangle$, from measurements of temperature at moorings (black) and reconstructed from interface fluctuations following Eq. 3.21 (gray), assuming the upper layer temperature is -1°C and the lower layer is 3°C.

eliminate the heat/salt content variability. The nature of this storage term is illustrated by comparing a shorter averaging timescale, τ, of 2 days with the standard τ of 25 days (Fig. 3-12). When the averaging timescale is short, $\overline{H}_{Storage}$ fluctuates with the intermediary circulation on synoptic timescales. It has an average absolute value of 1.9×10^{12} W and frequently exceeds 5×10^{12} W. For comparison, the heat required to melt 1000 m^3/s of ice is 3.6×10^{11} W, which is an order of magnitude smaller than the storage term. When a longer averaging timescale of 25 days is applied, the impact of intermediary circulations is diminished, reducing the amplitude of both $\overline{H}_{Storage}$ and $H_1 + H_2$. Nevertheless, the advective heat transports are still balanced by changes in storage within our error bars. Even averaging over the entire season (Table 3.3) does not allow a residual to emerge.

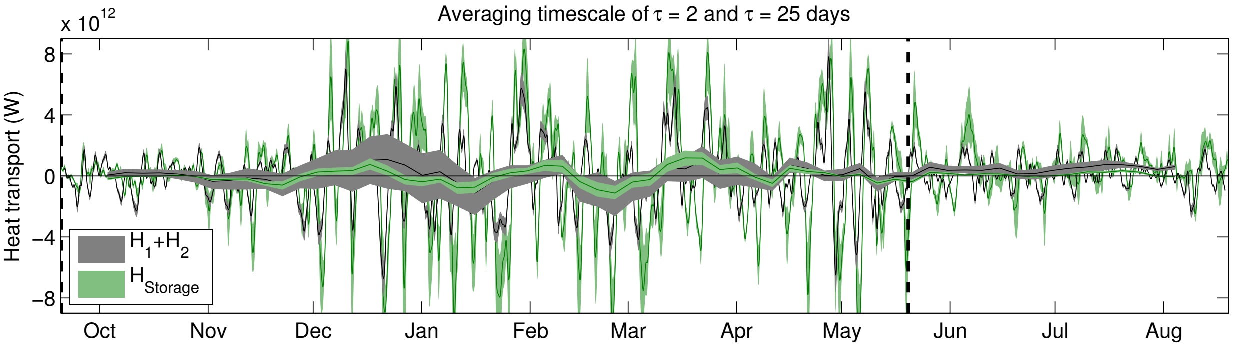

Figure 3-12: Comparison of heat storage ($H_{Storage}$) and cross-section transport ($H_1 + H_2$) for averaging timescales of both 2 days and 25 days. The shorter averaging timescale has larger amplitude fluctuation while the longer timescale is reduced in amplitude (and plotted on top).

Structure of the advective transports In the the non-summer months, the mean exchange transports associated with u_1 do not have a consistent sign. H_1 and F_1 fluctuate between positive and negative (Fig. 3-7 and 3-8), with large error bars due to shelf-forced variability and a significant spread from the extrapolation techniques. During this period, the mean exchange velocity, u_1, is almost an order of magnitude smaller than the fluctuating component (Fig 3-6). The same structure, however, emerges when both non-summer periods are averaged: in Fig. 3-13d, the average u_1 profiles show up-fjord flow centered at 100 m, with weaker outflowing velocity at $\sim$ 220 m and inflowing velocity below $\sim$300 m. There also appears to be outflow near the surface, though this part of the water column is poorly sampled, which might suggest multiple outflows from the glacier. However, the u_1 field in the winter is not necessarily a signal of a buoyancy-driven flow from freshwater inputs – given the small magnitude of u_1 relative to synoptic-scale flows, u_1 could be a residual from other fjord dynamics or partially a sampling bias (see Section 3.6.1).

Although the exchange transports do not have a consistent sign and are not necessarily driven by glacier buoyancy forcing, there are consistent patterns in the water properties that are imported and exported by the u_1 field, as shown in Fig. 3-14. In the fall months, deep AW and the warm surface layer on the shelf are imported into the fjord while a layer of glacially modified water that diverges from shelf properties is often exported between 100 to 200 m. The early winter is difficult to interpret, but a clear pattern emerges again in the February-May panel of Fig. 3-14. During this late winter and spring period, the fjord water properties resemble the shelf water masses with modification from submarine meltwater. The properties that match the shelf are preferentially inflowing while the modified properties (to the left in θ-S space) are, on average, outflowing.

For the fluctuating transports, we observe correlations between u_2, θ_2 and S_2 that result in transports of heat and salt away from the glacier (Fig. 3-7 & 3-8). The structure of this signal is shown in Fig. 3-15, where $\overline{u_2\theta_2}$ and $\overline{u_2 S_2}$ are plotted as a function of depth and time. One can see export of heat and salt in the upper layer, with peak values between between 100 m and 250 m. In the non-summer months, the total fluctuating heat transport (H_2 in Fig. 3-7 or the vertical integral of Fig. 3-15) typically exports 1×10^{11} to 3×10^{11} W, equivalent to the latent heat to melt/freeze 270 to 820 $\mathrm{m}^3\ \mathrm{s}^{-1}$ of ice.

Part of this observed signal could arise from neglecting cross-fjord variability while sampling on the eastern side of the fjord – the net fluctuating transport might be closer to zero if we had full coverage of the cross-section. If pycnocline heaving is accompanied by cross-fjord geostrophic tilt, then assuming that our eastern-side measurements are representative of the whole cross-section

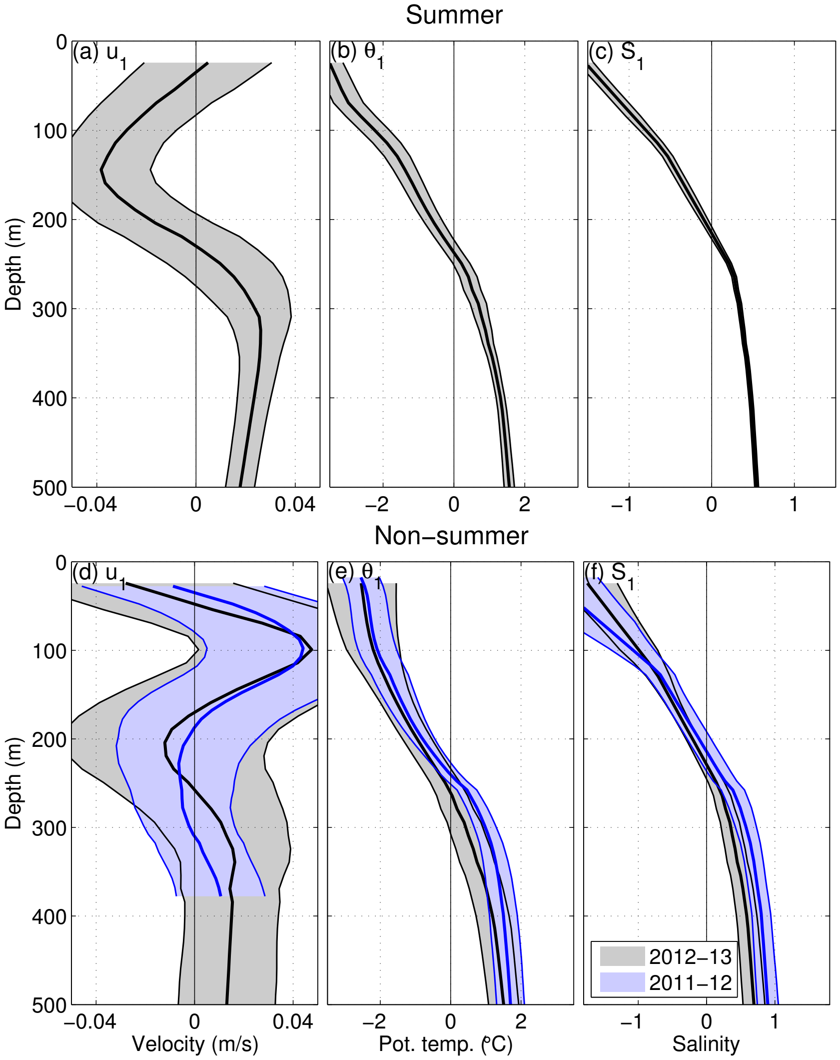

Figure 3-13: Average of u_1, θ_1 and S_1 fields during the summer months (May 20 to Aug 20) in a, b & c, and the non-summer months (Sept 20 to May 20) in c, d, & e. Error bars show one standard deviation of the exchange fields over the time period (*not* the standard deviation of the full fields which include u_2, θ_2 & S_2).

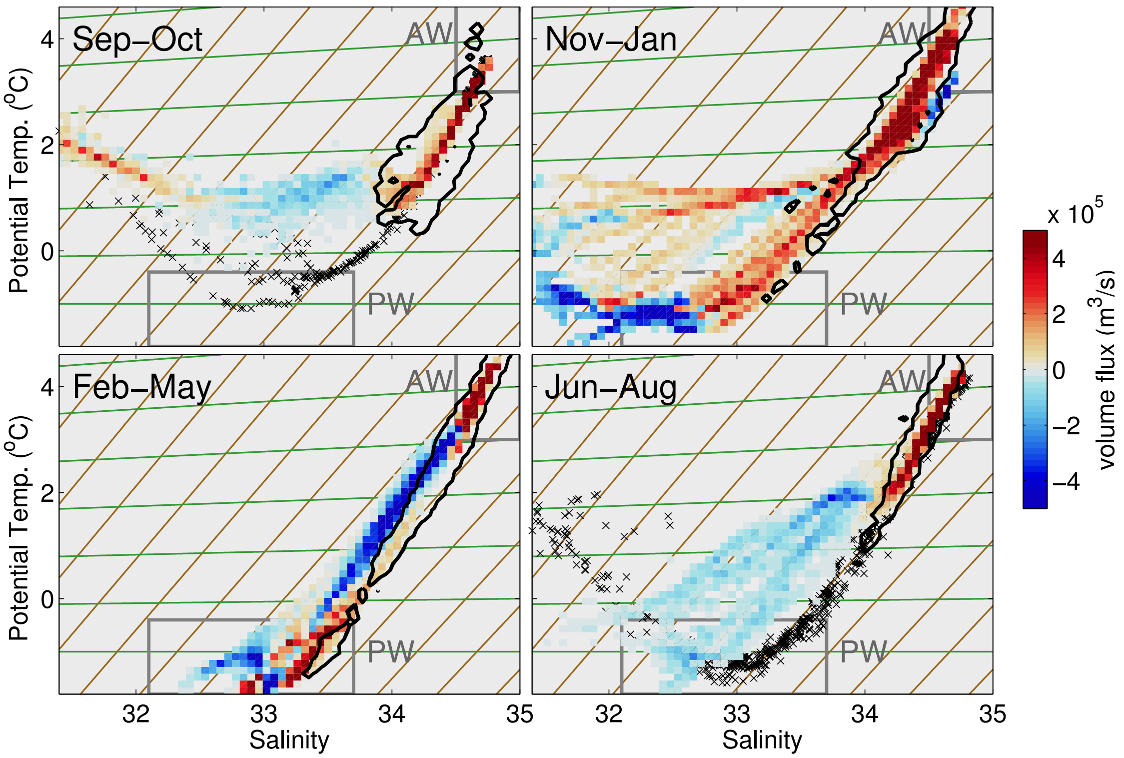

Figure 3-14: Volume transport from the u_1 field binned in θ-S space for four different periods in 2012-13. The mid-fjord θ-S properties are binned in the same manner as Fig. 3-5 but the color is the average volume flux from the u_1 field in that bin, defined as $\Sigma[u_1 dA_x]$ for all points within the θ-S bin. Positive values are towards the glacier, into the control volume. As described in Fig. 3-5, the black contour encloses bins with $> 0.1\%$ of shelf measurements and the black crosses in first and last panel are from CTD surveys of the shelf in Sept. 2012 and Aug. 2013, respectively. Brown lines are meltwater mixing lines and green lines are runoff mixing lines. Grey boxes show typical AW and PW properties.

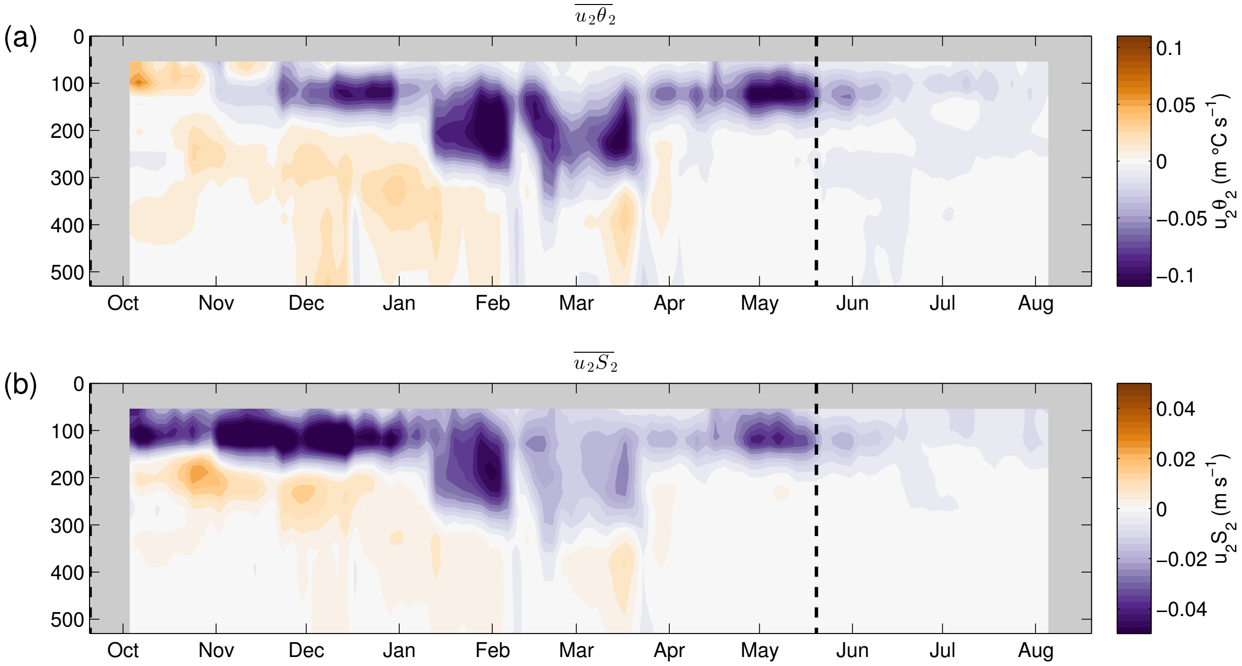

Figure 3-15: Correlations in the fluctuating velocities and water properties. (a) $\overline{u_2\theta_2}$ and (b) $\overline{u_2S_2}$ as a function of depth and time for the second year of records. Positive values are heat/salt fluxes towards the glacier or into the control volume.

could lead to spurious results for F_2 and H_2. This possibility is explored in Section 3.6.1 and Appendix B.

We find that the fluctuating velocity plays a role in exporting glacially modified water, which could also explain some of the heat/salt export in F_2 and H_2. Fig. 3-16 shows a θ-S diagram for January to May with u_2 transport mapped onto the θ-S bins. Below the surface layer (i.e. S>33.5), u_2 field is positive on average when fjord θ-S properties match the shelf. When fjord properties diverge from the shelf and look glacially modified, u_2 is typically negative. Thus, there are persistent correlations between u_2 and the presence of glacially modified water, suggesting that the fluctuating velocity exports meltwater during this non-summer period.

We expect the fluctuating export of glacially modified water to result in a flux of heat and salt away from the glacier. This might seem counterintuitive, since the glacier is ultimately a net source of freshwater and sink of heat. However, based on the slope of the ambient shelf properties in θ-S space, we expect modification from meltwater or runoff to cause warm, salty anomalies in the fjord relative to the shelf (in most of the water column) (e.g. Gade, 1979; Jenkins, 1999). This can be seen in the θ-S diagrams: when deep AW is mixed along the meltwater or runoff mixing lines, the

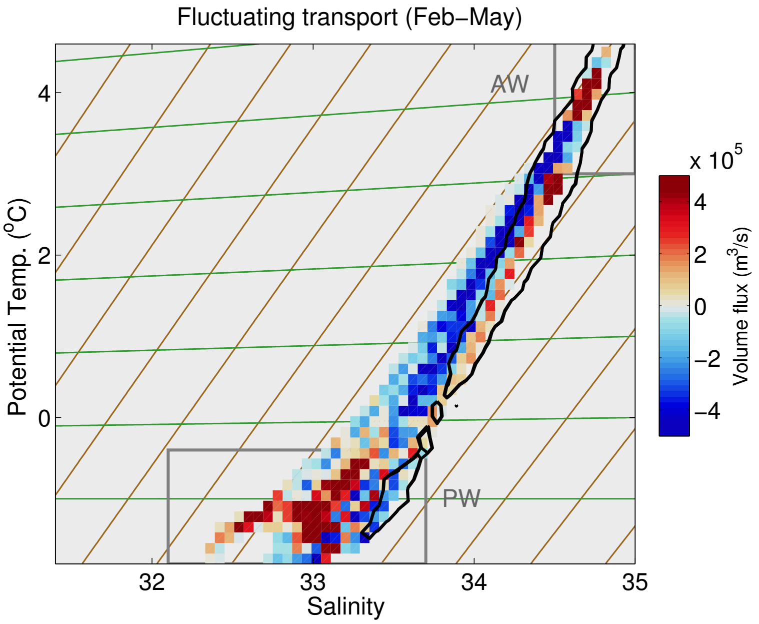

Figure 3-16: Volume transport from the u_2 field over bins in θ-S space for February-May, 2013. The mid-fjord θ-S properties are binned in the same manner as Fig. 3-5 but color is the average volume flux from the u_2 field, defined as $\Sigma[u_2 dA_x]$ for all points within a θ-S bin. While u_2 has a zero time-average at any depth, the time-average in θ-S bins is not zero. Positive values are towards the glacier, into the control volume. As described in Fig. 3-5, the black contour encloses bins with $> 0.1\%$ of shelf measurements. Brown lines are meltwater mixing lines and green lines are runoff mixing lines. Grey boxes show typical AW and PW properties.

water becomes fresher and cooler, but the mixture, now a lower density than the original AW, will be a warm, salty anomaly compared to ambient shelf water of this new density. Thus we expect that, if u_2 fluxes heat and salt down the gradients between the ambient shelf water and glacially modified fjord water, it would result in a net export of heat and salt.

While we have evidence that the u_2 field exports glacially modified water, we do not attribute the entire signal for H_2 and F_2 to this process. Sampling biases, as discussed above, or other processes, such as mixing in the control volume or temporal variability in shelf properties, are likely contributors to the observed fluctuating transports.

Estimating the residual terms in the heat/salt budgets While it is impossible to infer a residual from the measurable terms in the heat or salt budgets, we can put some constraints on the unknown terms of the non-summer budgets. The latent heat for melting ice, $\overline{H}_{Melting}$ is constrained to be less than 1×10^{12} W for most of the winter (Fig. 3-7) and, physically, it must be positive; it could be a trivial term or could be of a similar magnitude as the advective and storage terms. Throughout the year, we expect there to be melting of ice that extracts heat from the ocean, but we cannot measure it within the 'noise' of other fjord processes during the non-summer months. The barotropic heat flux divergence, also indistinguishable from zero because the freshwater fluxes are indistinguishable from zero (see Eq. 3.14), is constrained to be less than 1×10^{11} W – i.e. an order of magnitude smaller than other terms in the heat budget (Fig. 3-7).

During the winter, there are likely $\mathcal{O}(10^{10} - 10^{11})$ W leaving the control volume from surface fluxes (Appendix C), which would be equivalent to the latent heat for $\mathcal{O}(10 - 100)$ m^3 s^{-1} of meltwater. Although these surface fluxes are not a leading order component of the heat budget, they would need to be included to measure the meltwater with an accuracy of $\mathcal{O}(100)$ m^3 s^{-1}. Additionally, in winter, the volume of sea ice formed in the fjord might not be negligible compared to the meltwater volume flux. In our formulation of the budgets, sea ice formation would appear as a negative contribution to the total inferred freshwater flux.

3.5.2.2 Dominant balances in the summer months

In the summer salt budget, we measure F_1, F_2 and $\overline{F}_{Storage}$, and we are able to estimate F_0 as a residual (Fig. 3-8). Since F_0 is proportional to $\overline{Q}_{FW}$, this means that the total freshwater flux becomes distinguishable from zero in the summer months. The salt budget is primarily a balance between imported salt from the exchange, F_1, and exported salt from the barotropic flux, F_0 (Fig. 3-

8 and schematic in Fig. 3-10). The storage term fluctuates between positive and negative, while the fluctuating transport exports a relatively small quantity of salt.

The leading order terms in the summer heat budget are the exchange transport, H_1, the storage term, $\overline{H}_{Storage}$, and the heat for melting, $\overline{H}_{Melting}$ (Fig. 3-7 and schematic in Fig. 3-10). The exchange transport imports heat into the control volume, part of which goes into warming the control volume (hence the positive $\overline{H}_{Storage}$) and part goes to melting ice. The fluctuating transport, H_2, and the barotropic heat flux divergence, H_0^{tot}, both play a minor role in exporting heat from the control volume.

Storage The shelf-forced flows, primarily captured in the u_2 field, become weaker in the summer (Fig. 3-6). The corresponding reduction in water property variability leads to smaller storage terms, as shown in Fig. 3-12 comparing 2 and 25 day averaging timescales. With the short averaging timescale, the measured cross-section transports equals $\overline{H}_{Storage}$ (with a one day lag) within the error bars, as in the winter; estimating the residual $\overline{H}_{Melting}$ is impossible at this short averaging timescale. On the other hand, with a longer averaging timescale of 25 days, the impact of shelf-forcing is diminished, and there is a statistically significant difference between heat storage and cross-section transport, which allows us to infer the residual heat for melting in summer. Nevertheless, $\overline{H}_{Storage}$ (and also $\overline{F}_{Storage}$) remain leading order terms throughout the year. A summer-long average further reduces the storage terms (Table 3.3) but hinders our ability to see any seasonal evolution.

Advective transports In the summer, when shelf-forcing is reduced, u_1 and u_2 are of a similar magnitude, and there is a clear and evolving structure in the mean exchange (Fig 3-6). In June, there is a thick outflowing layer from approximately 250 m to 100 m depth, with inflow above and below. Over the course of the summer, this outflowing layer thickens and shoals, extending from approximately 200 m to above the range of our ADCP measurements. We cannot exclude the possibility that there is another inflow or inflow/outflow in the upper tens of meters, and our calculation of the heat and salt transports attempts to take into account this uncertainty by including a variety of extrapolation techniques (Section 3.5.1). The average profile of u_1 over the entire summer (Fig. 3-13) shows a thick outflowing layer above a deep inflowing layer. The outflow is subsurface intensified, resembling the glacier-driven flow in the modeling study of Carroll et al. (2015).

In the summer, the observed exchange flow imports heat and salt into the control volume, as shown by the positive values for H_1 and F_1 in Fig. 3-7 & 3-8. This is the result of warm, salty water inflowing at depth and relatively cooler, fresher water outflowing in the upper layer. The average summer profiles of u_1, θ_1 and S_1 that form the exchange transports are shown in Fig. 3-13. θ_1 and S_1, which are the time-averaged fields with the depth-average removed, are positive when u_1 is up-fjord and negative when u_1 is outflow, resulting in an overall import of heat and salt from the exchange flow.

This exchange flow in the summer consists of inflowing AW and outflowing glacially modified water. We illustrate this by mapping the mean transport from the u_1 field onto θ-S diagrams in Fig. 3-14. One can see that, in the panel for June-August, the inflowing water at depth has AW properties that match the shelf. The outflowing water falls in the part of θ-S space that diverges from the shelf properties in a manner consistent with modification from meltwater and runoff (Straneo et al., 2011), i.e. it is a mixture of the deep inflowing AW and glacial freshwater inputs.

The fluctuating transports export small quantities of heat and salt, consistent with the export of glacially modified water as discussed in Section 3.5.2.1. These fluctuating transports are an order of magnitude smaller than the exchange and storage for most of the summer.

Estimating the residual terms in the heat/salt budgets In the summer salt budget, the barotropic salt transport can be inferred from the residual of the exchange, fluctuating and storage terms. Export of salt from the barotropic transport primarily balances the import of salt from the exchange flow and changes in salt storage.

The measured terms in the salt and heat budgets allow for estimates of $\overline{H}_{Melting}$ and H_0^{tot}. The latent heat for melting becomes distinguishable from zero in July and is a leading order term in the heat budget by August. The heat flux divergence is negative, by defintion (Eq. 3.14), and an order of magnitude smaller than the exchange, storage and latent heat for melting terms.

Surface heat fluxes have not been included in these calculations, but they are expected to be an order of magnitude smaller than the estimated latent heat for melting (Appendix C). Since the control volume would gain heat at the surface during the summer, the neglect of the surface heat flux should lead to a small underestimation of the meltwater flux.

3.5.3 Magnitude and variability of freshwater fluxes

In the non-summer months, $\overline{Q}_{FW}$, $\overline{Q}_{MW}$, and $\overline{Q}_R$ are indistinguishable from zero (Fig. 3-9), with the 10-month-average freshwater flux only constrained to be less than $\sim$1000 m^3 s^{-1} (Table 3.3). While the error bars are still significant during the summer, the fluxes become more narrowly constrained and distinguishable from zero. The total freshwater entering the fjord increases from 800±500m^3 s^{-1} in June to 2400±500m^3 s^{-1} in late July and early August (Fig. 3-9). The lower bound on the total freshwater estimate in this latter period exceeds the upper bound from January through May.

Runoff does not become distinguishable from zero until late July, reaching a value of $\overline{Q}_R = 1200 \pm 700$ m^3 s^{-1} in August. The concurrent RACMO2.3 output for runoff entering upper Sermilik Fjord (i.e. into our control volume) is shown in Fig. 3-9c and agrees with our estimate of runoff within the uncertainty.

The submarine meltwater flux first becomes distinguishable from zero in late July. In June and early July, 600±600 m^3 s^{-1} of meltwater enters the fjord. In late July and August, Q_{MW} becomes more narrowly constrained, reaching 1500±500m^3 s^{-1}. It is important to note that this meltwater flux is the sum of both glacier and iceberg melt – we make no claims that this is an estimate of Helheim Glacier's melt-rate since we cannot separate the sources of submarine melting.

While there is a significant increase in the total freshwater flux over the summer, the meltwater and runoff fluxes do not have a discernible seasonality within their error bars. The seasonality in the total freshwater could be entirely related to runoff – from runoff itself and/or from runoff increasing glacier submarine melting (e.g. Xu et al., 2012; Sciascia et al., 2013). It is also possible that submarine melting increases during the summer for other reasons; for example, iceberg melting might increase as the upper 200 m warms due to glacial modification (see Fig. 3-2b and 3-2c).

3.6 Discussion

3.6.1 Errors and uncertainties

3.6.1.1 Resolving the fjord cross-section

The error bars in this analysis are of crucial importance. Uncertainties and errors have been underemphasized and likely underestimated in many previous studies that infer submarine melt rates from measurements of ocean heat transport. In our calculations, the largest source of uncertainty is from incomplete coverage of the water column and the required extrapolation. Most previous studies have used synoptic surveys, which sometimes provide better spatial resolution of a fjord cross-section but no temporal resolution. Here, we have somewhat limited spatial coverage but a more comprehensive picture of the system's time variability.

For the cross-section transports, our spatial coverage is lacking in two ways. First, we do not sample the surface layer: in velocity, we are missing the range of 0-27 m and 0-39 m in the first and second years, respectively; in salinity and temperature, we are missing 0-13 m and 0-50 m in the first and second years. We try to account for this by extrapolating with several different techniques and including their spread in our error bars. A comparison with the shipboard surveys suggests that this extrapolation spread should do well at capturing the surface properties during the non-summer and should do well below 10 m in the summer, but it likely overestimates salinity in the top 10 m during the summer. Second, we neglect lateral variability between our moorings and assume that these records are representative of the entire cross-section, thereby neglecting cross-fjord variability. In calculating the storage term, we make an additional assumption by estimating the control volume's water properties from the records at the southern boundary, i.e. at the mooring location.

To evaluate the limitation of our cross-fjord coverage, we estimate the magnitude of cross-fjord gradients and their potential manifestation in our observations and calculations. Assuming that the along-fjord velocity is in geostrophic balance, we estimate the cross-fjord tilt in the pycnocline to be ∼30 m across the fjord width during peak velocity shears in winter (Appendix B). A simple model for the shelf-forced flows in Appendix B indicates that the observed exchange velocity and fluctuating transports in the non-summer months could be an artifact of our sampling locations, which are biased towards the eastern side of the fjord. In this two-layer model, there is no net mass, heat, or salt transport in either layer; however, if the pycnocline heaving has a cross-fjord tilt, one would observe mean velocities and fluctuating transports in the depth range of pycnocline excursions when measuring off-center in the fjord. The sign, magnitude and structure of these signals in the model are similar to our non-summer observations of a mean inflow between 50-200 m and fluctuating export of heat/salt at mid-depth. The mean velocities observed in summer, however, could not be attributed to this sampling bias.

In order to reduce the error bars and better constrain the freshwater fluxes in a system like Sermilik, one would need to have both good spatial and good temporal coverage – either one alone is not sufficient. Mooring arrays that cover the upper tens of meters at the surface, as well as the cross-fjord structure, would be ideal (but logistically difficult). However, this cannot come at the expense of coverage in time. The temporal variability in a system like Sermilik Fjord imprints on the budgets in many ways, e.g. in the important role of heat/salt storage or fluctuating transports, so any snapshot of cross-section transports should not be used to infer freshwater fluxes.

3.6.1.2 Control volume size

In this analysis and all previous studies, any variability in the size of the control volume has been neglected; the volume of liquid water (V_c) on the landward side of the cross-section is assumed to remain constant. There could, however, be significant variability in V_c from changes in the glacier terminus position, from changes in iceberg volume, or from changes in sea surface height. If V_c is allowed to vary in time, the full mass budget from Eq. (3.1) becomes:

$$\int_{A_x} u dA + Q_{FW} = \frac{\partial V_c}{\partial t} \tag{3.22}$$

and the changes in V_c can be written as the sum of three components:

$$\frac{\partial V_c}{\partial t} = -\frac{\partial V_{glac}}{\partial t} - \frac{\partial V_{iceb}}{\partial t} + \frac{\partial \eta}{\partial t} A_{Surf} \tag{3.23}$$

where $\frac{\partial V_{glac}}{\partial t}$ is the change in glacier volume below sea level from terminus advance and retreat, $\frac{\partial V_{iceb}}{\partial t}$ is the change in iceberg volume below sea level within the control volume, η is the sea surface height, and A_{Surf} is the surface area of the control volume. Changes in the volume of ice result in V_c changes of the opposite sign, because we have defined V_c as the volume of *liquid* water upstream of a fixed cross-section.

While we cannot directly evaluate these terms for Sermilik Fjord, we can estimate their magnitude. Jackson et al. (2014) find an increase in sea surface height of ~15 cm for synoptic downwelling events with timescales of 3-11 days, corresponding to $\frac{\partial \eta}{\partial t} A_{Surf} \approx 200 \text{m}^3 \text{ s}^{-1}$. With our averaging timescale of 25 days, this would reduce to ~40 $\text{m}^3 \text{ s}^{-1}$ and thus be insignificant in the time-averaged mass budget. The volume variability resulting from glacier advance/retreat can be estimated with measurements of the glacier terminus position. Helheim Glacier has a typical summer retreat of 2.2 km over an average of 120 days (Schild and Hamilton, 2013), which would correspond to $\frac{\partial V_{glac}}{\partial t} = -760 \text{m}^3 \text{ s}^{-1}$, assuming a submarine glacier terminus area of 3.6 km^2. During our observational period in the summer of 2013, Helheim Glacier retreated by more than 1 km over less than three weeks (Bevan et al., 2015), corresponding to $\frac{\partial V_{glac}}{\partial t} < -2000 \text{m}^3 \text{ s}^{-1}$. If the freshwater fluxes are $\mathcal{O}(1000 \text{m}^3 \text{ s}^{-1})$, then $\frac{\partial V_{glac}}{\partial t}$ could be a leading order term in the mass budget at certain times. The volume change in icebergs, $\frac{\partial V_{iceb}}{\partial t}$, is the hardest term to estimate and might partially counteract changes in glacier volume: when the glacier retreats, the calving rate typically increases and the volume of icebergs in the control volume might increase. It is difficult, however, to evaluate the extent to which these components balance, and we expect that at times their sum, $\frac{\partial V_c}{\partial t}$, will be of the same magnitude as Q_{FW}.

Although variability in control volume size ($\frac{\partial V_c}{\partial t}$) might be a leading order term in the mass budget, its effect is drastically diminished when inferring freshwater fluxes from the salt and heat budgets. When variability in V_c is included, the equation for inferring Q_{FW} from the combined salt and mass budgets [Eq. (3.16)] becomes:

$$\overline{Q}_{FW} = \frac{1}{S_0}\left[F_1 + F_2 - \overline{F}_{Storage}\right] + \left(1 - \frac{\langle S \rangle}{S_0}\right)\frac{\partial V_c}{\partial t} \tag{3.24}$$

where $\langle S \rangle$ is the average salinity in V_c (see derivation in Appendix A). The last term on the right side is the only difference between this equation, which accounts for volume changes, and Eq. (3.16), which neglects volume changes. One can see that the impact of $\frac{\partial V_c}{\partial t}$ on the freshwater flux calculation will go to zero as the average cross-section salinity (S_0) approaches the volume averaged salinity ($\langle S \rangle$). Physically, this condition means that the along-fjord horizontal salinity differences must be small compared to the depth-averaged salinity. Based on surveys of Sermilik Fjord (e.g., Fig. 3-2; Straneo et al., 2011; Sutherland et al., 2014b), the horizontal salinity gradient is small and $(1 - \frac{\langle S \rangle}{S_0}) < 0.02$. Therefore, even though $\frac{\partial V_c}{\partial t}$ might be an order of magnitude larger than Q_{FW} in the mass budget, the error on the freshwater flux calculation from neglecting $\frac{\partial V_c}{\partial t}$ will be at least an order of magnitude smaller than the total freshwater flux. This allows us to neglect variability in the control volume size when estimating the freshwater fluxes from heat and salt budgets.

The factor of $(1 - \frac{\langle S \rangle}{S_0})$ might be significantly larger in other systems. If there is a strong horizontal salinity gradient, the cross-section salinity at the edge of the control volume could be substantially higher than the volume averaged salinity such that changes in the control volume size might not be negligible. The underlying principle is that we do not attempt to measure the barotropic velocity (u_0), while we do rely on measuring the depth-average water properties, θ_0 and S_0. If these measured water properties, θ_0 and S_0, are sensitive to small displacements in the location of the cross-section, then the overall results will be sensitive to changes in the control volume size.

3.6.2 Interpreting the observed freshwater fluxes

Previous estimates of submarine melting in fjords purport to measure glacier (as opposed to iceberg) melting and often present their results as a melt-rate (in m/yr) across the glacier's terminus. Our results, however, are reported in terms of a total liquid meltwater flux from glaciers and icebergs, with no attempt made to distinguish between the two. This, plus the fact that we do not expect the same meltwater fluxes in different fjord/glacier systems, complicates any comparison between our meltwater fluxes and previous results. Studies from other Greenlandic and Alaskan fjords (Motyka et al., 2003; Rignot et al., 2010; Motyka et al., 2013; Xu et al., 2013; Bartholomaus et al., 2013; Inall et al., 2014) report meltwater fluxes between 5 and 830 $\mathrm{m}^3\ \mathrm{s}^{-1}$, with our measured meltwater flux falling at the upper end of this range. In a more apt comparison, our observed meltwater flux is notably higher than a previous estimate for Sermilik Fjord: Sutherland and Straneo (2012) find a meltwater flux of 86 $\mathrm{m}^3\ \mathrm{s}^{-1}$ in August of 2009, which is below the range of our summer estimates in July and August.

Perhaps a more interesting comparison is between our measured meltwater flux and estimates of total ice discharge (iceberg calving plus submarine melting) from the glaciers that drain into Sermilik. Mernild et al. (2010) estimate an annual average ice discharge of 821±82 $\mathrm{m}^3\ \mathrm{s}^{-1}$ (water equivalent) from Helheim and 253±48 $\mathrm{m}^3\ \mathrm{s}^{-1}$ from the two smaller glaciers in Sermilik. Other measurements of Helheim ice discharge (e.g. Enderlin et al., 2014; Enderlin and Howat, 2013) agree with those discharge numbers, and the seasonal cycle of discharge is less than ∼20% (Bevan et al., 2015; Moon et al., 2014).

Our summer-average estimate of $Q_{MW} = 900 \pm 540\mathrm{m}^3\ \mathrm{s}^{-1}$ is similar in magnitude to the total estimated ice discharge from the glaciers; based on 1100 $\mathrm{m}^3\ \mathrm{s}^{-1}$ of ice discharge and the lower bound of our estimate, at least $\sim 30\%$ of the total ice discharge melts within the fjord. In a steady state, the difference between the total ice discharge and the submarine melting within the control volume is the solid iceberg flux that leaves the control volume. Our results suggest that a substantial portion ($> 30\%$) of the total ice flux from the glaciers either melts at the terminus or melts from icebergs within the fjord.

The measured meltwater flux undoubtably contains iceberg meltwater, though the fraction cannot be quantified with our methods. A recent attempt to measure submarine melting of icebergs in Sermilik suggests that iceberg melting might be a significant fraction of our total meltwater flux. Enderlin and Hamilton (2014) find that ten large icebergs, which constitute 5% of the mélange surface area, contribute 25 m^3 s^{-1} of meltwater. This result indicates that icebergs throughout the fjord might contribute $\mathcal{O}(100)$ m^3 s^{-1} of meltwater, illustrating the potentially important but unconstrained role of icebergs in the meltwater flux.

Lastly, as shown in Fig. 3-9, our runoff estimate agrees with runoff output from RACMO2.3, within our error bars. As another point of comparison, Mernild et al. (2010) uses SnowModel to estimate an annual average runoff entering upper Sermilik Fjord from 1998-2008 of 3.2×10^9 m^3 yr^{-1}, equivalent to ~ 410 m^3 s^{-1} if evenly distributed over three summer months. This is slightly lower than our runoff estimate, though the time periods being compared do not overlap.

3.6.3 Across Greenland's fjords: previous methods and future studies

Here we attempt to generalize some of our results and explore how the dominant balances in the heat and salt budgets might change in other systems. This has important practical implications for assessing when various terms in the budgets can be dropped – both in future studies and past attempts.

All previous studies have used simplified budgets to infer meltwater fluxes. One approach is to directly equate some portion of the cross-section heat transport to the heat extracted for melting (e.g. Sutherland and Straneo, 2012). Other approaches employ both heat and salt budgets and retain more components of the budgets (e.g. Motyka et al., 2003; Rignot et al., 2010; Xu et al., 2013; Motyka et al., 2013). In all cases, the storage terms ($F_{Storage}/H_{Storage}$), surface heat fluxes (H_{Surf}) and fluctuating transports (F_2/H_2) have been neglected. Additionally, the advective fluxes are never included completely, with potential problems arising from the neglect of, or ambiguity in handling, the barotropic heat fluxes.

3.6.3.1 Barotropic heat flux divergence

The barotropic heat flux divergence, H_0^{tot}, will be negative in all glacial fjords. This term is associated with the difference in temperature between freshwater when it enters the fjord (at approximately the freezing temperature) and when it leaves the control volume in the mean barotropic component at θ_0 [Eq.3.14]. Since θ_0 will always be greater than the temperature of runoff or meltwater, this barotropic term will represent a divergence of heat and thus be a negative component of the heat budget. In Sermilik, we have found that it is at least an order of magnitude smaller than other terms in the heat budget (Fig. 3-7). However, this will not be the the case in all systems.

The ratio of H_0^{tot} to $H_{Melting}$ is:

$$f_B = \frac{H_0^{tot}}{H_{Melting}} = \frac{\rho c_p[Q_R(\theta_R - \theta_0) + Q_{MW}(\theta_{MW} - \theta_0)]}{\rho L_{adj} Q_{MW}}$$
$$= \frac{c_p}{L_{adj}}\left(\frac{Q_R}{Q_{MW}}(\theta_R - \theta_0) + (\theta_{MW} - \theta_0)\right) \quad (3.25)$$

The magnitude of the barotropic fraction, f_B, increases as a function of Q_R/Q_{MW} and θ_0, as shown in Figure 3-17. One can see that when $Q_R/Q_{MW} \sim O(1)$, as in Sermilik, H_0^{tot} will be an order of magnitude smaller than $H_{Melting}$. However, when $Q_R/Q_{MW} > 10$, H_0^{tot} becomes a similar magnitude as or larger than $H_{Melting}$.

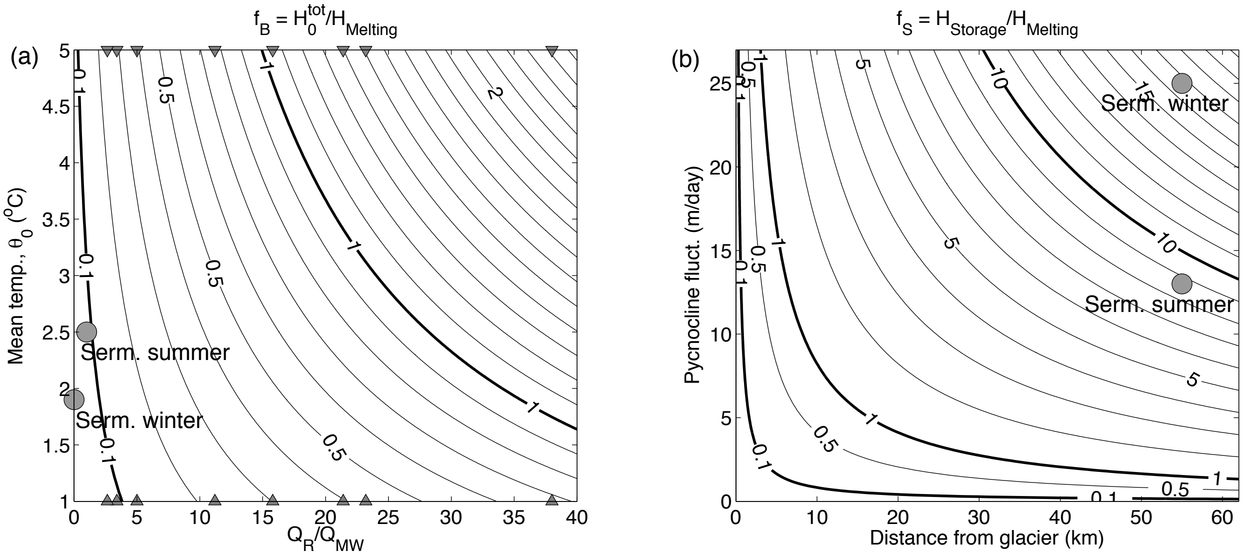

Figure 3-17: (a) Ratio of barotropic heat flux divergence to heat for melting, $f_B = H_0^{tot}/H_{Melting}$, as a function of mean cross-section temperature, θ_0, and Q_R/Q_{MW}. This is based on Eq. 3.25 with values of: $\theta_R = -0.5$ C and $\theta_{MW} = -1.5$ C. Grey circles indicate Sermilik summer and winter in this parameter space. Grey triangles along the x-axis indicate published values of Q_R/Q_{MW} from Motyka et al. (2013), Sutherland and Straneo (2012), Rignot et al. (2010), Motyka et al. (2003), and Xu et al. (2013). (b) Ratio of heat storage to heat for melting, $f_S = H_{Storage}/H_{Melting}$, as a function of the amplitude of interface fluctuations and the distance of the cross-section measurements from the glacier. This is based on Eq. 3.27 with values of $W = 7.5$ km , $Q_{MW} = 400$ m^{3}s $^{-1}$ and $\Delta\theta = 5^o$C. The black dots shows our observations in Sermilik winter and summer in this parameter space.

Neglecting the barotropic component The studies of Motyka et al. (2013), Xu et al. (2013), Rignot et al. (2010) and Motyka et al. (2003) find ratios of Q_R/Q_{MW} (grey triangles in Fig. 3-17) between 5 and 38, such that the barotropic heat flux divergence would often be significant compared to the heat used for melting. If fjords fall in the part of parameter space that those papers claim ($Q_R \gg Q_M$), the barotropic fluxes must not be ignored. Thus, their results indicate that their methods might be problematic because there is not an explicit separation of the unknown barotropic fluxes.

Sutherland and Straneo (2012), Johnson et al (2011) and others remove the net transport through the fjord cross-section, forcing the mass flux to zero and effectively dropping H_0^{tot} from the heat budget. This will produce errors on the melt-rate estimate as a function of Q_R/Q_{MW}, as shown in Fig. 3-17. In the case of Peterman Fjord in Johnson et al. (2011), runoff should be small so neglecting H_{tot} should only create a ~5% error in the heat budget. Forcing the mass flux to zero and dropping H_0^{tot} will be inconsequential in fjords with low runoff, but it could create melt-rate errors of more than 150% in fjords with $Q_R \gg Q_{MW}$. A more problematic approach than dropping H_0^{tot}, however, is including any barotropic fluxes without properly constraining the mass budget, as will be shown next.

Separating the barotropic components Large errors can arise if the barotropic component of the cross-section velocity is not treated as an unknown. For example, consider a common equation for total heat transport in past literature: $H = c_p\rho \iint u(\theta - \theta_f)dA$. If the observed velocity contains some barotropic error, u_0^{err}, which could be from instrument error, incomplete sampling coverage, tides, etc., then the error in the heat transport would be: $H^{err} = c_p\rho u_0^{err}(\theta_0 - \theta_f)A_x$. For Sermilik Fjord values of $\theta_0 - \theta_f = 4.5°\text{C}$ and $A = 4.5 \times 10^7$ m^2, a barotropic velocity error of only 0.5 cm s^{-1} (a very small instrumental error or a small fraction of tidal velocities) would result in an enormous heat transport error of 3.7×10^{12} W, equivalent to 1000 m^3/s of meltwater. If the barotropic velocity that balances the freshwater flux were measurable, a salt or heat budget would not be necessary to infer the total freshwater flux. Since this is not the case, the barotropic velocity should be separated and treated as an unknown.

3.6.3.2 Storage of heat and salt

Sermilik connects to a shelf region with exceptionally strong wind forcing and high variability, resulting in large fjord velocities and heat/salt content variability. Similar shelf-forced flows are expected in other fjords of southeast Greenland with deep sills and an energetic adjacent shelf. Evidence of this has been found in Kangerdlugssuaq Fjord (Jackson et al., 2014). Fjords on the west coast (e.g. Gladish and Holland, 2015; Mortensen et al., 2014), however, are found to have much weaker flows, and the fluctuating and storage terms should be reduced when shelf-forcing (and the associated pycnocline heaving) is smaller. The question remains whether they would be small enough to neglect.

The potential importance of the storage term is explored with a simple scaling. If temperature variability in the control volume arises from pycnocline heaving, then an expression for $H_{Storage}$ can be written using Eq. 3.21:

$$H_{Storage} = \rho c_p \left(\frac{\partial \langle \theta \rangle}{\partial t} \right) V_c = \rho c_p \left(\frac{\theta_U - \theta_L}{H} \right) \frac{\partial h}{\partial t} V_c \tag{3.26}$$

where $\langle \theta \rangle$ is the volume averaged temperature, θ_U and θ_L are the average temperatures of the upper and lower layers, respectively, H is the total depth, and $\frac{\partial h}{\partial t}$ is the rate of vertical pycnocline displacements. The storage term increases with the amplitude of the pycnocline fluctuations, with the temperature difference between layers, and with the control volume size. To assess when this term can be neglected, it is scaled relative to the heat for melting to create a storage fraction ratio:

$$f_S = \frac{H_{Storage}}{H_{Melting}} = \frac{c_p(\theta_U - \theta_L)\frac{\partial h}{\partial t} W L}{L_{adj} Q_{MW}} \tag{3.27}$$

where we have approximated the control volume to be rectangular with a constant width, W, and length, L (the distance from the cross-section to the glacier).

Fig. 3-17 shows the magnitude of the storage fraction, f_S from Eq. (3.27), as a function of the distance from the glacier and of pycnocline heaving, with fixed values of $\theta_U - \theta_L = -5^oC$, $W = 7.5$ km, and $Q_{MW} = 400$ m^3 s^{-1}. One can see that our budgets for Sermilik Fjord are on the outer part of the shown parameter space, with measurements made far from the glacier ($L = 55$ km) and energetic pycnocline fluctuations ($\frac{\partial h}{\partial t} \approx 25$ or 13 m/d in winter and summer, respectively). With measurements at our mooring location, the error from neglecting the storage (without time-averaging) would be equivalent to $\pm 3.6 \times 10^5$ m^3 s^{-1} in summer and $\pm 6.4 \times 10^5$ m^3 s^{-1} in winter – much larger than any plausible freshwater flux. In Sermilik, one would need ocean measurements within a few kilometers of the glacier, right in the mélange, for the storage term to smaller than the heat for melting. This is not realistic with current technologies, so the storage terms must be assessed in budgets for Sermilik.

All previous studies have neglected the storage of heat and salt in their control volumes. The extent to which this is problematic depends on the fjord and the location of measurements: the storage terms are expected to be smaller in many previous studies of less energetic fjords with more accessible water near the glacier. Fig. 3-17, however, shows that the instantaneous heat storage can still be large compared to melting even if pycnocline heaving is significantly smaller than in Sermilik or if measurements are made closer to the glacier. For the storage term to be small relative to the latent heat for 400 $\mathrm{m}^3\ \mathrm{s}^{-1}$ meltwater, measurements would need to be made within $O(100)$ m of the glacier and/or pycnocline fluctuations would need to be $O(1)$ m/d. These are quite extreme conditions that might be met by some previous studies (e.g. Motyka et al., 2013, 2003) but certainly not all. The implication is that, in many cases, the heat storage term cannot be neglected – it must be evaluated directly or at least averaged in time to reduce its amplitude.

It should be noted that Eq. 3.26 will not always be a valid approximation for the storage term. For example, when measurements are made very close to the glacier, within the convective plume region, it is likely that this scaling breaks down. Furthermore, measurements close to the glacier might be plagued by smaller scales of spatial variability as plumes emanate from the glacier (Stevens et al., 2015).

3.6.3.3 Measuring a mean velocity profile

Almost all previous studies (except Mortensen et al., 2014) use short-term measurements of velocity or water properties to infer a quasi-steady exchange velocity, somewhat analagous to u_1. A variety of methods have been employed to extract a certain part of the velocity field. In some cases, the raw snapshots of velocity and water properties are used to calculate cross-section transport (Xu et al., 2013; Motyka et al., 2003, 2013; Rignot et al., 2010). In others, geostrophic velocities are calculated from water properties (Johnson et al., 2011; Inall et al., 2014) or a high frequency mode is removed from the velocity field (Sutherland and Straneo, 2012).

In Sermilik, we have found that measurements over at least several weeks are needed to separate an underlying exchange flow from the reversing synoptic-scale flows; the instantaneous velocity field, or even measurements over a week, are not long enough to resolve u_1. Furthermore, it should be noted that both the u_1 profile in summer (Fig. 3-6) and the reversing shelf-forced flows of u_2 have a vertical structure that resembles the first baroclinic mode (Jackson et al., 2014). Therefore, any attempt to remove u_2 by fitting a first-mode structure to the observed velocity field could also remove a significant part of the u_1 signal. This could explain why the mean exchange velocity that we observe in summer is different, both in magnitude and structure, than the exchange velocity reported for Sermilik Fjord in Sutherland et al. (2014b) and Sutherland and Straneo (2012). This highlights the difficulty in disentangling a mean exchange flow from high-frequency flows without explicitly averaging in time, and we expect this problem to exist in many other systems.

3.6.3.4 The in-situ freezing point and reference temperatures

While it is common practice to include a reference temperature in heat budgets, it should be noted that any particular choice of a reference temperature will not impact the total budget nor one's ability to measure glacial fluxes from measurements of heat transport. The reference temperature will only change the relative magnitude of H_0, $\overline{H}_{MW}$ and $\overline{H}_R$ – all of which are unknowns (Section 3.3.3). A reference temperature close to θ_{MW} and θ_R will reduce the amplitude of $\overline{H}_{MW}$ and $\overline{H}_R$ relative to H_0, but the sum of all three unknowns, H_0^{tot}, will not change.

Furthermore, a non-constant reference temperature will distort the heat budget and lead to erroneous meltwater estimates. Many studies (e.g. Sutherland and Straneo, 2012; Xu et al., 2013; Johnson et al., 2011) use a reference temperature of the in-situ freezing temperature, $\theta_f(S, P)$, which is a function of the local salinity and pressure, in an attempt to account for variability in the submarine meltwater temperature. However, a reference temperature can only be added to the heat budget if it is constant in space and time.

For example, in Sermilik and likely many other fjords, AW flows towards the glacier at depth, upwells when mixed with glacial inputs and flows away from the glacier in an upper layer of glacially modified water. With an in-situ freezing point reference temperature, the inflowing AW would be referenced to a colder temperature ($\theta_f \approx -2.2^\circ$ at 400 m) while the outflowing AW is referenced to a warmer temperature ($\theta_f \approx -1.8^\circ$ at 70 m). More generally, if any water mass transformations occur within the control volume that change the pressure and/or salinity of water masses, then a pressure and salinity dependent reference temperature of $\theta_f(S, P)$ will give erroneous results.

To quantify this, consider the exchange heat transport, H_1, that is independent of a constant reference temperature (since $\int_{A_x} u_1 dA = 0$). The erroneous heat transport that would arise from measuring this transport with an in-situ freezing point reference temperature would be: $H_{1,err} = \rho c_p \int_{A_x} u_1(-\theta_f) dA$. If the exchange velocity is primarily a two-layer flow, like the summer conditions in Sermilik, then this expression can be simplified to $H_{1,err} = \rho c_p Q_1 \Delta\theta_f$ where Q_1 is the exchange volume flux from u_1 in each layer and $\Delta\theta_f$ is the difference between the average freezing temperature in the upper and lower layers. The error from using this in-situ freezing temperature can be scaled relative to the heat used for melting as:

$$\frac{H_{1,err}}{H_{Melting}} = \frac{c_p}{L_{adj}} \Delta\theta_f \frac{Q_1}{Q_{MW}}$$

The error will increase as the exchange flow (Q_1) strengthens and as the freezing temperature diverges between the upper and lower layer (i.e. in deep fjords and fjords with strong vertical salinity gradients). In Sermilik during the summer, we find $Q_1 \approx 5 \times 10^4$ m^3 s^{-1} and $Q_{MW} \approx 800$ m^3 s^{-1}, while $\Delta\theta_f = -(1.8 - 2.2)$°C. Therefore, if we used the in-situ freezing point as a reference temperature, we could overestimate melting by 30%. This error might be significantly larger in fjords with more energetic exchange flows, e.g. fjords with high runoff.

A preferable approach to account for variability in freezing point is to use a variable meltwater temperature, θ_{MW}. In Sermilik, the meltwater temperature could be -2.0±0.4°C based on salinity of 30 to 35 and pressure of 0 to 630 db. This variability in θ_{MW} would change the multiplicative factor in Eq. (3.17) for Q_{MW} by only 0.5% – it would insignificant. Accordingly, it is far better to have an error in the meltwater temperature (based on a range of in-situ freezing temperatures) than a variable reference temperature.

3.7 Conclusions

We present complete mass, salt and heat budgets for glacial fjords and new equations for inferring the freshwater fluxes of submarine melting and runoff. Building on the estuarine literature for salt budgets, this method includes a decomposition of the cross-section transports into barotropic, exchange, and fluctuating components – a decomposition that ensures mass conservation in the evaluated budgets and appropriately accounts for temporal variability. This method includes many terms that have been neglected in previous studies of submarine melting, and we highlight the importance of appropriately separating known versus unknown components of the advective transports.

We apply this method to Sermilik Fjord, a major glacial fjord into which Greenland's fifth largest outlet glacier, Helheim Glacier, drains. We assess the budgets for Sermilik Fjord using mid-fjord moorings that provide some of the most comprehensive and long-term measurements of velocity and water properties in a Greenlandic fjord to date. We find two different regimes seasonally that are consistent with the seasonal variations in fjord forcings: shelf variability via barrier winds and freshwater discharge from runoff.

During the non-summer months (September through May), the fjord is dominated by shelf-forced flows which drive large variability in water properties. As a result, the leading order heat and salt balances are between cross-section transports and changes in storage. During this period, the freshwater fluxes from the glacier cannot be inferred as a residual – they are indistinguishable from zero within the uncertainty of our estimates.

In the summer (May through August), the fluctuating velocity from shelf forcing is reduced and a clear structure emerges in the exchange velocity. The exchange flow consists of deep Atlantic Water flowing towards the glacier and a thick upper layer flowing away from the glacier that is a mixture of AW and glacial inputs (meltwater plus runoff). During this period, the total freshwater flux becomes distinguishable from zero and increases from June to August. The inferred submarine melting in August ($1500 \pm 500\text{m}^3\ \text{s}^{-1}$) is larger the most previous estimates of submarine melting and might contain significant iceberg meltwater. In the salt budget, the mean exchange, F_1, imports salt and is primarily balanced by export from the barotropic transport, F_0. In the heat budget, the primary balance is between the import of heat from the exchange (H_1), the extraction of heat to melt ice ($H_{Melting}$), and changes in heat storage ($H_{Storage}$).

Beyond Sermilik, our methods and results have several important implications for inferring freshwater fluxes in other systems. The barotropic transports in fjords are typically not measurable but still important components of the budgets, requiring the use of both heat *and* salt budgets to accurately constrain the freshwater fluxes. The storage term will be important in most fjord budgets, unless a sufficiently long averaging timescale or small control volume is used. Temporal averaging is often necessary to resolve the mean exchange flow, which is found to be the dominant mode of heat/salt transport. Due to these and other findings, previous estimates of submarine melting are highly uncertain.

Ultimately, glacial fjord budgets are hard to evaluate for many reasons, including the presence of icebergs, the great depth of the fjords, and large temporal variability. In the future, more comprehensive mooring arrays, perhaps coupled with new methods for estimating submarine melting (e.g. from imaging of glacier fronts, Rignot et al., 2015; Fried et al., 2015), could provide a path forward for better constraining the freshwater fluxes. Additionally, icebergs might be a significant source of submarine melting in fjords, obscuring the glacier melt-rate and requiring new methods to partition glacier and iceberg melting if glacier melt rates are to be estimated from oceanic measurements.

In previous studies of Greenlandic fjords, heat budgets are employed for the sole purpose of inferring melting. However, the evaluation of heat and salt budgets has value beyond that narrow goal by elucidating the dominant balances in the fjord, how heat/salt are transported, and how meltwater is exported. An improved understanding of fjord budgets is a necessary step towards understanding the oceanic controls on submarine melting and the ice sheet's impact on the ocean.

Appendix

3.A Dropping cross-terms in the decomposed heat/salt transports

The heat and salt transports are decomposed into three components in Eq. 3.9. This decomposition, however, is missing terms because a low pass filter will not entirely separate energy at different timescales. The overbar is this paper is defined as a running mean (i.e. a low-pass filter with a boxcar of timescale τ), which does not perfectly eliminate energy at timescales of less than τ. Therefore, $\overline{u_2}$ does not exactly equal zero, even though u_2 is defined as $u_2 = u - \overline{u}$. Similarly, the running average of the running average, $\overline{\overline{u}}$, is not exactly equal to the running average, $\overline{u}$.

We have decomposed u as $u = u_0 + u_1 + u_2$, which can be rewritten as $u = \overline{u} + u_2$ (since $u_0 + u_1 = \overline{u}$). The relevant quantity of interest for the salt transport, neglecting the spatial integration, is $\overline{uS}$. The full decomposition for this term is:

$$\overline{uS} = \overline{\overline{u}\,\overline{S}} + \overline{u_2 S_2} + \overline{\overline{u} S_2} + \overline{u_2 \overline{S}} \tag{3.28}$$

None of these four terms is exactly zero, because $\overline{\overline{u}} \neq \overline{u}$ and $\overline{u_2} \neq 0$. Nevertheless, in this work we have used the approximation:

$$\overline{uS} \approx \overline{u}\,\overline{S} + \overline{u_2 S_2} \tag{3.29}$$

which has the following error:

$$E = \overline{\overline{u} S_2} + \overline{u_2 \overline{S}} + \overline{\overline{u}\,\overline{S}} - \overline{u}\,\overline{S} \tag{3.30}$$

When evaluated with our data sets, this error is less than 5% of $\overline{uS}$ so we neglect these cross-terms. The same is true for the neglected cross-terms in $\overline{uT}$ in the heat transports.

3.B Changes in control volume size

Here, we explore the effect of changes in control volume size on the equations for inferring freshwater fluxes. If the full mass budget including control volume variability (Eq. 3.1) is averaged in time, it can be written as:

$$u_0 A_x + \overline{Q}_{FW} = \frac{\partial V_c}{\partial t}. \tag{3.31}$$

The time-averaged and decomposed salt budget, with V_c variability now included, is:

$$\begin{aligned} u_0 S_0 A_x + F_1 + F_2 &= \frac{\partial}{\partial t} \int_{V_c} S dV \\ &= \frac{\partial \langle S \rangle}{\partial t} V_c + \frac{\partial V_c}{\partial t} \langle S \rangle \end{aligned} \tag{3.32}$$

where $\langle S \rangle$ is the volume averaged salinity such that $\langle S \rangle V_c = \int_{V_c} S dV$. Substituting the mass budget, $u_0 A_x = \frac{\partial V_c}{\partial t} - \overline{Q}_{FW}$, into the salt budget gives:

$$\left(\frac{\partial V_c}{\partial t} - Q_{FW} \right) S_0 + F_1 + F_2 = \frac{\partial \langle S \rangle}{\partial t} V_c + \frac{\partial V_c}{\partial t} \langle S \rangle \tag{3.33}$$

Solving for Q_{FW}:

$$\begin{aligned} Q_{FW} &= \frac{1}{S_0}(F_1 + F_2) - \frac{1}{S_0} \frac{\partial \langle S \rangle}{\partial t} V_c - \frac{1}{S_0} \frac{\partial V_c}{\partial t} \langle S \rangle + \frac{\partial V_c}{\partial t} \\ &= \frac{1}{S_0}(F_1 + F_2) - \frac{1}{S_0} \frac{\partial \langle S \rangle}{\partial t} V_c + \left(1 - \frac{\langle S \rangle}{S_0} \right) \frac{\partial V_c}{\partial t} \end{aligned}$$

where the last term on the right side is the only difference between this equation and Eq. 3.16 for Q_{FW} in which $\frac{\partial V_c}{\partial t}$ is neglected. The ratio of this neglected term ($Q_{FW,err}$, i.e. the error on our calculation) to the total freshwater flux is:

$$\frac{Q_{FW,err}}{Q_{FW}} = \left(1 - \frac{\langle S \rangle}{S_0} \right) \frac{\frac{\partial V_c}{\partial t}}{Q_{FW}} \tag{3.34}$$

As shown in Section 3.6.1.2, we expect $(1 - \langle S \rangle / S_0) < 0.02$ for Sermilik. Thus, even if $\frac{\partial V_c}{\partial t}$ is an order of magnitude larger than Q_{FW}, the error in the freshwater equation will be small.

Similarly, the difference between the total equation for Q_{MW} that includes $\frac{\partial V_c}{\partial t}$ and the version that neglects it (Eq. 3.17) can be scaled relative to the total meltwater flux:

$$\frac{Q_{MW,err}}{Q_{MW}} = \frac{T_0 - \langle T \rangle}{L_{adj}/c_p - (\theta_{MW} - \theta_R)} \frac{\frac{\partial V}{\partial t}}{Q_{MW}} \tag{3.35}$$

where $\frac{T_0 - \langle T \rangle}{L_{adj}/c_p - (\theta_{MW} - \theta_R)} < 0.01$ in Sermilik. Thus, we expect changes in V_c from the glacier terminus, icebergs or sea level variability to have an insignificant effect on estimating freshwater fluxes with the heat and salt budgets.

3.C Two-layer model for shelf-forced flows

Here, a simple model for the shelf-forced flows (alternatively called intermediary circulation or baroclinic pumping) is used to explore the cross-fjord structure that is neglected in our analysis. We construct a two-layer model for a rectangular fjord where mass conservation and geostrophy are used to relate the upper layer velocity to the pycnocline depth, the lower layer velocity, and the cross-fjord pycnocline tilt. Following Arneborg (2004), we assume that the pycnocline heaving is approximately uniform throughout the fjord (see justification in Section 3.5.2), so that the upper layer volume flux at any point is proportional to the rate of pycnocline displacement and the area upstream:

$$v_1 \overline{h} = \frac{\partial \overline{h}}{\partial t} L \tag{3.36}$$

where $\overline{h}$ is the spatially-averaged depth of the pycnocline (positive with increasing depth), v_1 is the upper layer velocity, and L is the length of the fjord upstream. By volume conservation, the volume flux in the lower layer must balance the upper layer:

$$v_1 \overline{h} = -v_2 (H - \overline{h}) \tag{3.37}$$

where H is the total fjord depth and v_2 is the lower layer velocity. Then, based on thermal wind balance for a two-layer system, the cross-fjord pycnocline tilt will be:

$$\frac{\partial h}{\partial x} = f(v_1 - v_2)/g'; \tag{3.38}$$

where $g' = \Delta\rho/\rho_0$ and $\Delta\rho$ is the density difference between layers. We expect the along-fjord velocity to be in geostrophic balance in Sermilik because the dominant timescale of fjord flows (3-10 days) is long compared to an inertial period (13 hrs) and the cross-fjord velocities are an order of magnitude smaller than the along-fjord velocities.

With these three governing equations, we impose a sinusoidal velocity in the upper layer, $v_1 = v_0 \sin(\omega t)$, so that the pycnocline depth can be solved from Eq. B1 as:

$$\overline{h} = h_0 e^{-\frac{v_0}{L\omega}\cos(\omega t)} \tag{3.39}$$

where h_0 is the time-average pycnocline depth. Since the fjord width (7 km) is less than the deformation radius (9 km) and we do not expect the pycnocline to outcrop, we make a final assumption that the pycnocline is linear across the fjord, such that its position is fully defined by the expressions for $\overline{h}$ and $\frac{\partial h}{\partial x}$.

We then assign the following values as representative for Sermilik Fjord in the non-summer months: $v_0 = 0.3$ m s^{-1}, $\omega = 2\pi/6$ days^{-1}, $h_0 = 180$ m, $H = 600$ m, $L = 90$ km, $g' = 9.5 \times 10^{-3}$ m s^{-2}. We construct a 600 m x 7 km grid for a fjord cross-section (with 5 m x 50 m resolution) and evaluate the layer velocities and pycnocline location over 10 periods.

One simple thing that we find from this model is that, at the peak of the velocity pulses, the pycnocline depth varies by $\Delta h \sim 30$ m across the 7 km wide fjord. This is smaller than the mean vertical displacements (i.e. heaving) of 100 m but not negligible.

More importantly, the cross-fjord structure in this model has implications for our measurements of average velocity and fluctuating transports. In the model, there is no time-averaged volume flux in either layer; the layers expand and contract with pycnocline heaving but there is no net transport. However, the mean velocity at every depth is not zero. Instead, in the depth range of pycnocline excursions, there will be a mean positive velocity (into the fjord) on the right side (looking up-fjord) and a mean negative velocity on the left side (Fig. 3-18). This could explain the mean inflow that we observe during both non-summer periods (Fig. 3-6 and 3-13). Our moorings are off-center to the right/eastern side of the fjord, and the sign and magnitude of the observed mean flow at mid-depth are consistent with this model.

Similarly, while there is no net transport of heat and salt in either layer of this model, there are fluctuating transports of heat and salt (F_2 and H_2) in the depth range of pycnocline heaving as shown in Fig. 3-18b and Fig. 3-18c. The sign and magnitude of these transports on the right side of the cross-section are similar to our measurements of H_2 and F_2 during the non-summer months (Fig. 3-15). This model presents compelling evidence that part of the mean exchange flow

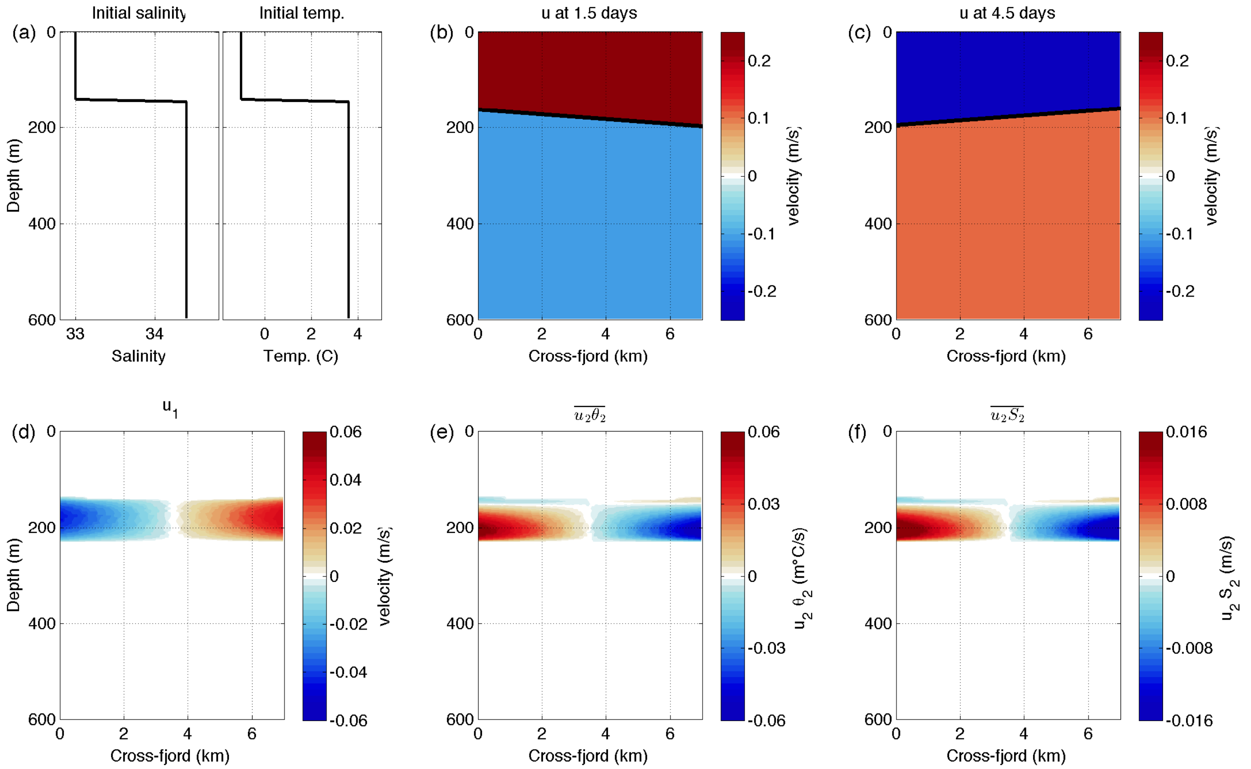

Figure 3-18: Idealized two-layer model of shelf-forced flows. (a) Salinity and temperature versus depth for initial conditions. (b) Snapshot of velocity at 1.5 days (quarter of 6-day period) with interface shown in black. Mean interface is deepening, with its cross-fjord tilt in geostrophic balance with vertical shear. (c) Snapshot of velocity at 4.5 days (three quarters of 6-day period) with interface shown in black. Mean interface is shoaling, with its cross-fjord tilt in geostrophic balance with vertical shear. (d) Time-averaged velocity, $\overline{u} = u_1$ (since $u_0 = 0$), as a function of depth and cross-fjord distance. (e) Fluctuating transport of temperature, $\overline{u_2\theta_2}$. (e) Fluctuating transport of salt, $\overline{u_2S_2}$. Note: the cross-section averages these three quantities (u_1, $\overline{u_2\theta_2}$, $\overline{u_2S_2}$) is zero – these plots highlight the biases that might arise from incomplete resolution of the fjord cross-section.

and fluctuating transports that are measured during the non-summer months in Sermilik could be partially or entirely an artifact of our limited cross-fjord coverage. During the summer, the shelf-forced pulses are significantly reduced and the mean exchange flow that we observe cannot be explained by this sampling bias.

3.D Surface fluxes

The surface heat fluxes are not directly evaluated, but their magnitude is estimated with the ERA-Interim reanalysis and local weather station data from the Sermilik region. A climatology of ERA-Interim in the coastal region outside Sermilik shows that in summer (May through August) the ocean typically gains 80 W m^{-2}, while in winter (December through March) there is a surface heat loss of -100 W m^{-2}. These approximate values are corroborated by separate estimates of surface fluxes from weather station data in the Sermilik Fjord region, as reported in Hasholt et al. (2004). Net longwave and shortwave radiation are measured at the weather station, with a summer average of $+117$ W m^{-2} and a winter average of -1 W m^{-2}. Sensible and latent heat fluxes are calculated with bulk formulas from measurements of wind speed, air temperature, relative humidity and estimates of ocean surface temperature and speed, giving average sensible heat fluxes of $+2$ W m^{-2} in summer and -42 W m^{-2} in winter, and latent heat fluxes of -3 W m^{-2} in the summer and -41 W m^{-2} in the winter. These sum to an average total surface heat flux of $+84$ W m^{-2} in the summer and -116 W m^{-2} in the winter, similar to the ERA estimates.

When the ERA values are multiplied by the surface area of our control volume, the surface heat flux in Eq. (3.11) would have a magnitude of -7.4×10^{10} W in winter and $+5.9 \times 10^{10}$ W in summer. During the summer, these values are relatively small compared to our measurements of H_1 and $H_{Storage}$, which are both $\mathcal{O}(10^{11} - 10^{12})$ W (Fig 3-7). Thus, during the summer, neglecting surface heat fluxes should not have a significant impact on our calculations of the freshwater fluxes. Neglecting this heat gain into the control volume means that we might underestimate submarine melting by $\sim$160 m^3 s^{-1}. In the winter, when the control volume loses heat to the atmosphere, we would overestimate submarine melting by $\sim$200 m^3 – though we are not able to infer freshwater fluxes during the non-summer months.

We have also neglected mass fluxes through the surface when simplifying the full mass budget for a glacial fjord (Eq. 3.1 reduced to Eq. 3.6). The mean annual precipitation from the nearby weather station is approximately 882 mm/yr (Hasholt et al., 2004), which corresponds to a mass flux into the control volume of 22 m^3 s^{-1}. This is almost two orders of magnitude smaller than the inferred meltwater fluxes, so neglecting precipitation will not have an appreciable effect.

Chapter 4

Modeling shelf-forced flows in Greenland's fjords

4.1 Introduction

Fjords connect the glaciers of the Greenland Ice Sheet to the ocean. They are the gateways for importing oceanic heat to melt ice and for exporting meltwater to the ocean. While submarine melting has been implicated as a driver of recent glacier acceleration (Holland et al., 2008a; Nick et al., 2009; Joughin et al., 2012), little is known about the fjord-scale processes that modulate melt-rates or transport meltwater (Straneo and Heimbach, 2013). The submarine melt rate is expected to vary with the near-glacier velocity and ocean temperature (Jenkins, 2011), but basic questions about what drives temperature variability near Greenland's glaciers remain unanswered. Resolving the drivers of fjord circulation and fjord-shelf exchange is crucial to understanding how heat is imported to melt ice and how glacial meltwater is exported. The processes that renew water and flux tracers through Greenland's fjords are integral to understanding ocean-glacier interactions.

There are a variety of potential drivers of fjord circulation, including: freshwater inputs from rivers, submarine melting or subglacial discharge, tides, local wind forcing, and shelf variability (see fjord reviews in Farmer and Freeland, 1983; Inall and Gillibrand, 2010; Stigebrandt, 2012; Straneo and Cenedese, 2015). While the majority of work on Greenland's fjords focuses on the freshwater-driven circulation, recent observational studies show that shelf-forced flows are the dominant mode of variability in east Greenland fjords (Straneo et al., 2010; Jackson et al., 2014). This is not surprising, given the long history of Scandinavian fjord studies that show shelf forcing to be the dominant driver of fjord-shelf exchange in several deep-silled fjords (e.g. Pettersson, 1920; Stigebrandt, 1981; Arneborg, 2004). Nevertheless, the underlying dynamics of these shelf-forced flows have been largely neglected, with no overarching framework for understanding shelf forcing across different fjords. Resolving the leading order dynamics of shelf forcing is critical for assessing its importance (particularly in transporting heat and meltwater) relative to other modes of circulation and for accurate modeling of ocean-glacier interactions.

4.1.1 Background on shelf forcing in fjords

In general, the literature on shelf forcing in fjords is fragmentary and inconsistent, both in its terminology and underlying framework. The basic principle is that density variations outside a fjord can set up a pressure gradient between fjord and shelf, driving baroclinic flows within the fjord. In the literature, this has been referred to as shelf forcing, baroclinic pumping, or, most commonly, intermediary circulation. This last term arose from the finding that shelf forcing existed in an intermediary layer between a surface brackish layer and the depth of a sill (Stigebrandt, 1990). However, this is something of a misnomer for Greenlandic fjords that often do not have a surface brackish layer nor isolated waters below a sill – the majority of the water column might be subjected to shelf forcing, not just an intermediary layer. In addition, 'intermediary circulation' has taken on several conflicting meanings in the literature (e.g. Sutherland et al., 2014b versus Sciascia et al., 2014), so in this term is avoided here in favor of 'shelf forcing' or 'shelf-forced flows' to refer to fjord flows driven by variability in the shelf pressure field.

The role of shelf forcing has primarily been studied in Scandinavian fjords, many of which are short and narrow compared to the fjords of Greenland. Pettersson (1920) first documented that density fluctuations outside a fjord's mouth drive a baroclinic response within the fjord, but it was not until the 1980's (e.g. Svendsen 1980; Klinck et al. 1981; Holbrook et al. 1983) that this baroclinic pumping was explored more extensively. Using a linear two-layer numerical model of a deep (500 m) fjord with no sill coupled to the shelf, Klinck et al. (1981) found that along-shore winds set up a boundary condition at the mouth of the fjord that drove a baroclinic circulation within the fjord. For example, during downwelling favorable winds, the pycnocline would be depressed at the mouth while the sea surface would rise, driving inflow in the upper layer of the fjord and outflow in the lower. Expanding upon Klinck's work, Stigebrandt (1990) found that shelf forcing drove at least ten times more exchange with the shelf than the estuarine circulation for a typical Norwegian fjord. Later studies by Aure et al. (1996) and Arneborg (2004) showed that high frequency fluctuations were more efficient at driving exchange than low frequency ones. Arneborg (2004) estimated the fjord turnover time (the time for the volume in basin to be diluted by 63%) to be several weeks and found that the exchange was dominated by shelf forcing.

There is very limited discussion in most of the aforementioned papers about how pycnocline disturbances are communicated to the fjord. The exceptions are a few studies of particularly long fjords that consider the propagation of density signals. Proehl and Rattray (1984) considered the wave response of the Strait of Juan de Fuca (typically classified as a fjord, despite its name) and found that disturbances from the mouth propagated up-basin as Kelvin waves. More recently, Inall et al. (2015) explored the propagation of coastal trapped waves (CTW) up one side of a wide Arctic fjord in Svalbard.

The literature on shelf forcing in fjords is mostly site-specific, with no overarching framework or theory to predict the shelf-driven flow in different fjords or the magnitude of fjord/shelf exchange. There are two partial exceptions. First, Aure et al. (1996) derived an empirical relationship for the mean exchange between fjord and shelf as a function of density variability on the shelf:

$$\overline{Q} = \beta\sqrt{HWA_f\frac{g\Delta M}{\rho}} \tag{4.1}$$

where $\beta = 1.7 \times 10^{-5}$ is an empirical constant, H is the fjord mouth depth, W is the fjord mouth width, A_f is the surface area of the fjord, and ΔM is the standard deviation of the weight of the shelf water column from the mean sea surface down to sill depth (in kg/m^2). Although this expression lacks a solid dynamical framework and is empirically tuned to observations from one Scandanvian fjord, this equation has seen a modest resurgence in recent fjord literature, being used by Sutherland et al. (2014b) and Inall et al. (2015) and discussed in reviews by Stigebrandt (2010) and Straneo and Cenedese (2015).

A simpler expression for volume flux, given by Arneborg (2004) and Stigebrandt (2012), is referred to as the slab model:

$$Q = A_f\frac{\partial \eta}{\partial t} \tag{4.2}$$

where A_f is the upstream surface area of the fjord, and η is the vertical displacement of the pycnocline. Eq. 4.2 is a simple expression of volume conservation in the upper layer or lower layer, where it is assumed that the pycnocline heaving is uniform throughout the fjord.

Parameter space of previous studies To categorize the existing literature, two non-dimensional numbers can be used to form a 2-D parameter space (Fig. 4-1): the fjord width divided by the deformation radius, W/R_d, and the along-fjord adjustment timescale divided by the forcing timescale, $\omega L/c$, where ω is the forcing frequency and L is the fjord length and c is the baroclinic phase speed. The latter ratio can also be written as kL, i.e. the ratio of the fjord length to the forcing wavelength, where $k = \omega/c$ is the wavenumber.

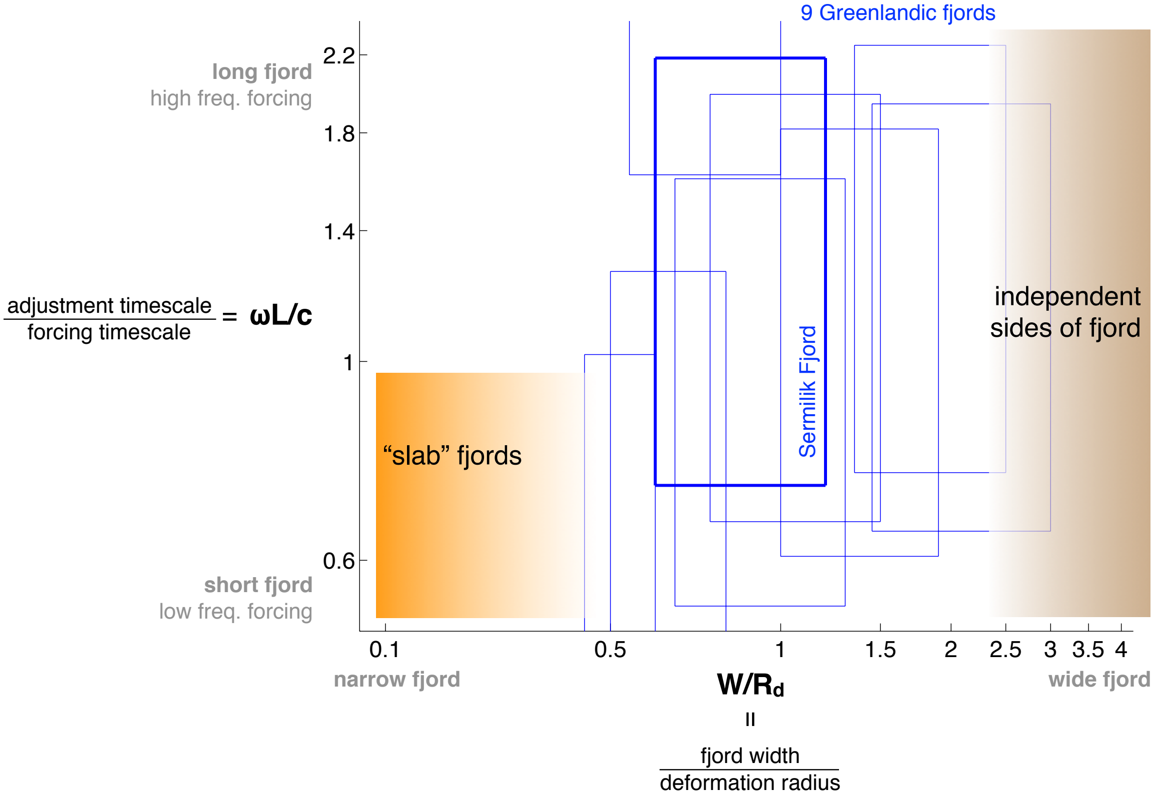

Figure 4-1: Parameter space of $\omega L/c$ versus W/R_d, showing the location of previous studies and Greenland's fjords. The slab model from Arneborg (2004) falls in the lower left corner by assuming that the fjord is short compared to the wavelength and that the fjord is narrow compared to the deformation radius. The framework for CTW or Kelvin Waves in very broad fjords in Inall et al. (2015) and Proehl and Rattray (1984) would fall on the far right of the domain. Nine Greenlandic fjords from Table 4.1 are shown with blue rectangles. Since $\omega L/c$ is a function of the shelf forcing frequency, we assume a broad synoptic band forcing at periods of 3 to 8 days to calculate the y-dimension of the rectangle for each fjord. Sermilik Fjord is shown in bold.

Most previous studies of Scandinavian fjords (e.g. Stigebrandt 1990; Arneborg 2004; Stigebrandt 2012) assume that the pycnocline heaves uniformly within the fjord, as in the slab model. This is based on two implicit assumptions. First, that the response can propagate throughout the fjord on a timescale much shorter than that of the forcing fluctuations on the shelf, i.e. $\omega L/c \ll 1$. This should be a sound assumption in these short fjords (e.g. 28 km in Arneborg (2004) or 15 km in Stigebrandt (1990), with $c \approx 1$ m/s in both). Second, these fjords are only a few kilometers wide, so they neglect rotational effects based on $W/R_d \ll 1$. Thus, these studies are situated in the lower left corner of the parameter space in Fig. 4-1.

The studies of Proehl and Rattray (1984) and Inall et al. (2015) fall on the opposite side of this parameter space. They study the propagation of coastally trapped waves in large fjords, where the width is several times the deformation radius. The effects of rotation and wave propagation are paramount, but they only consider fjords that are wide enough for the sides to be effectively independent (Fig. 4-1). There remains a large portion of this parameter space that is unexplored, particularly the transition through $W/R_d \sim \mathcal{O}(1)$.

4.1.2 Shelf forcing in Greenland's fjords

Many fjords in Greenland fall in the unexplored region of parameter space where $W/R_d \sim \mathcal{O}(1)$. Most recent modeling studies of Greenlandic fjords neglect cross-fjord variability and rotation based on the assertion that the fjord widths are generally less than the deformation radius (e.g. Carroll et al., 2015; Sciascia et al., 2014; Gladish and Holland, 2015; Xu et al., 2012; Cowton et al., 2015). However, the high-latitude fjords of Greenland are usually only slightly narrower than the deformation radius, if at all. The value of W/R_d for many fjords in Greenland is shown in Table 4.1: most have $W/R_d = 0.7 - 1.3$ and all listed fall between 0.5 and 3. They are *not* in a regime where $W/R_d \ll 1$.

Fjord	**W (km)**	$\mathbf{R_d}$ **(km)**	$\mathbf{W/R_d}$	Source
Sermilik Fjord	5-11	8.3	0.6 - 1.3	Sutherland et al. (2014b)
Petermann Fjord	15	5-10	1.5 - 3.0	Johnson et al. (2011)
Kangerdlugssuaq Fjord	7-14	7.3	1.0 - 1.9	Inall et al. (2014)
Sarqardleq Fjord	3-5	7.7	0.4 - 0.6	Stevens et al. (2015)
Jakobshavn/Ilulissat Fjord	6-8	9-12	0.5 - 0.8	Gladish and Holland (2015)
Rink Fjord	4-7	5.2-7.2	0.6 - 1.3	Chauché et al. (2014)
Store Fjord	5-8	5.2-7.2	0.7 - 1.5	Chauché et al. (2014)
79N	10	4-8	1.3 - 2.5	Wilson and Straneo (2015)
Godthabsfjord	5-6	7	0.7 - 0.9	Mortensen et al. (2011)

Table 4.1: Ratio of W/R_d for nine fjords around Greenland.

In terms of the along-fjord adjustment timescale, the large fjords in Greenland are long enough that a baroclinic signal could take ∼1 day to reach the head of the fjord – shorter than the timescale of most synoptic wind forcing but not significantly. By assuming that fjords are subjected to forcing in a broad synoptic time-band (here defined as periods of 3 to 8 day), each of the fjords from Table 4.1 is placed in the parameter space of Fig. 4-1 with a blue rectangle. Most of these Greenlandic fjords fall in the middle of Fig. 4-1, where the importance of cross-fjord structure and along-fjord propagation is not obvious.

Two recent modeling studies of Greenland's fjord have included some form of shelf forcing in their two-dimensional fjord/glacier models (Gladish and Holland, 2015; Sciascia et al., 2014). Similar to Stigebrandt (1990), they impose shelf forcing through a boundary condition at the fjord mouth, rather than modeling the shelf region outside. In Sciascia et al. (2014) (and perhaps also Gladish and Holland 2015), this boundary condition mixes the upper and lower layer near the mouth, creating an intermediate density water mass that propagates into the fjord as a gravity current. While this is an interesting process that might be relevant somewhere, it is not the mechanism that observations suggest of heaving/waves on the pycnocline (a process that does not require any mixing). Accurate modeling of the fjord-shelf exchange likely requires modeling the coastal shelf region outside the fjord (e.g. Klinck et al., 1981).

4.1.3 Driving questions

A framework for the leading order dynamics of shelf-driven flows is lacking. Analogous to tidal dispersion and tidal salt flux in estuaries, shelf-forced flows might play an important role in fluxing heat, salt, and meltwater in certain glacial fjords. The questions of tracer transport and renewal in these fjords, however, cannot be adequately answered without a better understanding of the shelf-forced flows. In this study, we investigate the role of shelf forcing across a range of parameter space that has been largely ignored. We attempt to address the following questions: What is the volume flux between fjord and shelf from shelf forcing? How does the fjord's response change with the forcing frequency and fjord geometry? When can a fjord be approximated as 2-D and when does cross-fjord structure become important? And finally, how does shelf forcing compare to other modes of circulation, particularly local wind forcing?

Here, we explore the role of shelf forcing across a range of fjord geometries and forcing frequencies using ROMS numerical simulations and two analytical models. Outside the fjord literature, there is a vast body of work on wave and wind forcing of estuaries, inlets, and straits that provides several frameworks for the study of shelf forcing in fjords. After presenting the models, we explore the contrasting behavior in the analytical models, and then we report on the ROMS results in the context of the analytical models.

4.2 Methods

4.2.1 Motivating observations from east Greenland fjords

The modeling in this study is guided by observations from two east Greenland fjords, Sermilik and Kangerdlugssuaq, described in Chapters 2 & 3. The most salient results are briefly reviewed here. Sermilik and Kangerdlugssuaq are deep-silled fjords (>500 m throughout) with no significant barriers to impede exchange between the fjord and shelf. In the fjords, shelf forcing dominates the variability in the velocity and density fields. In the moored records from Sermilik Fjord, the velocity is primarily a two-layer baroclinic flow with peak energy at 6 day periods. The fluctuating upper layer velocities are typically 30-50 cm/s, occasionally exceeding 80 cm/s, and they are associated with pycnocline heaving of tens to 100 m in the vertical. On synoptic timescales of 2 to 10 day periods (subinertial and subtidal), the fjord flows are highly coherent with upstream shelf density and also (to a lesser extent) shelf wind. Shelf density fluctuations are primarily driven by regional along-shore winds, but other sources of variability exist (Harden et al., 2014). The lag in density fluctuations between shelf and fjord moorings is approximately consistent with the pycnocline disturbances propagating in at the baroclinic phase speed ($c \approx 1$ m/s). Comparison of mid- and upper-fjord moorings show that, towards the head of the fjord, the velocity decays and the pycnocline fluctuations are mildly amplified.

These two fjords on the southeast coast of Greenland are in a region of exceptionally strong winds. On the shelf, low pressure storm systems compress against Greenland's steep topography and cause frequent, intense along-shore winds (Moore and Renfrew, 2005). Additionally, the fjords are subjected to much less frequent but even more powerful down-fjord winds from the ice sheet (Oltmanns et al., 2014). These local fjord winds might be important in driving fjord circulation, but it difficult to parse out their role relative to shelf forcing in the observations since shelf and local wind events often occur in close succession.

Based on these observations, we are interested in investigating the propagation of density signals from the shelf that drive baroclinic fjord flows at subtidal and subinertial timescales. On a realistic shelf with both topography and stratification, coastal trapped waves propagate signals along the coast and represent a hybrid between barotropic shelf waves and internal Kelvin waves (Allen, 1975; Huthnance, 1977). The non-dimensional slope Burger number is:

$$S = \frac{\alpha N}{f} \tag{4.3}$$

where α is the bottom slope and N is the buoyancy frequency. When $S \gg 1$, coastal trapped waves behave as pure internal Kelvin waves (e.g. Brink, 1991). Around Sermilik Fjord, the slope Burger number is estimated to fall between 17 and 29 in the non-summer and 33 to 56 in the summer. Thus, subinertial pycnocline variability in this region should propagate with the properties of Kelvin waves. This is likely true for much of the coast around Greenland, where topography is generally steep and the water column is highly stratified.

4.2.2 ROMS simulation of fjord and adjacent shelf

The response of a fjord to both shelf forcing and local wind forcing were simulated with an idealized fjord/shelf configuration in the Region Ocean Modeling System (ROMS, Shchepetkin and McWilliams, 2005). ROMS is an free-surface, hydrostatic, primative equation model with extensive use in modeling the coastal ocean. It uses a time-splitting scheme where the 2-D vertically integrated momentum equations are solved using a fast timestep to resolve barotropic flows and a slower timestep to compute the 3-D velocity field.

In the model simulations, a rectangular fjord connects to an adjacent shelf region, with a flat bottom at 600 m depth and vertical walls between the ocean and land (Fig. 4-2). While the fjord geometry varies between different runs, the size of the modeled shelf region remains constant at 310 km in the along-shore direction and 96 km in the cross-shore direction. The control run has fjord dimensions of 90 km long by 7 km wide to match the geometry of Sermilik Fjord. The simulations use a stretched grid of resolution $\Delta x = \Delta y = 250$ m in the fjord and on the nearby shelf (within 150 km of the fjord), which reduces to 1000 m horizontal resolution at the domain boundaries.

The model contains 30 levels of a stretched vertical grid, ranging from 7 m vertical resolution at the surface to 72 m at the bottom (Fig. 4-2b). The model was initialized with a nearly two-layer density stratification that resembles Sermilik Fjord in the non-summer months (Straneo et al., 2011): the pycnocline is centered at $\sim$160 m depth and has a density difference of 1.1 kg/m^3, resulting in a first mode phase speed of $c = 1.05$ m/s. The vertical grid spacing allows for relatively high vertical resolution in the surface Ekman layer and through the pycnocline (<200 m depth) and lower resolution in the weakly stratified deep layer. While ROMS uses terrain-following sigma coordinates, our vertical sigma levels are also horizontal because the domain has a flat bottom.

We used the default advection scheme in ROMS, which is third-order upstream horizontal advection of momentum and tracers. The model was run with a baroclinic timestep of 30 s and 16 barotropic timesteps between each baroclinic step. The barotropic timestep was determined by a

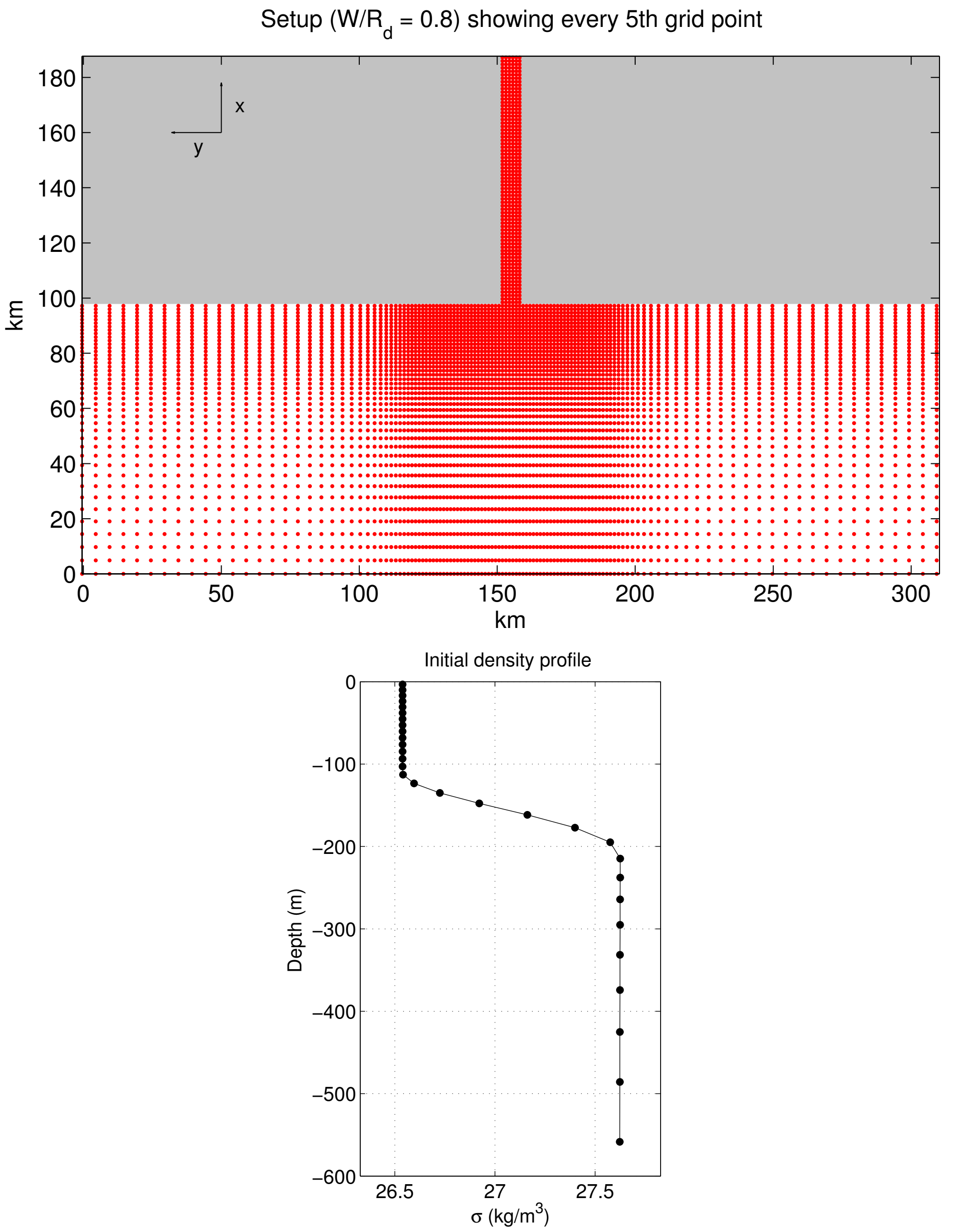

Figure 4-2: **a.** Domain of ROMS simulations, with land-masked areas shown in grey. Red dots are shown at every 5th grid point, to illustrate the stretched horizontal grid. The ocean has a flat bottom at 600 m throughout the domain and vertical walls between ocean and land. **b.** Initial density profile, with dots showing the 30 vertical levels in the model.

simple criteria for the barotropic Courant number, i.e. the timestep must be less than the time for a signal to propagate between grid points at the gravity wave speed, $\sqrt{gH}$. The baroclinic timestep was determined more subjectively since it is limited by a variety of factors including the vertical advection. History files of the entire domain were saved every 8 hours and stations at fjord and shelf cross-sections were saved every 4 hours. The model simulations were run for 30 to 80 days, depending on the forcing period.

A k-ϵ vertical mixing scheme was used, implemented with the generic length scale formulation from Warner et al. (2005) and with the stability function of Kantha and Clayson (1994). The Smagorinsky scheme was used to parametrize horizontal viscosity (Griffies and Hallberg, 2000), allowing for coefficients that vary with the grid spacing and with the evolving velocity field. Horizontal harmonic mixing of tracers was used, with coefficients that scale with the grid size and have a value of 2×10^2 m^2/s for the smallest grids (250×250 m). The model contains linear bottom drag with a coefficient of $r = 3\times10^{-4}$ m/s.

The following boundary conditions were applied to the eastern, southern and western boundaries: Chapman boundary condition for the free surface, Shchepetkin boundary condition for the barotropic velocity, and radiation-nudging for baroclinic velocities and tracers (T, S). The boundaries were nudged towards the initial stratification and zero velocity, with a nudging timescale of 2 days for inflow into the domain and 100 days for outflow. A closed, no-slip boundary was imposed between the ocean and land.

Periodic wind stresses, of various amplitudes and frequencies, were applied over either: (a) the shelf region, excluding fjord, in the along-shore direction, or (b) the fjord alone, along the fjord axis. The surface and bottom fluxes of mass and buoyancy were set to zero in all runs.

4.2.2.1 Description of model runs

Two sets of ROMS runs were used to explore the dynamics of shelf forcing and the relative importance of shelf versus local forcing.

In Set A, the fjord response to periodic shelf forcing was investigated across a range of fjord geometries and forcing frequencies (see Fig. 4-3 and Fig. 4-4). Shelf pycnocline fluctuations were generated with a sinusoidal along-shore wind stress on the shelf. These runs were forced with periods of 3 to 10 days, resulting in $\omega L/c$ from 0.6 to 2.1 (given a fixed fjord length of 90 km and c = 1.1 m/s). The ratio of the fjord width to the deformation radius, W/R_d, was varied between 0.1 and 3.2. For most of the runs, this ratio was changed by varying the fjord width from 5 km to 28 km while holding f constant at 1.3×10^{-4} s^{-1}. For the $W/R_d = 0.1$ runs, however, f was reduced to 0.3 $\times10^{-4}$ for a 7 km fjord in order to maintain sufficient resolution across the fjord without changing the model grid. The run with a width of 7 km and forcing period of 6 days (bold in Fig. 4-4) is referred to as the control run, as it has properties most closely resembling Sermilik Fjord.

While the wind frequency was varied, the wind amplitude was fixed at $\tau_S = 0.2$ N/m^2, gener-

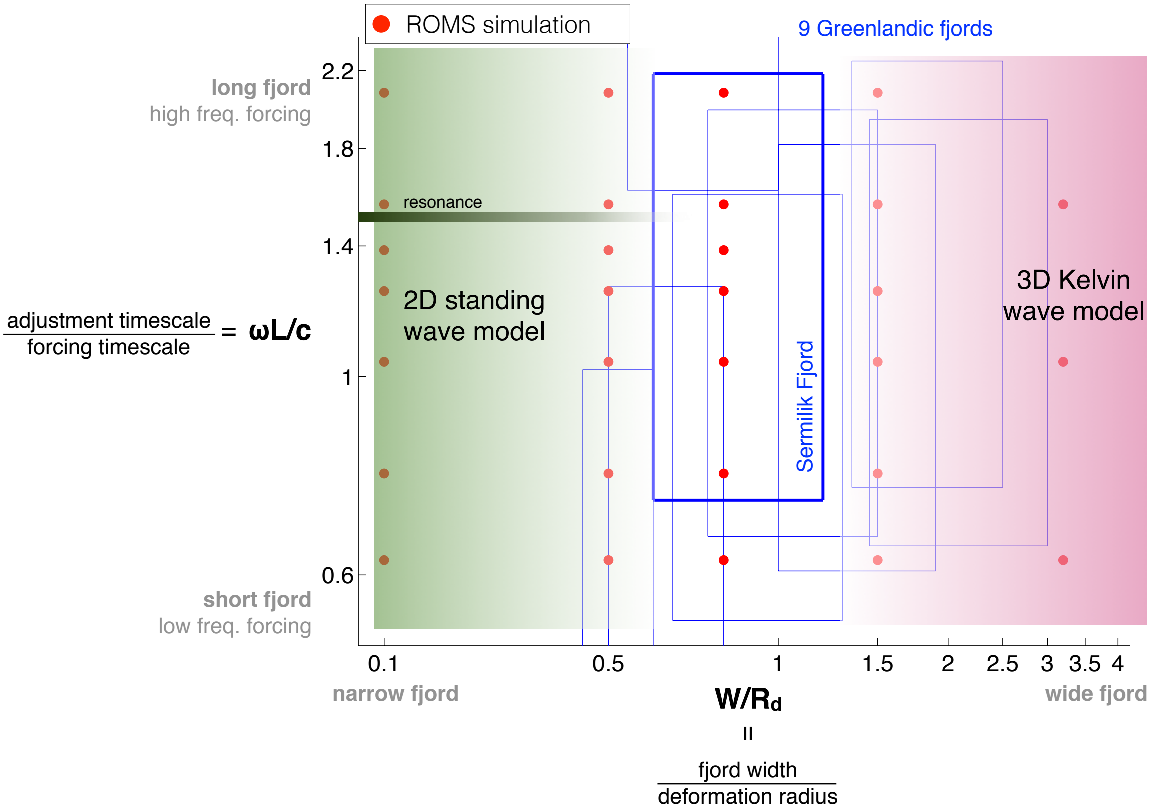

Figure 4-3: Same parameter space of $\omega L/c$ versus W/R_d from Fig. 4-1, but now showing the location of ROMS simulations and where the two analytical models of Section 4.2 are expected to be applicable. The standing wave model (e.g. Garvine, 1985; Janzen and Wong, 2002, used for barotropic signals in estuaries) allows for a range of frequencies but requires a narrow fjord. On the other hand, the Kelvin wave model should apply better to wider fjords. The transition between these regimes is deliberately ambiguous, since previous studies have ignored the region where $W/R_d \sim 1$. The locations of ROMS simulations (Set A) in this parameter space are shown with red dots. As described in Fig. 4-1, the blue rectangles indicate the approximate location of nine Greenlandic fjords from Table 4.1 in this parameter space.

ating shelf pycnocline amplitudes, η_S, between 11 and 15 m for the various runs. (The pycnocline frequency always matched the wind frequency.) While we might expect η_S to be inversely proportional to the wind forcing frequency, we found that η_S had only a very weak dependence on frequency and scaled primarily with τ across the ranges of frequencies (see Appendix 4.A). For this reason, we fixed the wind stress while varying the frequency to generate shelf waves of roughly equal magnitudes in different runs. This study is not concerned with the generation of these shelf density fluctuations; instead, the focus is on the response of the fjord to imposed variability on the shelf. Thus, in analyzing the runs, we diagnose the amplitude of the shelf heaving, η_S, and compare it (*not* the shelf wind) with the fjord response. Additionally, the amplitude of the fjord response scales

SET A	L = 90 km , c = 1.1 m/s, shelf wind (τ = 0.2 N/m^2)				
	W/R$_d$	**W** (km)	**f** (1/s)	**ωL/c** (= kL)	**T** (days)
run159	0.1	7	2.5x10-5	2.08	3
run151	0.1	7	2.5x10-5	1.56	4
run170	0.1	7	2.5x10-5	1.39	4.5
run160	0.1	7	2.5x10-5	1.25	5
run148	0.1	7	2.5x10-5	1.04	6
run165	0.1	7	2.5x10-5	0.78	8
run167	0.1	7	2.5x10-5	0.62	10
run156	0.5	5	1.3x10-4	2.08	3
run146	0.5	5	1.3x10-4	1.56	4
run169	0.5	5	1.3x10-4	1.39	4.5
run157	0.5	5	1.3x10-4	1.25	5
run138	0.5	5	1.3x10-4	1.04	6
run158	0.5	5	1.3x10-4	0.78	8
run141	0.5	5	1.3x10-4	0.62	10
run152	0.8	7	1.3x10-4	2.08	3
run150	0.8	7	1.3x10-4	1.56	4
run168	0.8	7	1.3x10-4	1.39	4.5
run153	0.8	7	1.3x10-4	1.25	5
run129	**0.8**	**7**	**1.3x10-4**	**1.04**	**6**
run154	0.8	7	1.3x10-4	0.78	8
run139	0.8	7	1.3x10-4	0.62	10
run162	1.6	14	1.3x10-4	2.08	3
run149	1.6	14	1.3x10-4	1.56	4
run163	1.6	14	1.3x10-4	1.25	5
run137	1.6	14	1.3x10-4	1.04	6
run164	1.6	14	1.3x10-4	0.78	8
run140	1.6	14	1.3x10-4	0.62	10
run155	3.2	28	1.3x10-4	1.56	4
run142	3.2	28	1.3x10-4	1.04	6
run143	3.2	28	1.3x10-4	0.62	10

SET B	L = 90 km , W = 7 km, c = 1.1 m/s, T = 6 days	
	shelf τ (N/m^2)	**fjord τ** (N/m^2)
run128	0.1	0
run129	**0.2**	**0**
run166	0.3	0
run171	0.4	0
run172	0.5	0
run144	0	0.1
run130	0	0.2
run145	0	0.3
run167	0	0.5

Figure 4-4: Properties for ROMS runs in Set A and Set B. Run129 in bold is the "control run" with properties best resembling those of Sermilik Fjord.

linearly with the amplitude of the shelf wave for the range of amplitudes studied (Appendix 4.B), so we can normalize by η_S to remove the effect of forcing amplitude variability across Set A.

In Set B of ROMS simulations, the fjord width and forcing period were held constant at 7 km and 6 days, respectively, while winds of varying amplitude were applied to either the fjord or the shelf. These runs were used to assess the relative importance of shelf versus local wind forcing across a range of forcing strengths.

4.2.3 Analytical models

Two simple analytical models are presented here to help interpret the numerical model, providing a framework for exploring shelf forcing and the relative importance of shelf versus local wind forcing. Both assume a two-layer fjord, while one is appropriate in the narrow limit $W/R_d \to 0$ and the other is more applicable for $W/R_d > 1$. These two analytical models can be thought of as asymptotic limits, and the numerical simulations from ROMS allows us to explore the transition between regimes when $W/R_d \sim 1$, as is the case in most Greenlandic fjords (Table 4.1).

After briefly introducing the analytical models, the contrasting dynamics in these two analytical models (including the implications of their assumptions and boundary conditions) will be discussed in Section 4.3, and then they are compared with ROMS simulations in Section 4.4.

4.2.3.1 Standing wave model of 2-D fjord

Many studies have used a simple standing wave model to study the barotropic response of estuaries to shelf forcing and/or local wind forcing (e.g. Garvine, 1985; Janzen and Wong, 2002; Wang, 1979). These studies solve for the barotropic velocity and sea surface displacement forced by a periodic shelf fluctuation or periodic local wind forcing. They neglect cross-estuary structure and the Coriolis term in the momentum budgets, and they impose a sea surface condition at the mouth. Their underlying assumption, that the width is much less than the barotropic deformation radius, should be well justified since $R_{d,barotrop} \sim \mathcal{O}(100 \text{ km})$ in mid-latitude estuaries. Thus, these studies are situated on the far left side of the parameter space in Fig. 4-3.

Here, we modify the standing wave framework of Garvine (1985) to address the baroclinic response of a narrow two-layer fjord. Neglecting friction, advection of momentum and cross-fjord

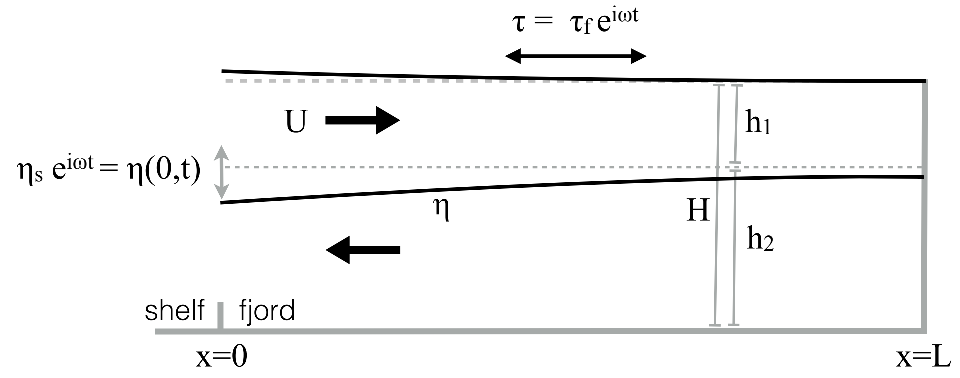

Figure 4-5: Schematic of 2-D standing wave model, showing depth versus along-fjord direction.

flow, the along-fjord momentum and continuity equations are:

$$\frac{\partial U}{\partial t} = c^2 \frac{\partial \eta}{\partial x} + \frac{h_2}{H}\frac{\tau}{\rho} \tag{4.4}$$

$$0 = \frac{\partial \eta}{\partial t} + \frac{\partial U}{\partial x} \tag{4.5}$$

where U is the depth-integrated upper layer velocity, η is the interface displacement, τ is the local wind stress, $c^2 = g'h_1h_2/H$, $g' = g\Delta\rho/\rho_0$, and $\Delta\rho$ is the density difference between layers. These quantities are illustrated in Fig. 4-5. The along-fjord momentum budget is a balance between local acceleration, pressure gradient and wind stress. This also assumes that the interface displacements are small relative to layer thickness ($\eta \ll h_1, h_2$ so c can be treated as a constant) and that there is no mixing between layers. Combining Eq. 4.4 and 4.5 gives a governing wave equation:

$$\frac{\partial^2 U}{\partial t^2} = c^2 \frac{\partial^2 U}{\partial x^2} + \frac{h_2}{H\rho}\frac{\partial \tau}{\partial t} \tag{4.6}$$

Shelf forcing alone Shelf forcing is communicated to the fjord through a boundary condition at the mouth such that the interface, η, at $x = 0$ is forced to match an imposed shelf condition. We explore the fjord response to an infinite periodic shelf forcing of the form:

$$\eta(0, t) = \eta_S e^{i\omega t} \tag{4.7}$$

where ω is the frequency of the shelf forcing and η_S is the amplitude of the shelf wave. At the head of the fjord, $x = L$, the velocity is required to be zero:

$$U(L,t) = 0 \tag{4.8}$$

This gives the well-known standing wave solution:

$$\eta(x,t) = \eta_S \frac{\cos(k(L-x))}{\cos(kL)} e^{i\omega t} \tag{4.9}$$

$$U(x,t) = \frac{\eta_S \omega i}{k} \frac{\sin(k(L-x))}{\cos(kL)} e^{i\omega t} \tag{4.10}$$

where $k = \omega/c$. If friction were important, the solution could be modified such that k has an imaginary component: $k^2 = \frac{\omega(\omega - ir/h)}{c^2}$, where r is a linear drag coefficient. For this study of deep fjords, however, we neglect friction.

Local wind forcing This solution can be easily modified to include local wind forcing by including a non-zero τ in Eq. 4.6. For simplicity, the wind is given the same periodic form as the shelf forcing:

$$\tau(t) = \tau_f e^{i\omega t} \tag{4.11}$$

If the mouth boundary condition is $\eta(0,t) = 0$, i.e. the interface is clamped to a constant value at the mouth (no shelf forcing), then the response to the local wind forcing is:

$$\eta(x,t) = \frac{\tau_f h_2}{\rho c^2 k H} \frac{\sin(kx)}{\cos(kL)} e^{i\omega t} \tag{4.12}$$

$$U(x,t) = \frac{i\tau_f h_2}{\rho \omega H} \frac{\cos(kx) - \cos(kL)}{\cos(kL)} e^{i\omega t} \tag{4.13}$$

At low frequency, i.e. as $\omega \to 0$, the solution approaches the steady state of $U = 0$ and $\eta = -\frac{\tau x h_2}{\rho c^2 H}$. This happens when the pressure gradient term balances the wind stress, the steady state solution of Eq. 4.4.

The response to simultaneous shelf forcing ($\eta_S e^{i\omega t}$) and local wind forcing ($\tau_f e^{i\omega t}$) of the same frequency is just the linear combination of Eq. 4.9/4.10 and Eq. 4.12/4.13:

$$U(x,t) = \left[\frac{\eta_S \omega i}{k}\frac{\sin(k(L-x))}{\cos(kL)} + \frac{i\tau_f h_2 \omega}{\rho c^2 k^2 H}\frac{\cos(kx)-\cos(kL)}{\cos(kL))}\right] e^{i\omega t} \tag{4.14}$$

$$\eta(x,t) = \left[\eta_S \frac{\cos(k(L-x))}{\cos(kL)} + \frac{\tau_f h_2}{\rho c^2 k H}\frac{\sin(kx)}{\cos(kL)}\right] e^{i\omega t} \tag{4.15}$$

4.2.3.2 Kelvin wave model of 3-D fjord

The second analytical model allows for lateral variability in the cross-fjord direction. This framework is inspired by a series of studies of Kelvin waves propagating through straits (e.g. Toulany and Garrett, 1984; Durland and Qiu, 2003; Johnson and Garrett, 2006). These studies show that, unless a strait's width is considerably narrower than the deformation radius, the majority of incident Kelvin wave energy will be transmitted through the strait, as opposed to propagating past the mouth. This suggests that for fjords with $W/R_d \sim \mathcal{O}(1)$, the Kelvin wave propagation, including both along-coast and cross-coast structure, should be investigated.

An unforced, invicid Kelvin wave obeys the semi-geostrophic equations of motion, where the along-coast momentum balance is between local acceleration and the pressure gradient, while the cross-coast momentum is in geostrophic balance. The structure for a baroclinic Kelvin wave of frequency, ω, and amplitude, η_S is:

$$\eta(x,y,t) = \eta_S e^{-y/R_d} e^{i(kx-\omega t)} \tag{4.16}$$

$$U(x,y,t) = \frac{c^2}{f}\frac{\partial \eta}{\partial y} = -c\eta_S e^{-y/R_d} e^{i(kx-\omega t)} \tag{4.17}$$

when x is the along-coast direction, y is the cross-coast direction, $k = \omega/c$, $c = \sqrt{g' h_1 h_2/H}$, and $R_d = c/f$. The signal of the Kelvin wave decays away from the coast exponentially with a decay scale of the deformation radius.

To examine the response of a fjord to Kelvin waves on the shelf, we formulate a simple model where periodic Kelvin waves from the shelf propagate into the fjord, go up one side and down the other, and then exit freely (Fig. 4-6). Supported by the results of Durland and Qiu (2003), the portion of the Kelvin wave within a distance W of the coast is allowed to turn into the fjord of width W. Thus, if the fjord width is much larger than the deformation radius, then the entire cross-shore structure of the Kelvin wave will enter the fjord. If the cross-shore structure of the Kelvin wave is wider than the fjord width, only the portion within W of the coast will enter the

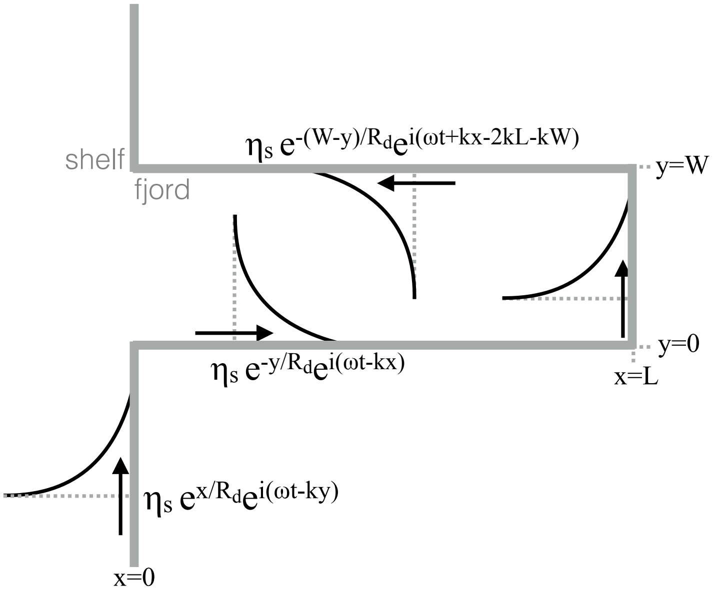

Figure 4-6: Schematic of 3-D Kelvin wave model, showing plan view of shelf (left) and fjord (right). The amplitude of the interface displacement is projected onto the along-shore direction, illustrating the cross-shore decay of Kelvin wave structure.

fjord.

The waves on either side of the fjord are assumed to add linearly and the waves are undistorted as they propagate around the head, as often assumed for barotropic tidal signals in large bays (e.g. Taylor, 1921; Gill, 1982). In the along-fjord direction, this is equivalent to reflecting the wave ($k \to -k$) and adding a phase lag of $\phi = Wk$, corresponding to the time for the wave to propagate across the width. Thus, the fjord solution for η is:

$$\eta(x,y,t) = \underbrace{\eta_0 e^{-y/R_d} e^{i(\omega t-kx)}}_{\text{incident}} + \underbrace{\eta_0 e^{-(W-y)/R_d} e^{i(\omega t+kx-2kL-kW)}}_{\text{reflected}} \tag{4.18}$$

The outgoing wave has no imposed boundary condition. It should be noted that this Kelvin wave solution obeys the along-fjord momentum budget of the standing wave (Eq. 4.4). The difference between these analytical models is the mouth boundary condition and in the allowance of cross-fjord structure.

For easier comparison with the standing wave model, the incoming and outgoing Kelvin waves are both phase shifted by a constant, $\phi = k(L + W/2)$, such that the full fjord response is:

$$\eta(x, y, t) = \eta_0 e^{-y/R_d} e^{i(k(x-L-W/2)-\omega t)} + \eta_0 e^{-(W-y)/R_d} e^{i(k((x-L-W/2)+\omega t))} \tag{4.19}$$

$$U(x, y, t) = -c\eta_0 e^{-y/R_d} e^{i(k(x-L-W/2)-\omega t)} + c\eta_0 e^{-(W-y)/R_d} e^{i(k((x-L-W/2)+\omega t))} \tag{4.20}$$

While this model accounts for the phase lag for the Kelvin wave to propagate across the width of the fjord at the head, the solutions for η and U do not describe the structure of the waves as they reflect around the head of the fjord – this solution would be invalid close to the head of the fjord, i.e. when $L - x = \mathcal{O}(R_d)$.

This model makes several assumptions. First, the waves on either side of the fjord are assumed to add linearly. Second, the reflection happens in a simple manner at the head of the fjord, with no dissipation of energy. And, perhaps most importantly, it assumes that the outgoing wave does not feel the upstream boundary condition that is imposed on the incoming Kelvin wave – the reflected wave can leave completely with a phase set by its propagation time around the fjord. As a fjord becomes sufficiently narrow, this last assumption should become problematic.

4.3 Exploring the fjord response in the analytical models

Before addressing the numerical model results, the expected behavior in the limits of the two analytical models is examined.

4.3.1 Standing wave model

In the 2-D wave model, by clamping the boundary condition at the mouth, the fjord response is required to be a standing wave that does not propagate energy: two waves of equal amplitude travel in opposite directions, adding to form a standing wave. Thus, there is no phase propagation in the density or velocity fields throughout the fjord. In velocity, there is a node at the head of the fjord, while in the pycnocline there is an antinode at the head of the fjord. The velocity and pycnocline oscillations are in quadrature.

The amplitude of the response varies as a function of the forcing frequency, with the largest response near the resonant frequency of $\omega_R = \pi c/2L$. In other words, when $\cos(kL) \to 0$ in Eq. 4.9, the fjord response blows up. For Sermilik Fjord conditions (L = 90 km, c =1.1 m/s), the resonant forcing period is $T_R = 3.9$ days.

Converging to slab model When the forcing period is long compared to the adjustment timescale (i.e. $wL/c = kL \to 0$ or $\cos kL \to 1$), this model reduces to the slab model of Arneborg (2004) for a rectangular fjord:

$$\eta(x,t) = \eta_S e^{i\omega t} \tag{4.21}$$

$$U(x,t) = (L-x)\frac{\partial \eta_s}{\partial t} = (L-x)\eta_S \omega i e^{i\omega t} \tag{4.22}$$

In this limit, the pycnocline heaving is uniform throughout the fjord, with the same phase *and* amplitude at all points. The velocity decays linearly towards the head of the fjord. The assumptions for this slab model, of small W/R_d and small $\omega L/c$, place it in the lower left corner of the parameter space in Fig. 4-1.

4.3.2 Kelvin wave model

The Kelvin wave model includes both the along- and cross-fjord structure. Down the middle of the fjord, at $y = \frac{W}{2}$, the amplitudes of the incident and reflected Kelvin waves are equal, such that the signal looks like a standing wave:

$$\eta_{\frac{W}{2}}(x,t) = 2\eta_S e^{-\frac{W}{2R_d}} \cos(k(x-L-W/2))\cos(\omega t) \tag{4.23}$$

As with the standing wave model, there is an antinode in the interface at the head of the fjord, and no phase lag in the pycnocline or velocity down the middle axis of the fjord.

Away from the center of the fjord, however, the waves do not add evenly and the signal looks partially or entirely progressive. With some manipulation and the use of trigonometric identities, Eq. 4.19 for $\eta(x,y,t)$ can be rewritten as:

$$\eta(x,y,t) = \eta_F(x,y)\sin\left[\omega t + \phi_F(x,y))\right] \tag{4.24}$$

such that the signal at any given location (x_1, y_1) is a simple sine wave of amplitude $\eta_F(x_1, y_1)$ and phase $\phi_F(x_1, y_1)$. These amplitude and phase functions are

$$\eta_F(x,y) = \sqrt{K^2 + M^2} \tag{4.25}$$

$$\phi_F(x,y) = \tan^{-1}\left(\frac{K}{M}\right) \tag{4.26}$$

$$\text{where:} \qquad K(x,y) = \eta_0(e^{-y/R_d} + e^{-(L-y)/R_d})\cos(k(x-L-W/2)) \tag{4.27}$$

$$M(x,y) = \eta_0(e^{-y/R_d} - e^{-(L-y)/R_d})\sin(k(x-L-W/2)) \tag{4.28}$$

This manipulation allow us to examine the spatial patterns of amplitude and phase throughout the fjord. Fig. 4-7 plots η_F and ϕ_F for the Sermilik-like control run: W = 7 km, L = 90 km, $T = 6$ days, and c = 1.1 m/s. In the cross-fjord direction, the amplitude of η and u are largest at the edges. In the along-fjord direction, velocity is largest at the mouth and decays towards the head, while the interface amplitude decays towards the mouth. One can see that there is no phase lag down the middle of the fjord, but there is propagation of phase in the signals away from the center axis. In velocity, the cross-fjord difference in phase is largest at the head (where its amplitude is smallest), while in η the cross-fjord difference in phase fjord is largest at the mouth (where its amplitude is smallest). These spatial patterns for $\phi_F(x,y)$ and $\eta_F(x,y)$ will be useful for testing the extent to which the numerical simulations in ROMS agree with this Kelvin wave model.

Cross-fjord averaged quantities For comparison with the standing wave model, we compute the cross-sectionally averaged response in the Kelvin wave model. The cross-fjord averages of the interface displacement and velocity are:

$$\overline{\eta}(x,t) = \frac{1}{W}\int_0^W \eta(x,y,t)dy = 2\frac{R_d}{W}\left(1 - e^{-W/R_d}\right)\eta_0\cos(k(x-L-W/2))\cos(\omega t) \tag{4.29}$$

$$\overline{U}(x,t) = \frac{1}{W}\int_0^W U(x,y,t)dy = 2c\frac{R_d}{W}(1 - e^{-W/R_d})\eta_0\sin(k(x-L-W/2)))\sin(\omega t) \tag{4.30}$$

These cross-fjord averaged properties also have the form of a standing wave. Although the signal looks like a (partially) progressive wave on either side of the fjord, the total energy in equals the totally energy out – there is no energy dissipation within the fjord.

As W/R_d approaches zero, the cross-sectionally average properties converge to the expression

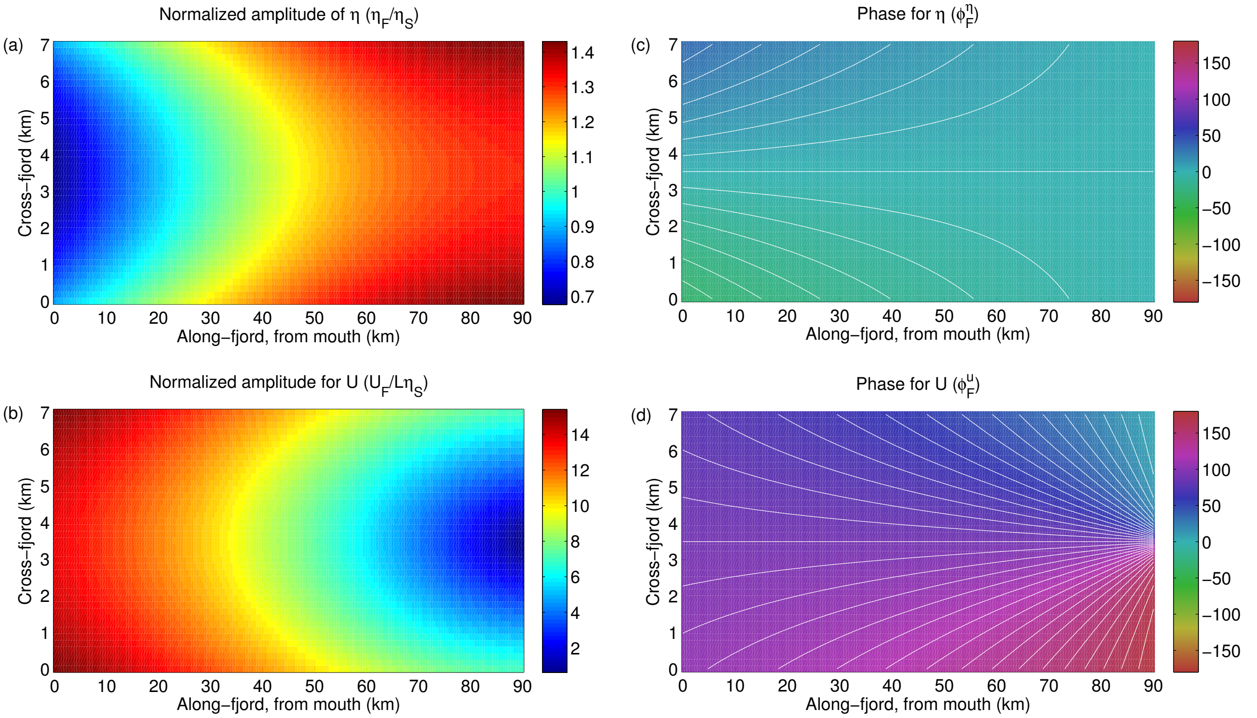

Figure 4-7: Amplitude and phase for velocity and pycnocline fluctuations (Eq. 4.24-4.28) for Sermilik-like condition of $L = 90$ km, $W = 7$ km, $c = 1.1$ m/s and $T = 6$ days. The interface amplitude is normalized by the shelf amplitude, η_S, and the depth-integrated velocity is normalized by $\eta_S L$.

down the middle from Eq. 4.23:

$$\overline{\eta}(x,t) \rightarrow \eta_{\frac{W}{2}}(x,t) = 2\eta_0 e^{-W/2a} \cos(k(x-L-W/2))\cos(\omega t) \tag{4.31}$$

While this resembles the standing wave model from Section 4.2.3.1 in the cosine terms, the amplitude does *not* in converge to the standing wave solution (Eq. 4.9) as $W/R_d \rightarrow 0$.

4.3.3 Contrasting behavior in models

The fact that the Kelvin wave model does not converge to the standing wave model for small widths can be explained by the difference in boundary conditions. For the standing wave model, the incoming and reflected wave must sum to an imposed boundary condition at the mouth. Put another way, the fjord is assumed to have no impact on the shelf. For the Kelvin wave model, the outgoing wave has no imposed boundary condition – only the incoming wave is specified. As $W/R_d \rightarrow 0$, one would expect the boundary condition in the Kelvin wave model to be problematic. Similarly, when $W/R_d \gg 1$, the boundary condition for the standing wave model is clearly invalid.

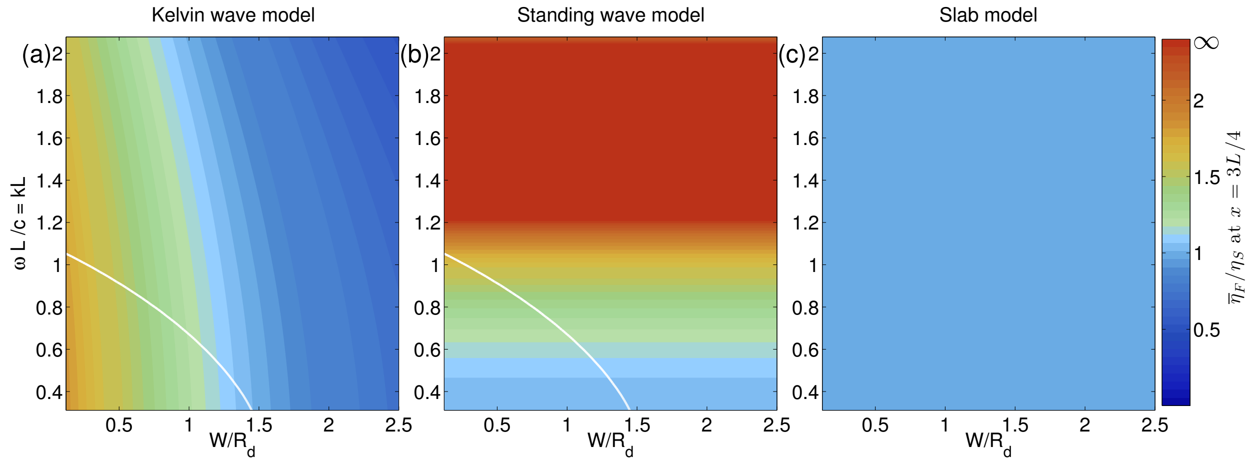

Figure 4-8: Amplitude of interface fluctuations (cross-fjord averaged and normalized by shelf amplitude) at x = 3L/4 for three analytical models. **a.** Kelvin Wave model; **b.** Standing wave model; **c.** Slab model. The white line in **a.** and **b.** indicates where the Kelvin wave solution equals the standing wave solution. The slab model in **c.** has the same amplitude as the standing wave solution at small ω, as expected since the slab model is the limit of the standing wave model as $\omega \rightarrow 0$. Note: the colorbar in panel **b.** is saturated at 2.4; the response goes to infinity at $\omega L/c = \pi/2 \approx 1.6$.

By comparing the cross-fjord averaged solution for the Kelvin wave model (Eq. 4.29 & 4.30), the standing wave model (Eq. 4.9 & Eq. 4.10), and the slab model (Eq. 4.21 & 4.22), one can see that the fjord response has a very different parameter dependence in these different models.

Fig. 4-8 shows the amplitude of pycnocline fluctuations near the fjord head (normalized by the shelf amplitude, $\overline{\eta}_F/\eta_s$) as a function of $\omega L/c$ and W/R_d for all three models. In the slab model, the pycnocline fluctuates uniformly throughout the fjord with the same amplitude as the shelf wave, so $\overline{\eta}_F/\eta_s = 1$, independent of the forcing frequency or fjord width. In the standing wave model, the fjord response is a function of $\omega L/c$, and the fjord amplitude increases with frequency up to the resonant frequency. The Kelvin wave model, however, has the opposite dependence on $\omega L/c$: as the frequency increases, the fjord response decreases. Furthermore, there is also a strong dependence on W/R_d in the Kelvin Wave model, with the fjord response increasing as the fjord width decreases.

This leads to the questions: what is the response of a fjord to shelf waves when $W/R_d \sim \mathcal{O}(1)$, as in the case for many Greenlandic fjords? Assuming these two simple analytical models capture the basic features of the fjord response at $W/R_d \ll 1$ and $W/R_d \gg 1$, respectively, what happens in the transition between these two regimes? And where in parameter space does that transition occur?

4.4 ROMS Results

4.4.1 Control run: Sermilik-like setup and forcing

A description of the ROMS control run will provide a basis for later analysis that compares different runs. In the control run (which has a Sermilik-like fjord of 7 km × 90 km, $W/R_d = 0.8$ and $\omega L/c = 1.0$), the shelf is forced by a periodic along-shore wind with 0.2 N/m^2 amplitude and a 6 day period (Fig. 4-10a). The shelf wind drives heaving in the shelf pycnocline with a 6-day periodicity. Fig. 4-10b shows the pycnocline fluctuations across section S1 on the shelf (location in Fig. 4-9). The amplitude of the shelf pycnocline fluctuations, η_S, is 14 m (28 m from crest to trough) at the coast and decays away from the coast, consistent with an e-folding decay scale of the deformation radius. The shelf interface is well represented by the Kelvin wave expression of: $\eta(x, y, t) = \eta_s e^{-x/R_d} \cos(ky - \omega t + \phi)$ where ω is the wind forcing frequency and ϕ is a constant. There is no phase lag in the cross-shore direction on the shelf.

The fluctuations in the shelf pycnocline propagate into the fjord and drive a modestly amplified heaving in the fjord pycnocline, as shown in Fig. 4-10c & d. Across the lower fjord section, F2, the amplitude of η varies between 16 and 19 m and there is a phase lag of ~20 hours between the east and west sides of the fjord, as predicted by the Kelvin Wave model (Eq. 4.26). At the upper fjord section, F4, the amplitude falls between 25 and 23 m, with only an 8 hour lag between east and west

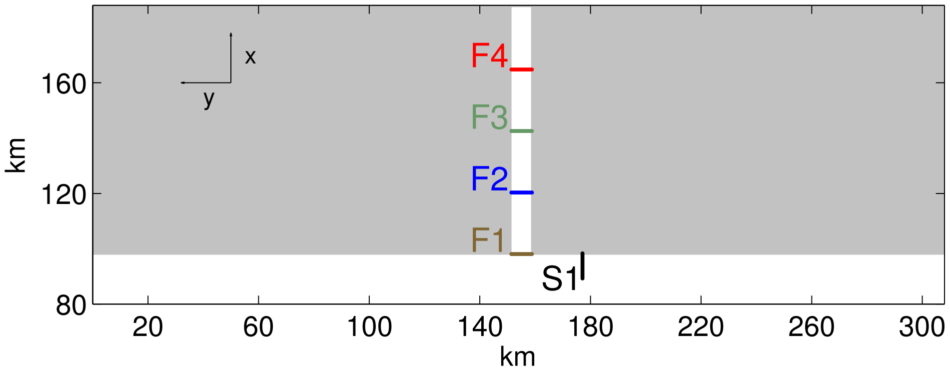

Figure 4-9: A portion of the model domain (for runs of $W = 7$ km; $W/R_d = 0.8$) with fjord and shelf sections indicated. The axes are rotated in a nonconventional way: positive y is along shelf in the direction of wave propagation and x is along-fjord, positive upfjord. Note: this is not the full model domain - only a portion of the shelf region is shown.

– also in agreement with the Kelvin wave model. In general, the phase propagation of the density signal around the fjord is consistent with the Kelvin wave model (and this phase propagation would be absent in the standing wave model). However, the overall amplitude of η is slightly higher than expected from the Kelvin wave model, falling between the predictions of the two analytical models.

Associated with these pycnocline fluctuations is a (primarily) baroclinic velocity field in the along-fjord direction. Fig. 4-11 shows a plan view of upper-layer velocity (at 75 m depth) at nine snapshots over a 6-day period, and Fig. 4-12 shows cross-sections of velocity through F3, at the same times as Fig. 4-11. As the pycnocline lowers, there is, for the most part, inflow in the upper layer and outflow in the lower layer. This flow reverses as the pycnocline rebounds. The velocity decays towards the head of the fjord.

In the cross-fjord direction, lateral shear exists in each layer, and there are lateral reversals in direction at the times of weak velocity. Since the along-fjord velocity is primarily in geostrophic balance, these cross-fjord changes in along-fjord velocity are associated with changes in the cross-fjord pycnocline tilt. While the dominant signal in the pycnocline is vertical heaving, small changes in the cross-fjord slope, on top of the heaving signal, result in lateral shear and occasional cross-fjord reversals in direction.

At the junction between fjord and shelf, the velocity field becomes more complicated (Fig. 4-11) with features resembling jets, eddies, or perhaps Poincare waves that cannot propagate (e.g. Durland and Qiu, 2003)

For comparison with the moored observations, Fig. 4-13a shows a depth versus time plot for a point in the middle of section F2 in the fjord. This is approximately equivalent to the location of the

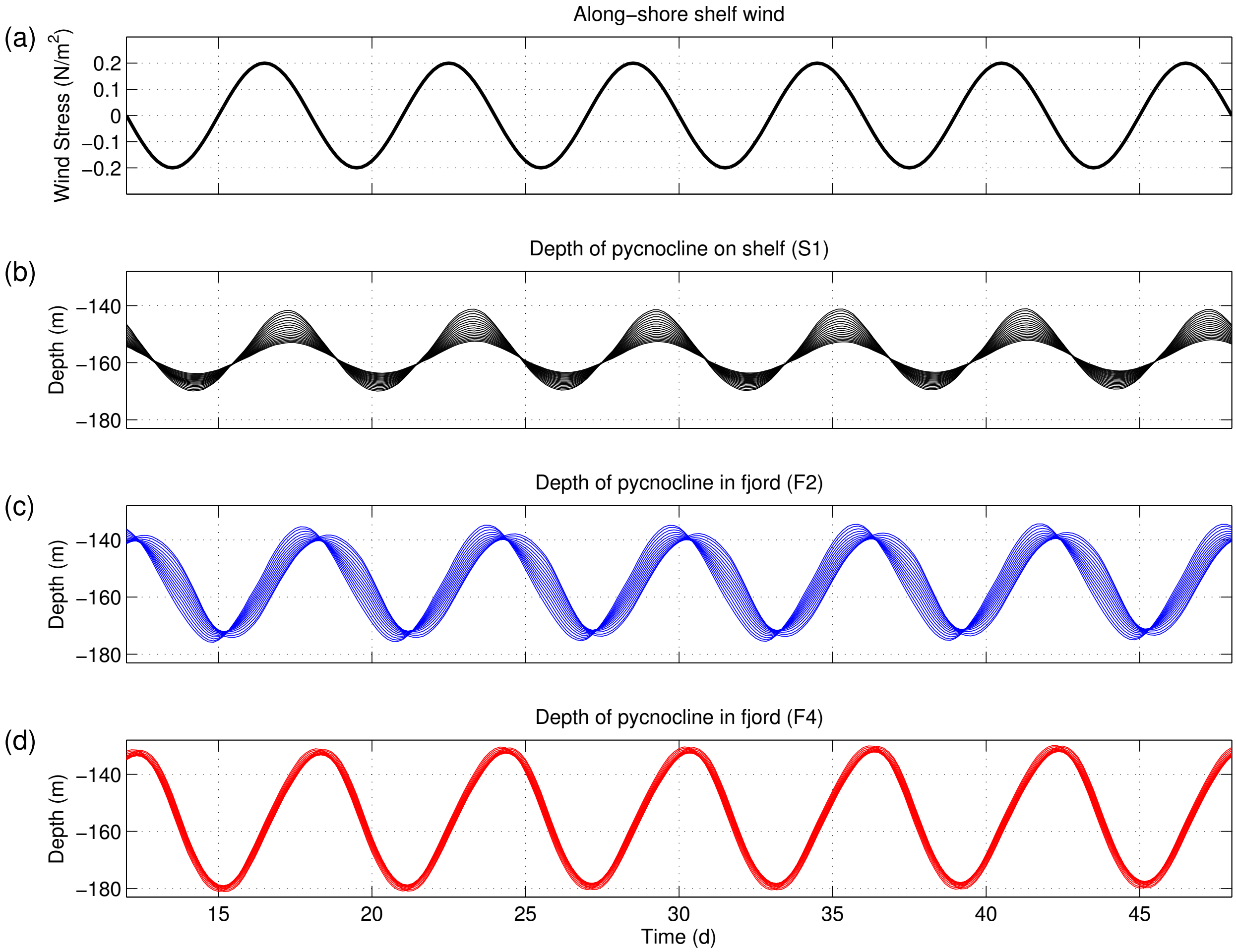

Figure 4-10: Control run: run129. **a.** Along-shore wind, applied to the shelf region of the domain. Positive is to the east and upwelling-favorable. **b.** Depth of the pycnocline (defined as $\sigma = 27$ kg/m^3) on the shelf at 17 points across section S1 (500 m spacing across 8 km). Section locations are shown in Fig. 4-9. **c.** Depth of pycnocline in lower fjord at 14 points across section F2 (every 500 m across 6.5 km section). **d.** Depth of pycnocline in the upper fjord at section F4 (every 500 m across 6.5 km section). Note: full run is 60 days (all simulations were run for 10 forcing periods) but only days 12-48 are shown here.

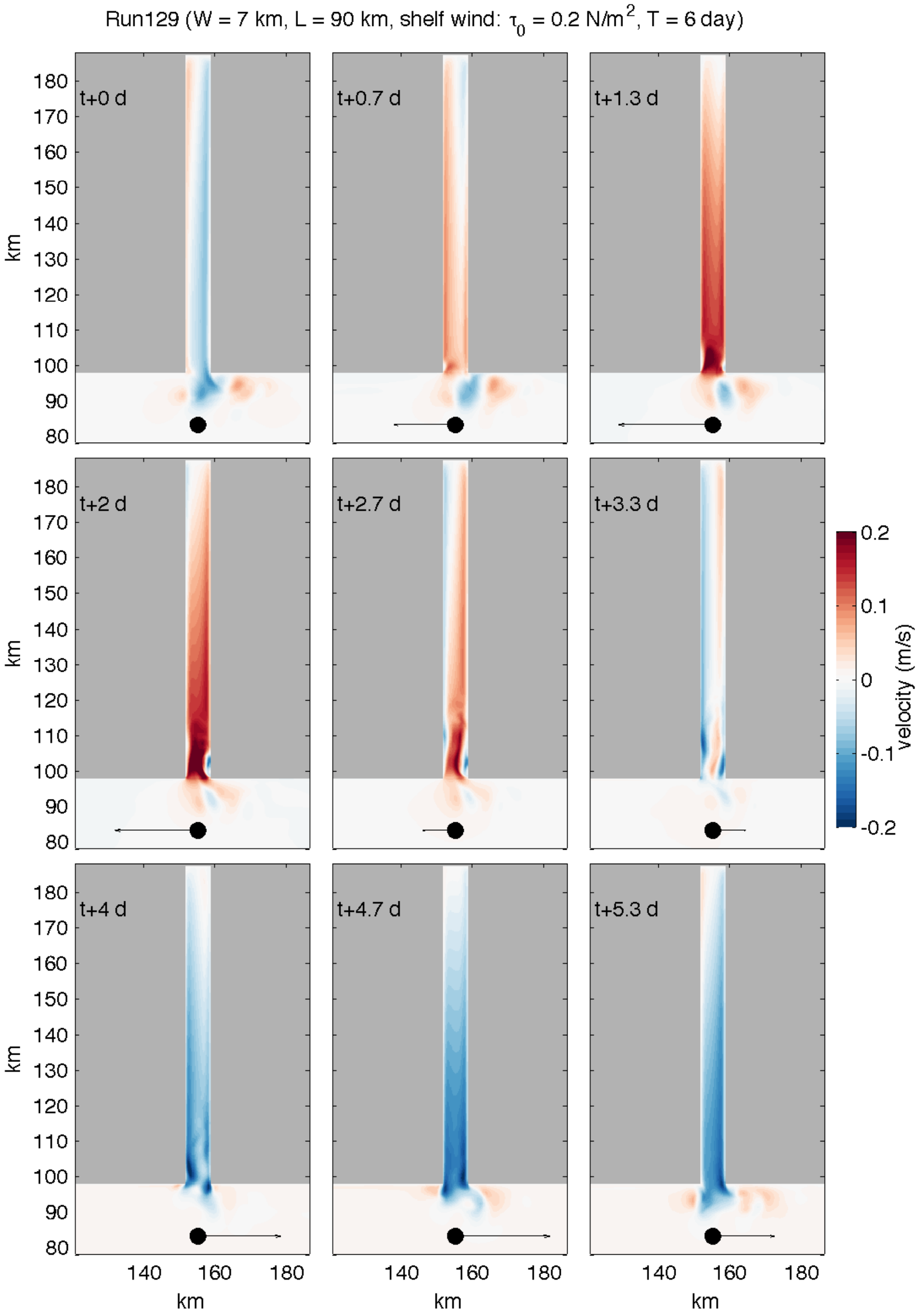

Figure 4-11: [Run129] North/south component of velocity at 75 m depth, i.e. above the pycnocline, for control run at 9 snapshots over a 6-day period. Black arrow and dot on the shelf show the direction shelf wind forcing: the first half of panels have down-welling favorable winds while the second half have upwelling favorable winds. Time in days indicated in the upper left corner of each panel, relative to t = 36 days from the start of a run. Note: the along fjord velocity is the *u* velocity component.

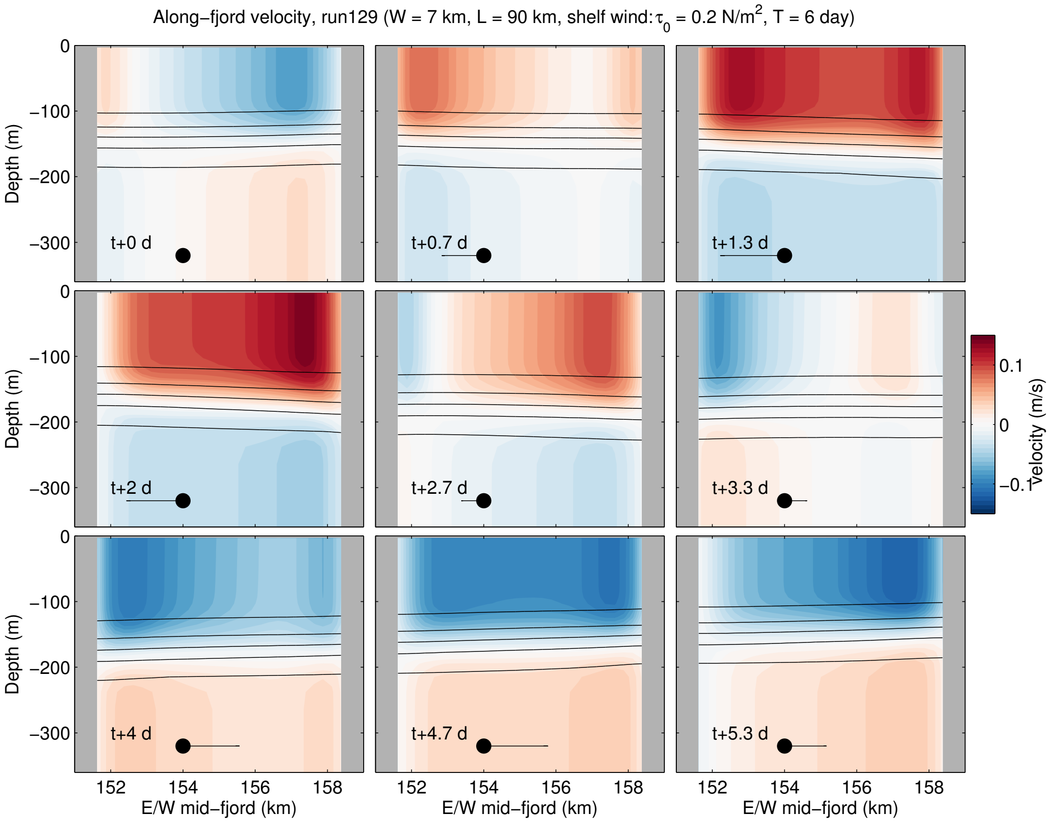

Figure 4-12: [Run129] Along-fjord velocity at fjord cross-section, F3 (see map in Fig. 4-9), with positive velocity into the fjord. Dot shows along-shore wind direction on the shelf. Note: the y-axis cuts off at 350 m but the bottom is at 600 m.

mid-fjord moorings described in Chapters 2 & 3 and shown in Fig. 4-13b & c. Although the modeled fjord is only forced at one frequency while the real fjord is subjected to a broad spectrum of forcing frequencies, the basic features of the observations are replicated in this model simulation: a two-layer flow with peak energy on synoptic timescales; vertical heaving of the pycnocline, with velocity and density approximately in quadrature. Both the model and upper fjord mooring (not shown here) show that the velocities decays towards the head of the fjord and that the pycnocline fluctuations are mildly amplified. In the observations, the fjord density and velocities are significantly coherent with shelf density at 2-10 day periods, with a phase relationship confirming the origin of these signals on the shelf.

In ROMS, when the fjord width is changed from 7 km to 14 km (W/R_d changed from 0.8 to 1.6), the cross-fjord variability increases. Appendix 4.C shows plan view and cross-sections of velocity where the velocity and interface fluctuations are more markedly concentrated on the edges of the fjord. For the same forcing amplitude and period, the amplitude of the fjord response, both in velocity and the pycnocline, is smaller for the wider fjord.

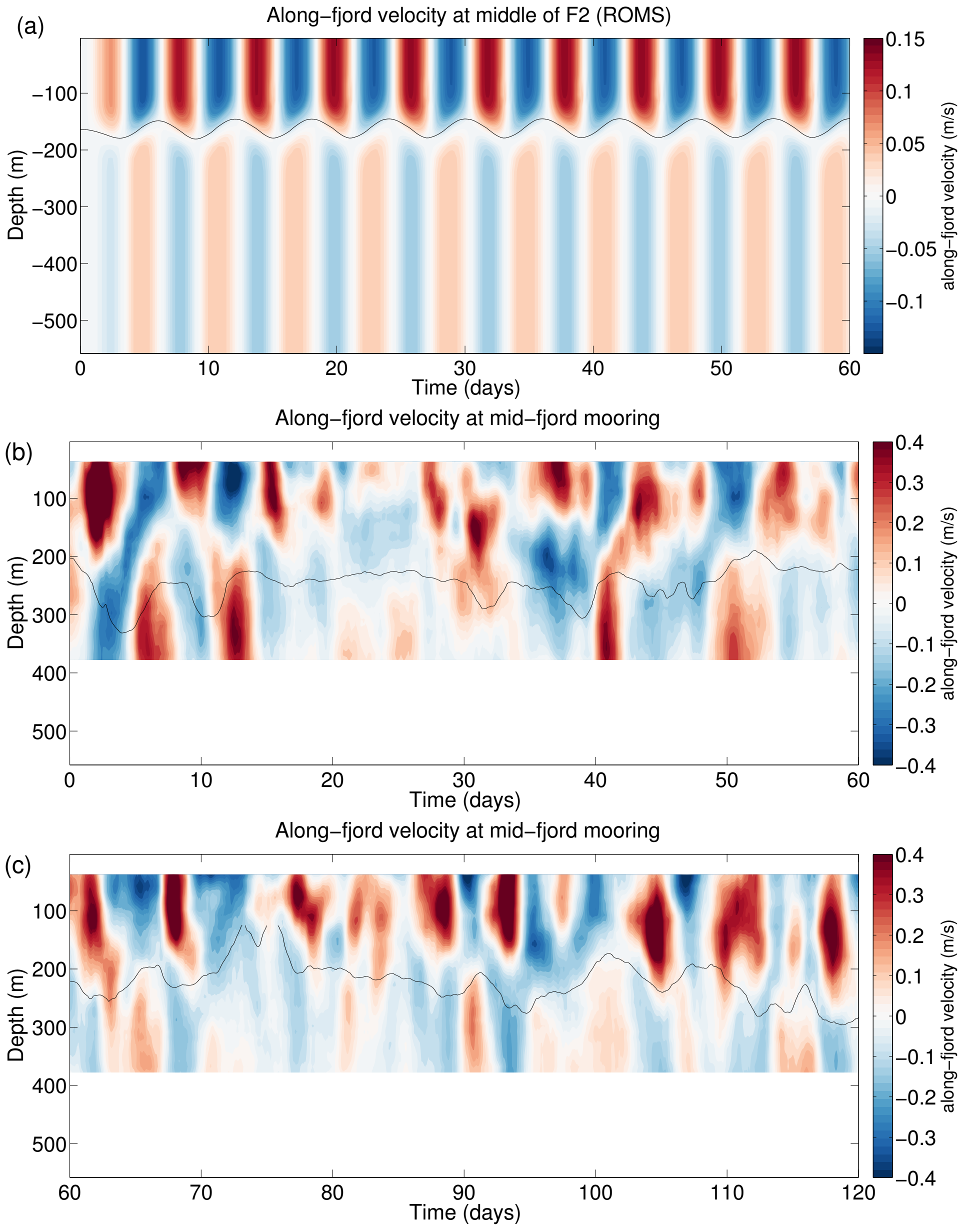

Figure 4-13: **a.** Along-fjord velocity in ROMS at a station in the middle of fjord section F2 (location in Fig. 4-9) as a function of depth versus time. Black contour is the isopycnal of $\sigma = 27$ kg/m^3. **b & c.** Along-fjord velocity from mid-fjord mooring (MM, described in Chapters 3 and 4) with isopycnal of $\sigma = 27$ kg/m^3 for two consecutive 60 day periods (time in days relative to Oct 12, 2011). Depth and time axes are the same scale in all three plots, but colorbars are different.

4.4.2 Fjord response as function of $\omega L/c$ and W/R_d

Set A of ROMS runs are used to test the dependence of the fjord pycnocline and velocity response on W/R_d and $\omega L/c$. Fig. 4-14 shows the amplitude of the fjord pycnocline (cross-sectionally averaged, $\overline{\eta}_F$) in the upper fjord as a function of forcing period for all runs in Set A. These ROMS runs (in dots) are compared with the expected response from the Kelvin Wave model (Eq. 4.29, dashed color lines) and the standing wave model (Eq. 4.9, solid grey line).

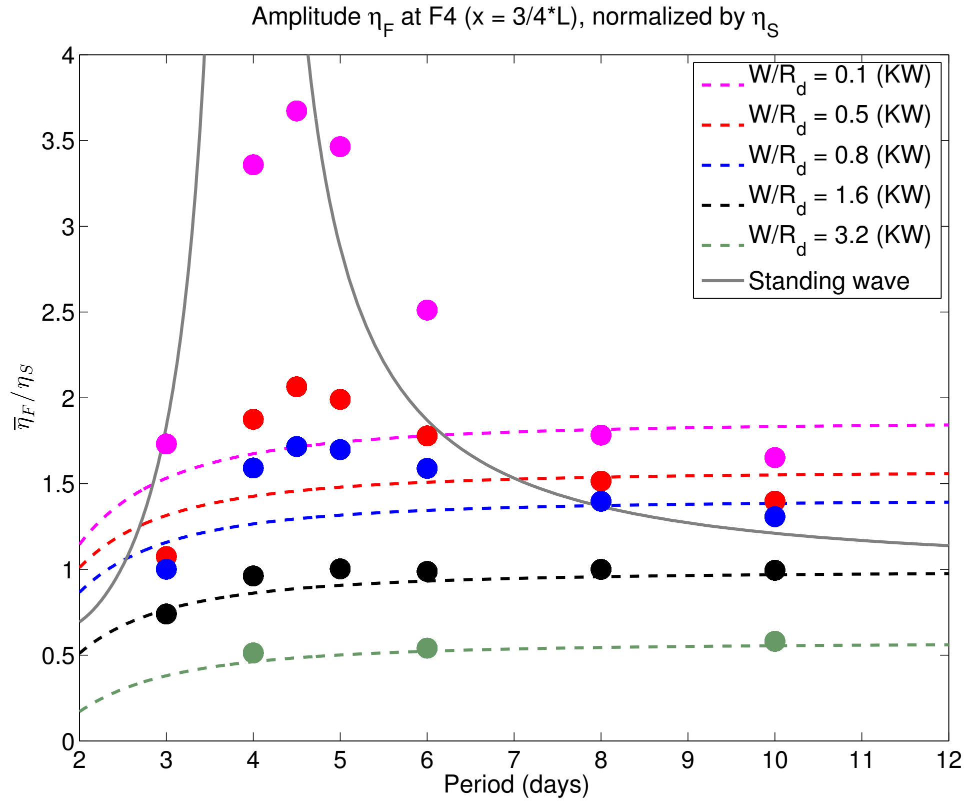

Figure 4-14: Mean amplitude of pycnocline heaving at $x = \frac{3}{4}L$ (section F4), normalized by the shelf pycnocline amplitude, as a function of forcing period. The colored dashed lines give the predicted solution from the Kelvin wave model (from Eq. 4.29) for the various ROMS values of W/R_d, and the solid grey line gives the solution from the standing wave model (from Eq. 4.9). Note that the standing wave solution does not vary with W/R_d.

In the relatively wide fjords, with W/R_d of 1.6 and 3.3, the ROMS runs match the corresponding Kelvin wave prediction (black/green in Fig. 4-14). For these runs, there is a weak dependence on the forcing period and the amplitude increases with decreased fjord width. For the narrowest fjord runs of $W/R_d = 0.1$ (magenta), the fjord roughly follows the standing wave prediction: the response varies strongly with the forcing frequency and becomes large (3.5 times the shelf amplitude) near the resonant frequency. Thus, the two analytical models capture the basic features of the cross-sectionally averaged behavior in the numerical simulations for the two limits $W/R_d \lesssim 0.1$ and $W/R_d \gtrsim 1.5$

Most interesting are the runs with W/R_d equal to 0.5 and 0.8 (red/blue in Fig. 4-14). They appear to fall in the transition between regimes: the dots for ROMS runs lie between the dashed lines for the Kelvin wave model and the solid line for the standing wave model. There is a modest amplification near the resonant frequency, but it is far smaller than would be expected for the full standing wave solution. Instead, the response falls closer to the Kelvin Wave solution, with some deviation. This is worth emphasizing: even when the fjord width is half the deformation radius, the cross-fjord structure cannot be neglected and there is not a large amplification at the resonant frequency. Put another way, the upstream forcing from the shelf, $\eta_s e^{i\omega t}$, does not exert a strong control on the fjord's reflected/outgoing wave.

At large forcing periods (i.e. small values of $\omega L/c = kL$), the fjord response plateaus. This is expected from examining Eq. 4.29 for $\overline{\eta}$ in the Kelvin wave model. As kL approaches zero, $\cos(k(L-x)) \rightarrow 1$, so that:

$$\overline{\eta}(x,t) \rightarrow 2\frac{R_d}{W}\left(1 - e^{-W/R_d}\right)\eta_0 \cos(\omega t)$$

For small $\omega L/c$ (i.e. low forcing frequencies and/or short fjords), the amplitude of the fjord response is only a function of W/R_d, increasing with narrower fjords.

A similar picture emerges when the mean velocity field is examined for Set A of ROMS simulations. Fig. 4-15 plots the cross-sectionally averaged amplitude of velocity at the mouth as a function of forcing period. The wide fjord simulations (green and black) match the Kelvin wave model, while narrow fjord (magenta) simulations follow the standing wave patterns. The runs with $W/R_d = 0.5$ and 0.8 fall in between, with some amplification near the resonant frequency.

In the limit of low frequency forcing, the fjord velocity approaches zero in all models. This can be seen in Eq. 4.30 for $\overline{U}$: as $\omega L/c \rightarrow 0$,

$$\overline{U}(x,t) \rightarrow -2\frac{R_d}{W}(1 - e^{-W/R_d})\eta_0 \omega L \sin(\omega t) \tag{4.32}$$

so that the velocity field approaches zero.

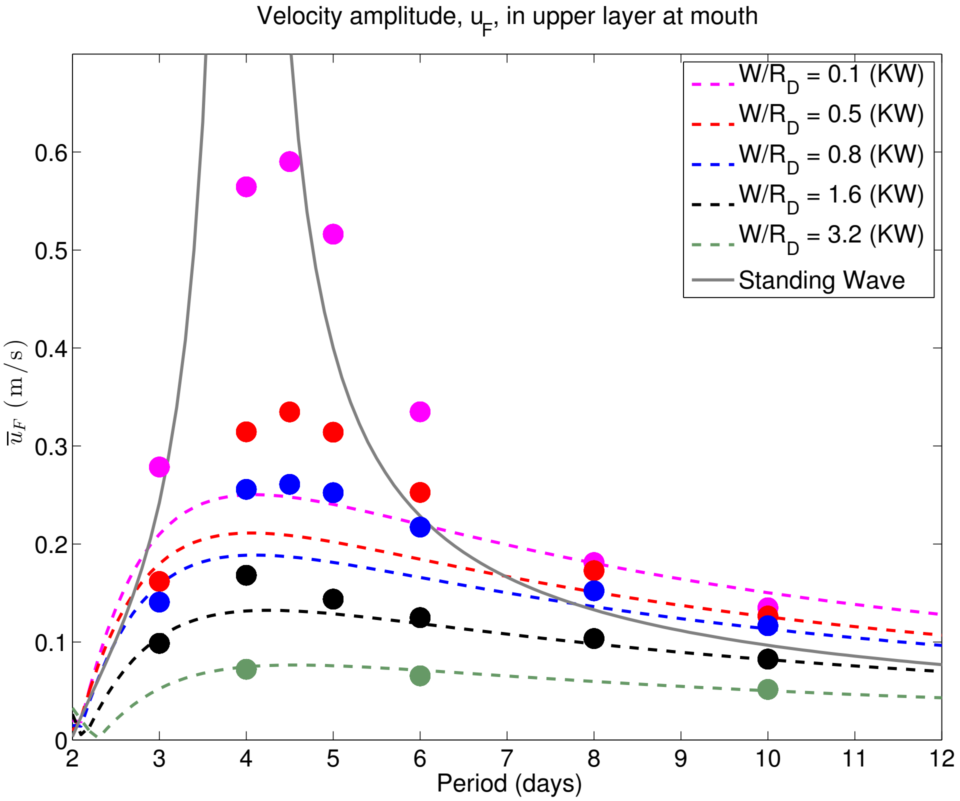

Figure 4-15: Mean amplitude of the upper layer velocity at the mouth (x=0) as a function of forcing period. The colored dashed lines give the predicted solution from the Kelvin wave model (from Eq. 4.30) for the model run values of W/R_d, and the solid grey line gives the solution from the standing wave model (from Eq. 4.10). The velocities have been normalized by $\frac{20\ m}{\eta_S}$ to remove variability from slightly different forcing amplitudes (Appendix 4.A & 4.B).

4.4.2.1 Best fit to numerical simulations

It has been shown that neither analytical model can fully describe the shelf-forced flows as a fjord transitions through the $W/R_d \sim \mathcal{O}(1)$ regime. However, it is still worth examining how well each can do at predicting the volume flux between fjord and shelf in ROMS, and by extension perhaps in a real fjord. To examine the relative accuracy of the analytical models, Fig. 4-16 compares the mean velocity at the mouth in ROMS as a function of the predicted mean velocity from the Kelvin wave model, the standing wave model and the slab model, across a range fjord widths from $W/R_d =$ 0.5 to 3.2 (but excluding the unrealistic $W/R_d = 0.1$). One can see that the Kelvin wave model does far better than the 2-D models at describing the volume flux between fjord and shelf in this parameter range. The R-squared value for ROMS versus the Kelvin wave model is 0.8, compared to 0.03 for ROMS versus standing wave model and 0.05 for ROMS versus the slab model.

For ROMS runs with the largest velocities, the Kelvin wave model under-predicts the fjord response. These runs correspond forcing at 4 to 6 day periods, the local maximum in blue/red dots of Fig. 4-15, where one can see that the ROMS runs are amplified near the resonant frequency (above the local peak predicted by the Kelvin wave model and pulled towards the resonant peak of the standing wave model). This deviation is relatively small compared to the spread in the other analytical model comparisons. Thus, in the parameter space of $W/R_d =$ to 0.5 to 3.2 and $\omega L/c =$ 0.5 to 2, the Kelvin wave model can broadly capture the nature of the fjord response, both in its spatial structure throughout the fjord and in the mean properties. However, the Kelvin wave model cannot capture the full frequency-dependent response.

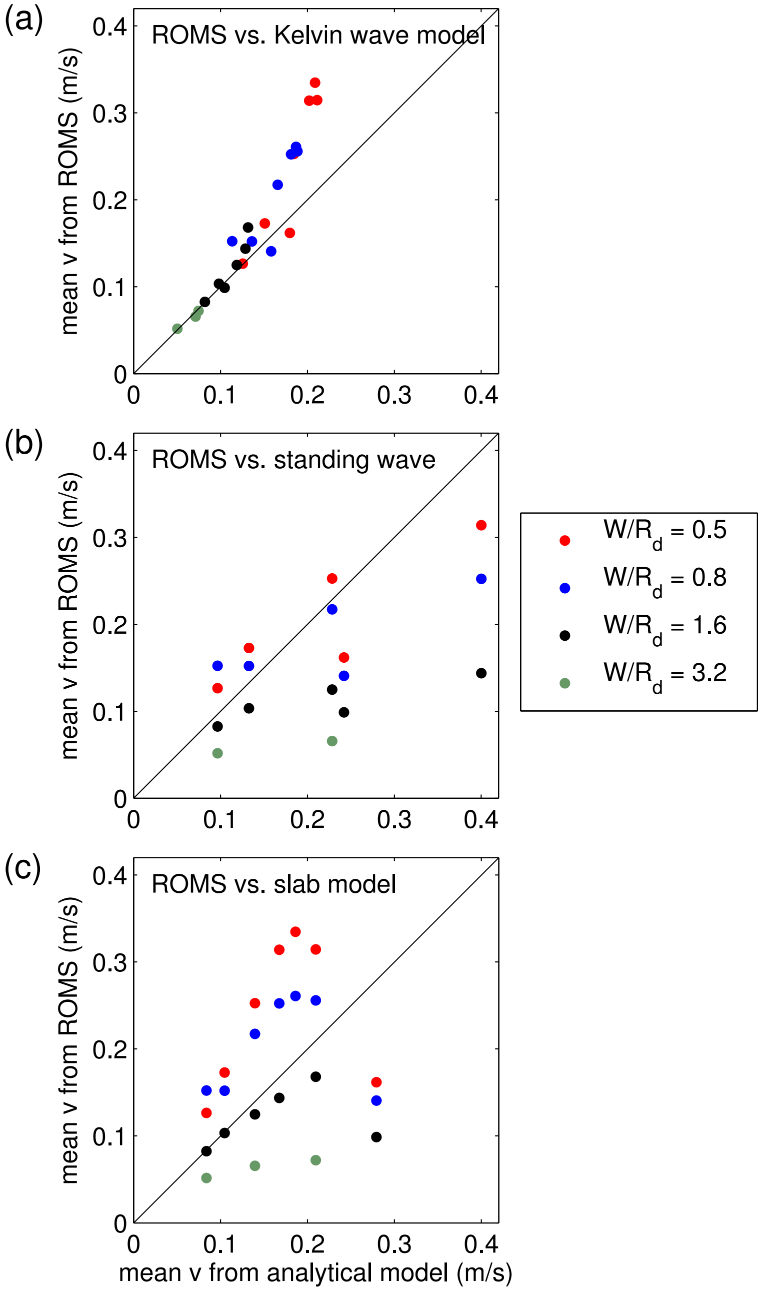

Figure 4-16: Comparison of the cross-fjord average velocity amplitude at the mouth from: **a.** ROMS. vs. Kelvin wave model, Eq. 4.30, **b.** ROMS vs. standing wave model, Eq. 4.10, and **c.** ROMS vs. slab model, Eq. 4.22. Black line at x=y in all. In panel **b.**, several points fall outside the plot domain to the right, where the standing wave model overpredicts ROMS by more than a factor of 2.

4.4.3 A metric for the impact on the fjord: excursion lengthscale

In considering the overall impact of these shelf-forced flows on the fjord, the amplitude of the velocity or pycnocline fluctuations are somewhat limited metrics, since they do not reflect the timescale of the fluctuation. The excursion length-scale better captures the integrated magnitude of the oscillatory flow and is defined as the velocity integrated over half a period:

$$L_e = \frac{T(\frac{2u_F}{\pi})}{2} = \frac{Tu_F}{\pi} \tag{4.33}$$

where u_F is the velocity amplitude, and T is the period. Physically, it is the approximate distance that a water parcel would travel over half of a period. The excursion length-scale at the mouth indicates approximately how far shelf water would travel into the fjord on each pulse; or, put another way, it indicates the region of the fjord where water exits the fjord over each cycle. If the water that exits the fjord is swept away (e.g. by a coastal current such as the East Greenland Coastal Current) and does not reenter the fjord with the return flow, the fjord region within an excursion length-scale of the mouth would be entirely renewed over each forcing period.

While the excursion length-scale is not a direct measure of the net exchange between fjord and shelf, it is likely to scale with the renewal rate of fjord waters. For example, the tidal excursion relative to the length-scales of estuaries has been shown to indicate the strength of tidal dispersion (e.g. Geyer and Signell, 1992).

The excursion length-scale at the mouth, normalized by the fjord length, is explored in Fig. 4-17 for set A of ROMS simulations. As with the velocity and interface response, the ROMS simulations match the analytical models for large and small values of W/R_d but fall in a transition regime for $W/R_d = 0.5$ and 0.8. For the Kelvin wave model, the ratio L_e/L at $x = 0$ is:

$$L_e/L = 4\frac{R_d}{W}(1 - e^{-W/R_d})\frac{\sin(kL)}{kL}\frac{\eta_S}{h_1} \tag{4.34}$$

As can be seen in Fig. 4-17, L_e/L increases with forcing period until the response plateaus at long forcing periods, i.e. small values of kL, to:

$$L_e/L \approx 4\frac{R_d}{W}(1 - e^{-W/R_d})\frac{\eta_S}{h_1} \tag{4.35}$$

One can see that the excursion length-scale increases as the shelf wave amplitude becomes large relative to the layer thickness (η_S/h_1) and as the fjord becomes narrower. For a Sermilik-like fjord, the fraction of the fjord within L_{ex} of the mouth is about twice the ratio of the shelf amplitude to the layer thickness: $L_{ex}/L \approx 2.5\frac{\eta_S}{h_1}$. Thus, η_S of 30 m (typical for Sermilik Fjord) would result in $L_{ex}/L = 0.5$, i.e. shelf water would make it half way up the fjord with every pulse.

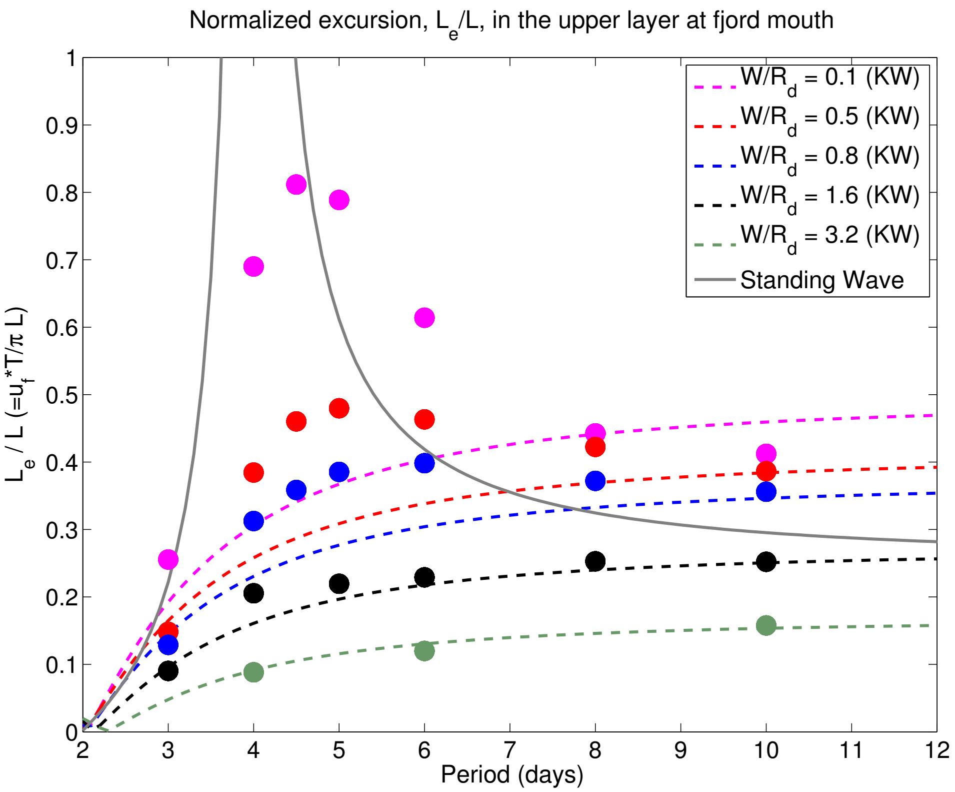

Figure 4-17: Mean excursion length-scale at the mouth (x=0) normalized by L, as a function of forcing period. The colored dashed lines give the predicted solution from the Kelvin wave model (from Eq. 4.34) for the model run values of W/R_d, and the solid grey line gives the solution from the standing wave model (from Eq. 4.10). Note that the standing wave model does not vary with W/R_d.

For wide fjords with $W/R_d \gtrsim 1.5$, the effectiveness of shelf forcing is diminished for high frequency forcing, i.e forcing periods less than 5 days or $\omega L/c > 1.2$, while the the response is almost equal across lower frequency forcing ($\omega L/c > 1.2$). When $W/R_d \approx 0.5 - 1.0$, the fjord response has a local maximum near the resonant frequency, with the amplitude going to zero at higher forcing frequencies and plateauing at lower forcing frequencies. This peak appears to be shifted to slightly longer periods than the resonant frequency (i.e at $T = 5$ days in Fig. 4-17 versus $T_{res} = 4.1$ d). Across all frequencies, the magnitude of the fjord response increases for narrower fjords.

Overall, the fjord response can be summarized in terms of the three non-dimensional parameters, W/R_d, $\omega L/c$ and η_S/h_1, as shown in Fig. 4-18. There is a surprisingly weak dependence on the forcing frequency, except at large values of $\omega L/c$ (i.e. high frequency forcing). The fjord response is strongly dependent on W/R_d and linear with η_S/h_1. It should be emphasized the L_e/L ratios are large, in the range of 0.2 to 0.6 for the parameter values that are expected around Sermilik and other Greenlandic fjords. If the excursion lengthscale at the mouth is a decent proxy for exchange between fjord and shelf, these results suggest that a significant fraction of the fjord is flushed over each cycle of shelf forcing.

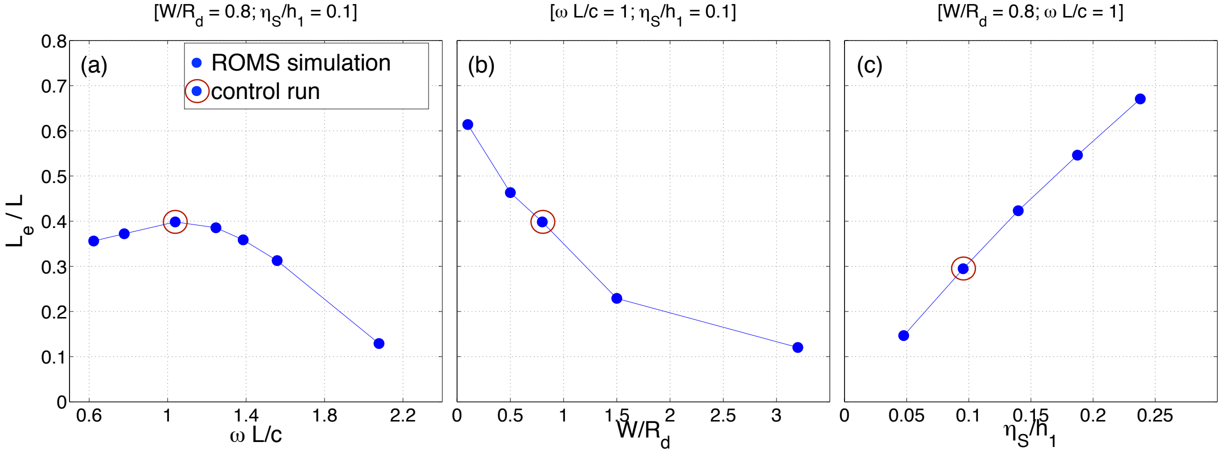

Figure 4-18: Mean excursion at the mouth, normalized by L, as a function of **(a)** $\omega L/c$, **(b)** W/R_d, and **(c)** η_S/h_1. In each panel, the other two parameters are held constant at the control run values of $\omega L/c = 1$, $W/R_d = 0.8$ and $\eta_S/h_1 = 0.1$. The control run is shown in each panel with a red circle.

4.4.4 Quantifying volume flux

In the two preceeding sections, cross-fjord averages of η, u and L_{ex} have been examined, glossing over the cross-fjord lateral structure. To quantify the magnitude of this lateral structure, we compare the integrated velocity in the upper/lower layer (Q_{up}/Q_{low}) with the integrated velocity that is inflow/outflowing (Q_{in}/Q_{out}). This distinction might be important when thinking about the renewal of waters in the fjords. If the water that exits the fjord is swept away (e.g. by a coastal current) so that it does not come back into the fjord with the next pulse, the mean renewal would be a function of Q_{out}, the outflowing volume flux. If there are no cross-fjord reversals in direction, Q_{out} would also equal the absolute value of the volume flux in either upper or lower layer, Q_{up} or Q_{low}. If there is sufficient lateral structure in the shelf-forced flows, however, the magnitude of the volume flux above/below the pycnocline might diverge significantly from the volume flux in either direction.

These two different types of volume fluxes are compared in Fig. 4-19. The dashed lines show the volume flux in the upper and lower layer, defined as above and below $\sigma = 27$ kg/m^3, respectively, which are proportional to the cross-sectionally averaged velocities presented in the proceeding sections ($Q_{up} = \overline{u}A_{up}$ where A_{up} is the cross-sectional area of the upper layer). The solid lines show the volume flux in either the inflowing or outflowing direction: the inflowing volume flux is the velocity integrated over the portion of the cross-sectional area that has positive velocity at any given moment. Since these flows are almost entirely baroclinic, $Q_{in} = -Q_{out}$ and $Q_{up} = -Q_{low}$ at all times.

These different volume fluxes are equal during times of peak flow; for example, the inflowing volume flux equals the upper layer volume flux during peak inflow. But, when the upper/lower layer volume flux crosses through zero, there is non-zero inflow/outflow within each layer. This can be seen by examining the cross-fjord velocity structure in Fig. 4-12 or Fig. 4-25.

For the control run (run127, $W = 7$ km) shown in Fig. 4-19a&b, the difference in average volume flux of upper/lower versus in/out is small: the average (absolute value) upper layer volume flux is 6.0×10^4 m^3 s^{-1}, compared to $6.3\ \times10^4$ m^3 s^{-1} for the average inflowing volume flux. The difference becomes more notable for a wider fjord of 14 km, shown in Fig. 4-19c&d. For this wider run (still with 6 day forcing), the average upper/lower layer volume is 20% smaller than the average inflow/outflowing volume flux .

The importance of the lateral shear is explored across the runs in Set A to address the question: when is the upper/lower layer volume flux a good representation for the volume exchanged between fjord and shelf and when does that break down? In Fig. 4-20, the ratio of mean upper layer volume flux to mean inflowing volume flux ($|Q_{up}|/Q_{in}$) is plotted as a function of fjord width. For narrow fjords, these quantities are approximately equal and the role of lateral shear in the total volume flux is minimal. However, for fjords with $W/R_d > 1.5$, the lateral shear becomes important and the layer volume flux can be 10 to 55% less than the total inflowing flux. This ratio of volume fluxes is also strongly dependent on forcing frequencies; lower frequency shelf forcing results in stronger lateral shear and a larger difference between layer volume flux and directional volume flux. These differences in the structure of the volume flux between shelf and fjord (for wide fjords or low forcing frequencies) could be important for eventually assessing the overall renewal rate for fjord waters.

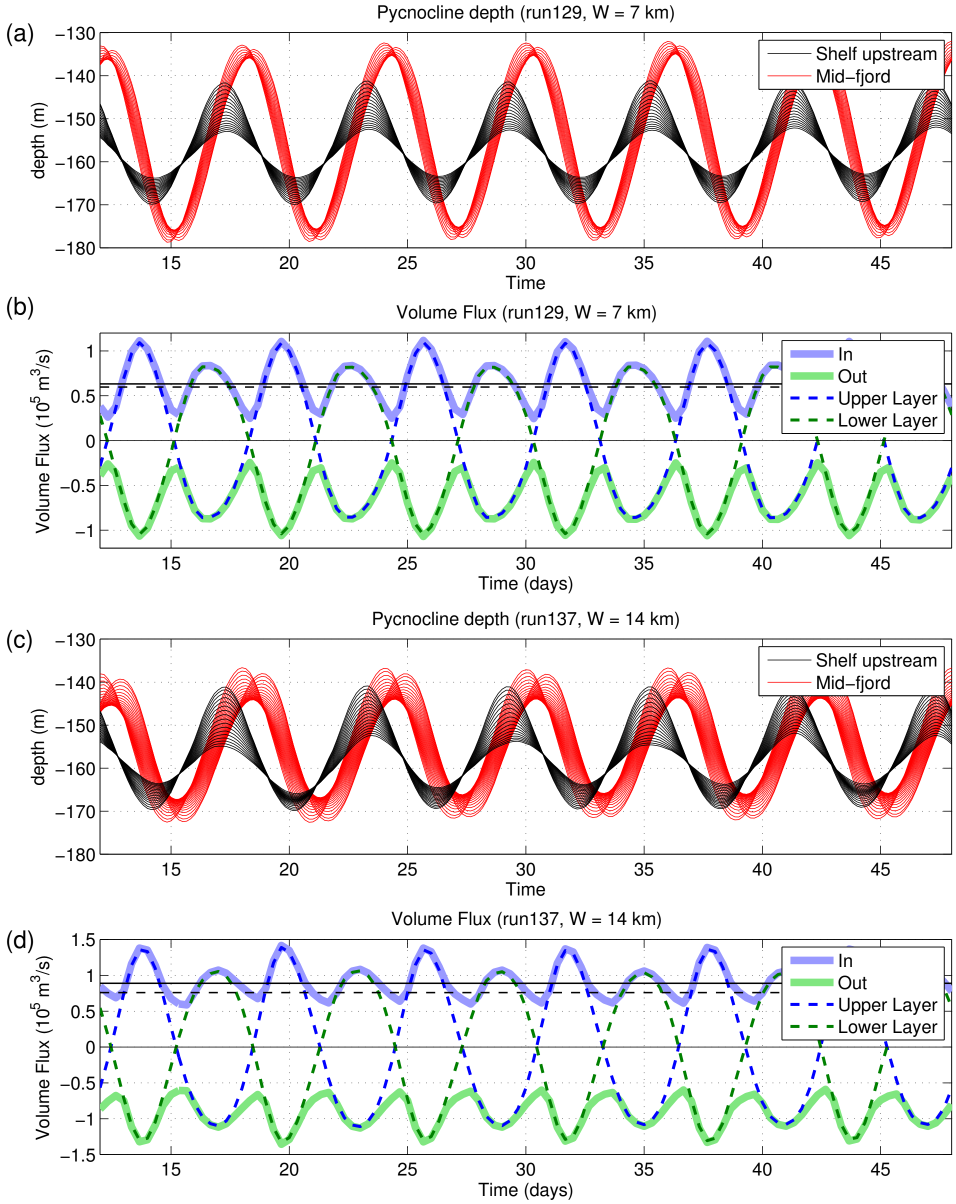

Figure 4-19: Run129 [$W = 7$ km, $T = 6$ d; $W/R_d = 0.8$, $\omega L/c = 1$] is shown in **a** and **b**; Run137 [$W = 14$ km, $T = 6$ d; $W/R_d = 1.6$, $\omega L/c = 1$] is shown **c** and **d**. **a.** and **c.**: Pycnocline fluctuations on shelf (section S1) and mid-fjord (section F3). **b.** and **d.**: Volume fluxes at mid-fjord (section F3). Dashed lines are volume flux in upper and lower layers, defined as above and below $\sigma = 27$ kg/m^3. Solid lines: volume flux in outflowing/inflowing direction (i.e. integrated velocity over the cross-sectional area that has negative/positive velocities). Horizontal dashed line marks the mean absolute value of the upper layer volume flux; horizontal solid line marks the mean inflowing volume flux.

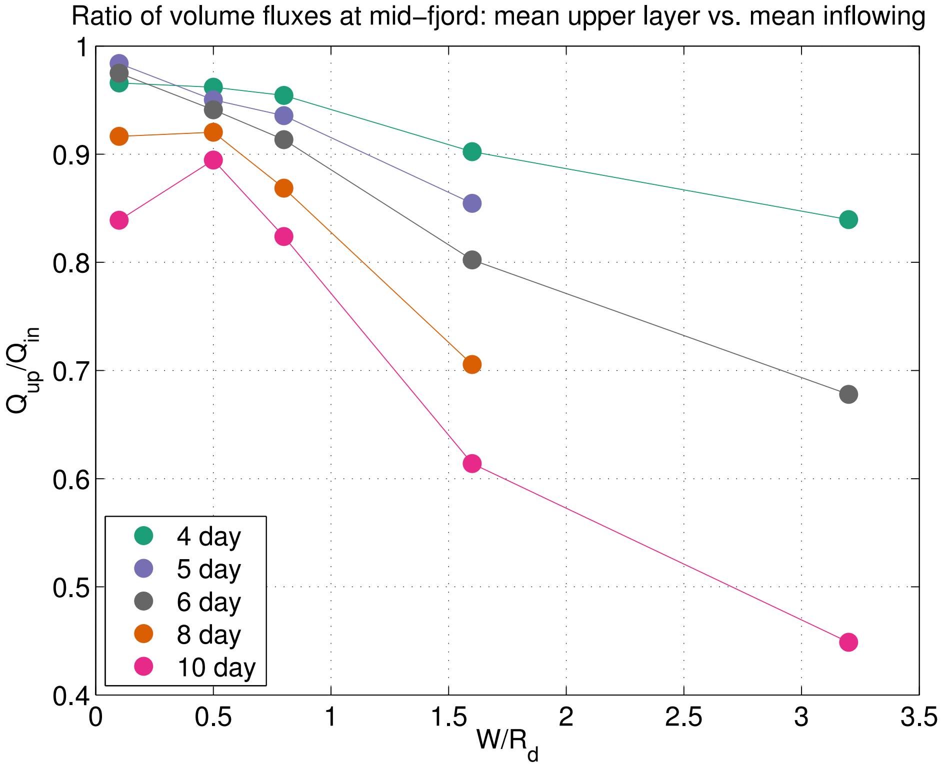

Figure 4-20: Ratio of mean upper layer volume flux (Q_{up}) to mean inflowing volume flux (Q_{in}) as a function of W/R_d for ROMS runs in set A. Colors indicate the forcing period.

4.4.5 Shelf versus local forcing

Having explored the shelf forcing alone, the relative magnitude of shelf forcing versus local wind forcing in fjord/shelf exchange is now examined. For a given fjord, when will shelf forcing dominate and when will local wind forcing dominate? To start, the standing wave model with both shelf and local wind forcing can provide a possible scaling for the relative importance of these two modes of circulation. From Eq. 4.14, the ratio of the local wind-driven velocity to shelf driven velocity is:

$$\frac{U_{\tau_w}}{U_s} = \frac{\tau_f}{\rho c^2 k \eta_S} \frac{\cos(kx) - \cos(kL)}{\sin(k(L-x))} \tag{4.36}$$

At the mouth ($x = 0$), this becomes:

$$\frac{U_{\tau_w}}{U_s} = \frac{\tau_f}{\rho c^2 k \eta_S} \frac{1 - \cos(kL)}{\sin(kL)} \tag{4.37}$$

If we assume small kL, this reduces to:

$$\frac{U_{\tau_w}}{U_s} \approx \frac{\tau_f L}{2\rho c^2 \eta_S} = R_W \tag{4.38}$$

by using the Taylor expansions of $\cos(kL) \approx 1 - (kL)^2/2$ and $\sin(kL) \approx kL$. This non-dimensional number, $R_W = \frac{\tau_f L}{2\rho c^2 \eta_S}$, reflects the relative magnitude of shelf versus local forcing: when $R_W < 1$, shelf forcing is expected to dominate; when $R_W > 1$, local wind forcing should be more important. Physically, R_W can be viewed as the ratio of the wind-driven setup to the amplitude of shelf heaving. If wind setup results in a pressure gradient that balances wind stress, $c^2 \frac{\partial \eta}{\partial x} \approx \tau/\rho$, then the setup, if linear along the fjord length, is: $\Delta\eta_\tau = \tau L/2c^2\rho$. Thus, R_W is the ratio of the wind-driven setup to the shelf wave amplitude: $R_W = \Delta\eta_\tau/\eta_S$.

The non-dimensional number R_W, which compares local wind to shelf forcing, is somewhat analogous to the estuarine Wedderburn number, the ratio of local wind forcing to estuarine gravitational circulation:

$$W_e = \frac{\tau L}{(\Delta_H \rho) g h_1^2} \tag{4.39}$$

where $\Delta_H \rho$ is the horizontal density gradient (e.g. Geyer, 1997; Sutherland et al., 2014b; Inall et al., 2015). Note that this estuarine Wedderburn number is different than the original Wedderburn number, which is inverted and related to the vertical density stratification as opposed to the horizontal density gradient: $W_o = \frac{g' h_1^2 \rho L}{\tau h_1}$ (e.g. Spigel and Imberger, 1980; Monismith, 1986). This new non-dimensional number, R_W, is also related to the original Wedderburn number by $R_W = \frac{h_1}{\eta_0} W_o^{-1}$.

It should be noted that R_W in Eq. 4.38 was derived by assuming that W/R_d and kL are both small. Eq. 4.37 is a more complete (but also more opaque) version of the ratio that does not rely on kL being small. It is less obvious, however, how the ratio would be modified as W/R_d increases.

The applicability of this non-dimensional number is tested with Set B of ROMS runs. With the geometry, stratification, and forcing frequency held constant, the runs are either forced by (a) periodic along-fjord winds over the fjord only, with a variety of wind magnitudes or (b) periodic along-shore winds on the shelf with a variety of shelf wind magnitudes. The ratio of locally wind-forced volume flux to shelf-forced volume flux is plotted as a function of R_W in Fig. 4-21. The non-dimension number R_W does remarkably well at predicting the relative amplitude of shelf versus local forcing for these sets of runs. Thus, R_W might be a valuable metric for predicting the relative importance of these two forcing mechanisms in fjords around Greenland. In general, the relative strength of wind forcing is proportional to the fjord length (fetch) and inversely proportional to c^2 (stratification and upper layer thickness).

For the geometry and stratification in Sermilik ($L = 90$ km, $c = 1.1$ m/s), R_W and the ROMS simulations suggest that shelf heaving of $\eta_S = 20$ m is equivalent to local wind of $\tau_f = 0.5$ N/m^2 (or $\eta_S = 10$ m is equivalent to $\tau_f = 0.25$, etc).

4.5 Discussion

4.5.1 Comparing results with previous fjord studies

Our results suggest that the cross-fjord averaged expressions from the Kelvin wave model are relatively good approximations for fjords with $W/R_d \gtrsim \mathcal{O}(1)$. For the excursion length-scale, volume flux and upper layer velocity, these are:

$$\overline{L_e}/L = 4\frac{R_d}{W}(1 - e^{-W/R_d})\frac{\eta_S}{h_1}\frac{\sin(kL)}{kL} \tag{4.40}$$

$$\overline{Q}(x,t) = 2cR_d(1 - e^{-W/R_d})\eta_S \sin(kL) \tag{4.41}$$

$$\overline{u}_1(x,t) = 2\frac{c}{h_1}\frac{R_d}{W}(1 - e^{-W/R_d})\eta_S \sin(kL) \tag{4.42}$$

when cross-fjord averaged at the mouth. Thus the fjord response is dependent on both W/R_d and kL ($= \omega L/c$). Generally, the fjord response increases for narrower fjords and lower forcing

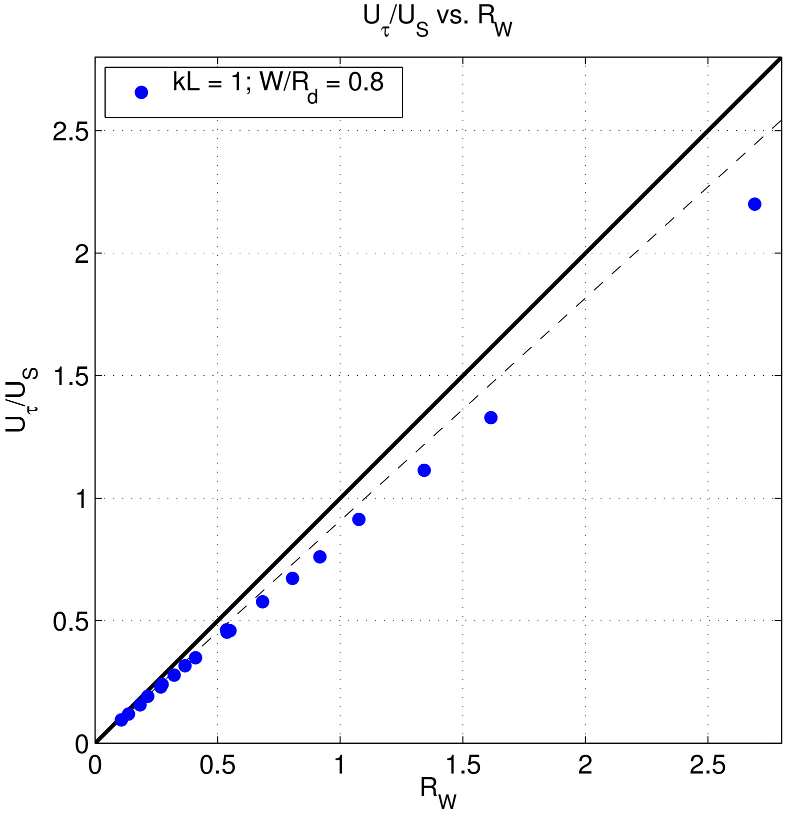

Figure 4-21: The relative magnitude of local wind versus shelf forcing as a function of $R_W = \frac{\tau L}{2\rho c^2 \eta_S}$ (Eq. 4.38) for Set B of ROMS simulations [$W/R_d = 0.8$; $\omega L/c = 1$ for all runs]. Each point is derived from a pair of runs: one with local wind forcing and one with shelf forcing. The y-axis is the ratio of mean velocities near the mouth (at F2) for the pair of runs. The value of R_W for each pair is calculated from τ in the local wind forced run and η_S in the shelf forced run. All possible combinations of run pairs in Set B are plotted here. The solid black line shows the prediction: $U_\tau/U_S = R_W$. The dashed line shown the prediction for U_τ/U_S from Eq. 4.37 which does not assume small $\omega L/c$.

frequencies. This has already been contrasted with the standing wave model and the slab mode, but now we turn to the empirical relationship from Aure et al. (1996), which has recently been used to estimate the shelf-driven fluxes in Greenlandic and Norwegian fjords (e.g. Sutherland et al., 2014b; Inall et al., 2015). For a rectangular two-layer fjord, the volume flux between fjord and shelf predicted by Aure et al. (1996) in Eq. 4.1 reduces to:

$$\overline{Q} = \beta W \sqrt{HL\frac{g'\eta_0}{\sqrt{2}}} \qquad\qquad \overline{u}_1 = \frac{\beta}{h_1}\sqrt{HL\frac{g'\eta_0}{\sqrt{2}}} \tag{4.43}$$

using $g\Delta M/\rho = g'\eta_S/\sqrt{2}$, where β is an empirical constant of 1.7×10^{-5} and ΔM is the standard deviation of the shelf water column weight (in kg/m^2). For the geometry and stratification used in our model, this expression would give $\overline{u}_1 = 0.06$ m/s. This value can be compared to $\overline{u}_1$ from ROMS in Fig. 4-15, which has values ranging from 0.04 to 0.6 m/s that vary with W/R_d and $\omega L/c$. The Aure model suggests that the fjord response is only a function of the forcing amplitude (sublinearly), and it does not account for any dependence on the fjord width or forcing frequency. Our modeling results show a very different relationship and indicate that the Aure model might not be applicable beyond Kristianssand Fjord, the site where the empirical relationship was derived.

4.5.2 Net exchange and fjord renewal

This study is a step towards understanding the impact of shelf forcing on fjords, but we have not directly addressed the question of net exchange or renewal rates from these flows. Instead, we have described the velocity and density response in the fjord, providing a dynamical framework for understanding these shelf-forced flows. This is a basic step needs to be addressed before answering questions about its impacts on renewal, heat transport and other trace transport (e.g. Gladish and Holland, 2015; Sciascia et al., 2014).

Our results for the excursion length-scale provide some indication of where and when the shelf forcing might be important for renewal and tracer transport. Analogous to the tidal excursion, oscillatory shelf forcing with larger excursions are likely to result in higher dispersion rates than those with shorter excursions. Dispersion from an oscillatory flow field has been studied extensively for tides in typical estuaries (e.g. Fischer, 1976; Geyer and Signell, 1992; MacCready and Geyer, 2010). Tidal dispersion can result in significant down-gradient salt fluxes in some estuaries but only limited fluxes in others. Similarly, there is evidence from the observations in Sermilik that the shelf forcing is important for exporting glacially modified water and renewing the Atlantic water layer

(Chapters 2 & 3).

A logical next step would be to put a tracer field into ROMS simulations to quantitatively assess the flushing of the fjord, the spatial patterns of the renewal rate, and the flux of tracer in various configurations. While useful, this sort of tracer study would be limited by the idealized geometry of the model. Realistic topography is likely to be an important component of modeling the dispersion rate in a fjord. Thus, simulations with more complex topography should eventually be used to answer questions about dispersion and net exchange between fjord and shelf from fluctuating shelf-forced flows.

Another simpler approach from the literature is to relate the oscillatory volume flux to an exchange rate by assuming some efficiency, ϵ. For example, Arneborg (2004) finds a 64% efficiency in Gullmar fjord by comparing the velocity field with time-rate of change in various tracers. However, this efficiency could vary significantly in different fjords, not to mention within a particular fjord, so we do not apply this calculation to our volume fluxes.

We expect that the exchange efficiency (which relates the volume fluxes to net exchange) varies with geometry/bathymetry, along-shore flow on the shelf, fjord width, and other factors. Within the fjord, the waters near the mouth and in the upper layer (where velocities are larger) should be flushed most rapidly. Towards the head of the fjord, where velocities approach zero, the net exchange from shelf-forcing should become negligible. Thus, in the near-glacier region, the buoyancy-driven circulation from a glacier is more likely to dominate the exchange.

In this study, we have made a step towards quantifying the volume fluxes from shelf forcing relative to local wind forcing. Ultimately, it would be desirable to investigate the relative importance of shelf forcing, local wind forcing, *and* buoyancy forcing on the net exchange between fjord and shelf.

4.5.3 Implications for observations: existing and future

The main features of the observations that motivate this modeling work are replicated in the model: a first-mode baroclinic flow with energy at synoptic timescales; high coherence between shelf density, fjord density and fjord velocity at synoptic timescales; velocity and density in quadrature in the middle of the fjord; decay in velocity towards the head of the fjord; and modest amplification of pycnocline fluctuations in the upper fjord.

Ultimately, it is hard to test the relative fit of the standing wave model versus the Kelvin wave model in the observations (i.e. the extent to which lateral structure really matters in Sermilik), because we do not have comprehensive measurements on the shelf nor cross-fjord resolution. Down the middle of the fjord (where our moorings exist), both analytical models have the same relationship between velocity and density, but different overall magnitudes for a given shelf forcing. The difference is in the relationship between shelf amplitude and fjord amplitude.

To test the modeling results, more comprehensive measurements on the shelf are needed. Ideally, a shelf mooring with several CTDs in the vertical could give the amplitude of heaving on the shelf and be compared with the amplitude of heaving within the fjord. Additionally, moorings on either side of the fjord would be valuable for observing the lateral structure and phase propagation around the fjord. Simple bottom-mounted pressure records at several locations along either side of a fjord could provide great insight into the dynamics of the shelf forcing.

In ROMS, as with the Kelvin wave solution, there is more lateral variability in the pycnocline near the fjord mouth, and more lateral variability in velocity near the head of the fjord. Thus, it would be easier to see the lateral variability in density near the fjord mouth but easier to see it in velocity in the upper fjord. Additionally, it is worth noting that the changes in cross-fjord pycnocline tilt, which result in lateral velocity reversals, are expected to be small compared to the vertical heaving, making them hard to observe.

Given the difficulty in instrumenting the shelf well enough to know η_S, it would be useful to eventually relate the fjord response to a different shelf metric that is more easily observable. For example, we can estimate the shelf wind field around Greenland, so relating the fjord response to the shelf wind field could be valuable next step.

4.5.4 Local versus shelf forcing in fjords around Greenland

The non-dimensional number $R_W = \frac{\tau L}{2\rho c^2 \eta_S}$ could be useful to predict the relative importance of shelf versus local forcing around Greenland. Depending on the fjord length, stratification and upper layer thickness, the effectiveness of shelf or local forcing in driving fjord flows could change drastically. For example, consider a fixed shelf forcing amplitude of $\eta_S = 15$ m. In a short fjord of 40 km with $c = 1.5$ m/s (i.e. strong stratification and/or a thick upper layer), the equivalent local wind forcing is $\tau_F = 0.9$ N/m^2, a very large wind stress. On the other hand, for a long fjord of 110 km with $c = 0.7$ m/s (i.e. weaker stratification and/or thin upper layer), the equivalent local wind forcing is only $\tau_F = 0.06$ N/m^2, a relatively common wind amplitude.

In Sermilik Fjord, the largest local wind forcing occurs with downslope wind events from the ice sheet that have typical along-fjord speeds of 20 m/s, equivalent to approximately 0.8 N/m^2

(Oltmanns et al., 2014). On average, there are about eight such events per year, while the mean wind speed in the fjord is only 6 m/s (0.05 N/m^2)(Oltmanns et al., 2014). According to the R_W scaling, the peak wind events with 0.8 N/m^2 are equivalent to $\eta_S = 35$ m, while the mean wind stress is equivalent to only $\eta_S = 2$ m. In the moored observations (Chapters 2 & 3), there are pycnocline fluctuations with amplitudes of 10 to 40 m on synoptic timescales throughout the year. Thus, the scaling from R_W confirms the observational result that shelf forcing is the primary driver of fjord flows during typical local wind conditions. The results also indicate that local wind forcing should be comparable to shelf forcing during the occasional strong downslope wind events from the ice sheet. This is suggested by the velocity observations, where there is typically strong outflow in the upper layer during downslope wind events. However, the impact of these local winds has been difficult to separate from the shelf forcing, since downslope wind events are usually triggered by a low pressure storm systems with strong along-shelf winds. Although these local wind events only happen sporadically, their impact on fjord circulation and mixing should be further explored.

It should be noted that R_W was derived from the standing wave model by assuming that $\omega L/c < 1$ and $W/R_d \ll 1$. It has been shown in this study that this latter assumption is problematic for understanding many aspects of the fjord response for Greenland's fjords with $W/R_d \sim \mathcal{O}(1)$. Nevertheless, Set B of ROMS simulations, which fall squarely within the parameter space of Greenland's fjords with $W/R_d = 0.8$ and $\omega L/c = 1$, follow the prediction from R_W as shown in Fig. 4-21. Thus, our results indicate that R_W might be relevant outside the narrow assumptions from which it was derived. Future work could test the relative importance of local versus shelf forcing across a wide range of W/R_d and $\omega L/c$ to explore when the scaling from R_W breaks down.

4.5.5 Limitations of idealized modeling

The modeling of this study is meant to capture the leading order dynamics of shelf forcing in fjords. There are several aspects of the idealized setup that might warrant further attention in future studies. First, we find that, in our ROMS simulations, the shelf Kelvin waves turn into the fjord and reflect at the head of the fjord with very little dissipation or distortion. In a real fjord, these two junctions could involve more complicated processes that change the nature of the fjord response. In particular, the reflection of the Kelvin wave at the head of the fjord, especially for narrower fjords or ones with complex geometry, might involve significant dissipation of energy. Proehl and Rattray (1984) suggests that most of the Kelvin wave energy that enters the Strait of Juan de Fuca is dissipated within the fjord. Our model contains a flat bottom, vertical walls and uniform initial stratification, so the wave guide does not vary over the domain. In reality, the slope Burger number could change along the coast, altering the nature of coastal trapped wave propagation. In particular, the stratification might be significantly different at the head of a fjord where glacial meltwater and discharge enter the fjord at depth.

Non-linear affects have only been cursorily addressed here. We show that, for the forcing amplitudes of interest ($\eta_S/h_1 < 0.2$), the fjord response scales linearly with the shelf forcing (Appendix 4.B). A few runs with larger amplitude show that the fjord response becomes weakly non-linear around $\eta_S/h_1 = 0.2$. Future runs with larger amplitude forcing could be used to test the role of non-linear effects, perhaps from eddies and jets at the mouth. Mixing within the fjord could also become more important for larger amplitude forcing. For all of the runs presented here, the bulk Richardson number across the pycnocline, $Ri = \frac{g/\rho \Delta\rho \Delta z}{(\Delta u)^2}$, is greater than 0.7 (and usually greater than 2), so we do not expect – nor do we see – significant vertical mixing within the main part of the fjord. (There must, however, be significant mixing in the near-ice regions where freshwater mixes with ocean water.)

Eventually, it would be desirable to build on this framework by adding some complexity to the model, such as more realistic bathymetry. In particular, a sill of various depths could be added to the fjord to test the effect of a sill on fjord-shelf exchange. While Sermilik and Kangderlugssuaq fjords have sills deeper than 500 m, some fjords around Greenland have shallower sills that might play an important role in controlling the along-fjord transport (e.g. Gladish and Holland, 2015). If a sill becomes sufficiently shallow (or the fjord narrow enough), the flow might become hydraulically controlled, as is the case in many non-Greenlandic fjords (Geyer and Ralston, 2011). Additionally, the presence of a sill might alter the stratification for the fjord basin water, thereby changing the wave guide for Kelvin wave propagation and the deformation radius. In the extreme, a sill that is shallower than the pycnocline on the shelf would significantly reduce or eliminate the role of shelf forcing.

4.6 Conclusions

In this study, we have investigated the role of shelf forcing in driving fjord circulation and transport between fjord and shelf across a range of fjord geometries and forcing. In the parameter space of Greenland fjords, we find that the fjord response will vary strongly with two non-dimensional numbers: the fjord width relative to the deformation radius (W/R_d) and the along-fjord adjustment timescale relative to the forcing timescale. A new set of expressions are derived for excursion length-scale and the volume flux through the fjord's mouth, providing a framework for assessing the magnitude of these shelf-forced flows in a wide variety of fjords. In general, the impact of shelf forcing increases for narrower fjords and lower forcing frequencies (or, equivalently, shorter fjords). We have quantified the bounds of where the asymmtotic limits of a narrow 2-D fjord and very wide fjord (independent sides) are applicable, and we have explored the transition between these regimes. For fjords with $W/R_d \sim 1$, there is a modest amplification in the fjord response near the resonant frequency, but not nearly as large as one would expect if cross-fjord variability were neglected (i.e. in a 2-D fjord). Overall, our results suggest that the cross-shore structure of Kelvin waves should be considered in Greenland fjords, contrary to the assumptions in many previous studies. Additionally, a new non-dimensional number is presented, which indicates the relative magnitude of shelf versus local wind forcing for fjords. With this improved framework for shelf-forced flows, future studies should further address the net exchange and the flux of heat, salt and meltwater through Greenland's glacier fjords.

Appendix

4.A Relationship between shelf wind and shelf pycnocline

On an infinite shelf with linear dynamics and periodic wind forcing, one might expect the amplitude of pycnocline heaving to be proportional to the wind stress amplitude and inversely proportional to the forcing frequency: $\eta_S \sim \tau/\omega$. The mean Ekman transport over one half period, π/ω, of wind forcing should be $\frac{2\tau}{\pi\rho f}$ in m^2/s. If this transport goes into depressing or raising the pycnocline over a length-scale of R_d, i.e. a triangle of cross-sectional area $R_d\eta_S/2$, then the wind stress amplitude and pycnocline amplitude at the coast would be related by:

$$\eta_S = \frac{2\tau}{\rho c\omega} \tag{4.44}$$

Our ROMS simulations, however, do not show this relationship between shelf wind and shelf heaving. In Fig. 4-22a, there is a good deal of scatter when η_S is plotted versus τ/ω for many simulations. In ROMS, η_S has a weaker depedence on the forcing period than expected. Fig. 4-22b&c how that η scales more closely with $\tau/\omega^{1/3}$ or just τ. This could be an artifact of our upstream boundary condition (radiation nudging to zero velocity and the initial density stratification). For longer forcing periods, the effect of the boundary condition has sufficient time to propagate into the middle of the domain and might partially damp the shelf response.

Consequently, in order to have roughly the same shelf wave amplitude in Set A, we hold τ constant at $\tau = 0.2$ N/m^2 while varying ω. This results in some variability in η_S, but we can normalize by η_S (diagnosed from the model output) since the relationship between shelf amplitude and fjord response is linear for the amplitudes of interest (Appendix. 4.B).

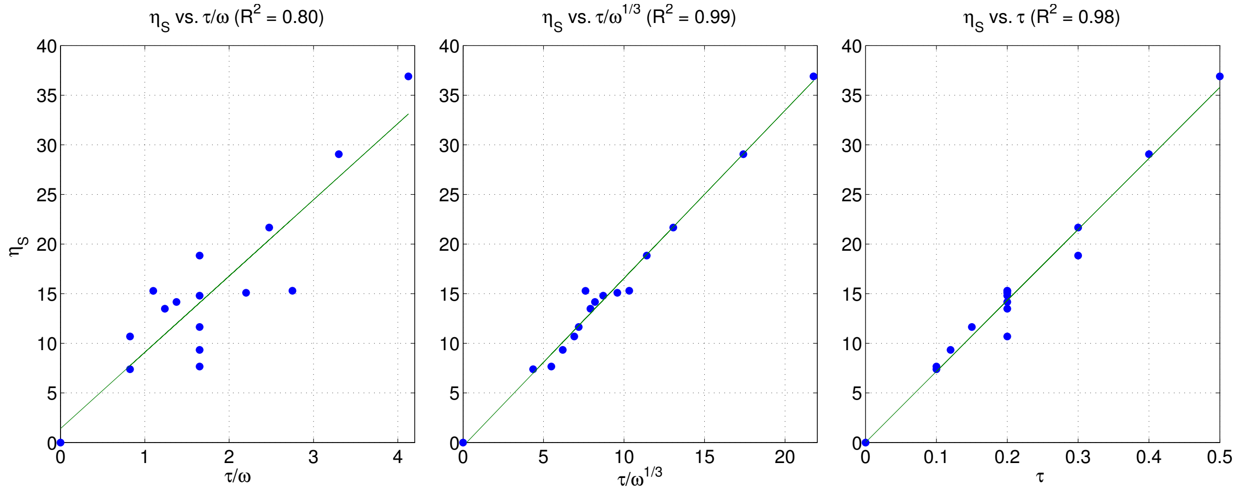

Figure 4-22: Amplitude of shelf heaving at the coast, η_S, as a function of: **a.** τ_S/ω, **b.** $\tau_S/\omega^{1/3}$, **c.** τ_S. Each plot has a linear least squares fit, with the R^2 value in the title.

4.B Linearity between shelf amplitude and fjord response

As shown in Fig. 4-23, the relationship between shelf forcing and fjord response is approximately linear when $\eta_S < 30$. This corresponds to $\eta_S/h_1 < 0.2$, where h_1 is the upper layer thickness. For larger amplitude runs with $\eta_S = 30$ and 36, the relationship becomes slightly non-linear.

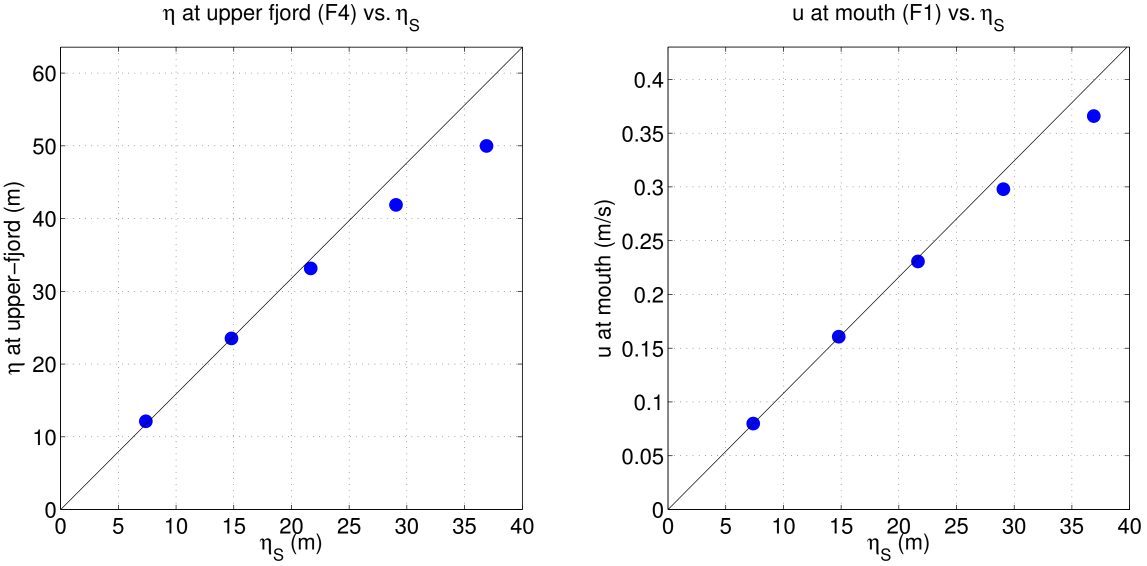

Figure 4-23: Set B runs with shelf forcing of varying amplitude (all with W = 7 km, L = 90 km, c = 1.1 m/s, T = 6 day. Each point is a run with a different amplitude of shelf forcing. **a.** Average amplitude of η at the upper fjord, section F4, vs. shelf wave amplitude, η_S. **b.** Average amplitude of u at the mouth, section F1, vs. shelf wave amplitude, η_S. Both plots include a linear best fit to the three points with smallest η_S values.

4.C Velocity for 14 km wide fjord ($W/R_d = 1.6$)

Fig. 4-24 shows a plan view of the along-fjord velocity for run139, with $W = 14$ km and $T = 6$ days, over one cycle. Fig. 4-25 show cross-fjord sections for the same run. One can see the enhanced cross-fjord structure in these plots compared to the equivalent ones for $W = 7$ km.

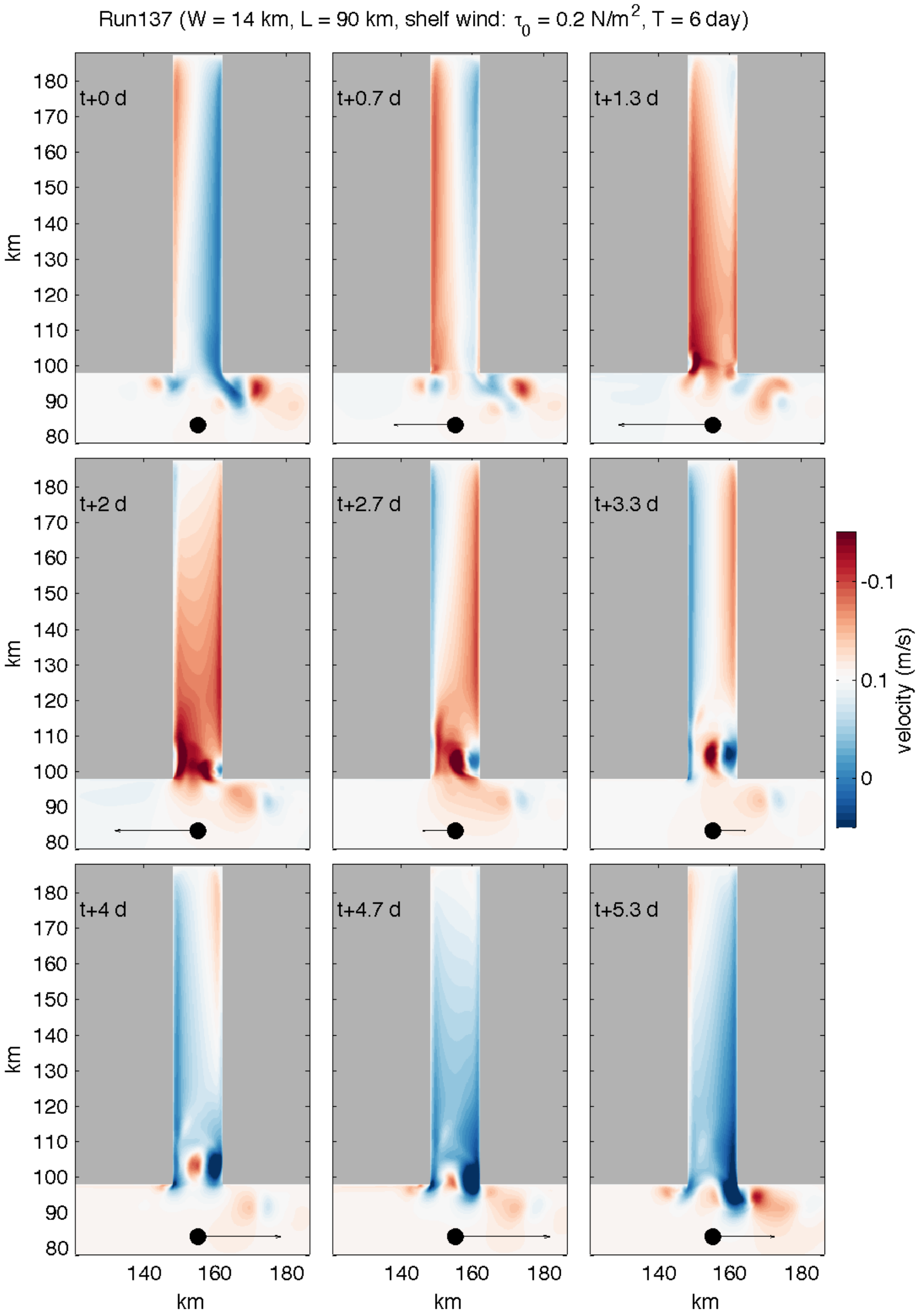

Figure 4-24: [Run137] Same as Fig.4-11b except for 14 km wide fjord ($W/R_d = 1.6$; $\omega L/c = 1$). North/south component of velocity at 75 m depth, i.e. above the pycnocline, for 9 snapshots over a 6-day period. Black arrow and dot on the shelf show the direction shelf wind forcing: the first half of panels have down-welling favorable winds while the second half have upwelling favorable winds. Time in days indicated in the upper left corner of each panel, relative to t = 36 days from the start of a run.

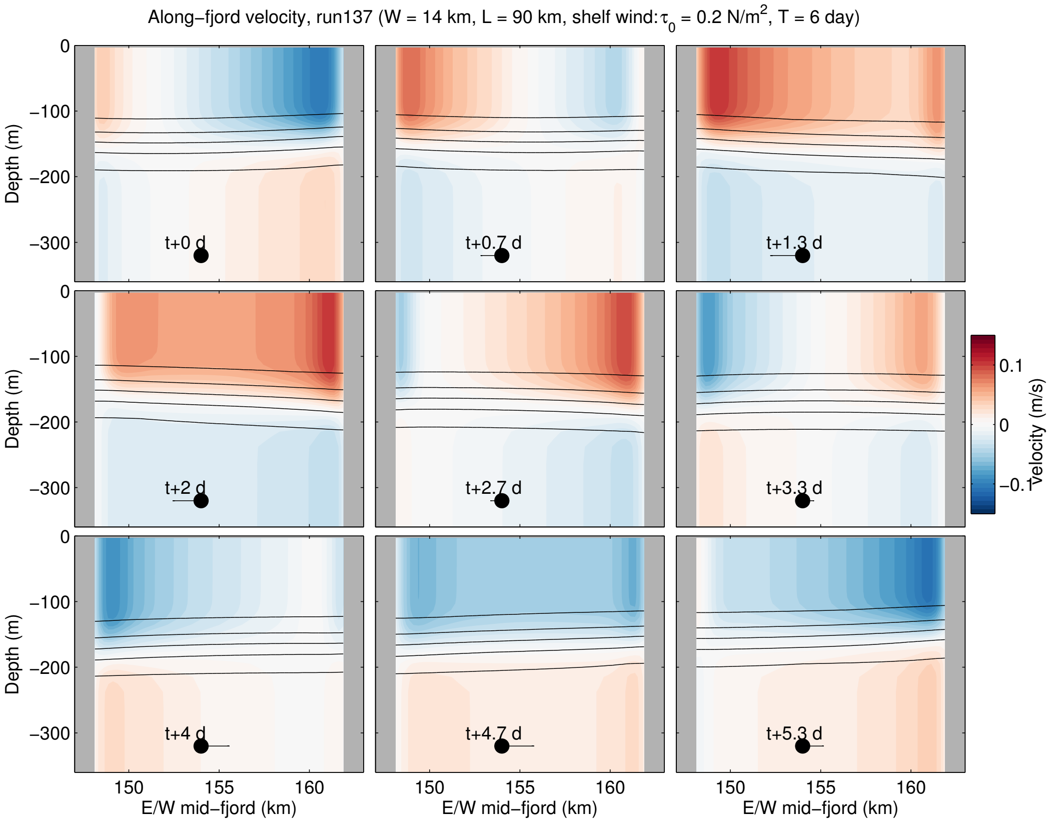

Figure 4-25: [Run 137] Same as Fig. 4-12b except for 14 km wide fjord ($W/R_d = 1.6$; $\omega L/c = 1$). Along-fjord velocity at fjord cross-section, F3, with positive velocity into the fjord. Dot shows wind direction on the shelf. Note: the y-axis cuts off at 350 m but the bottom is at 600 m.

Chapter 5

Conclusions

5.1 Summary

The shrinking ice sheets of Greenland and Antarctica currently contribute to a quarter of current sea level rise (Shepherd et al., 2012), yet our ability to predict future changes is hampered by a limited understanding of how the ocean impacts ice sheets. Ocean warming has been implicated as a driver of glacier acceleration and retreat, with enhanced submarine melting as the presumed connection (Holland et al., 2008a; Murray et al., 2010; Vieli and Nick, 2011; Straneo and Heimbach, 2013). In Greenland, however, we have no direct measurements of this melting and only limited understanding of the circulation in fjords where glaciers meet the ocean. This thesis has explored the circulation, budgets, and dynamics for glacial fjords by integrating observations, theory, and modeling.

The dominant drivers of fjord circulation and water property variability were explored in Chapter 2 with observations from Sermilik and Kangerdlugssuaq fjords, near the third and fifth largest outlet glaciers of the Greenland Ice Sheet, respectively. In the non-summer months, the fjord is dominated by shelf-forced flows, which drive large variability in the heat and salt content of the fjord and rapid exchange with the shelf. This fluctuating shelf-driven flow masks any signal of a mean exchange flow from freshwater forcing. During summer, the shelf forcing is reduced, though still the dominant mode of variability, and a mean exchange flow emerges: warm salty Atlantic water flows towards the glacier at depth and a thick upper layer of glacially modified water is exported. The seasonality in the fjord circulation aligns with the seasonality of shelf winds (strong in non-summer, weaker in summer) and freshwater forcing (large in the summer melt season, smaller in non-summer).

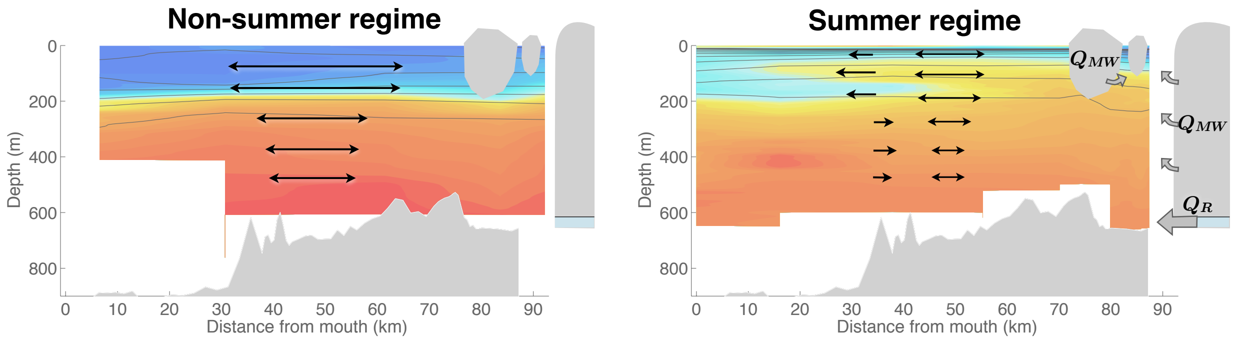

Figure 5-1: Along-fjord profiles of temperature from Sermilik Fjord in non-summer (March 2010) and summer (August 2011) with schematic representation of the fjord velocity. Double sides arrows represent the fluctuating component of the velocity while single sided arrows show the mean velocity profile. In the non-summer months, the circulation is dominated by shelf forced fluctuating velocity (and freshwater fluxes cannot be inferred). In the summer, shelf forcing is reduced and of the same magnitude as the mean exchange flow. During the summer, we can estimate the volume fluxes of submarine meltwater, Q_{MW}, and runoff, Q_R.

In order to assess the fluxes of heat, salt and meltwater from these modes of glacial fjord circulation, a new framework for glacial fjord budgets was developed in Chapter 4. While many studies have used measurements of ocean heat transport to infer submarine melt rates, the fjord budgets that underlie such methods have been largely overlooked. This work presents a new set of equations for evaluating fjord budgets and for inferring a glacier's freshwater fluxes from oceanic observations. Building on estuarine studies of salt budgets, the methods include a decomposition of the transports – to ensure mass conservation and to appropriately account for temporal variability – and many terms that have been neglected in previous studies.

When this new framework was applied to moored records from Sermilik Fjord, two different regimes were found seasonally, matching the seasonality of the fjord circulation. In the non-summer months, when the fjord is dominated by shelf-forcing, the leading order heat and salt balances are between along-fjord transports and changes in heat/salt storage. During this period, the freshwater fluxes from the glacier cannot be inferred as a residual in the budgets. In the summer, the mean exchange flow – consisting of inflowing Atlantic water and outflowing glacially modified water – transports heat and salt towards the glacier. In the heat budget, this imported heat is primarily balanced by heat deposited to melt ice and changes in heat storage. In the salt budget, the imported salt from the exchange flow is primarily balanced by a barotropic outflow. During the summer, the glacier's freshwater fluxes become distinguishable from zero and increase from June to August, with runoff and submarine meltwater of similar magnitudes. These results provide the first time-series of submarine meltwater and runoff fluxes through any glacial fjord.

Having found that the shelf forcing plays a leading role in fjord circulation and heat/salt budgets, the dynamics of shelf forcing were examined in Chapter 5 with ROMS numerical simulations. Analogous to tidal dispersion in estuaries, shelf-forced flows might play an important role in fluxing heat, salt, and meltwater in certain glacial fjords. The underlying dynamics of these shelf-forced flows, however, has been largely ignored in previous studies, with no general framework for understanding shelf forcing across different fjords. Chapter 5 explored the role of shelf forcing for a range of fjord geometries and forcing frequencies. The fjord response was found to be sensitive to two non-dimensional numbers: the fjord width relative to the deformation radius and the along-fjord adjustment timescale relative to the forcing timescale. The transition between narrow and wide fjords was explored, with a focus on the regime of most Greenlandic fjords where the width is of the same order as the deformation radius. Overall, the results show that the response to shelf forcing increases for narrower fjords and for lower forcing frequencies and suggest that the cross-shore structure of Kelvin waves should be considered in Greenlandic fjords.

Lastly, building on the same numerical and analytical modeling, the relative importance of shelf forcing versus local wind forcing was examined. A new non-dimensional number was derived that predicts the relative importance of these two drivers of fjord circulation across a range of forcing strengths and fjord properties. Understanding the basic dynamics of shelf-forced flows and their importance relative to other modes of circulation is an integral step towards accurate modeling of ocean-glacier interactions.

5.2 Future directions

The results from this thesis suggest many avenues for future research. Some desirable next steps towards understanding the dynamics of glacial fjords would include:

Icebergs in glacial fjords The results of Chapter 4 – particularly the large submarine meltwater flux relative to the total discharge from the glacier – suggest that icebergs are a significant contributor to the total meltwater flux in Sermilik Fjord. This is not too surprising, given the thick ice melange and deep iceberg keels that extend into the warm Atlantic Water layer (Andres et al., 2015). However, it is contrary to the assumption of most previous studies that iceberg melting is small compared to glacier melting. New techniques, such as inferring iceberg melt-rates from satellites (Enderlin and Hamilton, 2014) or tracking icebergs (Sutherland et al., 2014a), are opening many possibilities for studying the role of icebergs in glacial fjords and for isolating their meltwater contribution. The fjord circulation, mixing, and heat transport from this distributed buoyancy source has not been examined and could have very different impacts than a localized freshwater input at the glacier.

Additionally, putting aside the buoyancy forcing, the icebergs could alter fjord dynamics by their presence as solid, floating blocks. Their role in providing form drag or direct coupling between atmosphere and ocean should be explored. The presence of icebergs might alter the fjord response to shelf or local wind forcing discussed in Chapter 5, and modeling studies that include icebergs could be used to address these questions.

Integrated glaciology and oceanography studies of submarine melting Chapter 4 highlights the difficulty of inferring a glacier's freshwater fluxes (submarine meltwater and subglacial discharge) from ocean measurements and proposes new methods. In the future, combining oceanic observations with independent glaciological measurements could improve our understanding of submarine melt rates or reveal the mysterious path of subglacial discharge as it transits under the glacier and then mixes into the fjord. In particular, recent studies have used repeat side-scan sonar surveys to measure the morphology of submarine termini and estimate melt rates (Fried et al., 2015; Rignot et al., 2015). Independent estimates of submarine meltwater from oceanic budgets and side-scan sonar could test the accuracy of the different approaches to quantifying meltwater fluxes.

Beyond the bulk melt rates, this type of integrated oceanographic and glaciological study could also provide key insights into the spatial distribution of submarine melting and the resulting terminus morphology, which have important implications for glacier dynamics. For example, the measurements from Fried et al. (2015) show terminus undercutting due to submarine melting, which has been suggested to enhance calving (O'Leary and Christoffersen, 2012; Bartholomaus et al., 2013) and thus present a mechanism for submarine melting to trigger dynamic glacier changes.

The buoyancy-driven exchange flow in glacial fjords Despite significant progress in observing glacial fjords and modeling near-glacier plumes, a coherent understanding of the fjord-scale exchange flow is missing. This thesis provides the most comprehensive picture of the mean exchange flow in any glacial fjord from the records of velocity throughout a summer. With the fjord budgets, we are also able to estimate the freshwater flux that presumably plays a role in driving the exchange flow. The dynamics of this buoyancy-driven exchange flow, however, remain elusive. While we expect there to be a mean pressure gradient associated with the mean velocity field, we cannot observe any persistent density gradients in the fjord surveys, which alias synoptic-scale variability. (A partial exception: several summer surveys show isopycals deepening towards the glacier with 15 km of the glacier.) In a mid-latitude estuary, friction often balances the mean along-estuary pressure gradient, but the momentum balance might be drastically different in a deep glacial fjord. Building on the observational results from this thesis, the dynamics of the glacier-driven exchange flow should to be explored and used to extend our understanding of estuaries to include glacial fjords.

Mixing in glacial fjords Tightly linked to the buoyancy-driven exchange are questions of mixing within the fjord. Our observations from Sermilik Fjord suggest that the shelf-forced flows do not drive significant mixing within the main part of the fjord. However, the freshwater that enters the fjord is converted from zero salinity to > 30 psu within the fjord, so there is undoubtably significant mixing. We speculate that the majority of this mixing occurs in the near-glacier (or near-iceberg) region where convective plumes form, but the details of this mixing are largely unknown. Modeling studies of glacial plumes and submarine melt-rates find that their results are sensitive to their parameterizations of turbulent mixing. Therefore, observations of turbulent fluxes in fjords are needed to test and validate the proliferating field of ocean-glacier modeling. To better understand fjord dynamics, future studies should investigate the relative importance of mixing from upwelling freshwater plumes, outflowing freshwater plumes/jets, and down-stream fjord processes.

Further exploring the shelf-forced dynamics with observations While the oceanic data presented in this thesis constitutes a major step forward in observing glacial fjords, our understanding of glacial fjords is still limited by a dearth of observations. Chapter 5 signals the importance of understanding the cross-fjord structure in fjords whose width is approximately equal to the deformation radius and the along-fjord structure in fjords whose adjustment timescale is comparable to the forcing timescale – both of which are the case for many Greenland fjords. Future moorings arrays that can show signal propagation in both the along and across-fjord direction would provide valuable testing of the modeling results of Chapter 5. These could be simple bottom-mounted pressure sensors along either side of the fjord that could measure the synoptic pressure anomalies. Additionally, more comprehensive shelf moorings with CTDs at multiple depths are needed to be able to compare the amplitude of pycnocline heaving on the shelf with the amplitude in the fjord.

Innovative observing platforms Other open questions require not only more observations but also new observing techniques. Innovative platforms are required to measure the near-glacier region – an area often inaccessible by boat – and the surface waters where icebergs transit. Incomplete mooring coverage near the surface leads to the largest source of uncertainty in the budgets of Chapter 3. Furthermore, the fjord-scale dynamics that are the focus of this thesis are only part of resolving ocean-glacier interactions in fjords: the small-scale dynamics in the near-glacier region are also key. The turbulent exchanges of heat and freshwater near the ice-ocean boundary layer, where upwelling plumes emanate from glaciers, should modulate submarine melting, but they have never been directly measured at calving-front glaciers and are crudely parameterized in models. Bulk estimates of fjord heat transport, such as those presented here, should eventually be complemented with measurements of turbulent heat fluxes at the ice-ocean boundary.

5.3 A final thought

The polar oceans – an integral piece in the climate system – are undergoing rapid change, and the nexus of ocean, ice, land, and atmosphere exists in the coastal regions. Though coastal physical oceanography is an expansive field, its literature largely omits high-latitude processes. Glacial fjords are estuaries, but the current understanding of estuarine dynamics does not encompass these outliers. Nevertheless, the uniqueness of glacial fjords should not be overemphasized, for the ocean-glacier community is at risk of reinventing the estuarine wheel. The work here has shown that a wide range of topics in the existing coastal dynamics literature – from salt budgets and tidal dispersion in estuaries to Kelvin waves in straits – form relevant analogies for glacial fjords. In doing so, this thesis hopefully makes a step towards integrating the disparate fields of ice-ocean interactions and coastal physical oceanography.

Bibliography

Allen, J. S., 1975: Coastal trapped waves in a stratified ocean. *Journal of Physical Oceangraphy*, **5**, 300–325.

Amundson, J. M., M. Fahnestock, M. Truffer, J. Brown, M. P. Lüthi, and R. Motyka, 2010: Ice mélange dynamics and implications for terminus stability, Jakobshavn Isbræ, Greenland. *Journal of Geophysical Research*, **115 (F1)**, F01 005.

Andersen, M. L., et al., 2010: Spatial and temporal melt variability at Helheim Glacier, East Greenland, and its effect on ice dynamics. *Journal of Geophysical Research*, **115 (F4)**.

Andres, M., A. Silvano, F. Straneo, and D. R. Watts, 2015: Icebergs and Sea Ice Detected with Inverted Echo Sounders. *Journal of Atmospheric and Oceanic Technology*, **32 (5)**, 1042–1057.

Arneborg, L., 2004: Turnover times for the water above sill level in Gullmar Fjord. *Continental Shelf Research*, **24 (4–5)**, 443–460.

Aure, J., J. Molvær, and A. Stigebrandt, 1996: Observations of inshore water exchange forced by a fluctuating offshore density field. *Marine Pollution Bulletin*, **33 (1–6)**, 112–119.

Bamber, J., M. van den Broeke, J. Ettema, J. Lenaerts, and E. Rignot, 2012: Recent large increases in freshwater fluxes from Greenland into the North Atlantic. *Geophysical Research Letters*, **39 (19)**.

Bartholomaus, T. C., C. F. Larsen, and S. O'Neel, 2013: Does calving matter? Evidence for significant submarine melt. *Earth and Planetary Science Letters*, **380**, 21–30.

Beaird, N., F. Straneo, and W. Jenkins, 2015: Spreading of Greenland meltwaters in the ocean revealed by noble gases. *Geophysical Research Letters*, **42**.

Bevan, S. L., A. Luckman, S. A. Khan, and T. Murray, 2015: Seasonal dynamic thinning at Helheim Glacier. *Earth and Planetary Science Letters*, **415 (C)**, 47–53.

Brink, K., 1991: Coastal-Trapped Waves and Wind-Driven Currents Over the Continental-Shelf. *Annual Review of Fluid Mechanics*, **23**, 389–412.

Carroll, D., D. A. Sutherland, E. L. Shroyer, J. D. Nash, G. A. Catania, and L. A. Stearns, 2015: Modeling Turbulent Subglacial Meltwater Plumes: Implications for Fjord-Scale Buoyancy-Driven Circulation. *Journal of Physical Oceanography*, **45**, 2169–2185.

Chauché, N., et al., 2014: Ice–ocean interaction and calving front morphology at two west Greenland tidewater outlet glaciers. *The Cryosphere*, **8 (4)**, 1457–1468.

Christoffersen, P., R. Mugford, K. Heywood, I. Joughin, J. Dowdeswell, J. Syvitski, A. Luckman, and T. Benham, 2011: Warming of waters in an East Greenland fjord prior to glacier retreat: mechanisms and connection to large-scale atmospheric conditions. **5**, 701–714.

Christoffersen, P., M. O'Leary, J. H. Van Angelen, and M. van den Broeke, 2012: Partitioning effects from ocean and atmosphere on the calving stability of Kangerdlugssuaq Glacier, East Greenland. *Annals of Glaciology*, **53 (60)**, 249–256.

Chu, V. W., 2014: Greenland ice sheet hydrology: A review. *Progress in Physical Geography*, **38 (1)**, 19–54.

Cottier, F. R., F. Nilsen, R. Skogseth, V. Tverberg, J. Skarðhamar, and H. Svendsen, 2010: Arctic fjords: a review of the oceanographic environment and dominant physical processes. *Geological Society, London, Special Publications*, **344 (1)**, 35–50.

Cowton, T., D. Slater, A. Sole, D. Goldberg, and P. Nienow, 2015: Modeling the impact of glacial runoff on fjord circulation and submarine melt rate using a new subgrid-scale parameterization for glacial plumes. *Journal of Geophysical Research-Oceans*, **120 (2)**, 796–812.

Durland, T. S. and B. Qiu, 2003: Transmission of subinertial Kelvin waves through a strait. **33 (7)**, 1337–1350.

Enderlin, E. M. and G. Hamilton, 2014: Estimates of iceberg submarine melting from high-resolution digital elevation models: application to Sermilik Fjord, East Greenland. *Journal of Glaciology*, **60 (224)**, 1084–1092.

Enderlin, E. M. and I. M. Howat, 2013: Submarine melt rate estimates for floating termini of Greenland outlet glaciers (2000–2010). *Journal of Glaciology*, **59 (213)**, 67–75.

Enderlin, E. M., I. M. Howat, S. Jeong, M.-J. Noh, J. H. Van Angelen, and M. R. van den Broeke, 2014: An improved mass budget for the Greenland ice sheet. *Geophysical Research Letters*, **41 (3)**, 866–872.

Farmer, D. and H. Freeland, 1983: The Physical Oceanography of Fjords. *Progress in Oceanography*, **12 (2)**, 147–219.

Fischer, H. B., 1976: Mixing and dispersion in estuaries. *Annual Review of Fluid Mechanics*, 107–133.

Foga, S., L. A. Stearns, and C. J. van der Veen, 2014: Application of Satellite Remote Sensing Techniques to Quantify Terminus and Ice Mélange Behavior at Helheim Glacier, East Greenland. *Marine Technology Society Journal*, **48 (5)**, 81–91.

Fried, M. J., G. A. Catania, and T. C. Bartholomaus, 2015: Distributed subglacial discharge drives significant submarine melt at a Greenland tidewater glacier. *Geophysical Research Letters*, **42**, 1–9.

Gade, H., 1979: Melting of ice in sea water: A primitive model with application to the Antarctic ice shelf and icebergs. *Journal of Physical Oceangraphy*, **9 (1)**, 189–198.

Garvine, R. W., 1985: A simple model of estuarine subtidal fluctuations forced by local and remote wind stress. *Journal of Geophysical Research*, **90 (C6)**, 11 945–11 948.

Geyer, W. R., 1997: Influence of Wind on Dynamics and Flushing of Shallow Estuaries. *Estuarine Coastal and Shelf Science*, **44**, 713–722.

Geyer, W. R. and D. Ralston, 2011: The Dynamics of Strongly Stratified Estuaries. Elsevier Inc., 37–52.

Geyer, W. R. and R. P. Signell, 1992: A Reassessment of the Role of Tidal Dispersion in Estuaries and Bays. *Estuaries*, **15 (2)**, 97–108.

Gill, A. E., 1982: *Atmosphere-Ocean Dynamics.*

Gladish, C. V. and D. M. Holland, 2015: Oceanic Boundary Conditions for Jakobshavn Glacier. Part I: Variability and Renewal of Ilulissat Icefjord Waters, 2001–14. *Journal of Physical Oceanography*, **45**, 3–32.

Harden, B. E., I. A. Renfrew, and G. N. Petersen, 2011: A Climatology of Wintertime Barrier Winds off Southeast Greenland. *Journal of Climate*, **24 (17)**, 4701–4717.

Harden, B. E., F. Straneo, and D. Sutherland, 2014: Moored observations of synoptic and seasonal variability in the East Greenland Coastal Current. *Journal of Geophysical Research-Oceans*, **119 (12)**, 8838–8857.

Hasholt, B., B. U. Hansen, O. Humlum, and S. H. Mernild, 2004: Meteorological stations at the Sermilik Station, Southeast Greenland: physical environment and meteorological observations 2002. *Danish Journal of Geography*, **104 (2)**, 47–58.

Holbrook, J. R., C. Cannon, and D. G. Kachel, 1983: Two-year observations of coastal-fjord interactions in the strait of Juan de Fuca. *Coastal Oceanography*, H. Gade, A. Edwards, and H. Svendsen, Eds., Plenum, New York, 411–426.

Holland, D. M., R. H. Thomas, B. de Young, M. H. Ribergaard, and B. Lyberth, 2008a: Acceleration of Jakobshavn Isbræ triggered by warm subsurface ocean waters. **1 (10)**, 659–664.

Holland, P. R., A. Jenkins, and D. M. Holland, 2008b: The Response of Ice Shelf Basal Melting to Variations in Ocean Temperature. *Journal of Climate*, **21 (11)**, 2558–2572.

Howat, I. M., I. Joughin, and T. A. Scambos, 2007: Rapid Changes in Ice Discharge from Greenland Outlet Glaciers. *Science*, **315 (5818)**, 1559–1561.

Huthnance, J. M., 1977: On Coastal Trapped Wves: Analysis and Numerical Calculation by Inverse Iteration. *Journal of Physical Oceanography*, **8**, 74–92.

Inall, M. E. and P. A. Gillibrand, 2010: The physics of mid-latitude fjords: a review. *Geological Society, London, Special Publications*, **344 (1)**, 17–33.

Inall, M. E., T. Murray, F. R. Cottier, K. Scharrer, T. J. Boyd, K. J. Heywood, and S. L. Bevan, 2014: Oceanic heat delivery via Kangerdlugssuaq Fjord to the south-east Greenland ice sheet. *Journal of Geophysical Research-Oceans*, **(119)**, 1–15.

Inall, M. E., F. Nilsen, F. R. Cottier, and R. Daae, 2015: Shelf/fjord exchange driven by coastal-trapped waves in the Arctic. *Journal of Geophysical Research-Oceans*, **120**, 1–21.

Jackson, R. H., F. Straneo, and D. A. Sutherland, 2014: Externally forced fluctuations in ocean temperature at Greenland glaciers in non-summer months. *Nature Geoscience*, **7 (7)**, 503–508.

Janzen, C. D. and K. C. Wong, 2002: Wind-forced dynamics at the estuary-shelf interface of a large coastal plain estuary. *Journal of Geophysical Research*, **107 (C10)**, 1–12.

Jenkins, A., 1999: The impact of melting ice on ocean waters. *Journal of Physical Oceanography*, **29 (9)**, 2370–2381.

Jenkins, A., 2011: Convection-Driven Melting near the Grounding Lines of Ice Shelves and Tidewater Glaciers. **41 (12)**, 2279–2294.

Jenkins, A., K. Nicholls, and H. Corr, 2010: Observation and parameterization of ablation at the base of Ronne Ice Shelf, Antarctica. **40 (10)**, 2298–2312.

Johnson, H. L. and C. Garrett, 2006: What fraction of a Kelvin wave incident on a narrow strait is transmitted? **36**, 945–954.

Johnson, H. L., A. Münchow, K. K. Falkner, and H. Melling, 2011: Ocean circulation and properties in Petermann Fjord, Greenland. *Journal of Geophysical Research*, **116 (C1)**, C01 003.

Joughin, I., R. B. Alley, and D. M. Holland, 2012: Ice-Sheet Response to Oceanic Forcing. *Science*, **338 (6111)**, 1172–1176.

Kantha, L. H. and C. A. Clayson, 1994: An improved mixed layer model for geophysical applications. *Journal of Geophysical Research-Oceans*, **99 (C12)**, 25 235–25 266.

Kimura, S., P. R. Holland, A. Jenkins, and M. Piggott, 2014: The Effect of Meltwater Plumes on the Melting of a Vertical Glacier Face. *Journal of Physical Oceanography*, **44**, 3099–3117.

Klinck, J., J. O'Brien, and H. Svendsen, 1981: Simple model of fjord and coastal circulation interaction. **11 (12)**, 1612–1626.

Knudsen, M., 1900: Ein hydrographischer lehrsatz . *Ann. Hydrogr. Marit. Meteor.*, **28**, 316–320.

Lemke, P., et al., 2007: Observations: Changes in snow, ice and frozen ground. Climate Change 2007: The Physical Science Basis, S. Solomon et al., Eds. Tech. rep.

Lenaerts, J. T. M., D. Le Bars, L. Kampenhout, M. Vizcaino, E. M. Enderlin, and M. R. Broeke, 2015: Representing Greenland ice sheet freshwater fluxes in climate models. *Geophysical Research Letters*, **42 (15)**, 1–9.

Lerczak, J. A., W. R. Geyer, and R. Chant, 2006: Mechanisms Driving the Time-Dependent Salt Flux in a Partially Stratified Estuary. *Journal of Physical Oceanography*, **36**, 2296–2311.

MacAyeal, D. R., J. Freed-Brown, W. W. Zhang, and J. M. Amundson, 2012: The influence of ice melange on fjord seiches. *Annals of Glaciology*, **53 (60)**, 45–49.

MacCready, P. and N. S. Banas, 2011: *Residual Circulation, Mixing, and Dispersion; Treatise on Estuarine and Coastal Science*, Vol. 2. Elsevier Inc.

MacCready, P. and W. R. Geyer, 2010: Advances in Estuarine Physics. *Annual Review of Marine Science*, **2 (1)**, 35–58.

Mernild, S. H. and G. E. Liston, 2012: Greenland Freshwater Runoff. Part II: Distribution and Trends, 1960–2010. *Journal of Climate*, **25 (17)**, 6015–6035.

Mernild, S. H., et al., 2010: Freshwater flux to Sermilik Fjord, SE Greenland. **4 (4)**, 453–465.

Moffat, C., 2014: Wind-driven modulation of warm water supply to a proglacial fjord, Jorge Montt Glacier, Patagonia. *Geophysical Research Letters*, **41**, 3943–3950.

Monismith, S. G., 1986: An experimental study of the upwelling response of stratified reservoirs to surface shear stress. *Journal of Fluid Mechanics*, 1–33.

Montgomery, R. B., 1974: Comments on 'Seasonal Variability of the Florida Current'. *Journal of Marine Research*, **32**, 1–5.

Moon, T., I. Joughin, B. Smith, M. R. Broeke, W. J. van de Berg, B. Noel, and M. Usher, 2014: Distinct patterns of seasonal Greenland glacier velocity. *Geophysical Research Letters*, **41 (20)**, 7209–7216.

Moon, T., I. Joughin, B. Smith, and I. Howat, 2012: 21st-Century Evolution of Greenland Outlet Glacier Velocities. *Science*, **336 (6081)**, 576–578.

Moore, G. and I. Renfrew, 2005: Tip jets and barrier winds: A QuikSCAT climatology of high wind speed events around Greenland. *Journal of Climate*, **18 (18)**, 3713–3725.

Mortensen, J., J. Bendtsen, K. Lennert, and S. Rysgaard, 2014: Seasonal variability of the circulation system in a west Greenland tidewater outlet glacier fjord, Godthåbsfjord (64 N). *Journal of Geophysical Research-Earth Surface*, **(119)**, 2591–2603.

Mortensen, J., K. Lennert, J. Bendtsen, and S. Rysgaard, 2011: Heat sources for glacial melt in a sub-Arctic fjord (Godthåbsfjord) in contact with the Greenland Ice Sheet. *Journal of Geophysical Research*, **116 (C1)**.

Motyka, R., L. Hunter, K. Echelmeyer, and C. Connor, 2003: Submarine melting at the terminus of a temperate tidewater glacier, LeConte Glacier, Alaska, USA. *Annals of Glaciology*, **36 (1)**, 57–65.

Motyka, R. J., W. P. Dryer, J. Amundson, M. Truffer, and M. Fahnestock, 2013: Rapid submarine melting driven by subglacial discharge, LeConte Glacier, Alaska. *Geophysical Research Letters*, **40 (19)**, 5153–5158.

Murray, T., et al., 2010: Ocean regulation hypothesis for glacier dynamics in southeast Greenland and implications for ice sheet mass changes. *Journal of Geophysical Research-Earth Surface*, **115**, 1–15.

Nick, F. M., A. Vieli, I. M. Howat, and I. Joughin, 2009: Large-scale changes in Greenland outlet glacier dynamics triggered at the terminus. **2 (2)**, 110–114.

Nick, F. M., et al., 2012: The response of Petermann Glacier, Greenland, to large calving events, and its future stability in the context of atmospheric and oceanic warming. *Journal of Glaciology*, **58 (208)**, 229–239.

Noel, B., W. J. van de Berg, E. van Meijgaard, P. Kuipers Munneke, R. S. W. van de Wal, and M. R. van den Broeke, 2015: Summer snowfall on the Greenland Ice Sheet: a study with the updated regional climate model RACMO2.3. *The Cryosphere Discussions*, **9 (1)**, 1177–1208.

O'Leary, M. and P. Christoffersen, 2012: Calving on tidewater glaciers amplified by submarine frontal melting. *The Cryosphere*, **7**, 119–128.

Oltmanns, M., F. Straneo, G. W. K. Moore, and S. H. Mernild, 2014: Strong Downslope Wind Events in Ammassalik, Southeast Greenland. *Journal of Climate*, **27 (3)**, 977–993.

Pettersson, H., 1920: Internal movements in coastal waters and meteorological phenomena. *Geogrfiska Annaler of Stockholm*, **1**, 32–66.

Pritchard, H. D., R. J. Arthern, D. G. Vaughan, and L. A. Edwards, 2009: Extensive dynamic thinning on the margins of the Greenland and Antarctic ice sheets. *Nature*, **461 (7266)**, 971–975.

Proehl, J. A. and M. Rattray, 1984: Low-Frequency Response of Wide Deep Estuaries to Non-Local Atmospheric Forcing. **14 (5)**, 904–921.

Rignot, E., I. Fenty, Y. Xu, and C. Cai, 2015: Undercutting of marine-terminating glaciers in West Greenland. *Geophysical Research Letters*, **42 (14)**, 5909–5917.

Rignot, E., M. Koppes, and I. Velicogna, 2010: Rapid submarine melting of the calving faces of West Greenland glaciers. *Nature Geoscience*, **3 (3)**, 187–191.

Salcedo-Castro, J., D. Bourgault, and B. deYoung, 2011: Continental Shelf Research. *Continental Shelf Research*, **31 (13)**, 1396–1406.

Schild, K. M. and G. S. Hamilton, 2013: Seasonal variations of outlet glacier terminus position in Greenland. *Journal of Glaciology*, **59 (216)**, 759–770.

Schjøth, F., C. S. Andresen, F. Straneo, T. Murray, K. Scharrer, and A. Korablev, 2012: Campaign to map the bathymetry of a major Greenland fjord. *Eos Trans. AGU*, **93 (14)**, 141.

Sciascia, R., C. Cenedese, D. Nicoli, P. Heimbach, and F. Straneo, 2014: Impact of periodic intermediary flows on submarine melting of a Greenland glacier. *Journal of Geophysical Research-Oceans*, **119**, 1–21.

Sciascia, R., F. Straneo, C. Cenedese, and P. Heimbach, 2013: Seasonal variability of submarine melt rate and circulation in an East Greenland fjord. *Journal of Geophysical Research-Oceans*, **118 (5)**, 2492–2506.

Shchepetkin, A. F. and J. C. McWilliams, 2005: The regional oceanic modeling system (ROMS): a split-explicit, free-surface, topography-following-coordinate oceanic model. *Ocean Modelling*, **9 (4)**, 347–404.

Shepherd, A., et al., 2012: A Reconciled Estimate of Ice-Sheet Mass Balance. *Science*, **338 (6111)**, 1183–1189.

Spigel, R. H. and J. Imberger, 1980: The classification of mixed-layer dynamics of lakes of small to medium size. *Journal of Physical Oceanography*, **10**, 1104–1121.

Stearns, L. and G. Hamilton, 2007: Rapid volume loss from two East Greenland outlet glaciers quantified using repeat stereo satellite imagery. *Geophysical Research Letters*, **34 (5)**, 5503–5508.

Stevens, L. A., F. Straneo, S. B. Das, A. J. Plueddemann, A. L. Kukulya, and M. Morlighem, 2015: Linking catchment-scale subglacial discharge to subsurface glacially modified waters near the front of a marine terminating outlet glacier using an autonomous underwater vehicle. *The Cryosphere Discussions*, **9 (5)**, 4583–4624.

Stigebrandt, A., 1981: A Mechanism Governing the Estuarine Circulation in Deep, Strongly Stratified Fjords. *Estuarine Coastal and Shelf Science*, **13 (2)**, 197–211.

Stigebrandt, A., 1990: On the response of the horizontal mean vertical density distribution in a fjord to low-frequency density fluctuations in the coastal water. **42 (5)**, 605–614.

Stigebrandt, A., 2010: Fiord circulation. *Encyclopedia of Ocean Sciences*, Ocean Currents: A Derivative of the Encyclopedia . . . , Boston.

Stigebrandt, A., 2012: Hydrodynamics and circulation of fjords. *Encyclopedia of Lakes and Resevoirs*, L. Bengtsson, R. W. Herschy, and R. W. Fairbridge, Eds., Springer Science, Dordrecht, 327–344.

Straneo and Cenedese, 2015: The Dynamics of Greenland's Glacial Fjords and Their Role in Climate. *Annual Review of Marine Science*, **7 (1)**, 89–112.

Straneo, F., R. G. Curry, D. A. Sutherland, G. S. Hamilton, Cenedese, K. Våge, and L. A. Stearns, 2011: Impact of fjord dynamics and glacial runoff on the circulation near Helheim Glacier. *Nature Geoscience*, **4 (5)**, 322–327.

Straneo, F., G. S. Hamilton, D. A. Sutherland, L. A. Stearns, F. Davidson, M. O. Hammill, G. B. Stenson, and A. Rosing-Asvid, 2010: Rapid circulation of warm subtropical waters in a major glacial fjord in East Greenland. *Nature Geoscience*, **3 (3)**, 1–5.

Straneo, F. and Heimbach, 2013: North Atlantic warming and the retreat of Greenland's outlet glaciers. *Nature*, **504 (7478)**, 36–43.

Straneo, F., et al., 2012: Characteristics of ocean waters reaching Greenland's glaciers. *Annals of Glaciology*, **53 (60)**, 202–210.

Straneo, F., et al., 2013: Challenges to Understand the Dynamic Response of Greenland's Marine Terminating Glaciers to Oceanic and Atmospheric Forcing. *Bull. Amer. Meteor. Soc.*, **94 (8)**, 1131–1144.

Sutherland, D. and R. Pickart, 2008: The East Greenland coastal current: Structure, variability, and forcing. *Progress in Oceanography*, **78 (1)**, 58–77.

Sutherland, D., G. E. Roth, and G. Hamilton, 2014a: Quantifying flow regimes in a Greenland glacial fjord using iceberg drifters. *Geophysical Research Letters*, **41**, 8411–8420.

Sutherland, D. A., Straneo, G. B. Stenson, F. J. M. Davidson, M. O. Hammill, and A. Rosing-Asvid, 2013: Atlantic water variability on the SE Greenland continental shelf and its relationship to SST and bathymetry. *Journal of Geophysical Research*, **118 (2)**, 847–855.

Sutherland, D. A. and F. Straneo, 2012: Estimating ocean heat transports and submarine melt rates in Sermilik Fjord, Greenland, using lowered acoustic Doppler current profiler (LADCP) velocity profiles. *Annals of Glaciology*, **53 (60)**, 50–58.

Sutherland, D. A., F. Straneo, and R. S. Pickart, 2014b: Characteristics and dynamics of two major Greenland glacial fjords. *Journal of Geophysical Research-Oceans*, **119**, 1–25.

Svendsen, H., 1980: Exchange processes above sill level between fjords and coastal water. *Fjord Oceanography*, H. Freeland, D. Farmer, and C. D. Levings, Eds., Plenum Press, New York, 355–355 362.

Taylor, G. I., 1921: Tidal Oscillations in gulfs and rectangular basins. *Proceedings of London Mathematical Society*, **20**, 148–181.

Thomas, R., 2004: Force-perturbation analysis of recent thinning and acceleration of Jakobshavn Isbrae, Greenland. *Journal of Glaciology*, **50 (168)**, 57–66.

Toulany, B. and C. Garrett, 1984: Geostrophic Control of Fluctuating Barotropic Flow through Straits. **14**, 1–7.

Våge, K., et al., 2011: The Irminger Gyre Circulation, convection, and interannual variability. *Deep-Sea Research Part I*, **58 (5)**, 590–614.

Van As, D., et al., 2014: Increasing meltwater discharge from the Nuuk region of the Greenland ice sheet and implications for mass balance (1960–2012). *Journal of Glaciology*, **60 (220)**, 314–322.

van den Broeke, M., et al., 2009: Partitioning Recent Greenland Mass Loss. *Science*, **326 (5955)**, 984–986.

Vieli, A. and F. M. Nick, 2011: Understanding and Modelling Rapid Dynamic Changes of Tidewater Outlet Glaciers: Issues and Implications. *Surveys in Geophysics*, **32 (4-5)**, 437–458.

Wang, D.-P., 1979: Wind-driven circulation in the Chesapeak Bay, Winter 1975. *Journal of Physical Oceanography*, **9**, 564–572.

Warner, J. C., C. R. Sherwood, H. G. Arango, and R. P. Signell, 2005: Performance of four turbulence closure models implemented using a generic length scale method. *Ocean Modelling*, **8 (1-2)**, 81–113.

Weijer, W., M. E. Maltrud, M. W. Hecht, H. A. Dijkstra, and M. A. Kliphuis, 2012: Response of the Atlantic Ocean circulation to Greenland Ice Sheet melting in a strongly-eddying ocean model. *Geophysical Research Letters*, **39 (9)**.

Wilson, N. J. and F. Straneo, 2015: Water exchange between the continental shelf and the cavity beneath Nioghalvfjerdsbræ (79 North Glacier). *Geophysical Research Letters*, **42 (18)**, 1–7.

Xu, Y., E. Rignot, I. Fenty, D. Menemenlis, and M. Mar Flexas, 2013: Subaqueous melting of Store Glacier, West Greenland from three-dimensional, high-resolution numerical modeling and ocean observations. *Geophysical Research Letters*, **40 (17)**, 1–6.

Xu, Y., E. Rignot, D. Menemenlis, and M. Koppes, 2012: Numerical experiments on subaqueous melting of Greenland tidewater glaciers in response to ocean warming and enhanced subglacial discharge. *Annals of Glaciology*, **53 (60)**, 229–234.